PhD Thesis

Precision measurement of the $e^+e^- \to \pi^+\pi^-\pi^0$ cross section using initial-state radiation

始状態輻射光子を用いた $e^+e^- \to \pi^+\pi^-\pi^0$ 過程の反応断面積の精密測定

Yuki SUE

須江祐貴

July, 2024

Graduate School of Science
Nagoya University

名古屋大学大学院 理学研究科

名古屋大学
NAGOYA UNIVERSITY

Abstract

This thesis reports a precise measurement of the $e^+e^- \to \pi^+\pi^-\pi^0$ cross section in the center-of-mass energies from 0.62 GeV to 3.5 GeV using the radiative-return method. We use a data sample of electron-positron collisions, corresponding to 191 fb^{-1} of the integrated luminosity, collected at a center-of-mass energy near the $\Upsilon(4S)$ resonance with the Belle II detector at the SuperKEKB collider. We measure the cross section and discuss the contribution to the hadronic-vacuum-polarization components of the muon anomalous magnetic moment from the 3π channel.

Contents

Chapter 1

Introduction

The standard model (SM) is a theory that describes the primordial composition of matter in the universe and the fundamental interactions between them: it consists of fermions with spin 1/2, gauge bosons with spin 1, and Higgs bosons with spin 0 that give them masses. In 2012, the ATLAS and CMS experiments at the LHC collider discovered the predicted Higgs boson, thus accomplished the SM [1, 2]. However, physics beyond the SM is still necessary to explain phenomena such as the existence of dark matter and the asymmetry between matter and antimatter. To test the predictive power of the SM, we are pursuing with two approaches: one is to directly produce and discover new particles through particle collisions at high energies, and the other is to precisely measure low-energy observables to test for possible physics beyond the SM that may appear as higher-order effects. Even in 2023, certain phenomena suggestive of physics beyond the SM have been observed, but no definitive discoveries have been made

The anomalous magnetic moment of muon, a second-generation lepton, is one of the most precisely measurable and predictable physical quantities and has been subjected to the SM test for over half a century. The Hamiltonian of the magnetic dipole moment $\vec{\mu}$ and electric dipole moment $\vec{d}$ of leptons in an electromagnetic field is given by

$$\mathcal{H} = -\vec{\mu} \cdot \vec{B} - \vec{d} \cdot \vec{E}, \tag{1.1}$$

where $\vec{B}$ and $\vec{E}$ are the magnetic and electric field. The muon with mass m_μ, spin vector $\vec{S}$, and electrical charge $q = e$ has a magnetic moment

$$\vec{\mu} = g_\mu \frac{e\hbar}{2m_\mu} \vec{S}, \tag{1.2}$$

where g_μ is the gyro-magnetic ratio. Although the Dirac theory predicts the value of g_μ to be exactly two, g_μ deviates slightly from this value due to radiation corrections. This deviation is known as the muon anomalous magnetic moment, defined as

$$a_\mu \equiv \frac{g_\mu - 2}{2}. \tag{1.3}$$

The predicted value in the SM is calculated as the sum over all Feynman diagrams via loop interactions of SM particles. Thus, most particles in the SM are involved, and the direct measurement value may incorporate a contribution from physics beyond the SM.

As of 2023, the situation is complex and puzzling: the significant difference of 5 standard deviations (σ) between measured values and theoretical predictions is questionable. Figure 1.1 summarizes the a_μ values and uncertainties of measurements and SM predictions. Both the measurement and prediction precision have reached the order of 0.1 parts-per-million (ppm).

The experimental value of a_μ is determined by measuring the spin dynamics of the muon in a static magnetic field using $\mu^+ \to e^+\bar{\nu}_\mu\nu_e$ decay. The measurements conducted at the Brookhaven National Laboratory (BNL) [3] and the Fermi National Laboratory (FNAL) [4, 5] are in good agreement, with the world average of

$$a_\mu(\text{Exp.}) = 116\,592\,059(22) \times 10^{-11}, \tag{1.4}$$

and the precision, the relative uncertainty, of 0.19 ppm. To confirm this, analysis using an even larger FNAL dataset and validation experiments at the Japan Proton Accelerator Research Complex (J-PARC) using a method independent of the previous ones are underway.

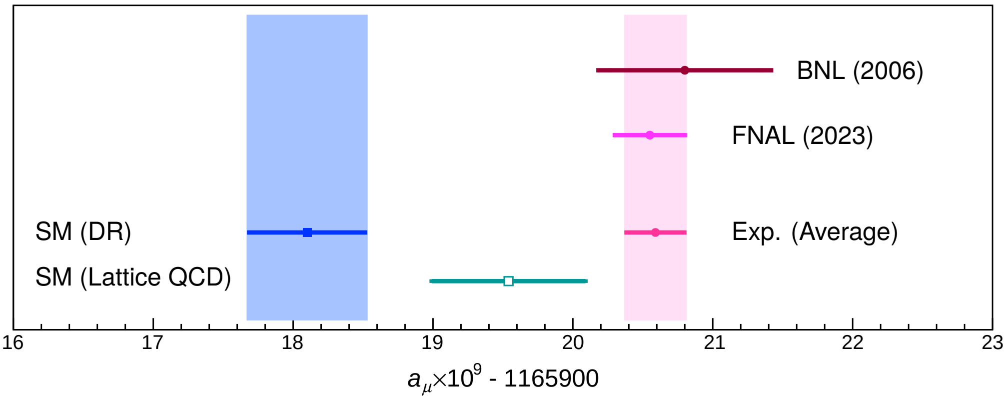

Figure 1.1: Muon anomalous magnetic moment of the direct measurement and SM prediction. The circles show the experimental results from BNL [3] and FNAL [4, 5], and the average. The filled and open squares with error bards represent the SM predictions with the HVP contributions calculated using the dispersion relation (DR) [6] and lattice QCD [7], respectively. The red and blue bands show the total uncertainty on measurement average and SM prediction using the DR, respectively.

The theoretical prediction of a_μ is the sum of contributions from all sectors, including quantum electrodynamics (QED), electroweak (EW), and quantum chromodynamics (QCD). The precision of the SM prediction is 0.37 ppm. The hadronic vacuum polarization (HVP) term in the QCD contribution dominates the uncertainty. Since a prediction using perturbative QCD at low energy is difficult, predictions in the energy range below 2–3 GeV are made by several alternative methods, using dispersion relations [1] and lattice QCD.

The dispersive method uses cross sections of the processes $e^+e^- \to hadrons$ as theoretical input via the dispersion relation. The cross sections for hadronic annihilation in various final states are exclusively measured by e^+e^- collider experiments. and contribution to a_μ is calculated as a sum of the cross sections. This calculation method has long been the standard for predicting HVP contribution. The predicted a_μ using the dispersive method is

$$a_\mu(\text{SM, DR}) = 116\,591\,810(43) \times 10^{-11}, \tag{1.5}$$

and the major uncertainty of HVP contribution derives from the inputs, i.e., the uncertainty on measured cross sections. The difference from the experimental average is

$$\Delta a_\mu = a_\mu(\text{Exp.}) - a_\mu(\text{SM, DR}) = 249(48) \times 10^{-11}, \tag{1.6}$$

which corresponds to a significance of 5.1σ.

On the other hand, the lattice QCD precision has been improving year by year thanks to advancements in computational power and methods, and a result in 2020 [7] finally achieved that is compatible with the precision of the dispersive method. However, this value is closer to the direct measurement; the difference from the experimental average is

$$a_\mu(\text{Exp.}) - a_\mu(\text{SM, Lattice QCD}) = 105(55) \times 10^{-11}. \tag{1.7}$$

This disagrees with the dispersive method by a significance of more than 2σ. Several independent groups have subsequently validated it using lattice QCD, and the results are consistent.

Another controversial point is that the discrepancies of measured cross section between e^+e^- experiments are becoming non-negligible in the dispersive method, particularly in the $e^+e^- \to \pi^+\pi^-$ cross section measurement, which is the most significant HVP contribution. Figure 1.2 compares the $e^+e^- \to \pi^+\pi^-$ contribution between experiments, especially the difference between the KLOE [8, 9, 10, 11], *BABAR* [12] and CMD-3 [13, 14], which are more accurate and cannot be ignored. The difference between the combination of the $e^+e^- \to \pi^+\pi^-$ cross section as of 2020 [6] and the CMD-3 result in 2023 [13, 14] is critical, reducing the significance between the measured a_μ (Exp.).

[1]It is also referred to as *the dispersive method* or e^+e^- *data-driven method*.

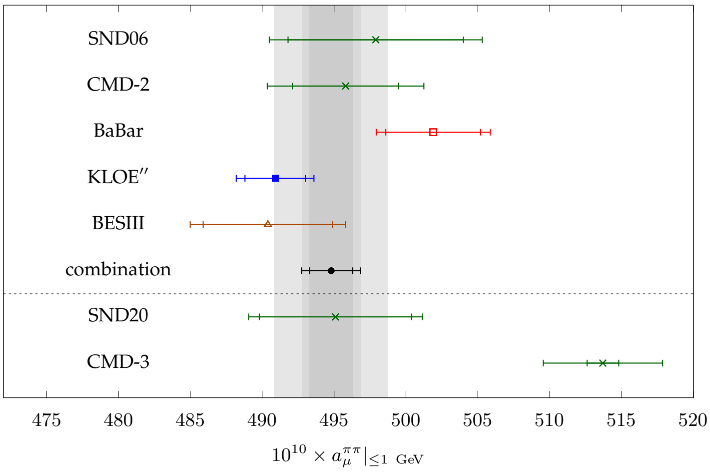

Figure 1.2: Results for $a_\mu^{\pi\pi}$ in the energy range $\leq$ 1 GeV. The gray bands correspond to the combined fit to all e^+e^- datasets apart from SND20 and CMD-3, with the largest band including the additional systematic effect due to the BABAR-KLOE tension. The plot is adapted from Ref. [20]

Another way to estimate the $\pi^+\pi^-$ HVP contribution with the dispersion relation is to use the τ hadronic spectral function obtained from the tau hadronic decay, $\tau^\pm \to \pi^\pm\pi^0\nu_\tau$ decay. Precision measurements have been made by Belle [15], CLEO [16], ALEPH [17] and others. If we replace only the $\pi^+\pi^-$ HVP contribution estimated from the e^+e^- data by from the τ data, the difference from the experiment average is [18]

$$a_\mu(\mathrm{Exp.}) - a_\mu(\mathrm{SM}, \tau) = 135(45) \times 10^{-11}. \tag{1.8}$$

This is close to the central value estimated by Lattice QCD.

Future validation is planned with the MUonE experiment, which measures muon-electron scattering angle, as a completely independent method to estimate HVP contribution [19].

If the difference between the experimental and SM predictions is due to physics beyond the SM, the contribution from new particles that are sufficiently heavier than the muon can be represented by a general form given by

$$a_\mu^{\mathrm{NP}} = \mathcal{C}\left(m_\mu/M_{\mathrm{NP}}\right)^2, \tag{1.9}$$

where $\mathcal{C}$ is a coupling constant and M_{NP} is the mass of a new particle. Its sensitivity is proportional to the square of the ratio of the lepton mass to the new particle mass, making it approximately 40000 times greater than that of the electron $g-2$. This property makes muon $g-2$ an ideal candidate for exploring physics beyond the Standard Model. The difference in Eq. (1.8) suggests the existence of new particles of about 100 GeV/c^2, assuming that the coupling constant is about α/π, which is the same size as the weak contribution,

In summary, it is necessary to clarify the deviations between experimental and theoretical values, variations in HVP calculation methods, and differences in the cross-section measurements. In these a_μ differences, have we have potentially underestimated or neglected systematic uncertainty in the direct $g-2$ measurements or the cross-section measurements? Are there any unaccounted effects in lattice QCD, or could we be encountering contributions from physics beyond the SM? It is vital to have more precise measurements of the cross section from independent experiments to confirm the dispersive method. This thesis presents a new experiment to measure the $e^+e^- \to \pi^+\pi^-\pi^0$ cross section, which would be a help in the enormous verification efforts to solve the muon $g-2$ puzzle.

The cross section for the $e^+e^- \to \pi^+\pi^-\pi^0$ process is the second largest contribution to the HVP term. Systematic uncertainty, particularly on the cross section below 1.1 GeV, is dominant. A precise evaluation of the detection efficiency is crucial in this measurement. This channel is expected to be statistically comparable to previous measurements based on a dataset collected during the early Belle II experimental period. Furthermore, this measurement of the first light-hadron production cross section measurement performed in the Belle II experiment could provide an indication of the challenges in the future analyses of other channels.

This thesis presents a measurement of the cross section of the $e^+e^- \to \pi^+\pi^-\pi^0$ process using the electron-positron collision dataset at or near a center-of-mass energy of 10.58 GeV collected by the Belle II experiment. The radiative return method is employed to scan the hadronic energy range of 0.6–3.5 GeV, which involves studying the $e^+e^- \to \pi^+\pi^-\pi^0\gamma$ process associated with energetic initial-state radiation photon emission. The thesis proceeds in the following structure. Chapter 2 introduces the theoretical prediction of a_μ, the measurement method of the hadronic annihilation cross section in e^+e^- experiments, and the analysis strategy, followed by the experimental setup in chapter 3. The analytical method is presented as follows: chapter 4 covers extraction of signal events, chapter 5 covers estimation of residual background processes, chapter 6 covers estimation of signal efficiency, and chapter 7 covers the mitigation of detector effects that may distort the energy spectrum. The results and a_μ contribution calculated from the measured cross section are summarized and discussed in chapter 8.

Chapter 2

Theoretical prediction of muon anomalous magnetic moment and hadronic annihilation cross section measurements in e^+e^- collisions

This chapter briefly reviews the theoretical predictions for the muon anomalous magnetic moment, the important technique for measuring $e^+e^- \to hadrons$ cross sections, the radiative return method, and the previous measurements of the $e^+e^- \to \pi^+\pi^-\pi^0$ cross section. Finally, a strategy of the measurements made in this thesis is presented.

2.1 Theoretical prediction of a_μ

The muon anomalous magnetic moment a_μ is predicted as a sum of contributions via virtual particles in all sectors of the SM. The contribution is divided into QED term, EW term, HVP term and hadronic light-by-light (HLbL) term:

$$a_\mu^{\mathrm{SM}} = a_\mu^{\mathrm{QED}} + a_\mu^{\mathrm{EW}} + a_\mu^{\mathrm{HVP}} + a_\mu^{\mathrm{HLbL}}.$$

The consensus of theorists as of 2020 is summarized in the Theory Initiative White Paper [6]. Table 2.1 shows the contributions of the theoretical values, where the HVP and HLbL contributions are divided into leading order (LO), next-to-leading order (NLO) and next-to-next leading order (NNLO) terms. The sub-sections provide a detailed description of the values and calculation methods for the contributions. These are based on Ref. [6] and the references listed in Table 2.1.

Contribution	Value $\times 10^{11}$	References
Experiment (World average)	116 592 059.(22)	Refs. [3, 5]
QED	116 584 718.931(104)	Refs. [21, 22]
Electroweak	153.6(1.0)	Refs. [23, 24]
HVP LO (e^+e^-)	6 931(40)	Refs. [25, 26, 27, 28, 29, 30]
HVP NLO (e^+e^-)	$-98.3(7)$	Ref. [30]
HVP NNLO (e^+e^-)	12.4(1)	Ref. [31]
HVP (e^+e^-, LO + NLO + NNLO)	6 845(40)	
HLbL (phenomenology + lattice + NLO)	92(18)	Ref. [6]
Total SM Value	116 591 810(43)	Refs. [6]
Difference: $\Delta a_\mu := a_\mu^{\mathrm{Exp.}} - a_\mu^{\mathrm{SM}}$	249(48)	

Table 2.1: Summary of the contributions to a_μ^{SM}, adopted from Ref [6].

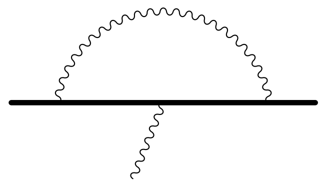

(a) One-loop diagram

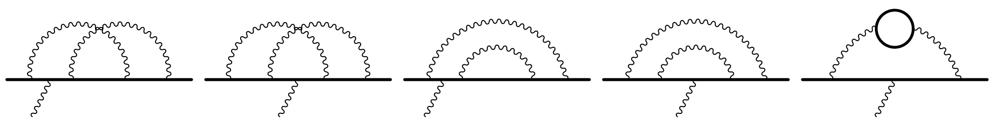

(b) Two-loop diagrams

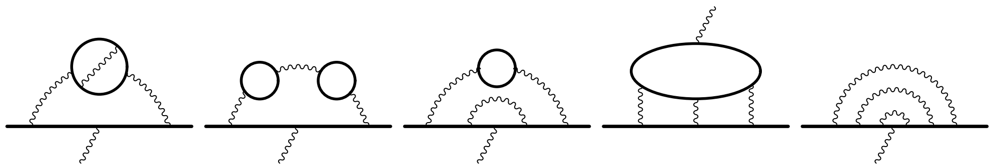

(c) Three-loop diagrams

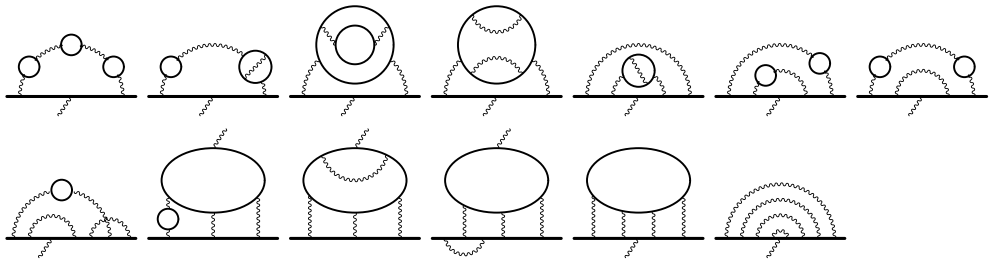

(d) Four-loop diagrams

Figure 2.1: (a) One-loop, (b) Two-loop, (c) three-loop and (d) four-loop Feynman diagrams contributing to a_μ^{QED}. The three-loop and four-loop diagrams are divided into gauge-invariant sets. The straight and wavy lines represent lepton and photon propagators, respectively. Adopted from Refs. [21, 22].

2.1.1 QED contribution

The QED contribution can be expressed using the perturbative expansion as

$$a_\mu^{\text{QED}} = \sum_n a_\mu^{\text{QED},n\text{-loop}} \tag{2.1}$$

$$= \sum_n \left(\frac{\alpha}{\pi}\right)^n A^{(2n)} \tag{2.2}$$

$$= \sum_n \left(\frac{\alpha}{\pi}\right)^n \left(A_1^{(2n)} + A_2^{(2n)}\left(\frac{m_\mu}{m_e}\right) + A_2^{(2n)}\left(\frac{m_\mu}{m_\tau}\right) + A_3^{(2n)}\left(\frac{m_\mu}{m_e}, \frac{m_\mu}{m_\tau}\right)\right), \tag{2.3}$$

where $a_\mu^{\text{QED},n\text{-loop}} = (\alpha/\pi)^n A^{(2n)}$ is the QED contribution of n-loop diagrams, corresponding to the $2n$ th-order of the perturbative series of QED. In Eq. (2.3), the coefficients of the series $A^{(2n)}$ are divided into the mass-independent and mass-dependent terms. Each coefficient $A_{i=1,2,3}^{(2n)}$ can be calculated in a technique with Feynman diagrams. The lowest term, which is the only mass-independent term, corresponds to the diagram in Fig. 2.1 (a), where $A_1^{(2)} = 1/2$; this is the famous Schwinger's calculation of the one-loop Feynman diagram of QED in 1947. The contribution with the QED coupling constant

$\alpha^{-1} = 137.035\,999\,046(27)$ is

$$a_\mu^{\text{QED,1-loop}} = \frac{\alpha}{2\pi} = 116\,140\,973.321(23) \times 10^{-11}\ [22]. \tag{2.4}$$

The number of Feynman diagrams increases as the number of loops, one diagram for $A^{(2)}$, seven for $A^{(4)}$, 72 for $A^{(6)}$ and 891 for $A^{(8)}$. The Feynman diagrams up to four-loop are depicted in Figs. 2.1 (b)–(d), and the contributions are [22]

$$a_\mu^{\text{QED,2-loop}} = 413\,217.625\,8(70) \times 10^{-11} \tag{2.5}$$
$$a_\mu^{\text{QED,3-loop}} = 30\,140.902\,33(33) \times 10^{-11} \tag{2.6}$$
$$a_\mu^{\text{QED,4-loop}} = 381.004(17) \times 10^{-11}. \tag{2.7}$$

The numerical and analytical calculations are in good agreement up to the four-loop diagrams. The five-loop term is numerically calculated with 12672 diagrams as shown in Fig 2.2, and results in

$$a_\mu^{\text{QED,5-loop}} = 5.078\,3(59) \times 10^{-11}\ [22]. \tag{2.8}$$

The contribution of higher-order term, the sixth-loop term, is expected to be the order of 10^{-12} and is negligibly small compared to the target uncertainty on a_μ [32]. In total, the QED contribution is

$$a_\mu^{\text{QED}} = 116\,584\,718.931(104) \times 10^{-11}\ [22]. \tag{2.9}$$

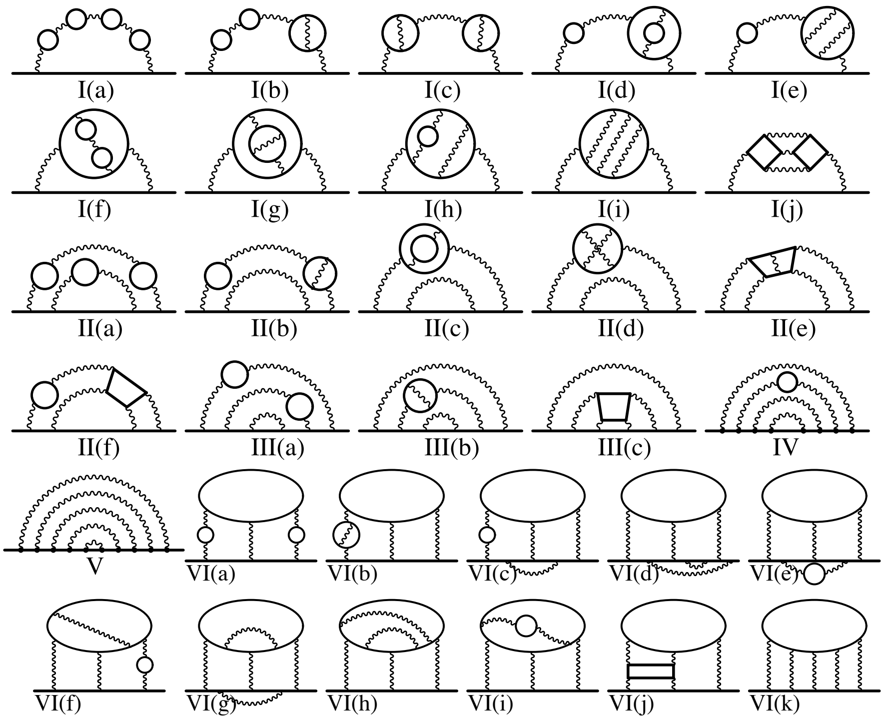

Figure 2.2: Five-loop Feynman diagrams contributing to a_μ^{QED}. They are divided into 32 gauge-invariant subsets over six super sets. The straight and wavy lines represent lepton and photon propagators, respectively. The external photon vertex is omitted for simplicity. Adopted from Ref. [21].

The precision of the QED contribution depends on the coupling constant α, which is determined by measurements. The recent situation for α measurements is shown in Fig. 2.3. The measured values in the atom-interferometry experiments using Cesium atoms and Rubidium atoms are

$$\alpha^{-1}(\mathrm{Cs}) = 137.035\,999\,046(27)[33] \tag{2.10}$$
$$\alpha^{-1}(\mathrm{Rb}) = 137.035\,999\,206(11)[34], \tag{2.11}$$

respectively, and differ by more than 5σ. The α value for Cesium is used in the calculations in this thesis. In another way, the α can be derived from the electron $g-2$. In contrast to muons, the significantly smaller mass of electrons than hadrons and EW bosons results in very small hadronic and electroweak contributions at sizes of 1.47 pats-per-billion (ppb) and 0.026 ppb, respectively [22]. This statement implies that the electron $g-2$ measurements, currently measured with a precision of 0.11 ppb, are precise measurements of the QED contribution. The α calculated from the measured electron $g-2$ is

$$\alpha^{-1}(a_e) = 137.035\,999\,166(15)[35], \tag{2.12}$$

which is smaller than the experimental value using Cesium by 3.9σ and larger than that using Rubidium by 2.1σ. Although such differences $\Delta a_e/a_e = \mathcal{O}(10^{-12})$ are visible at present, the uncertainty on the QED contribution to a_μ of $\mathcal{O}(10^{-9})$ is negligible compared to the differences in a_μ, $\Delta a_\mu/a_\mu = \mathcal{O}(10^{-7})$, which is currently under discussion.

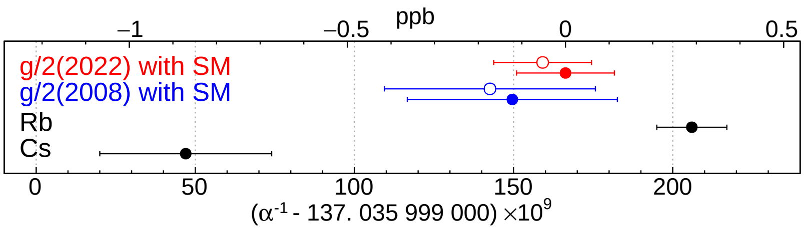

Figure 2.3: The coupling constant α determined from electron $g-2$ measurement by Northwestern in 2023 (red) [35], from electron $g-2$ measurement by Harvard in 2008 (blue) [36], and from atom-interferometry experiments using Rubidium [34] and Cesium [33]. The slight difference between solid and open points comes from the use of different $A^{(10)}$ values. Adopted from Ref. [35]

2.1.2 Electroweak contribution

The EW contribution includes all SM contributions except pure QED, HVP, and HLbL contributions. Hence, it corresponds to the Feynman diagram via the EW bosons and is strongly suppressed by the heavy masses of Z, W and H bosons. The contribution is divided into one-loop, two-loop and higher-order terms as [24]

$$a_\mu^{\mathrm{EW}} = a_\mu^{\mathrm{EW,1\text{-}loop}} + a_{\mu;\mathrm{bos}}^{\mathrm{EW,2\text{-}loop}} + a_{\mu;\mathrm{ferm}}^{\mathrm{EW,2\text{-}loop}} + a_\mu^{\mathrm{EW,>2\text{-}loop}}, \tag{2.13}$$

where the two-loop contribution is divided into bosonic and fermionic terms.

Typical diagrams of one-loop EW contribution are shown in Fig. 2.4. The lowest-order, one-loop, term is calculated as [24]

$$a_\mu^{\mathrm{EW,1\text{-}loop}} = \frac{G_F}{\sqrt{2}}\frac{m_\mu^2}{8\pi^2}\left(\frac{5}{3} + \frac{1}{3}\left(1 - 4\sin^2\theta_W\right)^2 + \mathcal{O}\left(\frac{m_\mu^2}{m_{Z,H}^2}\right)\right),\ \sin^2\theta_W = 1 - \left(\frac{m_W}{m_Z}\right)^2 = 0.2231 \tag{2.14}$$

where $G_F = 1.1663788(6) \times 10^{-5}\ \mathrm{GeV}^{-2}$ is the Fermi constant from muon lifetime [37], θ_W is the weak mixing angle, $m_{W,Z,H}$ are the masses of W, Z, and H bosons. The one-loop contribution is calculated to be

$$a_\mu^{\mathrm{EW,1\text{-}loop}} = 194.79(1) \times 10^{-11}\ [24,\ 6]. \tag{2.15}$$

The terms of $\mathcal{O}(m_\mu^2/m_{Z,H}^2)$ in Eq. (2.14) is negligibly small, less than 10^{-13}.

The two-loop contribution is a term proportional to $G_F\alpha$; the diagrams are shown in Fig. 2.5. The bosonic contribution is defined as the contribution of the two-loop diagram without a closed fermion loop such as Fig 2.5 (a)–(c), and the fermionic is a diagram including a closed fermion loop such as Fig 2.5 (d)–(f). The total two-loop contribution is

$$a_\mu^{\text{EW,2-loop}} = a_{\mu;\text{bos}}^{\text{EW,2-loop}} + a_{\mu;\text{ferm}}^{\text{EW,2-loop}} = -41.2(1.0) \times 10^{-11} \text{ [6]}. \tag{2.16}$$

The dominant contirbution beyond two-loop is estimated to be $a_\mu^{\text{EW},>2\text{-loop}} = (0 \pm 0.20) \times 10^{-11}$.

In total, EW contribution is

$$a_\mu^{\text{EW}} = 153.6(1.0) \times 10^{-11} \text{ [6]}. \tag{2.17}$$

This uncertainty is mainly caused by hadronic uncertainty in the two-loop fermionic loop diagram (see Fig. 2.5 (e)), and uncertainties arising from other effects, higher-order terms above the three-loop, and experimental uncertainty in boson masses and top-quark mass are considered negligible as they are less than 10^{-12}.

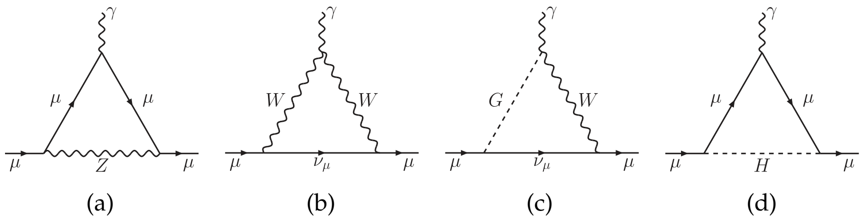

Figure 2.4: One-loop Feynman diagrams contributing to a_μ^{EW}, which is adopted from Ref. [6].

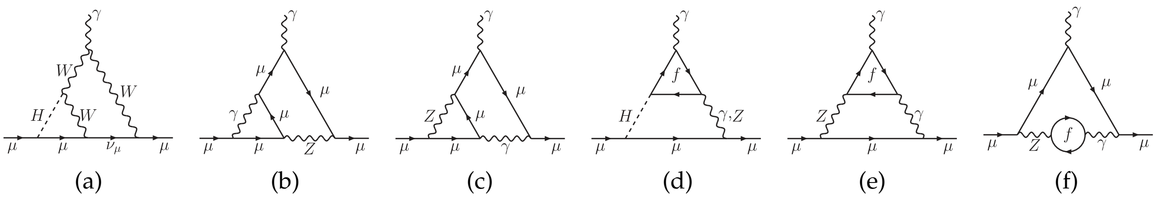

Figure 2.5: Bosonic (a)–(c) and fermionic (d)–(f) two-loop Feynman diagrams contributing to a_μ^{EW}, which is adopted from Ref. [6].

2.1.3 LO HVP prediction using dispersive relation

The HVP term is a contribution with quark and gluon via a virtual photon, as a diagram shown in Fig. 2.6. It is hard to analytically calculate the photon propagator including the HVP, in a perturbative way. Considering vacuum polarization in photon propagation, the vacuum polarization effects can be expressed by replacing free photon propagator in the one-loop diagram (Fig. 2.1 (a)) [38]

$$\frac{1}{q^2} \to \int_0^\infty \frac{ds}{s} \frac{1}{q^2 - s} \frac{1}{\pi} \text{Im}\Pi(s), \tag{2.18}$$

where q is the momentum of virtual photon, and $\text{Im}\Pi(s)$ is the imaginary part of the photon self-energy function. By using the optical theorem, we can obtain the relation between the imaginary part of the hadronic contribution to the photon self-energy Π_{had} and the hadronic cross section from electron-positron annihilation:

$$\text{Im}\Pi^{\text{had}}(q^2) = \frac{s}{4\pi\alpha} \sigma(e^+e^- \to hadrons). \tag{2.19}$$

Here, the ratio of hadronic cross section from e^+e^- annihilation to di-muon production as the $R(s)$ in a function of squared hadronic energy s, so-called hadronic R-ratio, is often defined as

$$R(s) := \sigma_{\text{tot}} / \frac{4\pi\alpha^2}{3s}, \tag{2.20}$$

where σ_{tot} is the total cross section of the hadron and the normalization factor $4\pi\alpha^2/3s$ is the point-like cross section (tree level) of the $e^+e^- \to \mu^+\mu^-$ process for $s \gg 4m_\mu$. The LO HVP contribution to a_μ, the contribution from the diagram shown in Fig. 2.6, can be calculated by replacing the a_μ contribution of a "massive photon" of $\sqrt{s}$ mass [39] with the HVP according to Eq. (2.18) [40, 38],

$$a_\mu = \frac{\alpha}{\pi}\int_0^\infty \frac{ds}{s}\frac{1}{\pi}\mathrm{Im}\Pi(s)K(s). \tag{2.21}$$

The $K(s)$ is the QED kernel function, which can be expressed as [41]

$$K(s) = (2-x^2) + \frac{(1+x^2)(1+x)^2}{x^2}\left(\ln(1+x) - x + \frac{x-2}{2}\right) + \frac{1+x}{1-x}x^2\ln x, \tag{2.22}$$

where $x = (1-\beta_\mu)/(1+\beta_\mu)$ and $\beta_\mu = \sqrt{1-4m_\mu^2/s}$. The R-ratio can be obtained using the perturbative QCD calculation on the high energy side, while on the low energy side, the measured R-ratio is used as input instead. Namely, the LO HVP contribution can be calculated using Eqs. (2.19), (2.21), and (2.20) as

$$a_\mu^{\text{LO,HVP}} = \frac{\alpha^2}{3\pi^2}\left(\int_{m_{\pi^0}^2}^{E_{\text{cut}}^2} ds\frac{R_{e^+e^-\text{data}}(s)K(s)}{s} + \int_{E_{\text{cut}}^2}^\infty ds\frac{R_{\text{pQCD}}(s)K(s)}{s}\right), \tag{2.23}$$

where $R_{e^+e^-\text{data}}(s)$ and $R_{\text{pQCD}}(s)$ are the R-ratios measured by the e^+e^- experiments and calculated from perturbative QCD, and E_{cut}^2 is a transition point of the R-ratios. Introducing the $\hat{K}(s) \equiv K(s)\cdot s\cdot m_\mu^2$, Eq. (2.23) is rewritten as [40]

$$a_\mu^{\text{LO,HVP}} = \left(\frac{\alpha m_\mu}{3\pi}\right)^2\left(\int_{m_{\pi^0}^2}^{E_{\text{cut}}^2} ds\frac{R_{e^+e^-\text{data}}(s)\hat{K}(s)}{s^2} + \int_{E_{\text{cut}}^2}^\infty ds\frac{R_{\text{pQCD}}(s)\hat{K}(s)}{s^2}\right), \tag{2.24}$$

The variable $\hat{K}(s)$ increases gradually from approximately 0.63 at the threshold of $s = 4m_\pi^2$, and reaches 1 at $s \to \infty$, as shown in Fig. 2.7. Thus, examining Eq. (2.24), we can see that the primary term within the integral is a product of the R-ratio and $1/s^2$. Therefore, the contribution of the R-ratio is significantly amplified in the low-energy region.

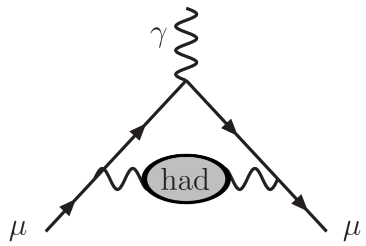

Figure 2.6: One-loop Feynman diagrams contributing to a_μ^{HVP}. The straight and wavy lines represent lepton and photon propagators, respectively. The grey blob represents hadronic vacuum polarization. Adopted from Ref. [21].

Figure 2.8 shows the measured R-ratio and perturbative QCD prediction over a wide energy range up to Z boson. In the cross section measurement, measurements are carried out at exclusive channels in the region below 2 GeV and are calculated as the integral sum of all channels. Figure 2.9 plots the contributions to the R-ratio from the exclusive final states. The precise measurements for the exclusive final states are conducted by electron-positron collider experiments: CMD-2, CMD-3 and SND at the VEPP-2M and VEPP-2000 collider, KLOE at the DAΦNE collider, BESIII at the BEPC collider, and BABAR at the PEP-II collider. Figure 2.10 plots the measured inclusive R-ratio and the estimate of perturbative QCD in the energy range of 1.937–4.50 GeV. Inclusive measurements in the energy region above 1.8 are made as well by BESII at the BEPC collider, BESIII, and KEDR at BINP. The breakdown of the contribution for each energy range is shown in Fig. 2.11, and it can be seen that it mostly depends on that below 1.8 GeV, i.e., in the region where the experimental values are used as input.

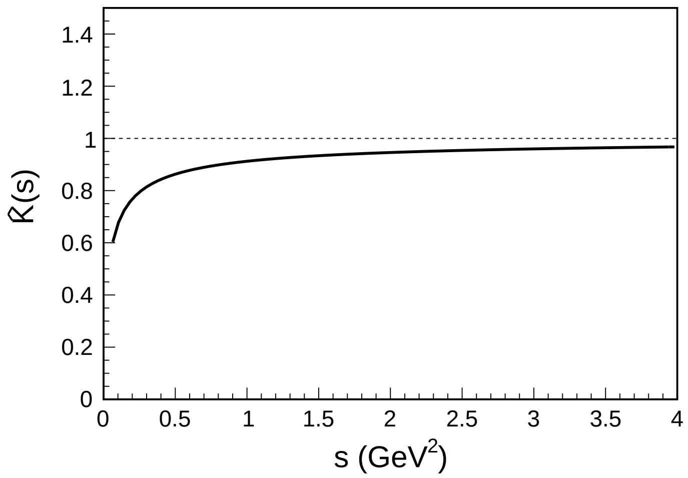

Figure 2.7: Graph of modified kernel function $\hat{K}(s) \equiv K(s) \cdot s \cdot m_\mu^2$ in the $g-2$ dispersion integral.

In the white paper [22], the results of the calculations of the two groups, DHMZ [25, 29] and KNT [26, 30], are combined, and the value is [6]

$$a_\mu^{\text{LO,HVP}} = 6\,931(40) \times 10^{-11}. \tag{2.25}$$

Each of these two groups calculates with different treatment of data and correlations. This uncertainty is due to the measurement of the cross sections. As a conservative value, the larger systematic error is taken for each channel, and the *BABAR*-KLOE discrepancy arises half of its difference as the systematic error. Figure 2.12 shows a breakdown of the contribution and uncertainty for various channels. Regarding contribution to $a_\mu^{\text{HVP,LO}}$, the $\pi^+\pi^-$ channel, which produces a $\rho(770)$ resonance of large cross section, accounts for the most significant proportion of 74%. The $\pi^+\pi^-\pi^0$ channel, which is the second largest, has a significant contribution from $\omega(782)$ and $\phi(1020)$ contributes about 7%. The other channels above and below $1.8\,\text{GeV}$ have contributions of about 10%. Regarding the uncertainty, the $\pi^+\pi^-$ channel represents the most significant proportion, accounting for 65%. Following this is the $\pi^+\pi^-\pi^0$ channel, which accounts for 16%, and the $\pi^+\pi^-\pi^0\pi^0$ channel, which accounts for 10%. The uncertainty resulting from $\pi^+\pi^-$ has been measured through various experiments, as aforementioned in chapter 1 and Fig. 1.2, particularly in KLOE and *BABAR*, the systematic uncertainty reaches a level of 0.5%. The tension between KLOE and *BABAR* has been conservatively factored into the uncertainty, although CMD-3 has not been considered in the value Eq. (2.25). As a result, approximately half of the $a_\mu^{\text{HVP,LO}}$ uncertainty of 4.0×10^{10} is attributed to the deviation between these two experiments, resulting in approximately 40% of the total uncertainty of a_μ^{SM}

Higher-order HVP contribution

The HVP contribution of the NLO comes from the Feynman diagrams such as Fig. 2.13. The diagrams (a) and (b) are the main contributions, where (a) has a contribution of about 1×10^{-9}, while (b) has a negative contribution of about 2×10^{-9}. The contribution from (c) is small, and in total, the NLO HVP contribution is

$$a_\mu^{\text{NLO,HVP}} = -98.3(7) \times 10^{-11}\ [30]. \tag{2.26}$$

The contribution from the NNLO is non-negligible, and its value is estimated at

$$a_\mu^{\text{NNLO,HVP}} = -12.4(1) \times 10^{-11}\ [31], \tag{2.27}$$

which is 0.1 ppm level of a_μ.

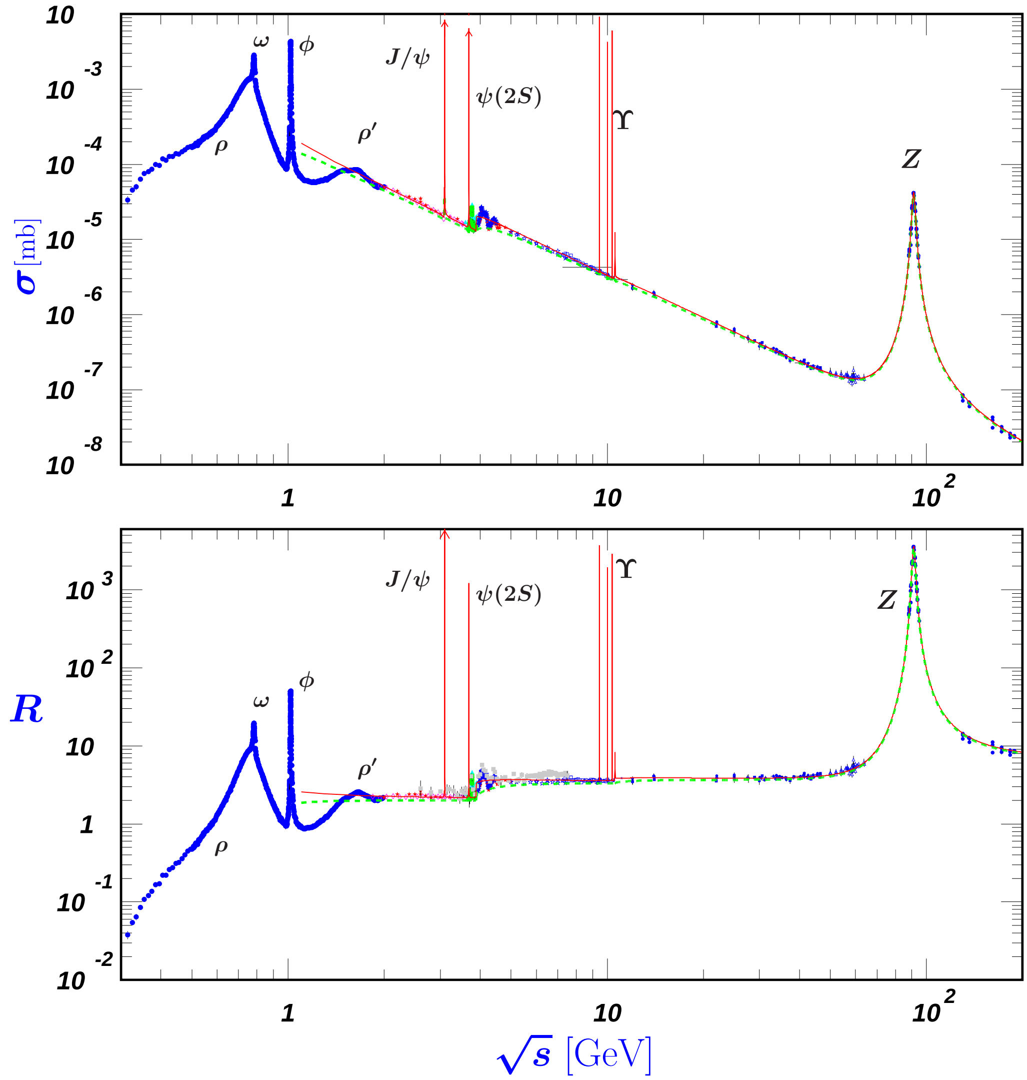

Figure 2.8: World data on the total cross section of $e^+e^- \to hadrons$ and the R-ratio. Adopted from Figure 53.2 in Ref. [37].

2.1.4 Hadronic Light-by-light contribution

The HLbL contribution arises from diagrams in which lepton current does not couple directly to the external field but via a hadronic blob; an example of a diagram of the LO is shown in the left-hand side of Fig. 2.14. This HLbL contribution causes the second-largest uncertainty in SM prediction after LO HVP, 18% of the a_μ^{SM} uncertainty. As with the HVP, this prediction is also difficult by perturbative QCD, so there are two methods: one based on data-driven phenomenological evaluation and the other on first-principles calculations using lattice QCD.

The data-driven approach is more complex than the HVP case because it has a four-point interaction. As shown in Fig. 2.14, the hadronic blob part can be decomposed into the diagrams on the right-hand side. The contribution of the exchanging light pseudo-scalars π^0, η, η' is the dominant part of the HLbL contribution, which can be calculated from the experimentally measured form factor through the two-photon process, e.g., the $\gamma\gamma^* \to \pi^0$ process. The remaining terms contribute around 1×10^{-10}–2×10^{-10}. The contribution using the dispersion relation is calculated up to NLO [6],

$$a_\mu^{\text{HLbL, LO}}(\text{DR}) = 92(19) \times 10^{-11}, \text{and} \tag{2.28}$$
$$a_\mu^{\text{HLbL, NLO}}(\text{DR}) = 2(1) \times 10^{-11}. \tag{2.29}$$

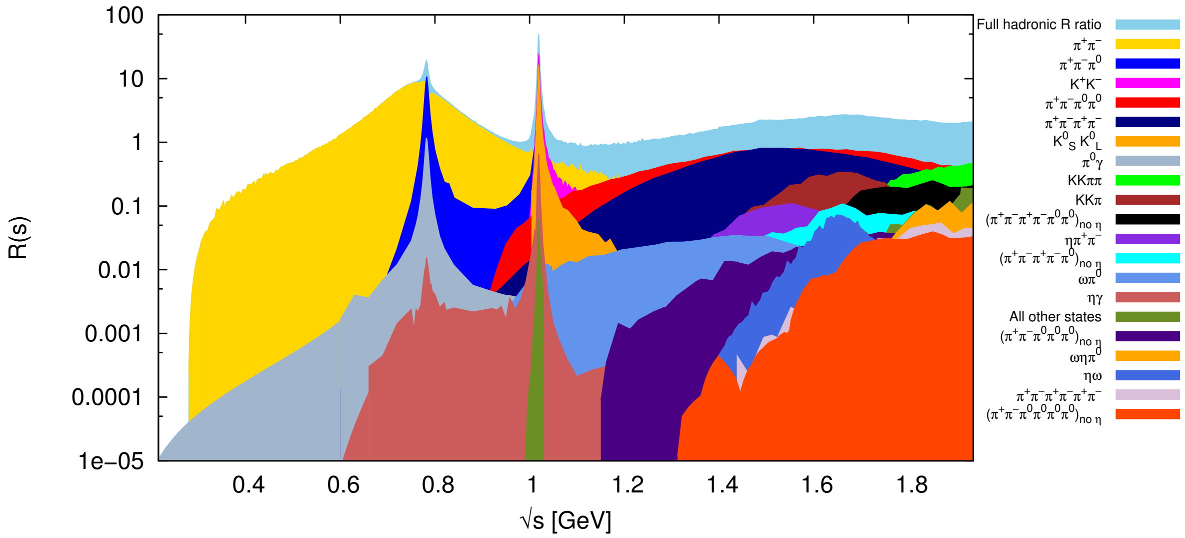

(a) The hadronic R-ratio

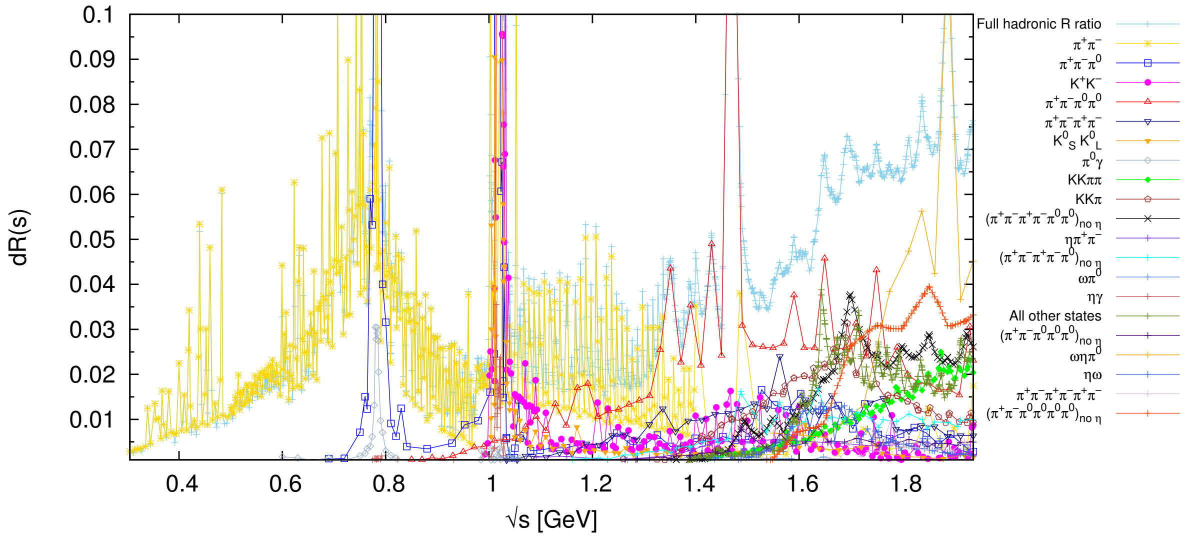

(b) The uncertainty for the hadronic R-Ratio

Figure 2.9: (a) The total hadronic R-ratio and (b) the uncertainty for the exclusive channels below 1.937 GeV. Adopted from Ref. [26].

The results of the LO HLbL using lattice QCD calculation,

$$a_\mu^{\text{hLbL, LO}}(\text{Lattice QCD}) = 79(35) \times 10^{-11}, \tag{2.30}$$

which is consistent with one using the dispersion relation. In total, the contribution is predicted as

$$a_\mu^{\text{HLbL}} = 92(18) \times 10^{-11} \text{ [6]}. \tag{2.31}$$

2.1.5 New physics contribution

The difference between the experimental value and theoretical prediction is $\delta a_\mu = (24.9 \pm 4.8) \times 10^{-10}$. The difference can be explained by the radiative correction through new physics, and its size can provide information about the energy scale of this new physics. Many new physics models, such as supersymmetry (SUSY), Leptoquark, Vector-like lepton, Axion-like particle and so on have been proposed to explain the currently visible difference [43, 44, 45, 46, 47, 48]. In this sub-section, the one of the case

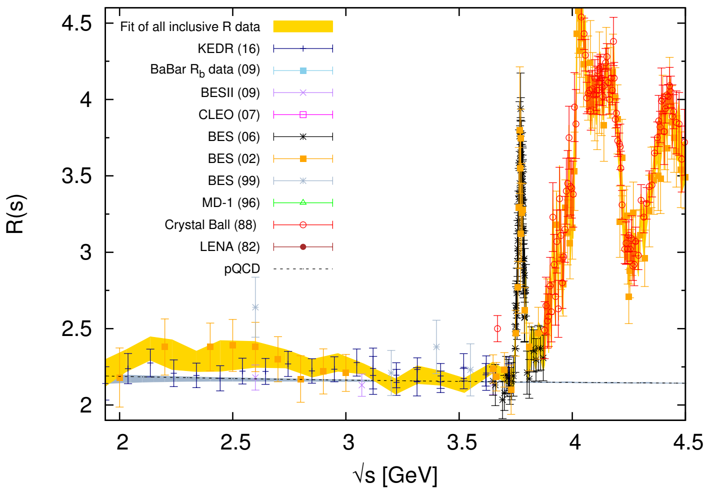

Figure 2.10: The inclusive R-ratio in the energy range of 1.937–4.50 GeV. Adopted from Ref. [26].

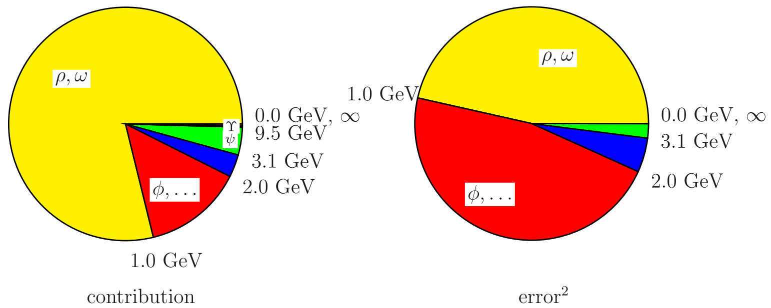

Figure 2.11: Breakdown of contributions and error squares from different energy regions. Adopted from Ref. [38].

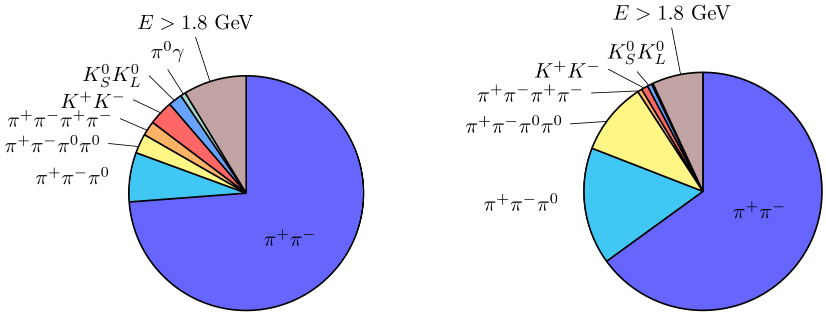

(a) Contribution

(b) Error^2

Figure 2.12: Contribution and error-square of each channel to $a_\mu(3\pi)$. The values are taken from KNT19 [30].

of the Minimal Supersymmetric Standard Model (MSSM) will be discussed to introduce the possibilities of the new physics.

Since this deviation is at the same level as the EW contribution, $a_\mu^{\mathrm{EW}} = 15.4\ (0.1) \times 10^{-10}$, physics on the same energy scale as EW is suggested as one of the scenarios. In particular, the MSSM, low-energy SUSY model, is one of the most promising candidates to explain this difference. SUSY itself is also very

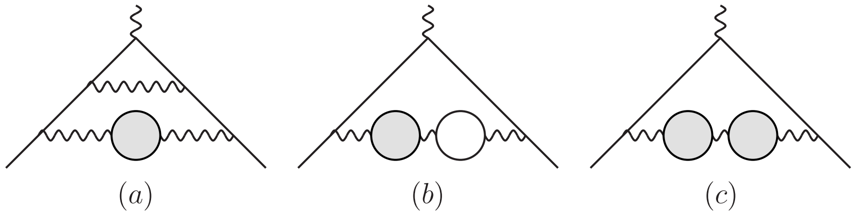

Figure 2.13: Next-to-leading-order Feynman diagrams contributing to a_μ^{HVP}. The straight and wavy lines represent lepton and photon propagators, respectively. The grey blob represents hadronic vacuum polarization. Adopted from Ref. [6].

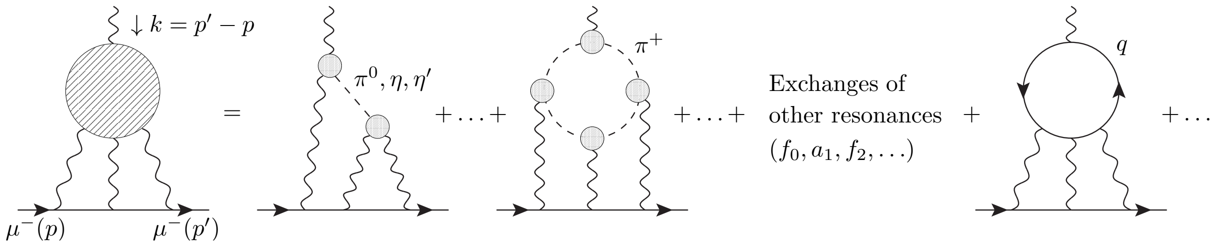

Figure 2.14: HLbL Feynman diagrams of hLbL contribution in model calculations. The blobs on the right-hand side of the equal sign are form factors that describe the interaction of photons with hadrons. Adopted from Ref. [42].

attractive in that it can explain multiple unsolved issues in the SM, such as the gauge hierarchy problem, gauge coupling unification, and relic density of dark matter.

The SUSY contribution, a_μ^{SUSY}, appears as radiative corrections associated with the newly introduced Supersymmetric partner particles: smuons, neutrino, bino, wino, and higgsino. The one-loop diagrams of the main contributions are shown in Figs 2.15, where each is labeled WHL, BHL, BHR and BLR, and the one-loop SUSY contribution is the sum of these. WHL (C) and WHL (N) represent the chargino-sneutrino

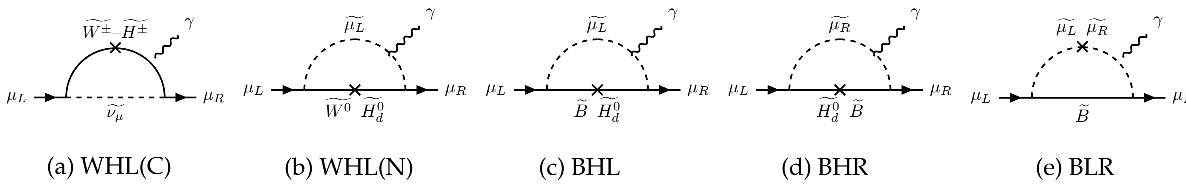

Figure 2.15: Feynman diagrams of SUSY loop. One-loop Feynman diagrams of SUSY contribution to a_μ in the gauge eigenstate basis.

loop and the neutralino-smuon loop, respectively. The numerical expressions are given by [44]

$$a_\mu^{\mathrm{WHL}} = \frac{\alpha_2}{4\pi}\frac{m_\mu^2}{M_2\mu}\tan\beta\cdot f_C\left(\frac{M_2^2}{m_{\tilde{\nu}_\mu}^2}, \frac{\mu^2}{m_{\tilde{\nu}_\mu}^2}\right) - \frac{\alpha_2}{8\pi}\frac{m_\mu^2}{M_2\mu}\tan\beta\cdot f_N\left(\frac{M_2^2}{m_{\tilde{\mu}_L^2}}, \frac{\mu^2}{m_{\tilde{\mu}_L^2}}\right), \tag{2.32}$$

$$a_\mu^{\mathrm{BHL}} = \frac{\alpha_Y}{8\pi}\frac{m_\mu^2}{M_1\mu}\tan\beta\cdot f_N\left(\frac{M_1^2}{m_{\tilde{\mu}_L^2}}, \frac{\mu^2}{m_{\tilde{\mu}_L^2}}\right), \tag{2.33}$$

$$a_\mu^{\mathrm{BHR}} = -\frac{\alpha_Y}{4\pi}\frac{m_\mu^2}{M_1\mu}\tan\beta\cdot f_N\left(\frac{M_1^2}{m_{\tilde{\mu}_R^2}}, \frac{\mu^2}{m_{\tilde{\mu}_R^2}}\right), \tag{2.34}$$

$$a_\mu^{\mathrm{BLR}} = \frac{\alpha_Y}{4\pi}\frac{m_\mu^2 M_1\mu}{m_{\tilde{\mu}_L^2} m_{\tilde{\mu}_R^2}}\tan\beta\cdot f_N\left(\frac{m_{\tilde{\mu}_L^2}}{M_1^2}, \frac{m_{\tilde{\mu}_R^2}}{M_1^2}\right), \tag{2.35}$$

where α_2 and α_Y are the gauge coupling constants of $SU(2)_L$ and $U(1)_Y$ gauge group, M_1 (M_2) is the bino (wino) soft mass, μ is the higgsino mass parameter, $\tan\beta = v_u/v_d$ is the ratio of the vacuum expectation values of the up- and down-type Higgs, and $m_{\tilde{\mu}_{L/R}}$ and $m_{\tilde{\nu}_\mu}$ are the masses of the left/right-handed smuon and the muon sneutrino, respectively. And the functions of the chargino-sneutralino and neutralino-smuon loop, f_C and f_N, are expressed as

$$f_C(x,y) = xy\left[\frac{5-3(x+y)+xy}{(x-1)^2(y-1)^2} - \frac{2\ln x}{(x-y)(x-1)^3} + \frac{2\ln y}{(x-y)(y-1)^3}\right], \tag{2.36}$$

$$f_N(x,y) = xy\left[\frac{-3+x+y+xy}{(x-1)^2(y-1)^2} + \frac{2x\ln x}{(x-y)(x-1)^3} - \frac{2y\ln y}{(x-y)(y-1)^3}\right]. \tag{2.37}$$

The required muon chirality symmetry breaking is caused by the Yukawa coupling to the Higgsino. Therefore, $a_\mu^{\mathrm{SUSY}}$is proportion to $\tan\beta$, appearing in the coupling constants. In the BLR case, this is realized by the smuon left-right flip based on the smuon mixing matrix. However, the constraints imposed by the proton-proton collision experiments at the LHC limit the SUSY parameters that can explain the $g-2$ discrepancy and have large $\tan\beta$. Here, as an example, we consider the pure-bino contribution (BLR) scenario (BLR; Fig. 2.15 (e) and Eq. (2.35)), which is one of several scenarios that is not completely explored by LHC experiments. In this case, the BLR contribution is dominant. Under these conditions, the lightest neutralino is the lightest supersymmetric particle, the so-called LSP, and is a good candidate for dark matter. Therefore, we can constrain the higgsino mass parameter from the measured thermal relic abundance of the neutralino. The bounds on the neutralino and muon masses at this time are shown in Fig. 2.16, where the orange region can account for the $g-2$ discrepancy. The blue region is limited by direct measurements of events from proton-proton collisions at the LHC. The muon $g-2$ discrepancy can be explained by 1σ for parameters with $\tan\beta = 5$ and smuon mass $\tilde{\mu_1} \lesssim 220\,\mathrm{GeV}/c^2$. These remaining regions are often difficult to measure even at the LHC, where the mass difference between the bino and the smuon is small, the detection efficiency suffers due to the low momentum of the lepton final state. But this is an example where $g-2$ provides a good constraint on the search targets of future energy frontier experiments.

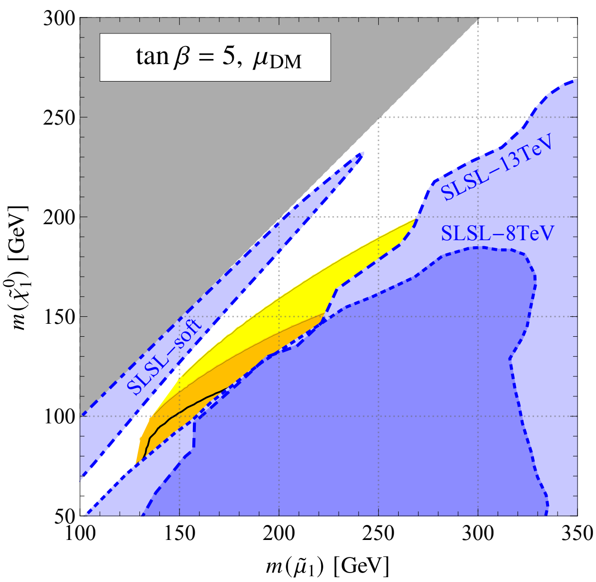

Figure 2.16: Constraints on mass parameters in the bino-dominated SUSY scenario (BLR) with dark matter relic abundance. The vertical and horizontal axis represent smuon and bino mass. The orange and yellow regions is the parameters that can solve the $g-2$ discrepancy at the 1σ and 2σ level. The blue area is excluded parameters by direct measurements. Adopted from Ref. [44].

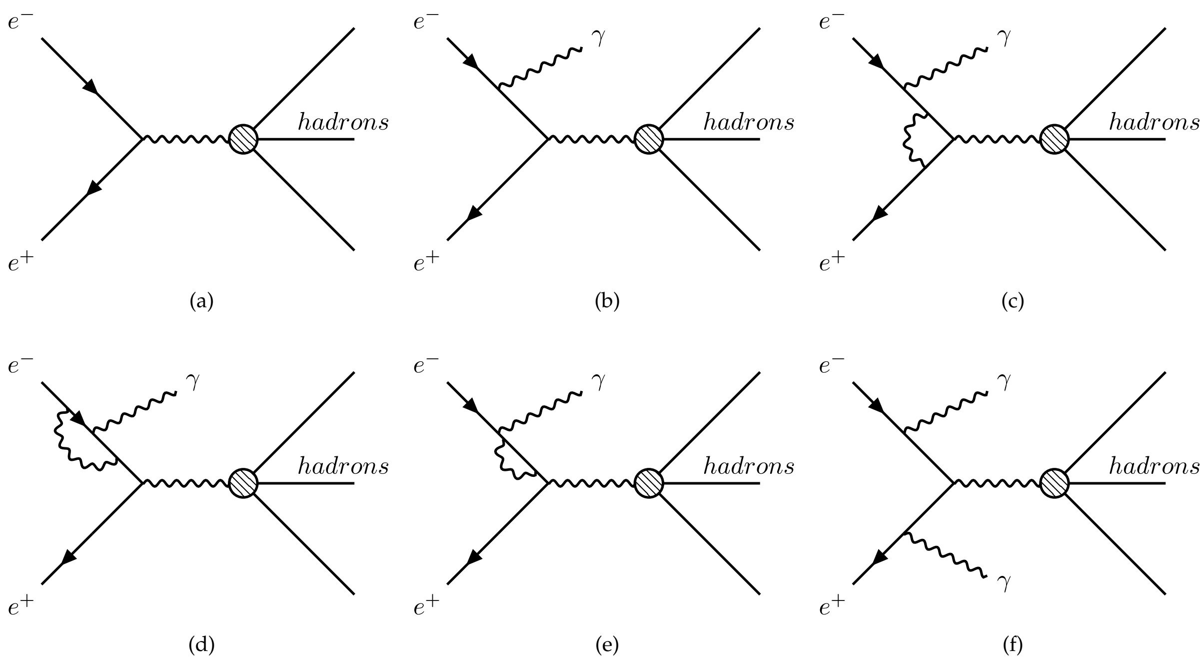

Figure 2.17: Feynman diagrams of $e^+e^- \to hadrons$ process with initial-state radiation. (a) represents a tree-level process without ISR emission. (b) represents the LO ISR process with a single hard photon emission. (c)–(f) represent NLO ISR process. (f) is the process with two hard photon emission

2.2 Cross section measurement at e^+e^- collision experiment

In straightforward terms, the total number of process occurrences can be given by the cross section for the process σ and the integrated luminosity index L_{int},

$$N = \int dt\sigma L. \qquad = \sigma L_{\mathrm{int}}, \tag{2.38}$$

where L_{int} is the index of the dataset size, obtained as an integral of the instantaneous luminosity L in that time direction. To measure the cross section σ, it is necessary to assess the size of the dataset and the signal efficiency of detectors. In addition, to obtain the cross section spectrum, the energy of this hadronic system must be scanned. For this purpose, an ISR-based technique, so-called radiative return method, is introduced in this analysis.

2.2.1 Radiative return method

The radiative return method is a technique used to scan hadronic energies at a fixed e^+e^--collision energy. Now we consider the lowest-order process, a hadron-production process that involves a single hard photon emission (see Fig. 2.17 (b)). A hadronic energy $\sqrt{s'}$ in the process is given by a relation of $s' = s - \sqrt{s}E_\gamma$, where the e^+e^- energy in the center-of-mass (c.m.) system $\sqrt{s}$ and the ISR photon energy in the e^+e^- c.m. E_γ. When the initial e^+e^- energy is $\sqrt{s} = 10.58\,\mathrm{GeV}$, the hadronic energy range 0.4–3.5 GeV corresponds to the ISR photon energy range 4.7–5.3 GeV. The probability of the ISR photon polar angle with respect to the e^+e^- collision axis in the e^+e^- c.m. system, θ_γ, and the photon energy with respect to beam energy, $x := 2E_\gamma/\sqrt{s}$, can be given up to m_e^2/s term by [49, 50]

$$w_0(\theta_\gamma, x) = \frac{\alpha}{\pi x} \frac{2(x^2 - 2x + 2)\sin^2\theta_\gamma - x^2\sin^4\theta_\gamma - 2\frac{m_e^2}{s}\left[(1-2x)\sin^2\theta_\gamma - x^2\cos^4\theta_\gamma\right]}{2\left(\sin^2\theta_\gamma + \frac{m_e^2}{s}\cos^2\theta_\gamma\right)^2}. \tag{2.39}$$

According to this function (shown in Fig. 2.18), most of the emitted photons are emitted at a small θ_γ, i.e., along the e^+e^- beam axis, and thus are not detected by detectors. For conditions where m_e^2/s is

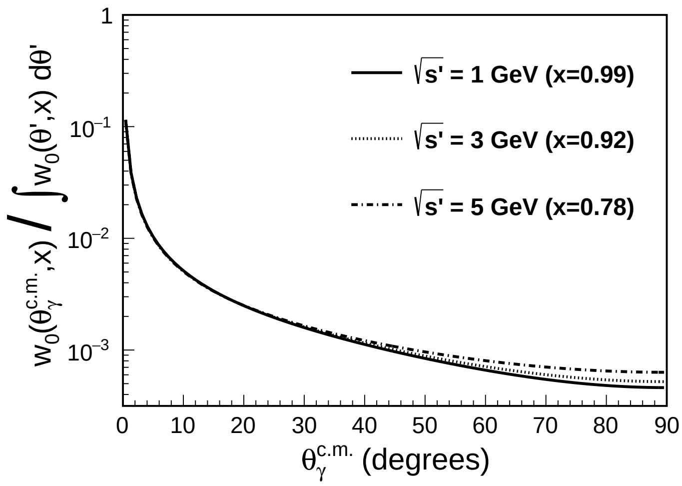

Figure 2.18: Fraction of an ISR emission angle θ_γ in the lowest order process, $w_0(\theta_\gamma, x)$, normalized by an integral over θ_γ.

sufficiently small, integrating Eq. (2.39) over the range of polar angle $\theta_{\text{min}} < \theta < \pi - \theta_{\text{min}}$ yields

$$W_0(\theta_{\text{min}}, x) = \int_{\theta_{\text{min}}}^{\pi-\theta_{\text{min}}} w_0(\theta_\gamma, x) \sin\theta_\gamma d\theta_\gamma. \tag{2.40}$$

We call this function the radiator function. When the integral range $\theta_{\text{min}}$is a sufficiently large angle $\theta_{\text{min}} \gg m_e/\sqrt{s}$, the radiator function is given by

$$W_0(\theta_{\text{min}}, x) = \frac{\alpha}{\pi x}\left[(2 - 2x + x^2)\ln\left(\frac{1+\cos\theta_{\text{min}}}{1-\cos\theta_{\text{min}}}\right) - x^2\cos\theta_{\text{min}}\right], \tag{2.41}$$

and when $\theta_{\text{min}} = 0$,

$$W_0(0, x) = \frac{\alpha}{\pi x}\left(\ln\left(\frac{s}{m_e^2}\right) - 1\right)(2 - 2x + x^2). \tag{2.42}$$

The cross section of the $e^+e^- \to \gamma hadrons$ process is

$$\frac{d\sigma_{\text{hadron}+\gamma}(m)}{dm} = \frac{2m}{s} \cdot W_0(\theta_{\text{min}}, x) \cdot \sigma_0(m), \tag{2.43}$$

where $\sigma_0(m)$ is the *born* cross section of the $e^+e^- \to hadrons$ process (Fig. 2.17 (a)). The radiator function can describe the cross section with an accuracy of 10%–20%, but in practice it is necessary to consider higher-order terms. The higher-order processes involving multiple photons, e.g., processes involving two photons (Fig. 2.17 (c)–(f)). Giving the ratio of the radiator function including higher-order photon emission $W(\theta_{\text{min}}, x)$ to the lowest-order photon radiation W_0 as a radiative correction

$$R_{\text{rad}} = \frac{W(\theta_{\text{min}}, x)}{W_0(\theta_{\text{min}}, x)}. \tag{2.44}$$

Here, $at\sqrt{s} = 10.58\,\text{GeV}$, the $R_{\text{rad}}$is found to be one within 2%, under the condition that the highest-energy ISR photon is limited to 20°–160° and the invariant mass of the photon and hadronic system is greater than 8 GeV/c^2. The latter condition is to drop collinear photons and soft photons in the process with two external photon emission.

The observed cross section is

$$\frac{d\sigma^{vis}(m)}{dm} = \frac{2m}{s} \cdot W_0(\theta_{\text{min}}, x) \cdot R_{\text{rad}} \cdot \sigma_0(m). \tag{2.45}$$

We call this *visible* cross section, which includes all radiative effects from ISR, final-state radiation (FSR), and vacuum polarization (VP). The spectrum observed by detectors can be obtained from Eqs. (2.38) and (2.45) as

$$\frac{dN}{dm} = \varepsilon(m) \cdot \frac{dL_{\text{eff.}}}{dm} \cdot R_{\text{rad}} \cdot \sigma_0(m), \tag{2.46}$$

where $\varepsilon(m)$ is the detection efficiency. The luminosity with the radiator function is considered as hadronic-mass-dependent luminosity, so-called effective luminosity, and expressed as

$$\frac{dL_{\text{eff.}}}{dm} = \frac{2m}{s} W_0(\theta_{\text{min}}, x) L_{\text{int}}. \tag{2.47}$$

The radiative return method has several advantages and disadvantages due to the emission of high-energy ISR compared to the scan method. Whereas the scan method requires changing accelerator conditions to measure a cross section at a given energy, the radiative return method allows measuring the entire spectrum below the collision energy with a single dataset. This makes it robust against accelerator/detector performance changes over time and beam energy. On the other hand, about the accuracy of hadronic energy m, the former can be determined by the beam energy resolution, while the latter requires an understanding of the detector resolution. The second difference is that the hadrons are boosted in the laboratory frame in the radiative-return method, which mainly affects detection efficiency. The higher hadronic momentum in the laboratory frame allows high efficiency to be maintained at low-energy regions, and a change in the momentum distribution as a function of hadronic energy is negligible. In addition, detected particles are in a closer detector area (with advantages and disadvantages). The significant disadvantage is that the cross section becomes smaller due to the ISR emission. Furthermore, as calculated from Eq. (2.41), ISRs of more than 90% are emitted along the beam axis and are therefore undetectable. The B-factory experiments, however, can also cover this point because it has relatively high instantaneous luminosity and can often prepare large datasets. Regarding other significant shortcomings, the radiative return method suffers from more substantial background events due to background processes from energies above the spectrum to be measured.

2.2.2 Measurements of $e^+e^- \to \pi^+\pi^-\pi^0$ cross section

The $e^+e^- \to \pi^+\pi^-\pi^0$ cross sections measured by several e^+e^- collision experiments are summarized in Fig. 2.19 The SND [51, 52, 53, 54] and CMD-2 [55, 56, 57, 58] experiments at the VEPP-2M collider measured the cross section up to 2.0 GeV by the scan method. The *BABAR* experiment [59, 60] at the PEP-II collider measured up to around 3.5 GeV by the radiative return method at $\sqrt{s} = 10.58\,\text{GeV}$. The BESIII experiment [61] at the BEPCII collider reported preliminary results using the radiative return method at $\sqrt{s} = 3.773\,\text{GeV}$.

The 3π cross section spectrum is characterized by the vector meson resonances: $\omega(782)$ and $\phi(1020)$ resonance below 1.05 GeV, the $\omega(1420)$ and $\omega(1650)$ resonances in a range of 1.1–1.8 GeV, and the J/ψ resonance at 3.09 GeV. The $\rho(770) \to 3\pi$ process, which is suppressed due to isospin-breaking, is also clearly observed by the SND [53] and *BABAR* [60]. Hereafter, we take the following notations for vector meson resonances $\rho = \rho(770)$, $\omega = \omega(782)$, $\phi = \phi(1020)$, $\omega' = \omega(1420)$ and $\omega'' = \omega(1650)$.

The cross section comparison of the ω and ϕ resonances between the *BABAR*, the currently the best precise measurement, and SND and CMD-2 are plotted in Fig. 2.20. In the ω energy region, the cross section difference of around 8% is visible between SND and CMD-2, and in the ϕ region, a difference of around 10% between *BABAR* and SND showing a higher cross section. In the 1.1–2.0 GeV ω' comparison, BESIII comes out higher cross section than *BABAR*.

In the energy range below 1.1 GeV, the precision of measurements is generally 1-2%. The systematic uncertainty at the ω (ϕ) resonance region is 1.5% (1.5%) for the *BABAR* [60], 3.4% (5%) for the SND [53, 51], 1.3% (2.5%) for the CMD-2 data [57, 58], and 2.1% (2.0%) for the BESIII data [61].

The $e^+e^- \to \pi^+\pi^-\pi^0$ contributions to muon $g-2$ for the energy range below 1.8 GeV, which is often used a transition energy with the R-ratio of inclusive data and perturbative QCD, is

$$a_\mu(3\pi) = (46.21 \pm 0.40_{\text{stat}} \pm 1.40_{\text{syst}}) \times 10^{-10} \qquad \text{(DHMZ 2019 [29])}, \tag{2.48}$$

$$a_\mu(3\pi) = (46.63 \pm 0.94) \times 10^{-10} \qquad \text{(KNT 2019 [30])}, \tag{2.49}$$

$$a_\mu(3\pi) = (45.91 \pm 0.53) \times 10^{-10} \qquad \text{(M. Hoferichter } et\ al. \text{ [65])}. \tag{2.50}$$

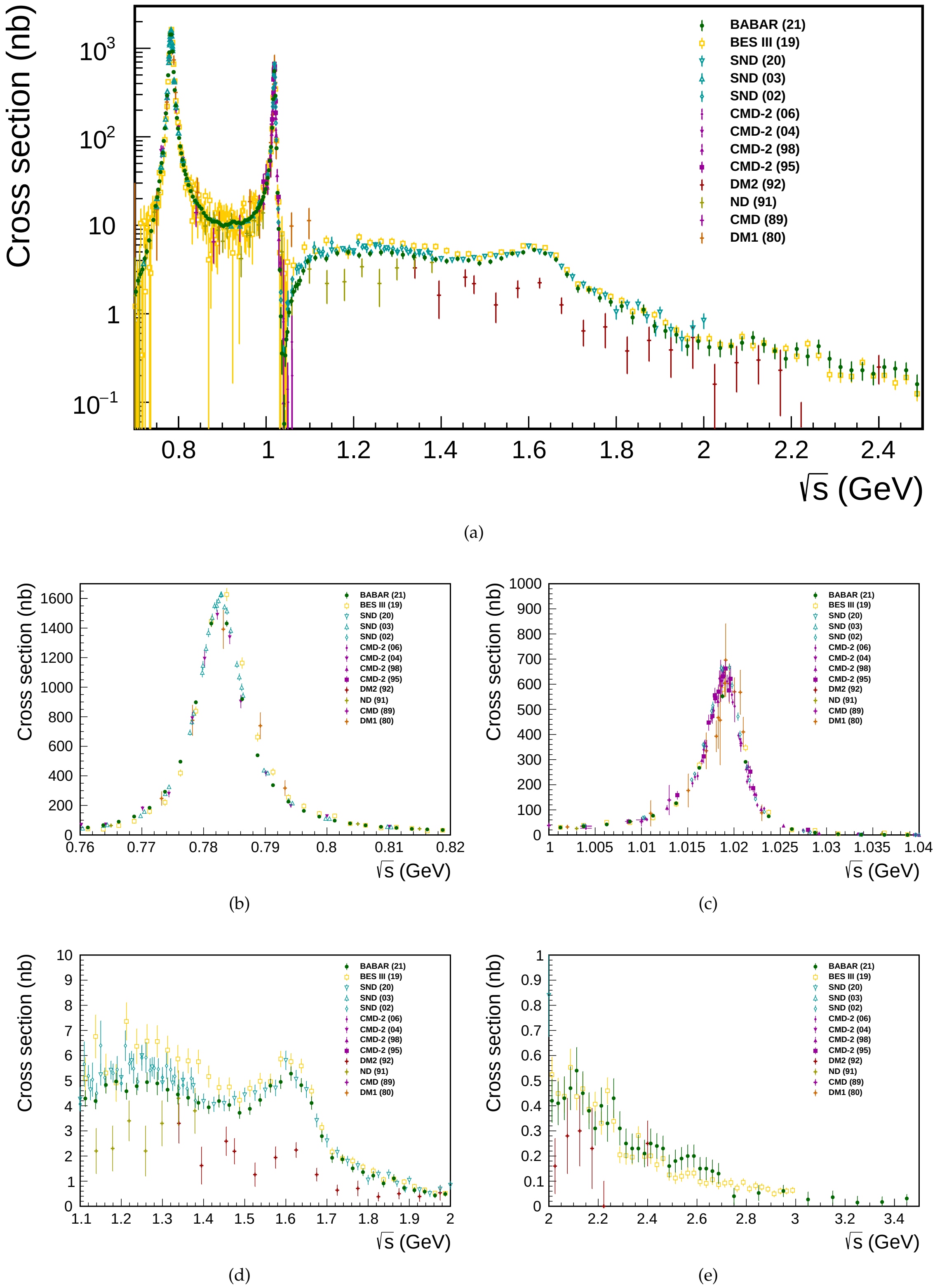

Figure 2.19: The measured cross section of $e^+e^- \to \pi^+\pi^-\pi^0$ process. (a) – (d) represent different energy regions. [62, 63, 64, 55, 56, 57, 58, 52, 53, 54, 61, 59]

The precision of a single measurement is 1.3% for the *BABAR* result and 1.9% for the preliminary BESIII result. Due to the slightly higher cross section, the BESIII alone results are slightly higher with respect to the average. The DHMZ and KNT results include the *BABAR* 2023 result [60], and the global fit by M. Hoferichter *et al.* includes it.

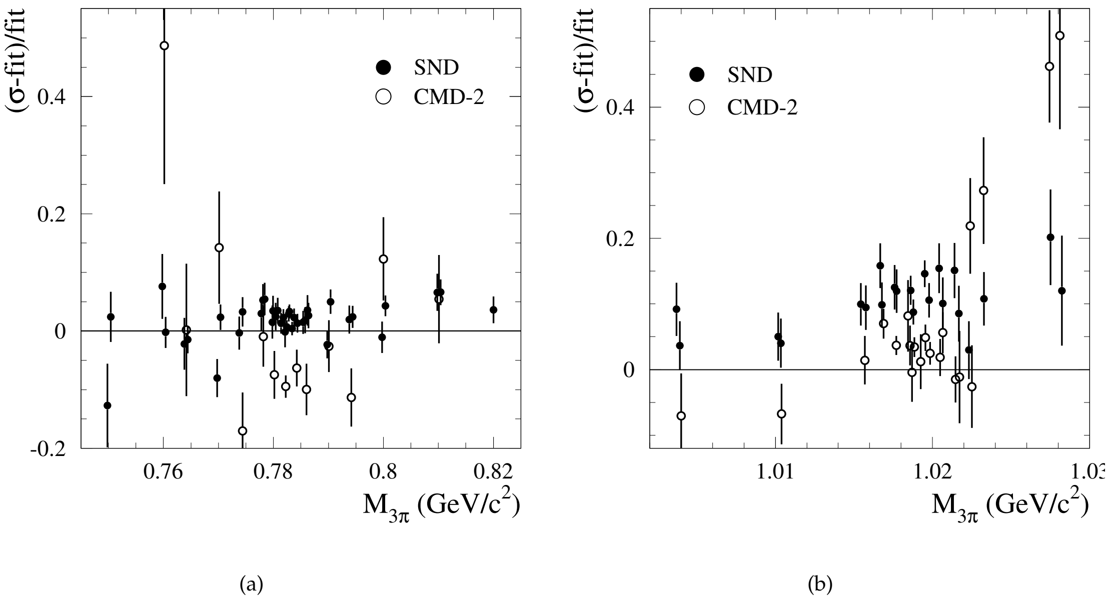

Figure 2.20: The relative difference of SND [51, 53] and CMD-2 [57, 58] data to *BABAR* fit result [60] on the $e^+e^- \to \pi^+\pi^-\pi^0$ dressed cross section. The uncertainties shown for the SND and CMD2 data are statistical. Adopted from Ref. [60].

2.3 Strategy of the 3π cross section measurement

This thesis reports the measurement of the $e^+e^- \to \pi^+\pi^-\pi^0$ cross section using the radiative return method with data of the integrated luminosity of 191 fb^{-1} corrected by the Belle II experiment. We measure the spectrum of cross section in the hadronic energy range of 0.6–3.5 GeV by studying the process

$$e^+e^- \to \pi^+\pi^-\pi^0[\to \gamma\gamma]\gamma_{\mathrm{ISR}}. \tag{2.51}$$

The observed (visible) mass spectrum can be expressed as Eq. (2.46). The analysis is performed with the following steps to obtain the "dressed" cross section for the $e^+e^- \to \pi^+\pi^-\pi^0$ process, $\sigma_{ee\to 3\pi}$. The dressed cross section is defined as a cross section that omits the radiative effects of the ISR but includes the ones of FSR and VP. The number of signal events (Eq. (2.51)) is counted by fitting an invariant mass of two-photon system from the π^0 decay observed events after event selection (Chapter 4). We check the correctness of the background expectation from simulation by using the data in various data control samples and subtract the backgrounds from the observed spectrum (Chapter 5). A signal efficiency depends on the detector acceptance, detection efficiency, and event selection efficiency. We use the signal Monte-Carlo (MC) simulation to obtain the signal efficiency as the first-order approximation. A possible difference between the simulation and the data is taken into account in a data-driven way by studying the difference between data and simulation using various data control samples and prepared data-MC correction factors (Chapter 6). We unfold the background-subtracted spectrum to correct the mass-smearing effects from detector resolution and NLO FSR effects (Chapter 7). The effective luminosity dL_{eff}/dm, which takes into account the probability to radiate an ISR photon, can be given from Eq. (2.47) and the measured integrated luminosity for the given range of the polar angle of the ISR photon. Finally, we discuss the LO HVP contribution to a_μ and $\Delta\alpha^{(5)}_{\text{had}}(M_Z^2)$ using the obtained spectrum (Chapter 8).

We pay attention to signal selection, background estimation, and efficiency determination to be robust against systematic uncertainty. We use several kinds of control samples in data to confirm the correctness of the simulation as well as to obtain the data-MC correction factors.

Blind analysis

To mitigate experimenter bias, this analysis is carried out by blinding the signal sample until the signal selections are elaborated and the correction factors are determined. The datasets and procedures are split into four steps as follows:

1. MC simulation study
2. Non-signal sample study
3. Partial data study
4. Full data unblinding

In step 1, the analysis program/software is prepared, and the primary event selection criteria are determined using signal and background MC sample. In step 2, background estimation and a part of the efficiency correction study are performed using non-signal samples. The full statistic is used since the control samples in step 2 does not include the signal. In step 3, the overall analysis procedure is confirmed using randomly-selected 10% data, corresponding to 20 fb^{-1}, and preserves the blindness to the final results. The method for determining the signal extraction and correction factor is fixed before step 4, and then the full data is analyzed in step 4. Third-party reviewers of the experiment collaborator review each step.

Chapter 3

Experiment apparatus and datasets

The measurement of the $e^+e^- \to \pi^+\pi^-\pi^0$ cross section using the radiative return method is performed using the SuperKEKB collider and Belle II detector located at the high energy accelerator research organization (KEK), Tsukuba, Japan. The Belle II experiment is a e^+e^--collider experiment operated at the e^+e^- center-of-mass energy at or near $\sqrt{s} = 10.58\,\mathrm{GeV}$. This chapter describes the experimental apparatuses, SuperKEKB collider and Belle II detector, e^+e^--collision data sample collected by the detector, and MC simulation sample calculated on computers.

3.1 SuperKEKB collider

The SuperKEKB collider [66, 67, 68] is an asymmetric electron-positron collider at or near the c.m. energy of $\sqrt{s} = 10.58\,\mathrm{GeV}$ upgraded from the KEKB B-factory [69] to achieve 30 times higher instantaneous luminosity, $6 \times 10^{35}\,\mathrm{cm}^{-2}\mathrm{s}^{-1}$. Figure 3.1 illustrates the schematics of the SuperKEKB facility. The SuperKEKB collider consists of the injector linear accelerator (linac), the 7-GeV electron storage ring (the high-energy ring, HER), the 4-GeV positron storage ring (the low-energy ring, LER) and the final-focus superconducting magnet system at the interaction point (IP). The linac consists of electron sources, the positron-generation target, the damping ring, and sixty units of superconducting radio-frequency cavities. The electrons are provided from the electron source, accelerated by the cavities up to $7\,\mathrm{GeV}$, and injected into the HER. The positrons are produced by hitting $3.5\,\mathrm{GeV}$ electrons on the positron-generation target. The positrons are temporally stored in the damping ring to reduce its beam emittance and injected into the LER after acceleration up to $4\,\mathrm{GeV}$. On the storage ring HER and LER with a circumference of about 3 km, accelerators are located to compensate for the energy lost by synchrotron radiation and collimators are equipped to drop particles that have deviated too far from the beam. To achieve the unprecedented instantaneous luminosity, beam currents in the both rings doubled those of KEKB and a novel collision scheme, the nano-beam scheme, was introduced for collision with a large crossing angle of 83 $\mathrm{milliradian}$ to avoid luminosity limitation due to the hourglass effect.

Various physical processes occur in the electron-positron collision environment at $\sqrt{s} = 10.58\,\mathrm{GeV}$. As summarized in Table 3.1, in addition to the $e^+e^- \to q\bar{q}$ process, $B\overline{B}$ events, The $e^+e^- \to \pi^+\pi^-\pi^0\gamma$ event, the target of this analysis, is categorized as a hadronic process $e^+e^- \to q\bar{q}$. Additionally, a hadronic process $e^+e^- \to \Upsilon(4S)(\to B\overline{B})$, the lepton pair production of the $e^+e^- \to \mu^+\mu^-, \tau^+\tau^-$ and QED processes of large cross sections $e^+e^- \to e^+e^-(\gamma), \gamma\gamma(\gamma), e^+e^-e^+e^-$ occur.

The SuperKEKB collider started its commissioning operation in 2016, and the physical data taking using the Belle II detector has been operated since March 2019. The history of beam currents, instantaneous luminosity, and integrated luminosity is plotted in Fig. 3.2. The instantaneous luminosity is gradually increased by increasing beam currents and reducing the beam size at the IP towards the design value of $6 \times 10^{35}\,\mathrm{cm}^{-2}\mathrm{s}^{-1}$. As of 2023, a world-record luminosity of $4.7 \times 10^{34}\,\mathrm{cm}^{-2}\mathrm{s}^{-1}$ was achieved. During the 2019–2021 summer, when data using this analysis had been taken, the instantaneous luminosity ranged from about $0.2 \times 10^{34}\,\mathrm{cm}^{-2}\mathrm{s}^{-1}$ to $3.1 \times 10^{34}\,\mathrm{cm}^{-2}\mathrm{s}^{-1}$.

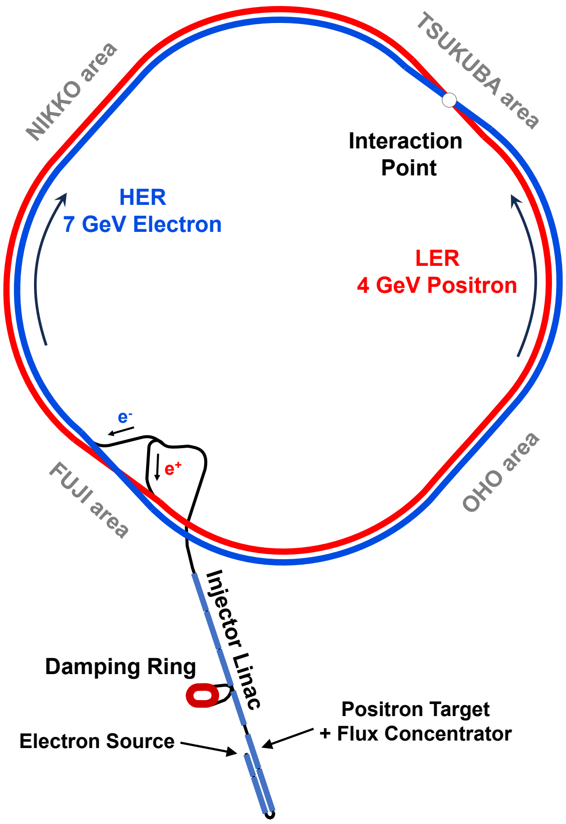

Figure 3.1: Schematic drawing of SuperKEKB collider

Table 3.1: Total production cross section of major physical processes in electron-positron collision at $\sqrt{s} = 10.58\,\mathrm{GeV}$ [70]. Event rate is calculated at the instantaneous luminosity of $6 \times 10^{35}\,\mathrm{cm^{-2}s^{-1}}$ $(= 600\,\mathrm{nb \cdot s^{-1}})$.

Process	Cross section (nb)	Rate (Hz)
$e^+e^- \to \Upsilon(4S)$	1.1	660
$e^+e^- \to q\bar{q}$	3.7	2200
$e^+e^- \to \pi^+\pi^-\gamma_{\mathrm{ISR}}$	0.17	100
$e^+e^- \to \pi^+\pi^-\pi^0\gamma_{\mathrm{ISR}}$	0.026	14
$e^+e^- \to \mu^+\mu^-(\gamma)$	1.1	660
$e^+e^- \to \tau^+\tau^-(\gamma)$	0.9	540
$e^+e^- \to e^+e^-(\gamma)$ [a]	300	180000
$e^+e^- \to \gamma\gamma(\gamma)$ [a]	5.0	3000
$e^+e^-e^+e^-$ [b]	40	24000
$e^+e^-\mu^+\mu^-$ [b]	19	11000

[a] Generator-level selection criteria for electrons with $10^\circ < \theta_e^{\mathrm{c.m.}} < 170^\circ$ and $E_e^{\mathrm{c.m.}} > 0.15\,\mathrm{GeV}$.
[b] Generator-level selection criteria for at least two particles with $p_{\mathrm{T}}^{\mathrm{lab.}} > 0.05\,\mathrm{GeV}/c$ and $15^\circ < \theta^{\mathrm{lab.}} < 155^\circ$.

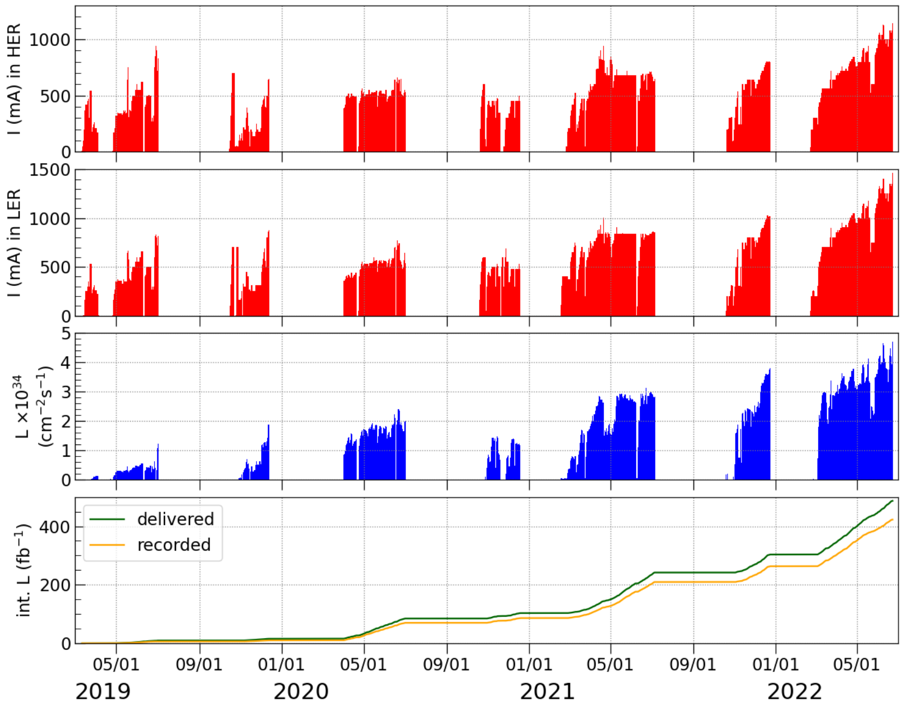

Figure 3.2: History of SuperKEKB operation. (top row) Beam currents of HER and (2nd row) LER, (3rd row) instantaneous luminosity, and (bottom row) integrated luminosity are plotted. In the bottom plot, the green line indicates the integrated luminosity of the collision, while the yellow line is the amount of physics data taken by the Belle II detector in it. [71]

3.2 Belle II detector

The Belle II detector [72] is a 4π general-purpose detector surrounding the IP. It is designed to study events occurring in 10.58 GeV electron-positron collision environment, allowing measurements of the position, momentum, energy, and mass (i.e. particle type) of relatively long-lived and stable particles. The SM charged particles that are directly detected by detectors are the electron, muon, pion, kaon, proton, and deuteron, while the neutral particles are the photon, K-long, and neutron. The layout and dimension are illustrated in Fig. 3.3. The detector geometry is forward-backward asymmetric, corresponding to the asymmetric collision. The detector consists of seven sub-detectors: these are arranged from the innermost layer as the two types of vertex detectors (VXD) surrounded by the central drift chamber (CDC) for tracking of charged particle, the time-of-propagation counter (TOP) and the aerogel ring-imaging-Cherenkov counter (ARICH) for charged hadron identification, the electromagnetic calorimeter (ECL) for photon detection and electron identification, and K-long and muon detector (KLM). A solenoid-type superconducting magnet is installed outside the ECL and provides a magnetic field of 1.5 T, with the KLM serving as a return yoke.

In this analysis, the coordinates of the laboratory frame are defined as a right-handed coordinate system with respect to the Belle II detector. The z-axis is defined by the magnetic field symmetry axis with the electron beam direction pointing towards the positive z direction. The x-axis denotes the horizontal direction. In naming the detector, the positive z side is referred to as forward and the negative z side as backward, and the cylindrical part is called barrel. This coordinate system can be viewed as a cylindrical system, with the polar angle θ defined as the opening angle from the positive z-axis and the azimuthal angle ϕ as the opening angle from the positive x-axis projected onto the x-y plane. The e^+e^- c.m. system is determined by the system calculated based on the boost vector in the laboratory frame $\vec{p} = (0.46, 0, 3.0)$ with units of GeV/c.

This section describes each detector component, trigger system and the data acquisition system (DAQ).

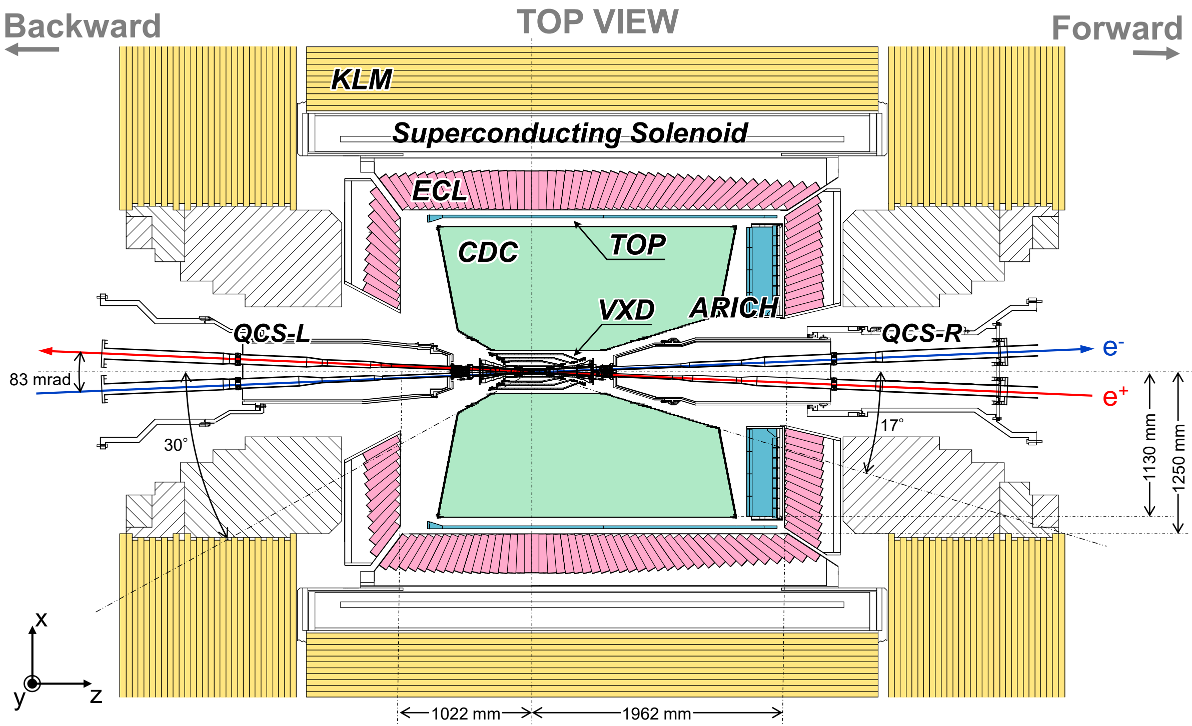

Figure 3.3: Horizontal cross section schematics of the Belle II detector, which is adopted from [73] and edited.

3.2.1 Vertex detector (VXD)

The VXD is a six-layer silicon detector used to improve the precision of the origins (vertices) of charged particles. The VXD is installed around a beryllium beam pipe made with a radius of 10 mm and covers a radius of 14–135 mm and a polar angle of 17°–150° as shown in Fig. 3.4; the inner two layers are the depleted P-channel field effect transistor pixel (DEPFET) sensors (PXD), and the outer four layers are the double-sided silicon strip sensors (SVD) [74]. Each module has rectangular sensors cylindrically arranged to overlap in the ϕ direction, avoiding sensor gap inefficiency. The PXD contains an array of 768×250 DEPFETs per module, with pixels of approximately 55–85 $\mu\mathrm{m}^2$ in size and arranged so that the granularity is higher in the area close to the IP.

The decay point is determiend by extrapolating the tracks reconstructed by CDC and the hits on the VXD, typically with an accuracy of the impact parameter of 15 μm for 3 GeV/c tracks [75].

As a special note, the second layer of the PXD was only installed in two out of twelve modules at the time of this experiment, as shown in Fig. 3.4 (b). It is arranged to complement the inadequate efficiency of one module in the first layer.

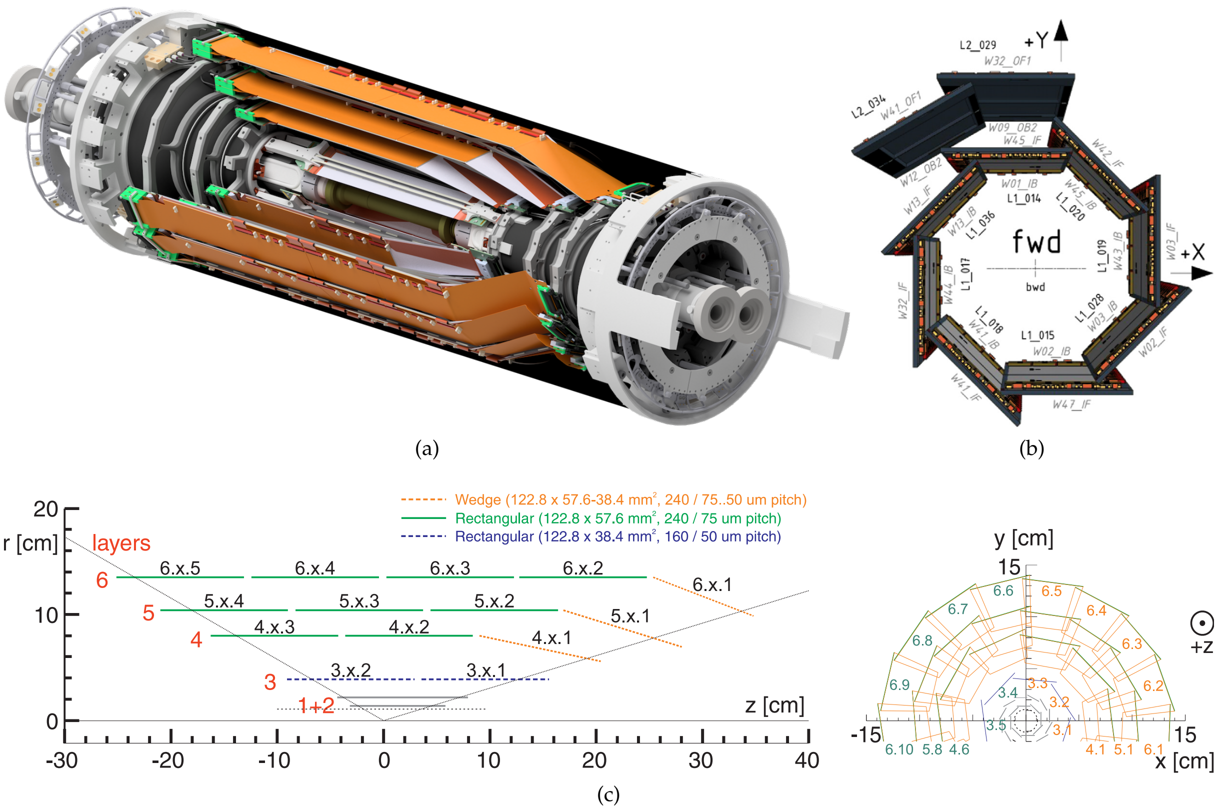

Figure 3.4: (a) 3D view of the Belle II VXD [74]. (b) Forward view of the Belle II PXD in 2019-2022 [76]. (c) Schematic layout of the Belle II VXD in longitudinal cut (left) and transverse cut (right). The numbers are the size of sensors in units of cm [74].

3.2.2 Central drift chamber (CDC)

The CDC is a cylindrical drift chamber located outside the VXD and plays a central role in tracking charged particles. It is also used for particle identification of low-momentum charged particles based on energy deposition. It has an inner diameter of 160 mm and an outer diameter of 1130 mm and covers a polar angle range of 17°–150°. The wires are attached in the direction of the magnetic field symmetry axis and form a cell with a sense wire surrounded by nine field wires. The wires (cells) arrangement is shown in Fig. 3.5. The cells form 56 layers, with the cell size in the radial direction of 8 mm for the innermost eight layers and 18 mm for the outer layers. The cell size in the ϕ direction is 6 mm for the innermost layer and 18 mm for the outermost layer. There are two types of wires: axial wires, which are horizontal to the magnetic field asymmetric axis, and stereo wires, which are twisted slightly in the direction of ϕ. The stereo wires are divided into U-type and V-type wires according to the twist direction and are twisted at an angle of about 45.4 milliradian to 74 milliradian. The gas is a mixture of 50% helium and 50% ethane. This has the advantages of small radiation length, high resolution and good energy loss resolution.

The performance evaluation of the CDC alone with cosmic-ray muons shows that for muons above transverse momentum more than $5\,\mathrm{GeV}/c$, the radial impact parameter resolution is 126 $\mu\mathrm{m}$, the longitudinal resolution is $1.4\,\mathrm{mm}$, the transverse momentum resolution is 0.73% and the ϕ resolution is $1.1\,\mathrm{milliradian}$ [77].

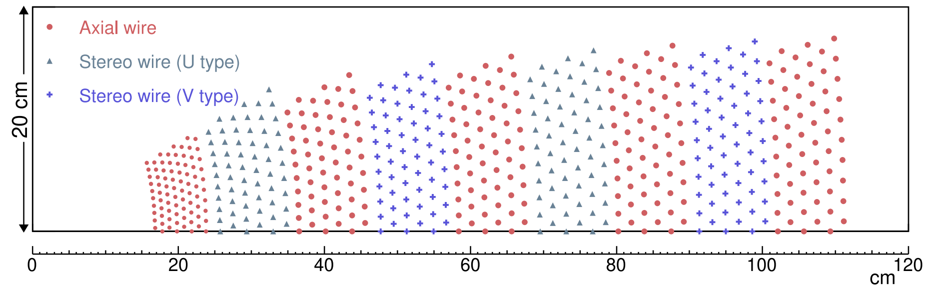

Figure 3.5: Wire configuration in x-y plane of the Belle II CDC, which is adopted from Ref. [77]. The horizontal axis is the distance from the IP.

3.2.3 Aerogel ring-imaging Cherenkov counter (ARICH) and Time-of-propagation counter (TOP)

The main purpose of the ARICH and TOP is to identify the type of charged particles of high momenta above $0.5\,\mathrm{GeV}/c$, especially pion-kaon identification, which is difficult with other detectors. The measuring principle of ARICH and TOP is based on the Cherenkov angle, the opening angle of the Cherenkov light from the direction of particle momentum, which depends on the velocity of the charged particle. This means that for the same momentum, the Cherenkov angle depends on the mass of the charged particle. As shown in Fig. 3.6, the mass of the particle can be estimated from the Cherenkov angle for a track with the same momentum and angle of incidence.

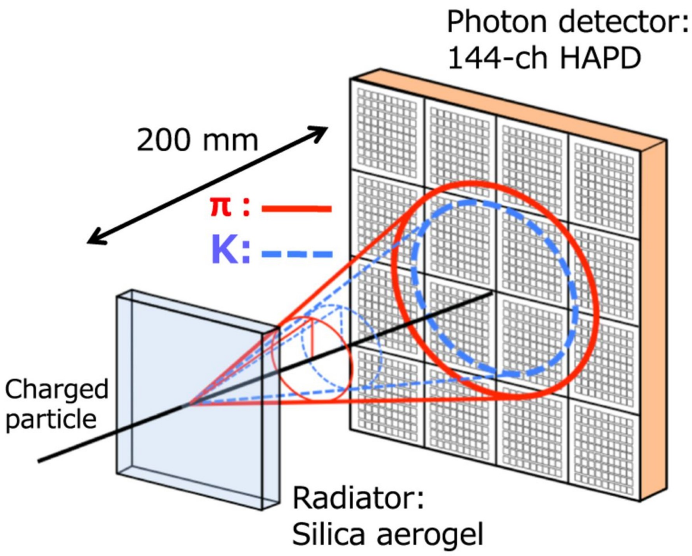

Figure 3.6: Principle of π/K identification for the ARICH counter. The solid-line (red) and dotted-line (blue) cones illustrate the emitted Cherenkov light for a injected charged pion and kaon, respectively. [78]

The ARICH is a disc-shaped structure covering a forward region, a polar angle of 14°–30°, with hybrid-avalanche photodetectors located at 200 mm forward of the two-layer 20 mm thick silica aerogel as shown in Fig. 3.7. The aerogels have a refractive index of 1.045 and 1.055, and the two layers of aerogel are designed so that the Cherenkov rings overlap on the photodetector, considering their offset and the difference in Cherenkov angle.

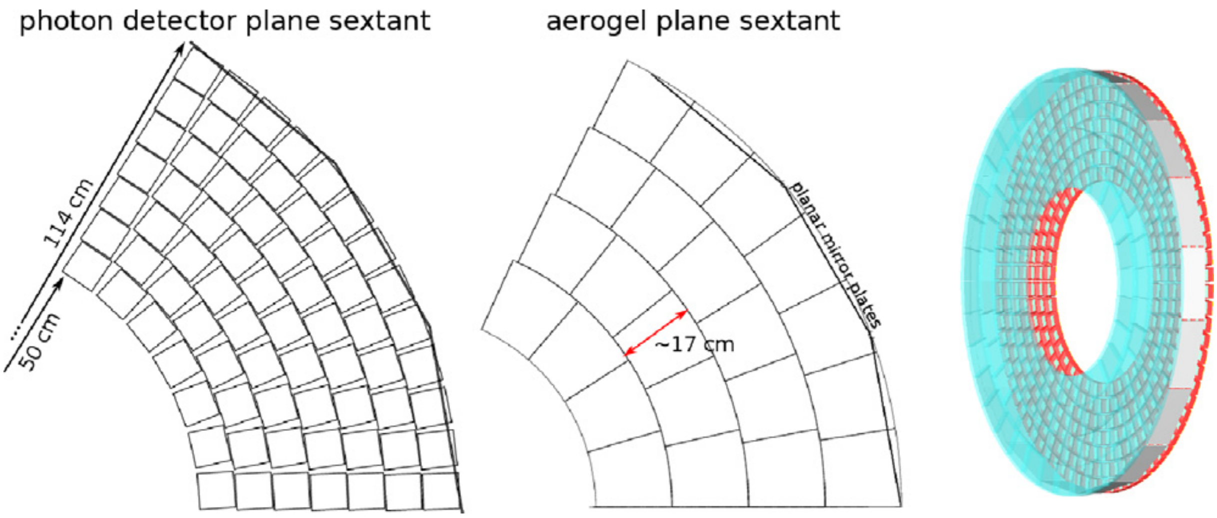

Figure 3.7: Illustration of the Belle II ARICH. Arrangement of photodetectors (left), aerogel plates (center) and image exported from detector simulation (right) [79]

The TOP covers the barrel part in a hexadecagonal shape with 16 quartz plates of $2600 \times 450 \times 20\,\mathrm{mm}$, which serve as Cherenkov radiators. One of the 16 modules is shown in Fig. 3.8. This thin structure provides lower mass and homogenization and enables the CDC to have a larger lever arm. A mirror is glued to the forward end face of each quartz plate, and a prism and photodetectors are glued to the backward end face. Cherenkov photons generated by the injection of charged particles are reflected and travel in the quartz to the photodetectors. The detection position and time of the Cherenkov photons are measured by micro-channel-plate photo-multiplier tubes with a very high time resolution of less than 50 pico seconds per single photon. Particle identification by the TOP is based on the time-of-flight, traveling time from the collision to the quartz injection, the time-of-propagation of the Cherenkov light in the TOP module and the count of Cherenkov photons. The probability density function of the measured position and time is calculated from which the CDC tracking information and the particle hypothesis can determine the momentum and position of incidence. A comparison of the probability density function (pdf) (coloured map) for different particle hypotheses with respect to the position and time of the detected photons (black points) is shown in Fig. 3.9. This example shows that the agreement with the pdf is very good under the kaon hypothesis.

Performance for π/K identification is evaluated using real data of $D^{*+} \to D^0\pi^+(D^0 \to K^-\pi^+)$ decays. As a typical performance value in forward end-cap (barrel), the percentage of pions misidentified as pions is 11% (7.8%) when identification is performed with a kaon identification efficiency of 94% (87%) [80, 79].

3.2.4 Electromagnetic calorimeter (ECL)

The ECL is used for the detection of photons from electromagnetic showers, electron identification, and triggering. The detector consists of 8736 Thallium-doped Cesium Iodide crystals arranged as shown in Fig. 3.10. The crystals are cylindrically arranged with an inner diameter of 125 cm, and the end cap is located 196 cm in front and 102 cm behind the IP. It covers a polar angle range of 12.4°–155.1°, corresponding to a solid angle of 92%, with a 1° gap between the barrel and the end cap. The crystals are trapezoidal and have different shapes depending on their location. It is typically $6 \times 6\,\mathrm{cm}$ in the front face and 30 cm length, corresponding to a 16.2 radiation length. The crystal is wrapped in 200 μm polytetrafluoroethylene, 25 μm aluminium and 25 μm mylar sheet. A $10 \times 20\,\mathrm{cm}^2$ photon detector is glued to the outer end face.

The crystals and photodetectors used in the Belle detector are also employed in the Belle II detector. The typical photon energy resolution is $\sigma_E/E = 4\%$ at $100\,\mathrm{MeV}$ and 1.6% at $8\,\mathrm{GeV}$. The angular resolution

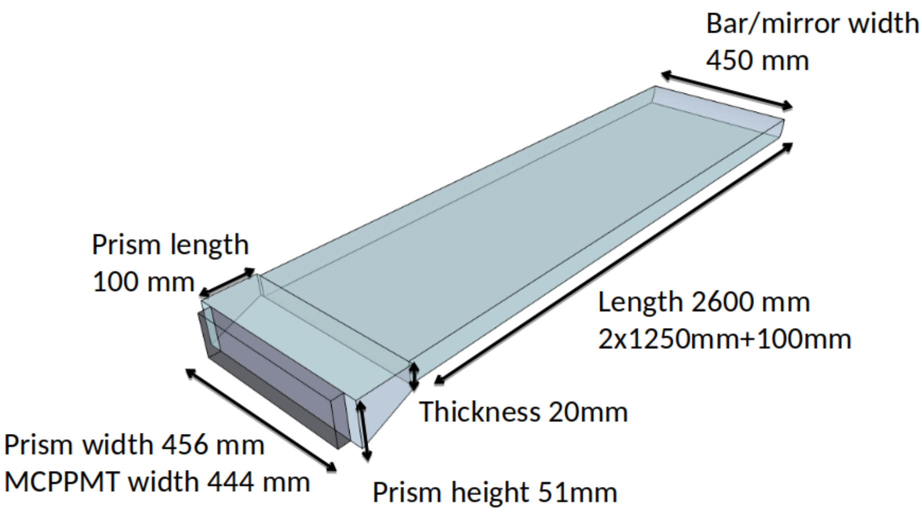

Figure 3.8: 3D view of a module of the Belle II TOP counter [81]

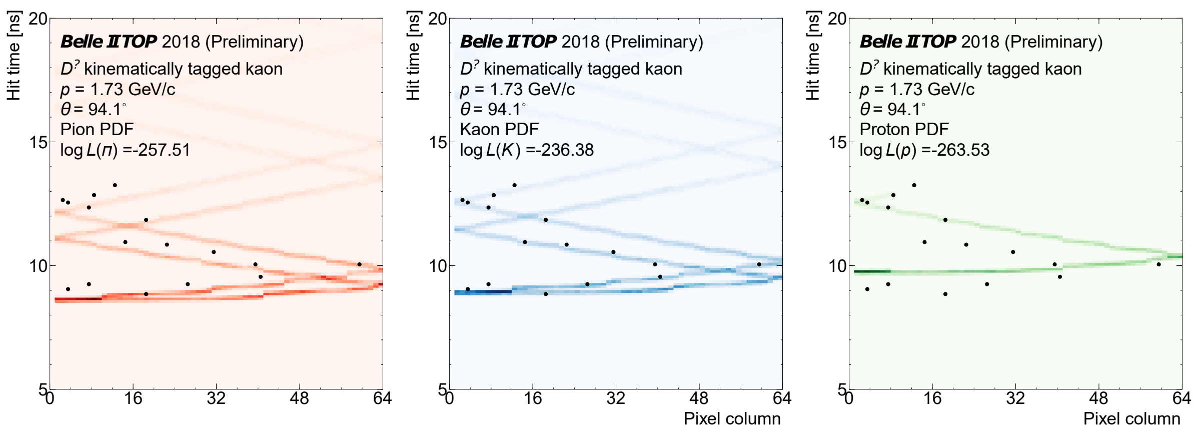

Figure 3.9: Space–time distribution of the hits associated with a kaon candidate track [81]. The x-axis represents the position of the detector pixel along the width direction of the quartz, while the y-axis represents the detection time with respect to the collision. The black points are the observed hits, while the coloured distribution is the pdf for a pion (left), a kaon (center) or a proton (right) hypothesis with the same measured track.

is 13 $\mathrm{milliradian}$ for low energy photons and 3 $\mathrm{milliradian}$ for high energy photons [70].

A ratio of ECL cluster energy to track momentum, measured by the CDC, is beneficial for electron identification. Electron identification, when combined with other detectors, has been evaluated using $J/\psi \to e^+e^-$, $e^+e^- \to e^+e^-$ and $Ks \to \pi^+\pi^-$ decays in real data. As a typical performance value, the percentage of pions misidentified as electrons is 2% when identification is performed with an electron identification efficiency of 94% [82].

3.2.5 K-long and muon detector (KLM)

The KLM is installed for the detection of hadron showers caused by K_L^0, which are long-lived neutral particles, and for the identification of muons, which have high penetrability of materials. The KLM is divided into a barrel section with an octagonal cylindrical shape and a disc-shaped end-cap section. It consists of 15 (14 in the end-cap) 4.7 cm-thick iron plates alternating with 14 charged particle detectors, ensuring 3.9 interaction lengths in the vertical direction. The barrel section covers a polar angle range

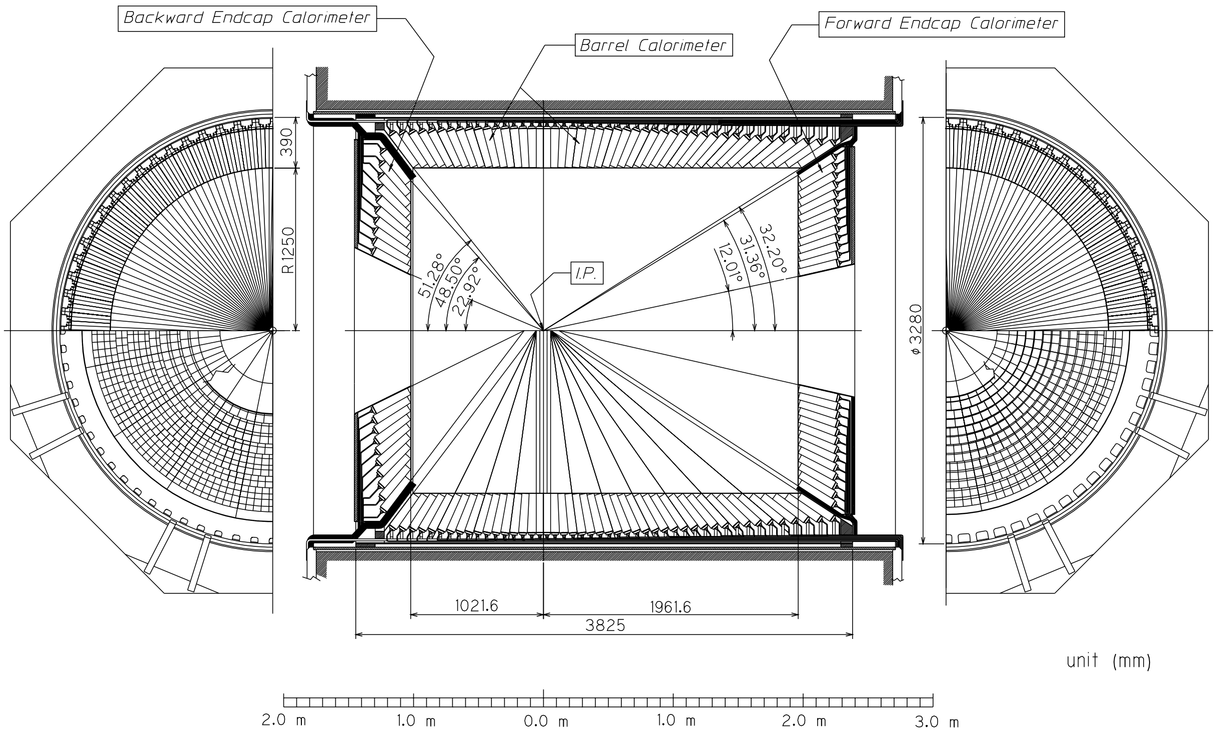

Figure 3.10: Overall configuration of the Belle II ECL. It is adapted from Belle paper [83] as the crystal layout is common. Upper (lower) half of side panels represents the layout in the barrel (end-cap) region.

of 45°–125° and the end-cap covers the outside of that range to 20°–155°. Two types of charged-particle detectors, scintillation counters and resistive plate chambers (RPC) are used for the charged-particle detection part. Scintillation counters are used in the inner two layers of the end-cap part and the barrel part to withstand neutron backgrounds from the accelerator, while RPCs are employed in the outer 13 layers of the barrel part.

Muon identification, when also combined with other detectors, has been evaluated using $J/\psi \to \mu^+\mu^-$ and $Ks \to \pi^+\pi^-$ decays in real data. As a typical performance value, the percentage of pions misidentified as muons is 7% when identification is performed with a muon identification efficiency of 89% [82].

3.2.6 Level-1 trigger

The level-1 trigger system is a group of electronics that uses detector information to invoke data acquisition pipeline. The main objectives are to find the event occurrences of interest, to determine their event times, and to suppress the data acquisition rate of some QED events with large cross sections within a bandwidth. Typical event rates are shown in Table 3.1, where event rates occurring at these frequencies are eventually reduced to a trigger rate of less than 30 kHz. The trigger system consists of complex logic circuits using electronics and field-programmable-gated-array circuits. The trigger signal must be fired and provided to the DAQ system at a latency of 5 μs from the event occurrence. Figure 3.11 illustrate the schematic view of the trigger system. The sub-triggers based on the CDC, ECL, TOP and KLM are used to reconstruct objects from the respective hit information and send information such as the number of tracks, number of clusters, energy sum of ECL clusters and so forth. The information is sent to the downstream electronics, the global reconstruction logic module (GRL), to match the information between sub-triggers. The processed information is eventually sent to the global decision logic module (GDL), which adjusts the timing of the beam crossing and fires the trigger information to the DAQ. Trigger configurations are changed as necessary based on trigger rates and instantaneous luminosity at (or during) each experimental period.

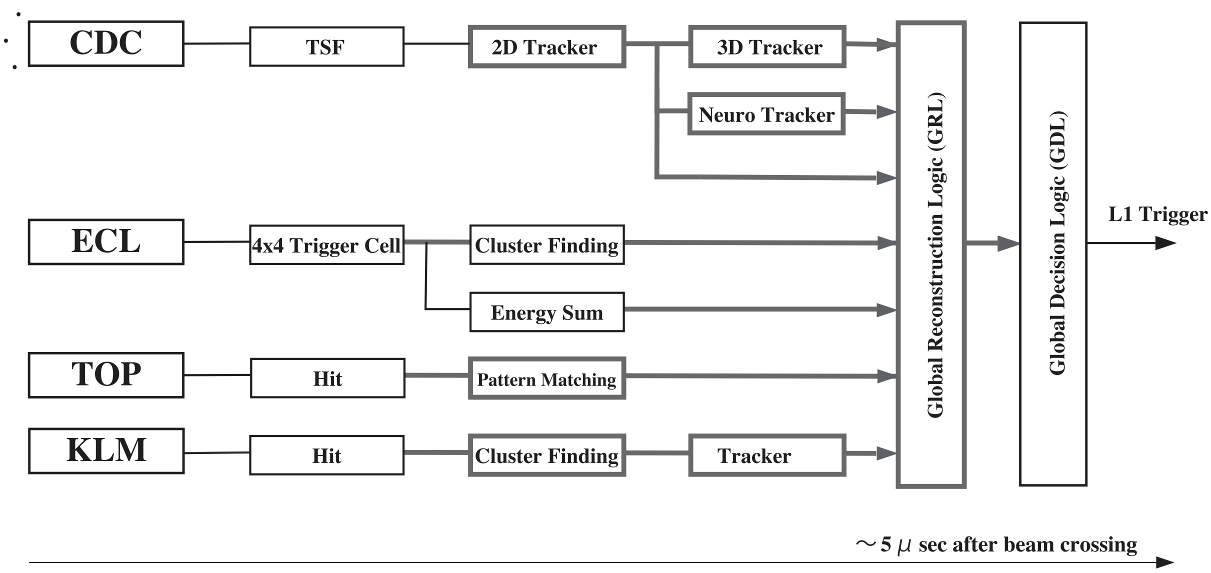

Figure 3.11: Schematic view of the Belle II Level-1 trigger system

3.2.7 Data acquisition system (DAQ) and High-level trigger

The DAQ system is designed to process data acquisition with a level-1 trigger rate coming at a maximum of 30 kHz with a dead time of 1% to store information from all the sub-detectors. The system is shown in Fig. 3.12. The trigger timing distribution system (TTD) is responsible for the distribution of the 127 MHz system clock synchronized to the 509 kHz of the SuperKEKB accelerator radio frequency and the distribution of the level-1 trigger timing. When the front-readout electronics on the detectors receive the trigger signal from the TTD, the event data is fragmented and read out to a common readout board *COPPER board* on readout computers. This readout is performed using a bi-directional high-speed serial communication protocol *Belle2link* designed for data readout at a speed of 2.54 Gbps via optical fibre. From winter 2021, COPPER boards are gradually converted to PCIe40 boards to enable more stable and faster readout [84]. The event rate is filtered by one fifth by applying the high-level trigger (HLT) from the reconstructed objects on the computers. Data health during data acquisition is checked at any time by fault detection in various parts of the system and by human monitoring of physical quantities using the reconstructed events. As the data size of PXD is large, information on the regions of interest, which is extrapolated from the tracks reconstructed by CDC and SVD, is determined by HLT to limit the data acquisition area of PXD. The raw data and its backup copy are transferred and stored in two data centers at KEK and Pacific Northwest National Laboratory (and BNL) using the Belle II distributed computing system [85].

3.3 Collision data sample

Experimental data used in this analysis were corrected from 2019 until summer 2021 on or near the $\Upsilon(4S)$ resonance, $\sqrt{s} = 10.58\,\mathrm{GeV}$, where experimental numbers are assigned according to time series and experimental conditions, and the dataset used in this analysis correspond to experiment number 7, 8, 10, 12, 14, 16, 17, and 18 in chronological order..

The integrated luminosity of the used dataset is measured to be $L_{\mathrm{int}} = 190.57 \pm 12.00\,\mathrm{fb}^{-1}$ [87] using the QED processes, Bhabha scattering ($e^+e^- \to e^+e^-$), and cross-checked using the $e^+e^- \to \gamma\gamma$ and $e^+e^- \to \mu^+\mu^-$ processes.

To distinguish it from the simulation samples described in later sections, actual data are referred to as “data”.

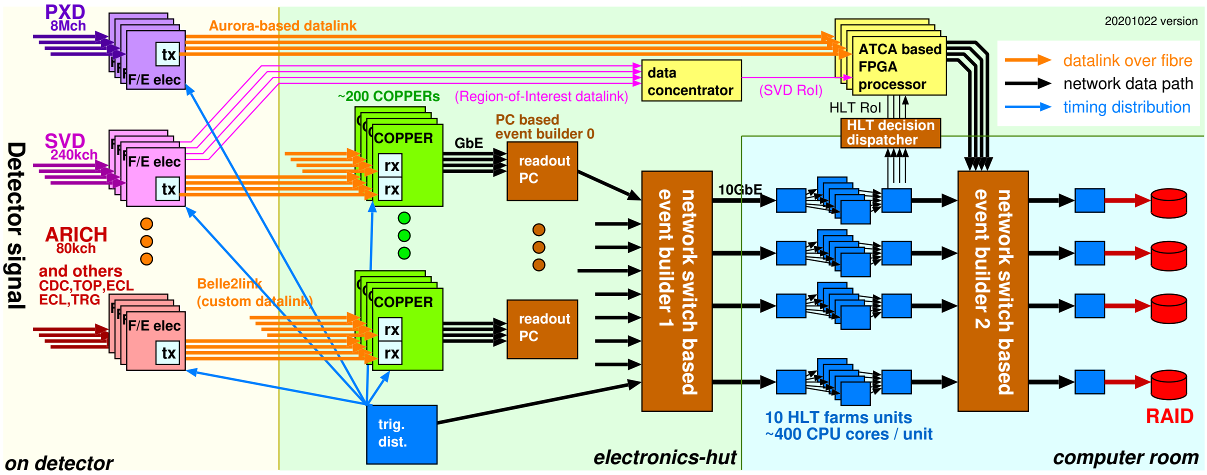

Figure 3.12: Schematic view of the Belle II DAQ [86]

3.4 Monte Carlo simulation sample

In MC simulations, MC event generator software calculates physical processes, its initial state and decay process, and the interaction of particles with the Belle II detector is simulated using a simulation toolkit GEANT4 [88] with the actual detector geometry. Various generators are used to simulate physical processes at e^+e^- collisions. We use about one order bigger simulation samples for the signal and the dominant background. Cross sections, statistics and generators for the used samples are summarized in Table 3.2.

Signal Monte Carlo sample

The signal MC simulation of $\pi^+\pi^-\pi^0$ process accompanying ISR radiation $e^+e^- \to \pi^+\pi^-\pi^0\gamma$ is generated using the PHOKHARA generator [89], version 9.1. The PHOKHARA generator program simulate $e^+e^- \to \gamma + hadrons$ processes in the NLO QED accuracy. The accuracy of NLO ISR means that the diagrams that include up to two ISR photons (Fig. 2.17 (c)–(f)) are taken into account, but the final-state radiation (FSR) is not simulated in the three-pion simulation. There is no limitation on the polar angle of the ISR photon at the sample production.

The hadronic cross section is simulated by a form factor model, where previous experimental data are used to determine parameters [90]. Intermediate states of three-pion decay consist of a mixture of the isospin-zero component and a slight isospin-one component. In isospin-zero component in PHOKHARA, the form factor take into account the vector meson resonances ω, ϕ, ω', ω'', ρ, and $\rho'' = \rho(1700)$ via the intermediate states $rho\pi$ and $\rho''\pi$ [Fig. 3.14 (a)]. The isospin-one processes $\rho \to \omega\pi^0 \to 3\pi$ and $\rho'' \to \omega\pi^0 \to 3\pi$ [Fig. 3.14 (b)] are modeled with fixed parameters based on past measurements. To model the isospin-one component, fourteen parameters are determined by fitting the data: the mass and width of the ω, ϕ, ω', and ω'' (8 parameters), the amplitudes of the processes of the four vector mesons via $\rho\pi$ intermediate state (4 parameters), and the amplitudes of the processes $\phi \to \rho'\pi$ and $\omega'' \to \rho''\pi$ (2 parameters). Fig. 3.14 shows a cross-section comparison of the data with that obtained by the fitted parameters.

Sharp resonances such as J/ψ are not simulated in PHOKHARA. The $e^+e^- \to J/\psi\gamma \to \pi^+\pi^-\pi^0\gamma$ was independently prepared by generating additional samples in 3π mass range of $3.09\,\mathrm{GeV} \pm 93\,\mathrm{keV}$ by PHOKHARA.

Background Monte Carlo sample

Other ISR-related background samples, $e^+e^- \to \pi^+\pi^-\gamma$, $e^+e^- \to \pi^+\pi^-\pi^0\pi^0\gamma$, and $e^+e^- \to K_S^0 K_L^0\gamma$, are generated using the PHOKHARA generator as well. The process $e^+e^- \to K^+K^-\pi^0\gamma$, which is not implemented in PHOKHARA, is also generated using PHOKHARA for NLO-ISR simulation and EVTGEN for hadronic decays. The continuum processes $e^+e^- \to q\bar{q}$ ($q\bar{q} = u\bar{u}, d\bar{d}, s\bar{s}, c\bar{c}$) is generated by KKMC includes the decay processes of all hadrons produced during the fragmentation performed by PYTHIA8.2. However, the hadronic cross section spectrum of KKMC is not as accurate as that of PHOKHARA. For $u\bar{u}$ and

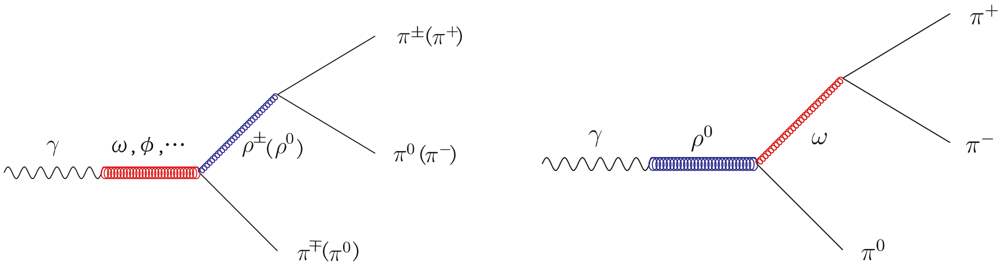

(a) (b)

Figure 3.13: Diagrams contributing to the three-pion current: (a) isospin-zero $I = 0$ component and (b) isospin-one $I = 1$ component. Adopted from Ref. [90].

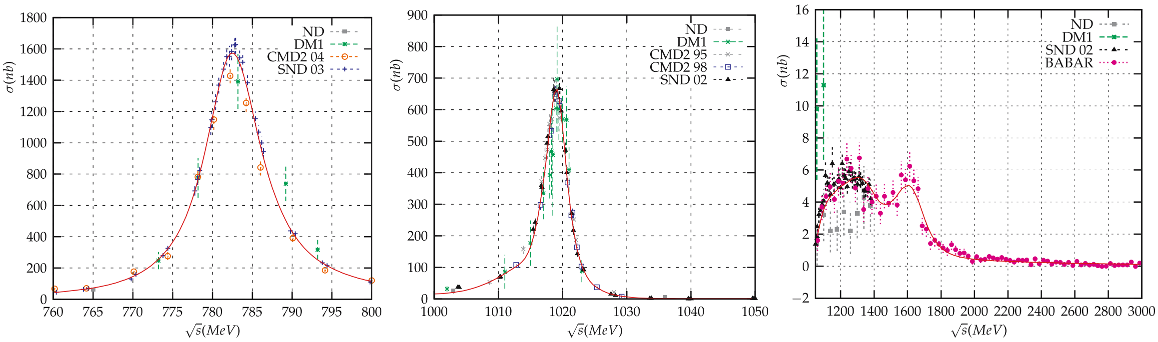

(a) (b) (c)

Figure 3.14: $e^+e^- \to \pi^+\pi^-\pi^0$ cross section of PHOKHARA parameters [90] and experimental data. (a)–(c) shows different mass ranges: (a) ω resonance, (b) ϕ resonance, and (c) 1.1–3.0 GeV. Adopted from Ref. [90].

$d\bar{d}$ samples, we reject events from $\pi^+\pi^-\gamma$, $\pi^+\pi^-\pi^0\gamma$, and $\pi^+\pi^-\pi^0\pi^0\gamma$ from KKMC to avoid the duplication with ones generated by PHOKHARA. Then, we call this KKMC MC sample as *Non-ISR* $q\bar{q}$ MC. Other ISR processes not provided by PHOKHARA also remain as background in partially reconstructed events. (see section 6.5 for the definition of the "partially" reconstructed events.) For this purpose, we use KKMC after removing the ISR processes discussed above. The lepton pair production $e^+e^- \to \mu^+\mu^-(\gamma), \tau^+\tau^-$ is generated by KKMC includes the decay processes of tau lepton performed TAUOLA2.7. (Radiative) Bhabha, $e^+e^- \to e^+e^-(\gamma)$, and $e^+e^- \to \gamma\gamma(\gamma)$ are generated by BABAYAGA@NLO.

Particles of the beam background from the accelerator are calculated using theoretical formulae and generators depending on each type of background, and their tracking in the accelerator is simulated and then overlaid before detector simulation [91].

Table 3.2: The summary of used MC samples.

Source	MC size (fb^{-1})	Cross section (nb)	Generator
$\pi^+\pi^-\pi^0\gamma$	2000	0.02594	PHOKHARA
$\pi^+\pi^-\pi^0\gamma$ (fake π^0)	2000	0.02594	PHOKHARA
$\pi^+\pi^-\gamma$	2000	0.1667	PHOKHARA
$\pi^+\pi^-\pi^0\pi^0\gamma$	1000	0.0395	PHOKHARA
$K^+K^-\pi^0\gamma$	1000	0.0006	PHOKHARA + EVTGEN
e^+e^- (γ)	50	295.8	BABAYAGA@NLO
$\gamma\gamma$	500	5.10	BABAYAGA@NLO
$\mu^+\mu^-\gamma$	1000	1.148	KKMC
$K_S^0\, K_L^0\, \gamma$	1000	0.008864	PHOKHARA
$u\bar{u}$	1000	1.605	KKMC + PHYTHIA + EVTGEN
$d\bar{d}$	1000	0.401	KKMC + PHYTHIA + EVTGEN
$s\bar{s}$	500	0.383	KKMC + PHYTHIA + EVTGEN
$c\bar{c}$	500	1.329	KKMC + PHYTHIA + EVTGEN
$\tau^+\tau^-$	300	0.919	KKMC + TAUOLA

Chapter 4

Event selection and signal extraction

This chapter describes reconstruction of particles, signal event selection, and signal extraction to obtain the mass spectrum. The particles, which is described by tracks and electromagnetic clusters, are reconstructed from detector signals in the sample. Then, the signal processes $e^+e^- \to \pi^+\pi^-\pi^0\gamma \to \pi^+\pi^-\pi^0\gamma\gamma\gamma$ are reconstructed from these particles and selected by applying event selection criteria to suppress the number of background events. Finally, the signal is obtained by fitting the two-photon invariant mass of the products of the π^0 decay. This fit is performed for each finely divided 3π mass bin to obtain the spectrum as a function of 3π mass (Eq. (2.46)).

Section 4.1 describes the trigger conditions used to filter the dataset for this analysis. Section 4.2 explains how the acquired data and simulated samples are processed to reconstruct charged and neutral particles based on detector signals. Section 4.3 describes selections for the signal process $e^+e^- \to \pi^+\pi^-\pi^0\gamma$. The agreement of kinematic variables of selected signal events between the data and the simulation is reviewed in Section 4.4. Section 4.5 accounts for obtaining the spectrum as a histogram of hadronic invariant mass $M_{3\pi}$.

4.1 Event triggering

ISR-related processes of interest, typically, involve an ISR photon with energies above 4 GeV, leaving signals on the ECL and can be triggered by ECL-based trigger lines. Different conditions of level-1 trigger are used in experiments 7–17, and 18 as summarized in Table 4.1. We use the trigger lines *hie* for expeirments 7–17 and *lml1* for experiment 18. The trigger line *hie* is fired by satisfying the total energy deposit of ECL crystals $E_{\text{tot}}^{\text{ECL}}$ is greater than 1 GeV. The trigger line *lml1* requires at least one ECL cluster to have the c.m. energy $E^{\text{c.m.,ECL}}$ of more than 2 GeV, which is higher enough than that of the signal ISR photon.

Efficiencies for the ISR signal on both trigger lines are 100% based on simulation. However, a scale-down filter was imposed on the *lml1* trigger during this experimental period due to limitations on the data-acquisition bandwidth, resulting in only 50% of the events being randomly selected.

Table 4.1: Hardware trigger condition used in each experimental number.

Experiment number	Integrated luminosity (fb^{-1})	Trigger condition	Random filtering
7-17	100.7	*hie* ($E_{\text{tot}}^{\text{ECL}} > 1\,\text{GeV}$)	100%
18	89.9	*lml1* ($E^{\text{c.m.,ECL}} > 2\,\text{GeV}$)	50%

4.2 Particle reconstruction

The detector signals in the data and the MC simulation are processed to reconstruct particles and compute variables through an event reconstruction algorithm using the Belle II analysis software framework BASF2 [92, 93].

4.2.1 Tracking

Charged particle is reconstructed as a track using hit information of VXD and CDC. Tracking algorithm consists of track finding [94] and track fitting [95].

Firstly, tracks and associated hits are found by complementary track-finding algorithms: the Legendle transformation, which targets global tracking, and the cellular automaton, which targets short tracks and tracks displaced from IP. The tracks detected by the two algorithms are combined and extrapolated to the SVD region using the combinatorial Kalman filter. After finding tracks using SVD hits, it is also extrapolated to the PXD region.

The precision of track momentum and position is enhanced by the track fitting algorithm, which fits the hits connected with the found track. The fit is implemented using a generic tracking toolkit GENFIT2 [96, 97], and the algorithm is based on the Kalman filter. In addition, the Deterministic Annealing Filter is applied to reduce hits wrongly connected to the track. Extrapolation among the detectors is calculated with the Runge-Kutta method based on the GEANT3 [98] simulation using realistic detector geometry and measured magnetic field mapping.

Variables related to tracks are defined as illustrated in Fig. 4.1. The origin point and momentum direction of a track are determined using the point of closest approach (POCA) on a track helix to the beam axis. Transverse (x-y) and longitudinal (z) distances from the POCA to IP are defined as dr and dz, respectively. Transverse component of momentum, perpendicular to the symmetric axis of the magnetic field, is defined as transverse momentum $p_T = \sqrt{p_x^2 + p_y^2}$. The number of CDC hits associated with the track after track fitting is defined as $N_{\rm cdchit}$.

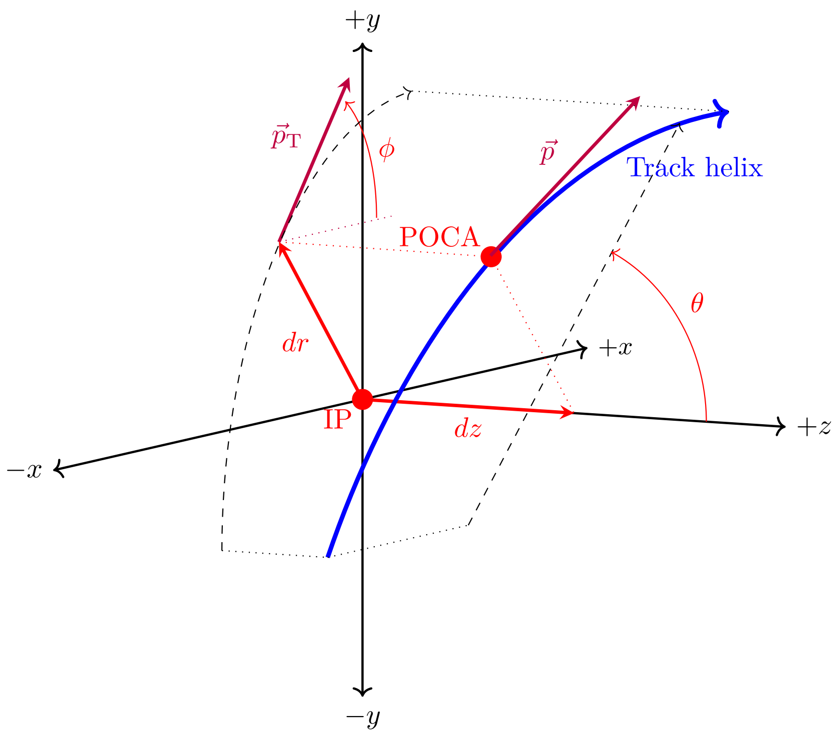

Figure 4.1: Track parametrization, adapted from [99]. It shows the relation between interaction point (IP), the point of closest approach (POCA) and the track helix obtained by the tracking fitting.

A bias of the track momentum due to the difference in magnetic field mapping is corrected. The process $D^0 \to K^+\pi^-$ is reconstructed from two charged particles, and the invariant mass of D^0 is compared to the mass measured by other experiments. As a result, the momentum of the track in data is collected with a scale factor of 0.99971.

4.2.2 Photon reconstruction

Photon is reconstructed as a cluster, a set of ECL crystals. Electromagnetic and hadronic shower is reconstructed as a cluster, and the energy, position and time of the energy deposits are obtained. Crystals with an energy deposit above $10\,\mathrm{MeV}$ are treated as seeds. Clusters are formed by an algorithm that connects the surrounding crystals. Up to 21 crystals with a maximum of 5×5, excluding four corners, are accounted for as one cluster. When multiple showers in the neighborhood and the clusters overlap, the energy of the overlapping crystals is divided into energy contributions. The cluster centroid is calculated by taking a weighted average based on the energy contribution of each crystal in the cluster. The clusters that do not match with any track extrapolated to the ECL region are treated as photons.

Photon variables are defined based on the assumption that photons are emitted from IP. The momentum vector of a photon is calculated with the cluster energy and the direction from IP to the cluster position. The weighted number of crystals in the cluster is defined as N_{crystal}. A cluster shape variable, *cluster second moment*, is a moment of cluster area weighted by crystal energy, which is defined as

$$S \propto A \frac{\sum_i^n E_i r_i^2}{\sum_i^n E_i}, \tag{4.1}$$

where i is the index of crystal, E_i is the single crystal energy, and r_i is the distance of the i-th digit to the shower center projected to a plane perpendicular to the shower axis [100]. The cluster second moment S is calibrated so that it is one for independent high-energy photons.

The energies of crystals are calibrated using the QED process $e^+e^- \to \gamma\gamma$. In addition, a bias of the reconstructed cluster energy in data is corrected using correction factors depending on the energy. The correction factors are evaluated using the processes $\pi^0 \to \gamma\gamma$ and $\eta \to \gamma\gamma\gamma$.

4.2.3 Particle Identification

Type of charged particle is identified by integrating the information of multiple detectors. The likelihood of each particle is calculated for each detector based on information such as energy deposition, energy-momentum ratio, time of flight, and radiation angles of Cherenkov photons.

The likelihood ratio of a pion with respect to an electron is defined as

$$\mathcal{P}_{\pi/e} = \frac{\prod_i L^i_{\pi/e}}{\prod_i L^i_{\pi/e} + \prod_i \left(1 - L^i_{\pi/e}\right)}, \tag{4.2}$$

where i is a detector index ($i =$CDC, ARICH, ECL, and KLM) and $L^i_{\pi/e}$ is a likelihood of a pion relative to an electron for a detector i.

As well, the likelihood ratio of a pion with respect to a kaon is defined as

$$\mathcal{P}_{\pi/K} = \frac{\prod_i L^i_{\pi/K}}{\prod_i L^i_{\pi/K} + \prod_i \left(1 - L^i_{\pi/K}\right)}, \tag{4.3}$$

where i is a detector index ($i =$CDC, ARICH, TOP, ECL, and KLM) and $L^i_{\pi/K}$ is a likelihood of a pion relative to a kaon for a detector i.

The likelihood ratio of a muon with respect to the other stable particles (electron, pion, kaon, proton, deuteron) is defined as

$$\mathcal{P}_{\mu} = \frac{\prod_i L^i_{\mu}}{\prod_i L^i_{\mu} + \prod_i \left(1 - L^i_{\mu}\right)}, \tag{4.4}$$

where i is a detector index ($i =$CDC, ARICH, TOP, ECL, and KLM) and L^i_{μ} is a likelihood of a muon relative to the other particles for a detector i.

4.3 Signal selection

The signal $e^+e^- \to \pi^+\pi^-\pi^0[\to \gamma\gamma]\gamma_{\mathrm{ISR}}$ candidates are reconstructed from a combination of two charged particles and three photons and selected by requiring several signal selection criteria, summarized in Table 4.2. After *baseline selection*, which loosely selects signal candidates, *background suppression criteria* are required to actively reduce individual background processes

Table 4.2: Summary of selection criteria for the signal event.

Quantity	Condition applied to select the signal
	Tracks
Transverse momentum	$p_T > 0.2\,\mathrm{GeV}/c$
Polar angle	$17.0° < \theta < 150°$
Closest distance to the IP	$dr < 0.5\,\mathrm{cm}$ and $\lvert dz\rvert < 2\,\mathrm{cm}$
CDC hits count	$N_{\mathrm{cdchit}} > 20$
	ISR photon
ECL crystal count	$N_{\mathrm{crystal}} > 1.5$
Energy in c.m. system	$E^{\mathrm{c.m.}} > 2\,\mathrm{GeV}$
Polar angle	$37.3° < \theta < 123.7°$
	$\gamma(\pi^0)$
ECL crystal count	$N_{\mathrm{crystal}} > 1.5$
Energy	$E > 100\,\mathrm{MeV}$
Polar angle	$17° < \theta < 150°$
	Event basis
Tracks count	$N_{\mathrm{track}} == 2$
Event charge	$\Sigma Q_{\mathrm{track}} == 0$
Photon count	$N_{\mathrm{gamma}} \geq 3$
	$\pi^+\pi^-\ \gamma\gamma\ \gamma$
Two-photon mass	$M_{\gamma\gamma} < 1.0\,\mathrm{GeV}/c^2$
ISR and hadron mass	$M(\pi^+\pi^-\gamma\gamma\gamma) > 8\,\mathrm{GeV}/c^2$
Four-conservation KFit χ^2	$\chi^2_{4\mathrm{C},2\pi3\gamma} < 50$
	π^0 (after 4C-KFit)
Daughter opening azimuthal angle	$\lvert\Delta\phi\rvert < 1.5\,\mathrm{rad}$
Daughter opening angle	$< 1.4\,\mathrm{rad}$
	Background rejection
Electron rejection	$\mathcal{P}_{\pi/e} > 0.1$
Kaon rejection	$\mathcal{P}_{\pi/K} > 0.1$
$\pi^+\pi^-\pi^0\pi^0\gamma$ rejection	$\chi^2_{4\mathrm{C},2\pi5\gamma} > 30$
$q\overline{q}$ rejection (1)	$M_{\pi^\pm\gamma_{\mathrm{ISR}}} > 2\,\mathrm{GeV}/c^2$
$q\overline{q}$ rejection (2)	$M_{\gamma_{\mathrm{ISR}}\gamma} < 0.11\,\mathrm{GeV}$ or $M_{\gamma_{\mathrm{ISR}}\gamma} > 0.17\,\mathrm{GeV}/c^2$
$q\overline{q}$ rejection (3)	$S_{\mathrm{ISR}} > 1.3$
$\pi^+\pi^-\gamma$ and $q\overline{q}$ rejection	$M^2_{\pi^+\pi^-,\mathrm{recoil}} > 4\,\mathrm{GeV}^2/c^4$

Baseline selection

Charged pion candidates are selected from the reconstructed tracks. Since the signal particles are emitted from the vicinity of the IP, the tracks are required to originate from the IP: $dr < 0.5\,\mathrm{cm}$ and $|dz| < 2\,\mathrm{cm}$. Polar angle must be in CDC acceptance, $17° < \theta < 150°$. Transverse momentum threshold $p_T > 0.2\,\mathrm{GeV}/c$ are required to avoid the curled tracks in the solenoid. These selections are loose and leave a large number of tracks, with a loss of tracks of around 4.5%. In addition, the number of CDC hits N_{cdchit} of more than twenty is required for good particle identification, which is a selection for background suppression.

Photons are selected from the neutral clusters of energy more than $100\,\mathrm{MeV}$. The polar angles of photons are required to be within the CDC acceptance $17° < \theta < 150°$ and have the weighted number of hit crystals in a cluster N_{crystal} more than 1.5. The energy cut is mainly intended to remove spurious photons that derive from low-energy beam background clusters; in simulation, the background cluster is reduced by about 80%, while the loss of signal photons is only about 10%. In the photons, ISR photon candidates are required to satisfy the level-1 trigger condition; the energy in the e^+e^- c.m. system is required to greater than 2 GeV and the polar angle in the laboratory frame is limited to the barrel region

$37.3^\circ < \theta < 123.7^\circ$.

π^0 candidates are reconstructed by taking any two-photon combinations in an event and requiring a proper π^0 mass region in the invariant mass of the two-photon system $M_{\gamma\gamma}$. We can take a combination that includes photons that do not originate from π^0 decay, and the candidates become backgrounds. We call this background a "combinatorial π^0 background" or "combinatorial background". A proper selection of photon candidates is important to reduce the fake photons and, then, to reduce this combinatorial background.

We select the signal candidates, $e^+e^- \to \pi^+\pi^-\pi^0\gamma_{\rm ISR}$ (we call this one as "$3\pi\gamma$" candidates), in the following conditions. There are two charged particles in an event with the opposite charge. We take all three-photon combinations in which one photon satisfies the ISR photon requirements and the other two photons have an invariant mass less than $1.0\,{\rm GeV}/c^2$. In order to perform an two-photon invariant mass fit at final step, the invariant mass criteria is considerably looser than width of the π^0 peak at the baseline selection. For each combination, we require the invariant mass of the $\pi^+\pi^-\gamma\gamma\gamma_{\rm ISR}$ system, where charged pion mass is assumed for the charged particles, is greater than $8\,{\rm GeV}/c^2$. The selected combinations are subject to the four-momentum conservation kinematic fit; we call this *4C-KFit* under the hypothesis $e^+e^- \to \pi^+\pi^-\gamma\gamma\gamma$: the summed four-momentum of all final states is constrained to the beam four-momentum [101, 102]. The π^0 mass is not constrained for the $M_{\gamma\gamma}$ fit. The number of measured parameters of photons and tracks are three (momentum) and six (vertex+momentum), respectively. The number of degrees of freedom is four. The chi-squared of the fitting result, which is a goodness of the fit, is denoted by $\chi^2_{4{\rm C},2\pi3\gamma}$.

After applying 4C-KFit, photon pairs of π^0 candidate are selected by requiring that the $\gamma\gamma$ opening angle is smaller than $1.4\,{\rm rad}$ and the difference of $\gamma\gamma$ in azimuthal angle $|\Delta\varphi|$ is smaller than $1.5\ {\rm rad}$. Signal efficiency for the angular selection is almost 100%, but it is effective to eliminate fake photons of background events. The $\gamma\gamma$ invariant mass selection optimizes efficiency and reduces combinatorial π^0 backgrounds.

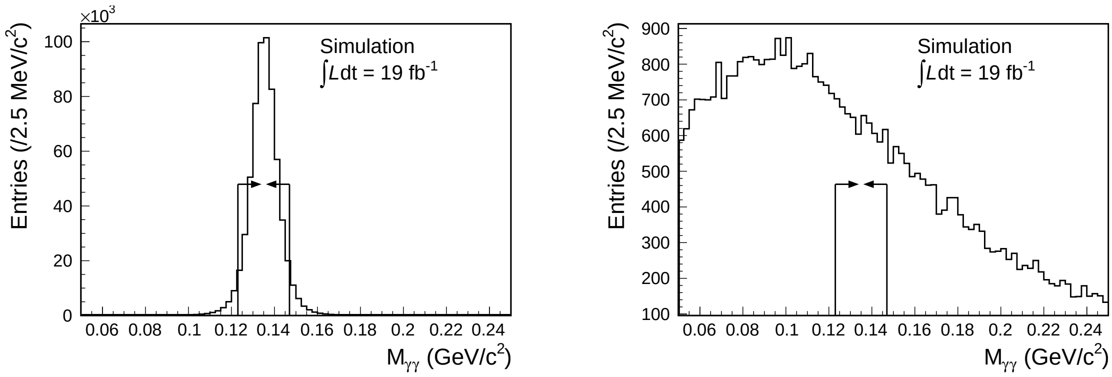

(a) Signal π^0

(b) Fake π^0

Figure 4.2: Invariant mass of the two-photon system after 4C-KFit in simulated signal events. (a) shows only two-photon combinations of "true" photons originating from π^0 signal in generator level. (b) shows two-photon combinations that contain "fake" photons that originate. We can see no π^0 signal peak in (b), the fake-photon combination.

The chi-squared of 4C-KFit, shown in Fig. 4.3, less than 50 is selected. The signal efficiency of this selection is 77.8%. This selection can drastically reduce backgrounds, i.e., 97% of $\pi^+\pi^-\gamma$ events, 96% of $\pi^+\pi^-\pi^0\pi^0\gamma$ events, and 89% of $\pi^+\pi^-\pi^0\gamma$ combinatorial background are removed. The cut-value of chi-squared is large, somewhat comparing the number of degrees of freedom since processes with more than two or more ISR/FSR emissions are included. Still, we chose the point that keeps the high efficiency for the signal and removes the backgrounds effectively.

Background suppression criteria

Since background events are expected to remain after the selection up to this point, background suppression criteria are applied to reduce these physical processes.

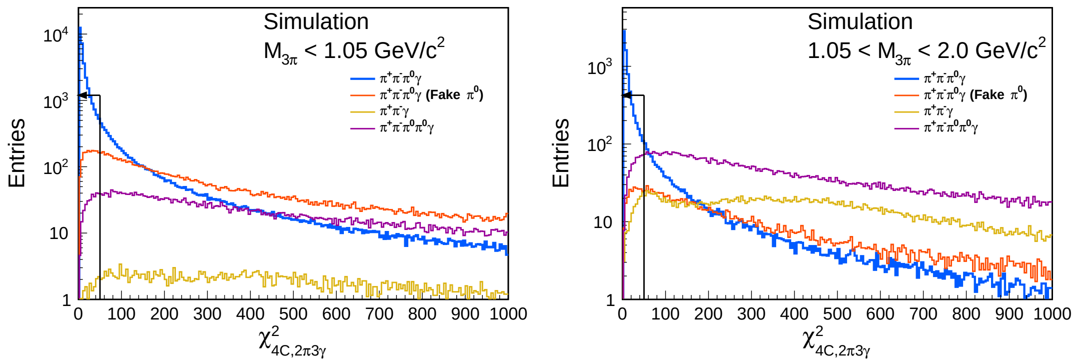

(a) (b)

Figure 4.3: Chi-squared distribution of 4C-KFit in simulation (a) the ω resonance region and (b) the higher mass region (1.05–2.0 GeV/c^2). The region shown by the arrow is accepted as a signal.

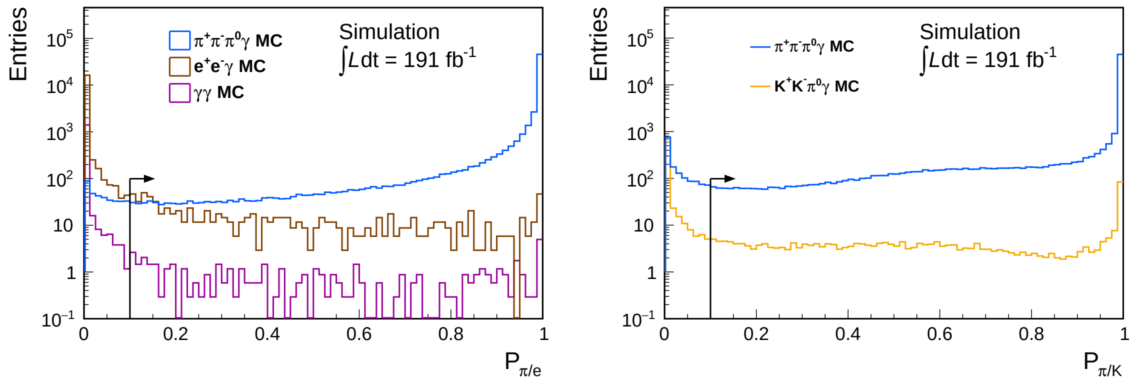

(a) (b)

Figure 4.4: Likelihood-ratio distribution for particle identification in simulated sample. The region shown by the arrow is accepted as a signal. The left (right) plot shows the lower pion-likelihood with respect to electron (kaon) among the two tracks.

Particle identification: electron and kaon background suppression

The particle identification is required for two tracks. The likelihood-ratio distribution is shown in Fig. 4.4. For separating a pion from an electron in (a) and from a kaon in (b).

Suppose either of the charged particles is identified as an electron with $\mathcal{P}_{e/\pi} > 0.9$; those events are rejected to reduce the radiative Bhabha and the single-tag two-photon events with photon-conversion. This selection reduces 99.5% of radiative Bhabha and 98.3% of two-photon backgrounds, keeping 98.9% signal efficiency.

We require that both charged particles should be identified as a pion with the condition $\mathcal{P}_{\pi/K} > 0.1$ to separate pion from kaon to reduce $e^+e^- \to K^+K^-\pi^0\gamma_{\mathrm{ISR}}$ background. As shown in Fig. 4.4(b), the signal efficiency is 95.6%. This selection rejects more than 80% of the $e^+e^- \to K^+K^-\pi^0\gamma$ background.

$e^+e^- \to \pi^+\pi^-\pi^0\pi^0\gamma$ suppression

One of the most significant backgrounds in the signal sample is from a process $e^+e^- \to \pi^+\pi^-\pi^0\pi^0\gamma_{\mathrm{ISR}}$. $\pi^+\pi^-\pi^0\pi^0\gamma$ candidates are reconstructed and applied a selection for χ^2 after 4C-KFit under $\pi^+\pi^-\pi^0\pi^0\gamma$ hypothesis to reduce $\pi^+\pi^-\pi^0\pi^0\gamma$ background. $\pi^+\pi^-\pi^0\pi^0\gamma$ candidates are reconstructed from two charged particles, an ISR photon, and four photons. If the event does not contain four photons that satisfy the two π^0 conditions given below, a $\pi^+\pi^-\pi^0\pi^0\gamma$ rejection is not imposed. The tracks and ISR

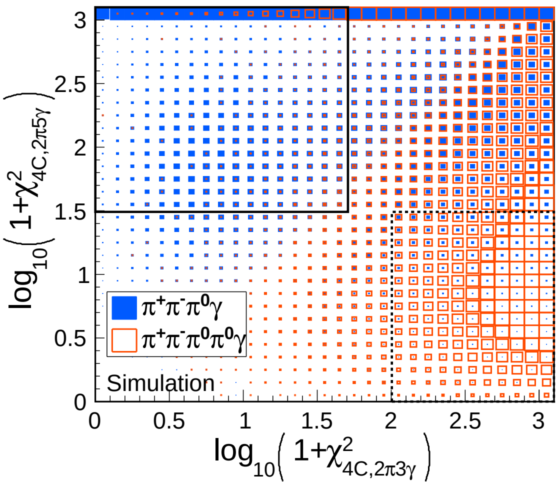

(a)

Figure 4.5: $\chi^2_{4C,2\pi3\gamma}$ (horizontal axis) and $\chi^2_{4C,2\pi5\gamma}$ (vertical axis) distribution. The red and blue square represents $\pi^+\pi^-\pi^0\gamma$ and $\pi^+\pi^-\pi^0\pi^0\gamma$ components, respectively. The top row shows the events in which no $\pi^+\pi^-\pi^0\pi^0\gamma$ candidate is found. The solid box corresponds to the signal selection, and the dotted box shows the requirement for a $4\pi\gamma$ control sample (used in chapter 5.2). The integrated luminosity of both MC samples are normalized to be same.

photon requirement is the same criterion used in the baseline selection. Two π^0's are reconstructed with different selection criteria. The minimum photon energy is 100 MeV for one π^0 and is 50 MeV for the other. The invariant mass selection $0.110 < M_{\gamma\gamma} < 0.158\,\mathrm{GeV}/c^2$ is applied to both π^0 before the kinematic fit. The two-photon opening angle selection is not applied. The chi-squared of the fitting result under the $\pi^+\pi^-\pi^0\pi^0\gamma$ hypothesis is denoted by $\chi^2_{4C,2\pi5\gamma}$. Figure 4.5 shows the two-dimensional plots of $\chi^2_{4C,2\pi3\gamma}$ and $\chi^2_{4C,2\pi5\gamma}$ for the signal $\pi^+\pi^-\pi^0\gamma$ and the $\pi^+\pi^-\pi^0\pi^0\gamma$ background MC samples. We can see a clear separation between the two chi-squared. In the $\pi^+\pi^-\pi^0\pi^0\gamma$ simulation, the $\pi^+\pi^-\pi^0\pi^0\gamma$ candidates are found in 56% of the $\pi^+\pi^-\pi^0\gamma$ candidates of $\chi^2_{4C,2\pi3\gamma} < 50$, and 64% in that of $100 < \chi^2_{4C,2\pi3\gamma} < 1000$. Figure 4.6 shows $\chi^2_{4C,2\pi5\gamma}$ distribution. The $\pi^+\pi^-\pi^0\pi^0\gamma$ events are clearly concentrated at $\chi^2_{4C,2\pi5\gamma} < 30$. To remove this contribution from our signal, we require $\chi^2_{4C,2\pi5\gamma} > 30$ and $\chi^2_{4C,2\pi3\gamma} < 50$. The requirement on $\chi^2_{4C,2\pi5\gamma}$ rejects 38% of $\pi^+\pi^-\pi^0\pi^0\gamma$ background, while this loss only 2.8% of our signal (see Fig. 4.6(a)). For example, $\pi^+\pi^-\pi^0\pi^0\gamma$ background enhanced sample is selected with the condition $\chi^2_{4C,2\pi5\gamma} < 30$ and $100 < \chi^2_{4C,2\pi3\gamma} < 1000$.

Non-ISR $q\bar{q}$ suppression

Selection for an invariant mass of charged pion and the highest energetic photon (γ_{ISR}), $M_{\pi^\pm\gamma_{\mathrm{ISR}}} > 2\,\mathrm{GeV}/c^2$, is required to reduce background from $\tau^+\tau^-$ and non-ISR $q\bar{q}$. [1] This selection aims to reduce the events including $\rho^\pm \to \pi^\pm\pi^0[\to\gamma\gamma]$ resonances. In this case, one or both photons of the π^0 daughter can have high energy and be reconstructed as an ISR photon. There are two cases in which $M_{\pi^\pm\gamma_{\mathrm{ISR}}}$ has a peak around the rho-mass, 770 MeV/c^2. One is that two photons from a π^0 are merged and reconstructed as a single hight-energy cluster. The second is a case where only one photon is energetic. To demonstrate the second case, the black line in Fig. 4.7 shows the generator-level $M_{\pi^\pm\gamma\gamma}$ distribution for the $u\bar{u}$ sample that contains $\rho^\pm$ and the one of the photon energy is greater than 2 GeV/c^2. The generator level means variable information before the detector simulation, As expected, the distribution has a peak of rho resonance. For this sample, both $M_{\pi^\pm\gamma_{\mathrm{ISR}}}$ and $M_{\pi^\pm\gamma\gamma}$ have a similar distribution as shown in Fig. 4.8. To avoid efficiency loss due to the requirement for the presence of two photons, a cut is applied to the $\pi^\pm$ γ invariant mass. Figure 4.9 shows $M_{\pi^\pm\gamma_{\mathrm{ISR}}}$ distribution of the reconstructed $\pi^+\pi^-\pi^0$ candidates in the signal and $q\bar{q}$ MC samples. The $M_{\pi^\pm\gamma_{\mathrm{ISR}}} > 2.0\,\mathrm{GeV}/c^2$ cut eliminates 0.85% of signal $\pi^+\pi^-\pi^0\gamma$, 35% of $u\bar{u}$ and $d\bar{d}$.

[1]Strictly speaking, this photon is the highest energy photon in the event but is denoted here as γ_{ISR} because ISR photon candidates correspond to the photon in more than 99% of signal-like events.

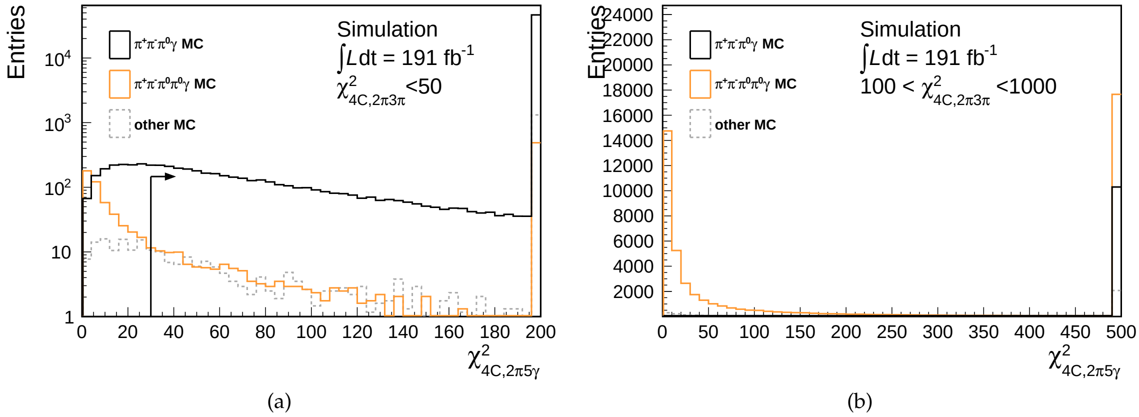

Figure 4.6: $\chi^2_{4C,2\pi5\gamma}$ distribution after applying all selections except for the quantity in question. (a) shows events in $\chi^2_{4C,2\pi3\gamma} < 50$ region. (c) shows events in $100 < \chi^2_{4C,2\pi3\gamma} < 1000$ region. The most right bin includes overflowed events and events where additional π^0 is not reconstructed.

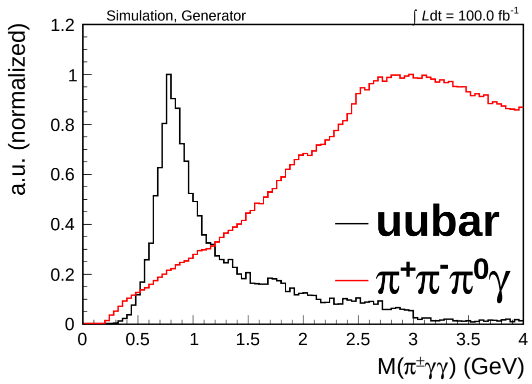

Figure 4.7: Generator-level $M_{\pi^\pm\gamma\gamma}$ distribution of $u\overline{u}$ and $\pi^+\pi^-\pi^0\gamma$ MC samples.

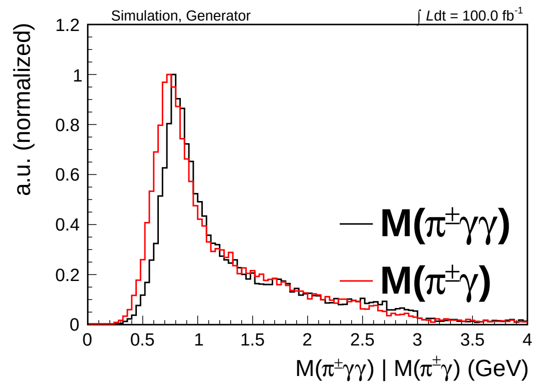

Figure 4.8: Generator-level $M_{\pi^\pm\gamma\gamma}$ distribution of $u\overline{u}$ and $\pi^+\pi^-\pi^0\gamma$ MC samples.

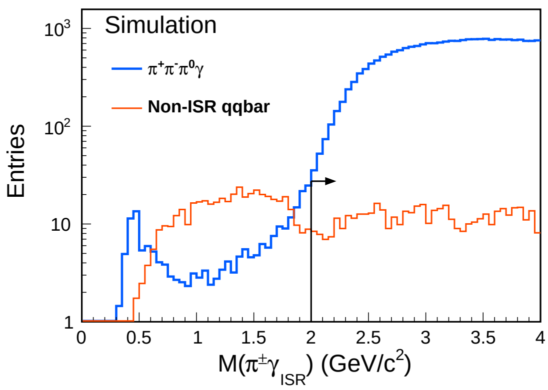

Figure 4.9: $M_{\pi^\pm\gamma_{\rm ISR}}$ distribution after applying all selections except for the quantity in question. The lower one in $\pi^+\ \gamma$ and $\pi^-\ \gamma$ combination is chosen.

To reduce further non-ISR $q\overline{q}$ where a daughter photon from π^0 is misidentified as the ISR photon but not reconstructed as a rho-signal, we use the invariant mass of ISR photon and the other photon with $E > 0.1\,\mathrm{GeV}$, $M_{\gamma_{\rm ISR}\gamma}$. The distribution is shown in Fig. 4.10(a). If multiple candidate photons exist, 4C-KFit with the hypothesis $e^+e^- \to \pi^+\pi^-\pi^0\gamma_{\rm ISR}\gamma$ is performed, and the photon with the smallest chi-squared is selected. The events containing a photon satisfying $0.10 < M_{\gamma_{\rm ISR}\gamma} < 0.17\,{\rm GeV}/c^2$ is rejected.

There is a candidate where the two daughter photons of energetic π^0 are detected as a single ECL cluster and reconstructed as an ISR photon. Some of these events can be distinguished from a second moment of the ECL cluster. Figure 4.10(b) shows the distribution of the cluster second moment for the ISR photon, $S_{\rm ISR}$. The $S_{\rm ISR}$ of single photon-like clusters are narrowly distributed around one, whereas merged cluster-like photons have the cluster second moment widely distributed from 1–4. Thus, we reject the ISR of the cluster second moment above 1.3. We can reject about 60% of non-ISR $q\bar{q}$ events by the $M_{\gamma_{\rm ISR}\gamma}$ and the second moment cut while the signal loss is 0.3%.

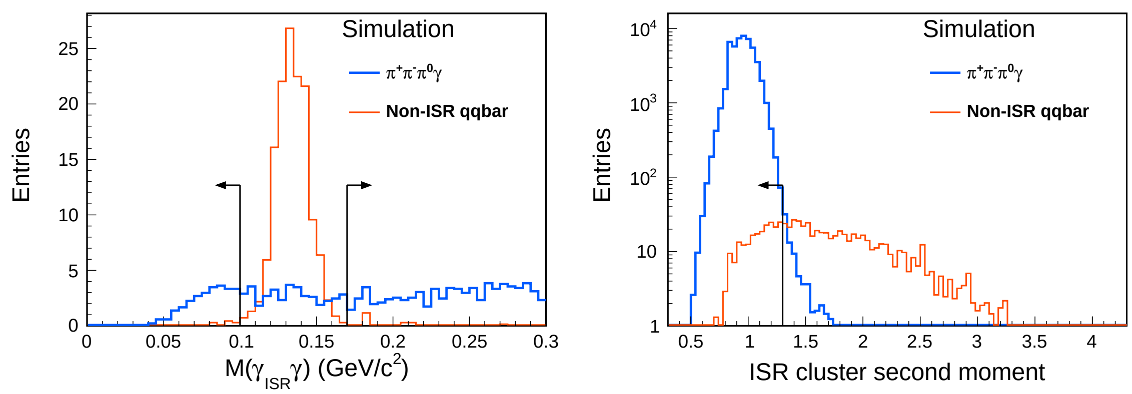

(a) $M_{\gamma_{\rm ISR}\gamma}$ (b) $S_{\rm ISR}$

Figure 4.10: $M_{\gamma_{\rm ISR}\gamma}$ and second moment of ISR cluster $S_{\rm ISR}$ distribution.

$e^+e^- \to \pi^+\pi^-\gamma$ and $e^+e^- \to \mu^+\mu^-\gamma$ suppression

To reduce $\pi^+\pi^-\gamma$ and $\mu^+\mu^-\gamma$ background, selection for recoil mass-square of $\pi^+\pi^-$ pair is required $M^2_{\pi^+\pi^-,{\rm recoil}} > 4\,{\rm GeV}^2/c^4$. The distributions for the simulation are shown in Fig. 4.11. The signal $\pi^+\pi^-\pi^0\gamma$ is lost by 0.14%, and $\pi^+\pi^-\gamma$ background is reduced by 24%. Figure 4.11 (b) shows that this selection effectively reduces $\pi^+\pi^-\gamma$ in $\chi^2_{4C,2\pi3\gamma}$ above 100, used as control samples for the background estimation.

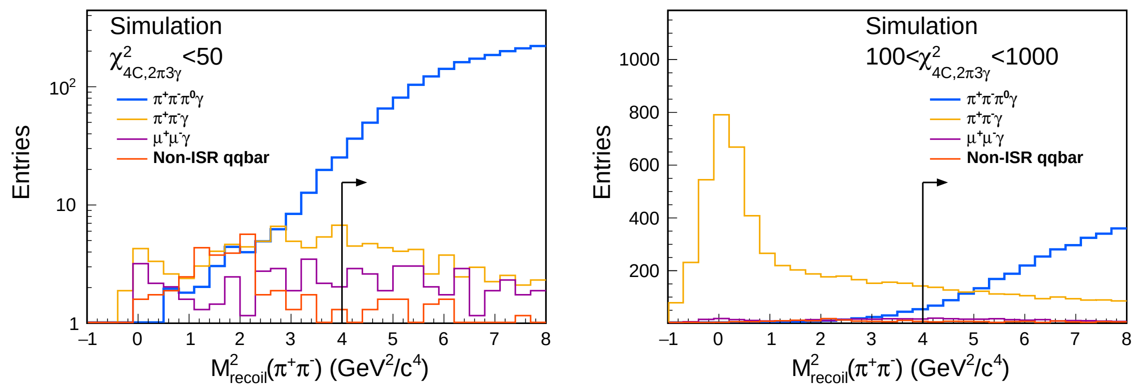

(a) $\chi^2_{4C,2\pi3\gamma} < 50$ (b) $100 < \chi^2_{4C,2\pi3\gamma} < 1000$

Figure 4.11: Recoil mass-square of $\pi^+\pi^-$ system for (a) the signal and (b) the control sample after applying all selections except for the quantity in question.

Best candidate selection

The number of combinations in an event after the selections is shown in Fig. 4.12. The fraction of events having more than one combination is 8%. We take the best candidate in an event based on the lowest $\chi^2_{4C,2\pi3\gamma}$, which is enough since the fraction is small.

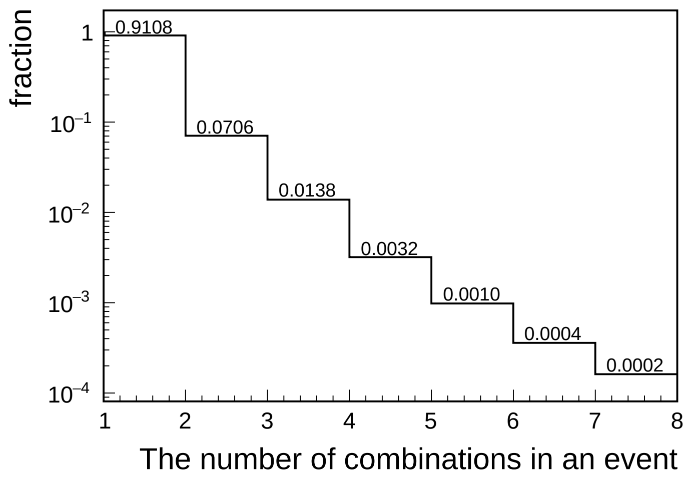

Figure 4.12: The number of combinations in a signal event.

Summary

Figure 4.13 shows the three-pion mass distribution expected from the signal and background MC samples after applying all selection criteria. The number of events after applying all selections is summarized in Table 4.3 for the signal and background MC samples. In total, the background suppression criteria increase the signal purity from 91% to 98%. For the latter sections, we call the events selected by the selection criteria as signal sample events.

Table 4.3: The Monte Carlo expectation of the number of residual signals and backgrounds before and after applying background suppression criteria. The size of simulated sample are scaled to be 191 fb^{-1}.

Source	No. of events w/o background suppression (A)	No. of events w/ background suppression (B)	$(A-B)/A \times 100(\%)$
$e^+e^- \to \pi^+\pi^-\pi^0\gamma$	55469.2	50374.9	9.18 ± 0.12
$e^+e^- \to \pi^+\pi^-\pi^0\pi^0\gamma$	1125.1	591.3	47.44 ± 1.54
$e^+e^- \to K^+K^-\pi^0\gamma$	972.7	131.4	86.49 ± 1.11
$e^+e^- \to \omega\pi^0$	279.9	69.4	75.20 ± 2.66
$e^+e^- \to q\overline{q}$ (No ISR)	1458.5	204.0	86.01 ± 0.92
$e^+e^- \to \pi^+\pi^-\gamma$	211.2	125.7	40.49 ± 3.66
$e^+e^- \to \mu^+\mu^-\gamma$	160.3	92.7	42.16 ± 4.25
$e^+e^- \to \tau^+\tau^-$	4.8	0.0	100.00 ± 0.00
$e^+e^- \to e^+e^-\gamma$	6663.1	8.7	99.87 ± 0.04
$e^+e^- \to \gamma\gamma$	875.2	2.9	99.67 ± 0.18
$e^+e^- \to B\overline{B}$	0.0	0.0	-
$e^+e^- \to B^0\overline{B}^0$	0.0	0.0	-

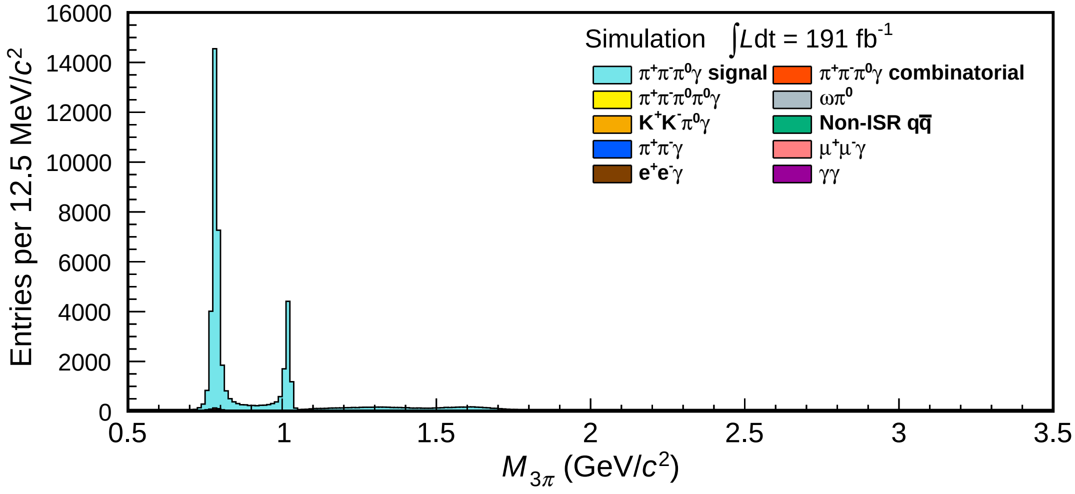

(a)

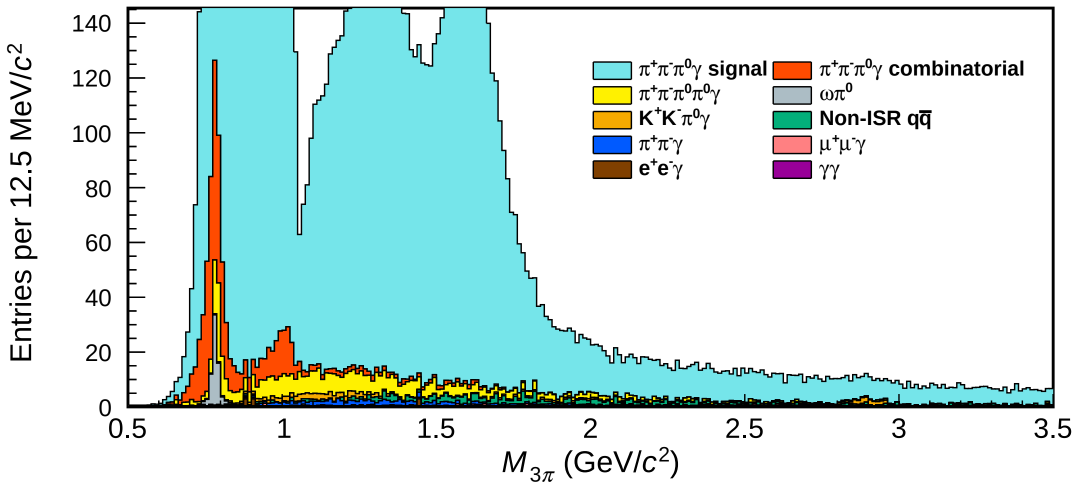

(b)

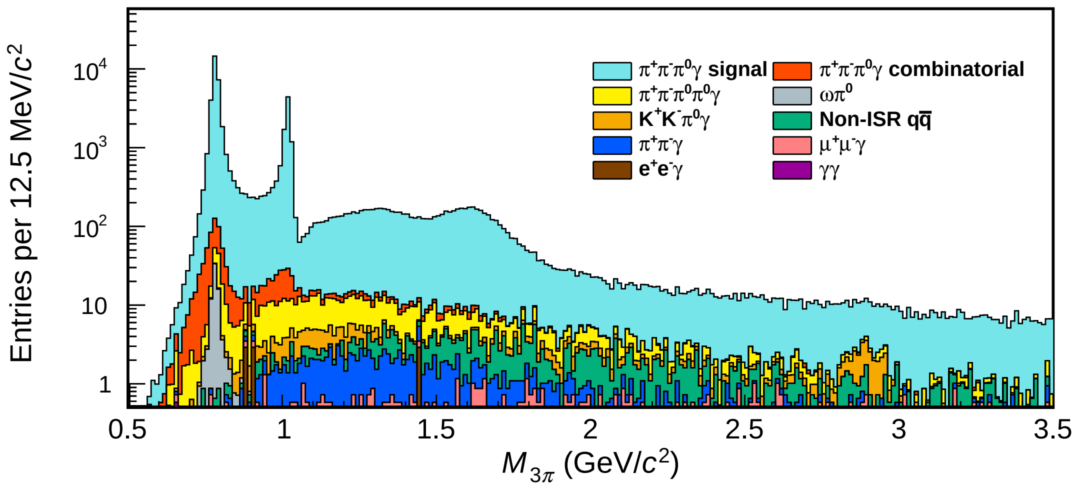

(c)

Figure 4.13: $M_{3\pi}$ distribution after applying the background suppression criteria. (a)–(c) show the distribution in different y-axis range and scale. The luminosity is scaled to 191 fb^{-1}. The $e^+e^- \to J/\psi\gamma \to \pi^+\pi^-\pi^0\gamma$ process is not plotted.

4.4 Comparison of kinematic variables for selected samples between data and simulation

For the sample remaining after all requirements, we show distributions of some kinematic variables to demonstrate how the simulation reproduces the data, and the level of background in the sample. Although we do not expect a perfect agreement between data and simulation, some level of consistency is needed since we obtain the first approximation of the signal efficiency relying on the simulation.

The energy and polar angle distributions of the ISR photon in data are shown in Fig. 4.14. The points with error bars are the data, and the blue solid histogram is the sum of the signal and the background expectation by MC simulation normalized to the data luminosity. The dotted histogram is the background expectation multiplied by a factor of 50. We note that the background is relatively small, at the level of 2 %. The ISR photon has an energy greater than 4 GeV. The polar angle of the ISR photon is limited in the barrel region.

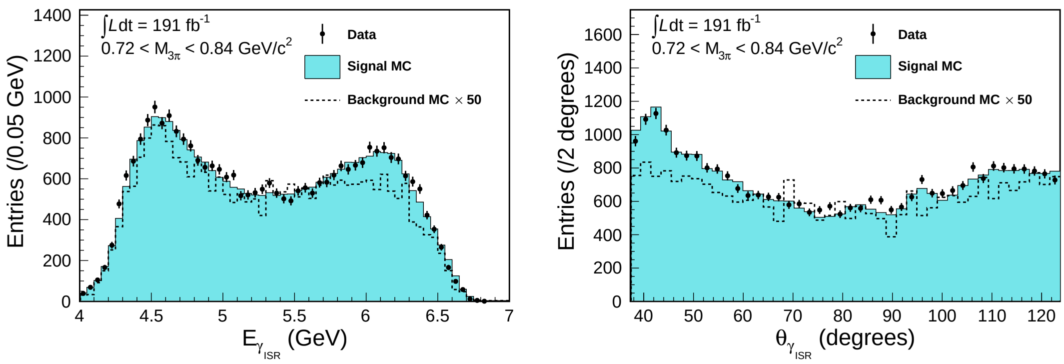

Figure 4.14: Distribution of (left) ISR energy and (right) polar angle in the laboratory frame. The points with error bars show the data after the signal selection. The filled and dashed histograms are the simulations for the signal and background, respectively. The MC expectation is normalized to the data luminosity. The background MC simulation is scaled by a factor of 50.

Figure 4.15 shows the momentum and polar angle distributions of charged pions. Figure 4.16 shows the invariant mass distribution of the two pions system when the invariant mass of the $\pi^+\pi^-\pi^0$ system is in the ω region, $M_{3\pi} \in [0.72, 0.84]\,\mathrm{GeV}/c^2$. The background MC simulation is scaled by a factor of 50 in these figures. The background is generally low, but careful checks on the MC predictions are needed. The good agreement in the variables confirms that the generator and detector simulation reproduce the basic variables well.

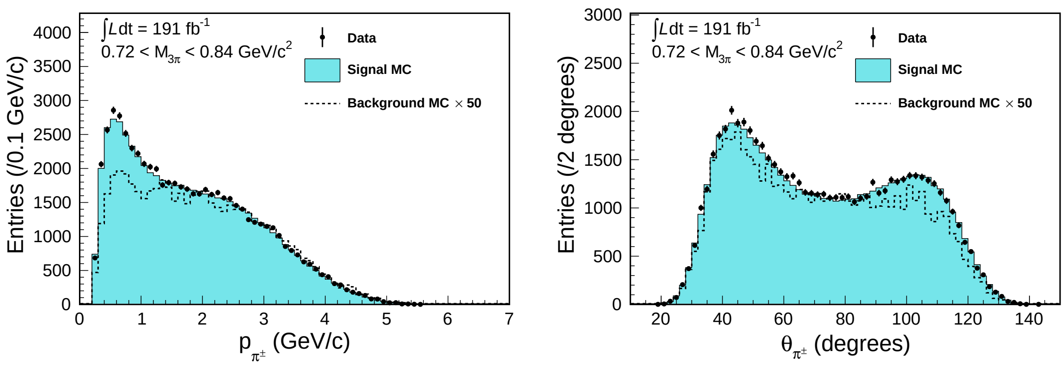

Figure 4.15: Distribution of (left) charged-pion momentum and (right) polar angle in the laboratory frame. The convention is the same as Fig. 4.14.

Figure 4.18 shows the number of combinations in a single event. The multiplecandidate is mainly due to the large number of π^0 combinations, but we can confirm that the simulations of spurious photons

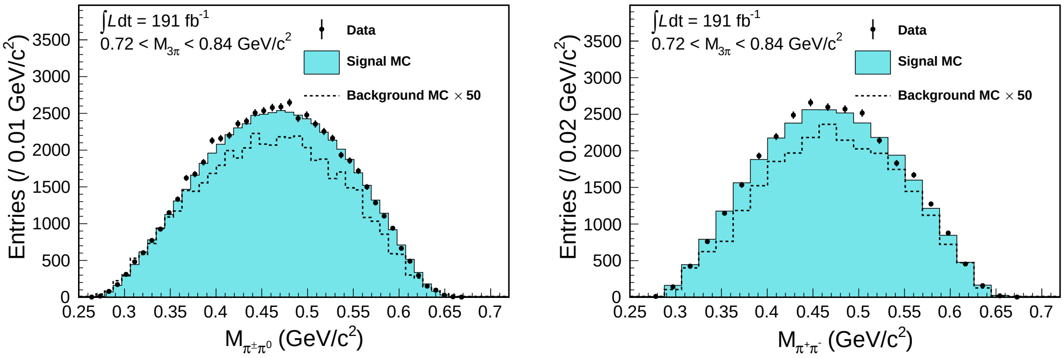

Figure 4.16: Distribution of dipion invariant mass. The left is the charged and neutral pion combination, and the right is the charged pion combination. The convention is the same as Fig. 4.14.

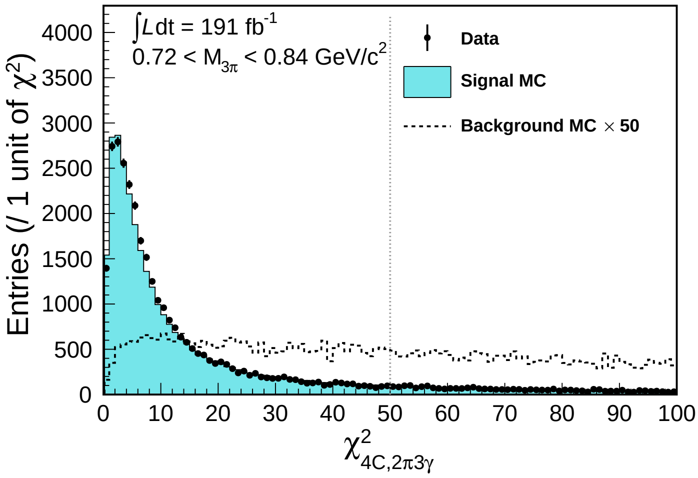

Figure 4.17: Distribution of $\chi^2_{4C,2\pi3\gamma}$ in the range $0.72 < M_{3\pi} < 0.84\,\mathrm{GeV}/c^2$. The convention is the same as Fig. 4.14.

are generally in good agreement.

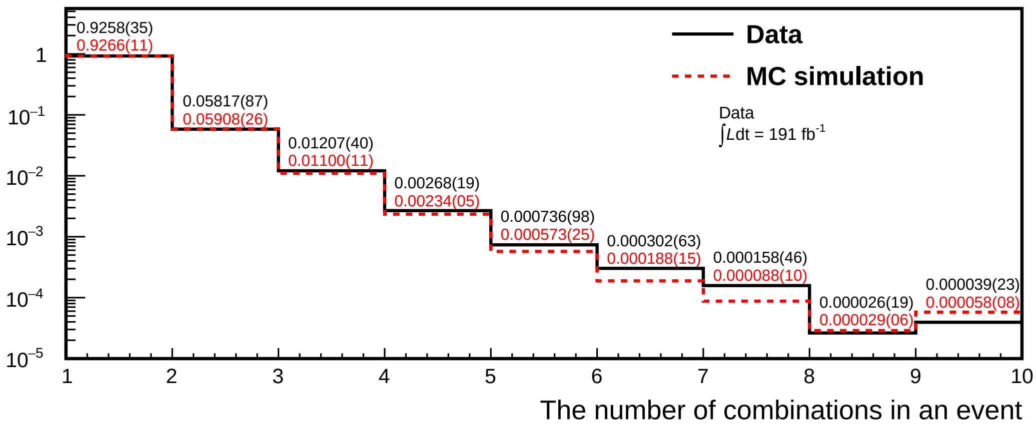

Figure 4.18: The number of combinations in a signal event in data (solid black) and simulation (red dashed).

4.5 Signal extraction

The signal events are estimated from the fitting of $M_{\gamma\gamma}$ for each $M_{3\pi}$ bin. To remove the combinatorial π^0 background in a model-independent way, we count the number of $\pi^+\pi^-\pi^0\gamma_{\rm ISR}$ events by fitting the $M_{\gamma\gamma}$ distribution in each $M_{3\pi}$ mass bin with the signal and smooth background. For this purpose, we first need to know the precise π^0 signal shape in $M_{\gamma\gamma}$ for data and MC. Then, bin-by-bin $M_{\gamma\gamma}$ fittings are performed to determine the spectrum based on the obtained π^0 signal shape information.

To obtain better mass resolution, the 3π invariant mass $M_{3\pi}$ is calculated using four-momenta of π^+,π^-, and π^0 obtained from the results of a five-constraint kinematic fit, where the summed four-momentum is constrained to the e^+e^- beam four-momentum and invariant mass of photon pair is constrained to the nominal π^0 mass. The detailed discussion on the mass resolution is discussed in chapter 7. To write clearly to avoid misunderstandings, the $M_{3\pi}$ binning is determined by the result of 5C-KFit (fit with four-momentum conservation + π^0 mass constraint), and the number of signals is extracted by a fit to the $M_{\gamma\gamma}$ distribution determined by 4C-KFit (fit with four-momentum conservation).

Unless explicitly stated as $M_{\gamma\gamma}$ fits, signal extraction in the background estimation (chapter 5 and signal efficiency evaluation (chapter 6) is not done by fits, but by simple counts of events within $0.123 < M_{\gamma\gamma} < 0.147\,\mathrm{GeV}/c^2$.

4.5.1 π^0 lineshape determination

The $M_{\gamma\gamma}$ distributions after applying all signal selection are shown in Fig. 4.19 for simulation, and in Fig. 4.20 for data. The lineshape of the π^0 determines the parameters of the signal function by performing a fit to the signal event. The parameters determined here are separated for the 3π mass region below and above $1.05\,\mathrm{GeV}/c^2$. Below $1.05\,\mathrm{GeV}/c^2$, the ω and ϕ resonances are used for fitting. Above $1.05\,\mathrm{GeV}/c^2$, a mass region from $1.05\,\mathrm{GeV}/c^2$ to $2.0\,\mathrm{GeV}/c^2$ is used. As long as MC simulation study, the signal π^0 lineshape $f(x)$ can be described as Novosibirsk function and single Gaussian:

$$f(x) = R_{nov.}A_{nov.}\exp\left(-\frac{1}{2\sigma_0^2}\ln^2\left(1-\frac{x-x_p}{\sigma_E}\eta\right)-\frac{\sigma_0^2}{2}\right)+(1-R_{nov.})\,\frac{1/\sqrt{2\pi}\sigma}{\exp}\left(-\frac{x-\mu}{2\sigma^2}\right), \qquad (4.5)$$

where the first term is the Novosibirsk function, which is a logarithmic Gaussian function [103], the second term is the Gaussian, and the ratio is $R_{nov.}$.

A quadratic function models the background. The number of floated parameters in this fit is six for the signal pdf, two for the background function, and the number of signal and background. The fit range differs depending on $M_{3\pi}$, summarized in Table 4.4. The parameters of fit results are summarized in Table. 4.6. In 1.05–$2\,\mathrm{GeV}/c^2$, the tail of the Novosibirsk function η is zero for the simulation, which means the Novosibirsk function is equivalent to a single Gaussian.

Table 4.4: $M_{\gamma\gamma}$ fit range as a function of 3π mass.

$M_{3\pi}$ region	$M_{3\pi} < 1.05\,\mathrm{GeV}/c^2$	$1.05 < M_{3\pi} < 2.0\,\mathrm{GeV}/c^2$	$2.00 < M_{3\pi} < 3.5\,\mathrm{GeV}/c^2$
$M_{\gamma\gamma}$ fit range	50–230 MeV	50–290 MeV	70–290 MeV

Table 4.5: π^0 lineshape parameters of the fitting results using simulation. The corresponding plots are Fig. 4.19. $R_{Nov.}$ is a ratio of the Novosibirsk function to the Gaussian in the signal pdf.

Parameter	Symbol	$M_{3\pi} < 1.05\,\mathrm{GeV}/c^2$	$1.05 < M_{3\pi} < 2.0\,\mathrm{GeV}/c^2$
Gaussian mean	μ	0.135510 ± 0.000034	0.13661 ± 0.00023
Gaussian sigma	σ	0.00964 ± 0.00009	0.00931 ± 0.00047
Nov. mean	x_p	0.135316 ± 0.000013	0.13621 ± 0.00005
Nov. width	σ_0	0.00501 ± 0.00003	0.00485 ± 0.0002
Nov. tail	η	0.000 ± 0.000016	0.0000 ± 0.0002
Ratio of Nov. to Gaussian	$R_{Nov.}$	0.6687 ± 0.0092	0.620 ± 0.056

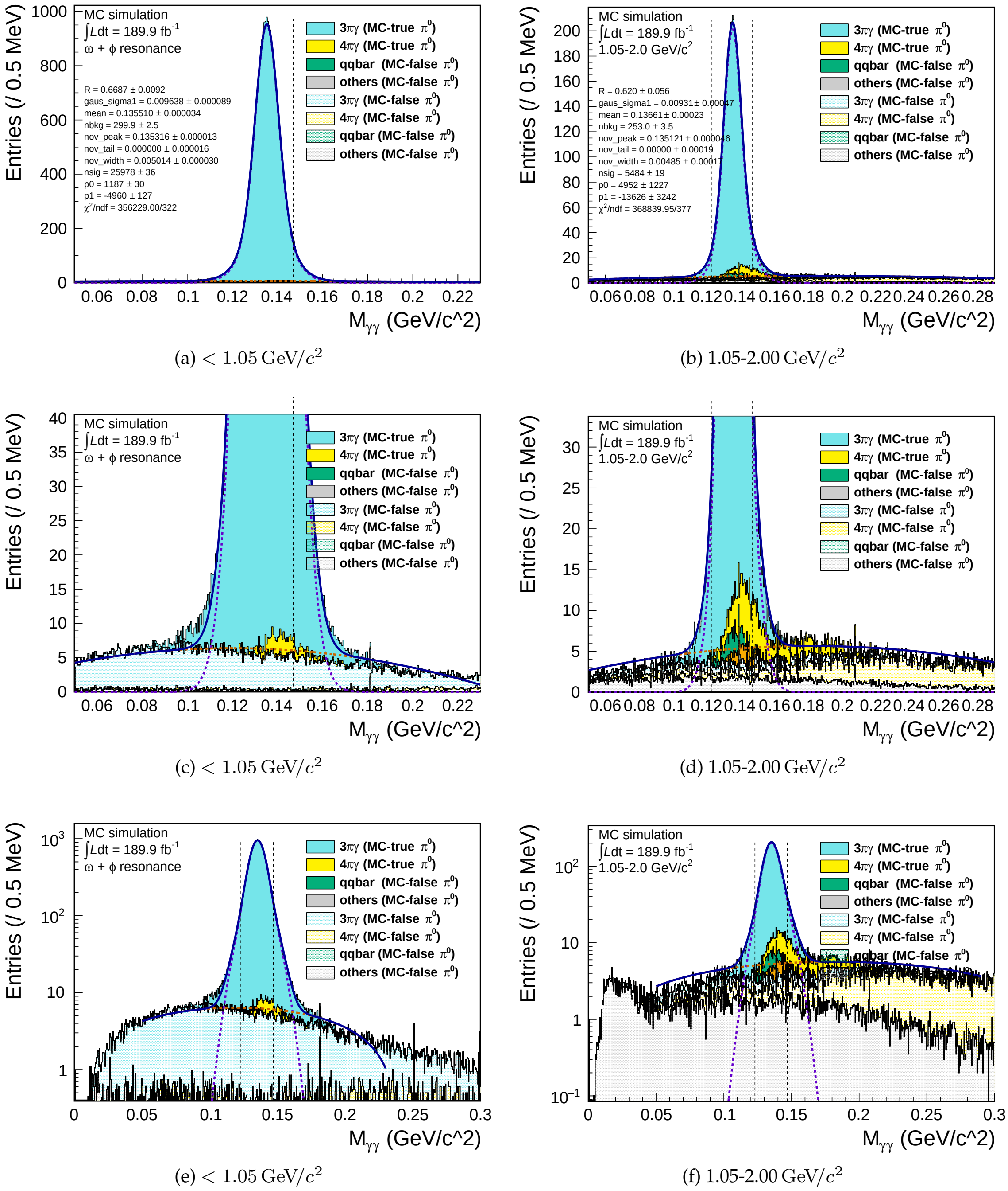

(a) $< 1.05\,\mathrm{GeV}/c^2$

(b) 1.05-2.00 GeV/c^2

(c) $< 1.05\,\mathrm{GeV}/c^2$

(d) 1.05-2.00 GeV/c^2

(e) $< 1.05\,\mathrm{GeV}/c^2$

(f) 1.05-2.00 GeV/c^2

Figure 4.19: $M_{\gamma\gamma}$ distribution of fit result for MC simulation (lines) and the breakdown (stacked histogram). The plots (a), (c), and (e) show the result for $M_{3\pi} < 1.05\,\mathrm{GeV}/c^2$. The plots (b), (d), and (f) show the result for $1.05 < M_{3\pi} < 2.00\,\mathrm{GeV}/c^2$. Difference among (a)(c)(e) ((b)(d)(f))is a range and scale of vertical axis. Only the small vertical axis is enlarged in (c) and (d) to make it easier to see at the foot. The wider $M_{\gamma\gamma}$ mass region is shown in (e) and (f) with a logarithmic scale for the y-axis. The *MC-true* and *MC-false* are identified using the generator-level information.

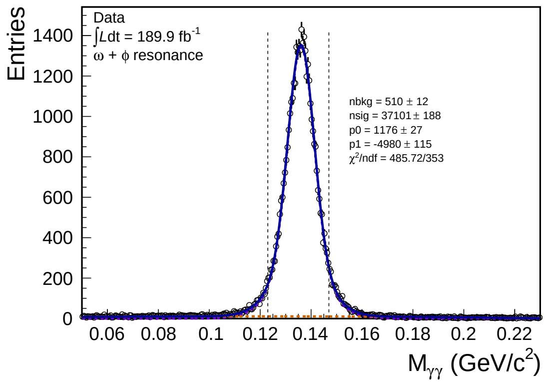

(a) $< 1.05\,\mathrm{GeV}/c^2$

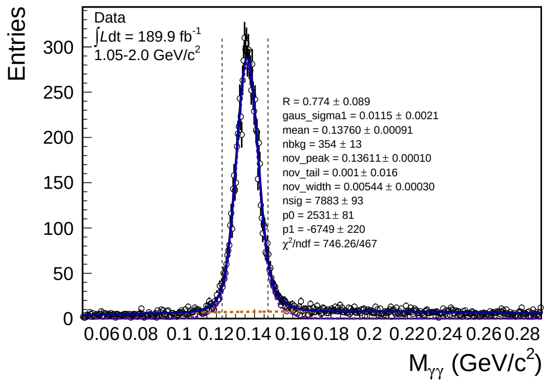

(b) 1.05-2.00 GeV/c^2

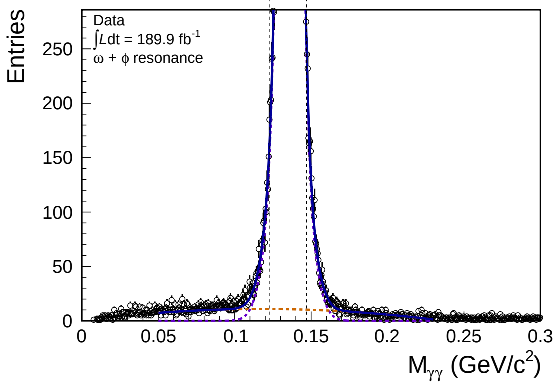

(c) $< 1.05\,\mathrm{GeV}/c^2$

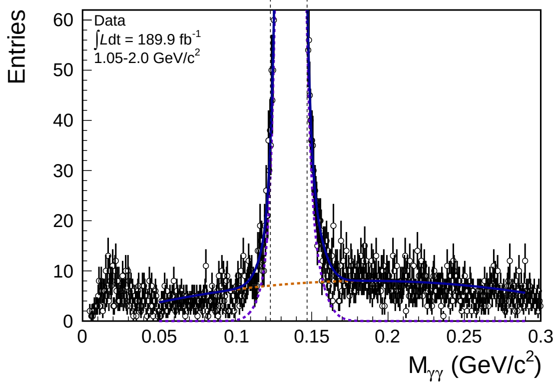

(d) 1.05-2.00 GeV/c^2

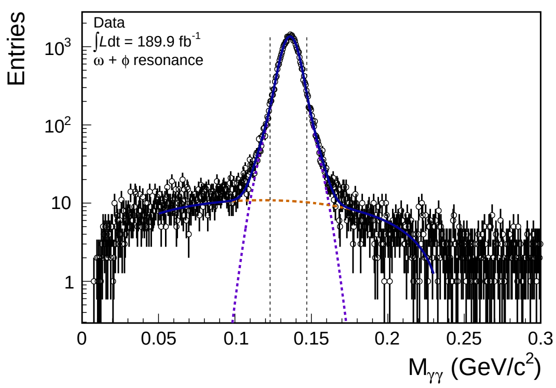

(e) $< 1.05\,\mathrm{GeV}/c^2$

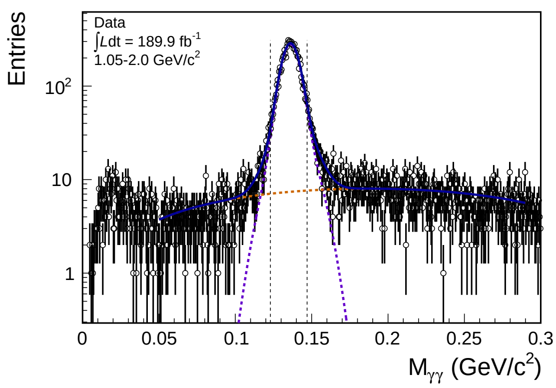

(f) 1.05-2.00 GeV/c^2

Figure 4.20: $M_{\gamma\gamma}$ distribution of fit result for data. A solid and dotted line shows the fit result for the total and the combinatorial background. The definition of each sub-figure is the same as Fig. 4.19

Table 4.6: π^0 lineshape parameters of the fitting results using the data The corresponding plots are Fig. 4.20. $R_{Nov.}$ is a ratio of the Novosibirsk function to the Gaussian in the signal pdf.

Parameter	Symbol	$M_{3\pi} < 1.05\,\mathrm{GeV}/c^2$	$1.05 < M_{3\pi} < 2.0\,\mathrm{GeV}/c^2$
Gaussian mean	μ	0.13556 ± 0.00029	0.1376 ± 0.00091
Gaussian sigma	σ	0.01010 ± 0.0003	0.0115 ± 0.0021
Nov. mean	x_p	0.13609 ± 0.00007	0.13611 ± 0.00010
Nov. width	σ_0	0.00508 ± 0.00009	0.00544 ± 0.00030
Nov. tail	η	0.000 ± 0.00015	0.001 ± 0.016
Ratio of Nov. to Gaussian	$R_{Nov.}$	0.676 ± 0.027	774 ± 0.089

4.5.2 Number of signal extraction in each $M_{3\pi}$ bin

Unequal bin width for an invariant mass of $\pi^+\pi^-\pi^0$ is adopted because the distribution varies drastically over the mass range. The optimal bin width changes from 2.5 MeV to 50 MeV depending on its statistics in $M_{3\pi} < 1.05\,\mathrm{GeV}/c^2$ region, from 50 MeV to 500 MeV depending on its statistics in $M_{3\pi} > 1.05\,\mathrm{GeV}/c^2$ region. We chose a bin width of 50 MeV for lower than $0.6\,\mathrm{GeV}/c^2$, 20 MeV for $0.6\,\mathrm{GeV}/c^2 < M_{3\pi} < 0.7\,\mathrm{GeV}/c^2$, 2.5 MeV for ω and ϕ region, $0.7\,\mathrm{GeV}/c^2 < M_{3\pi} < 1.05\,\mathrm{GeV}/c^2$, 25 MeV for $1.05\,\mathrm{GeV}/c^2 < M_{3\pi} < 2.00\,\mathrm{GeV}/c^2$ region, 50 MeV for $2.50\,\mathrm{GeV}/c^2 < M_{3\pi} < 3.50\,\mathrm{GeV}/c^2$ region.

We fit the π^0 signal and count the number of signals in each $M_{3\pi}$ mass bin with the signal pdf with six fixed parameters obtained in the π^0 lineshape determination (chapter 4.5.1) and the background function. The background function is modeled by a linear function to ensure stability in the fits. The floated parameters are the number of signal and background, and a parameter for the background pdf.

Figure 4.21 displays examples of the $M_{\gamma\gamma}$ fit in one $M_{3\pi}$ bin of large statistics, at the ω resonance peak, and small statistics, at the 900 MeV.

The obtained spectrum from the $M_{\gamma\gamma}$ fit in each $M_{3\pi}$ bin is shown in Fig. 4.22. No significant signal can be obtained in the $M_{3\pi}$ below $0.62\,\mathrm{GeV}/c^2$. Expected background distribution is also plotted as the stacked histogram, described in detail in chapter 5.

The combinatorial background is the mis-reconstructed π^0 caused by spurious γ. We can obtain the number of events in the same mass region, 0.123–0.147 GeV/c^2, as the signal from the fit results. For the validation, we compare the distribution of combinatorial background between data and simulation as shown in Fig. 4.23. Although the statistical error is significant, it can be seen that the amount of combinatorial background in data is larger than the sum of the background simulations. Since this combinatorial background depends on the correctness of the physics background simulation and the beam-induced background simulation, this level of difference is understandable.

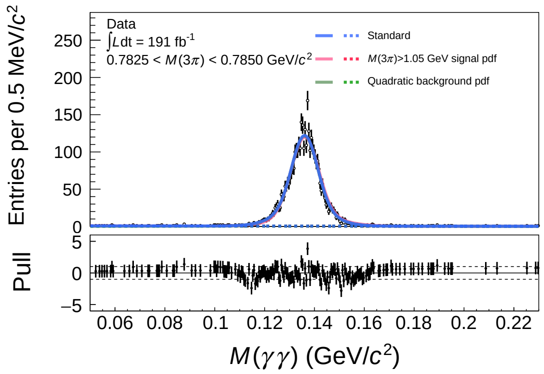

(a) ω peak

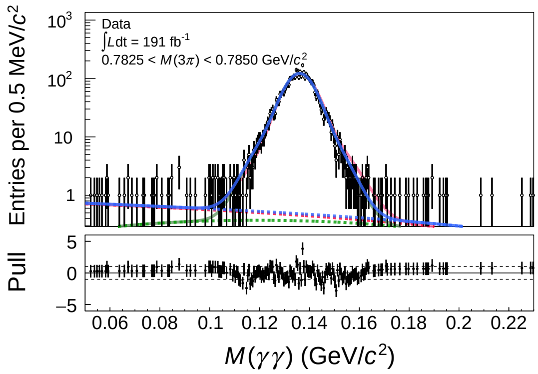

(b) ω peak (log-scale)

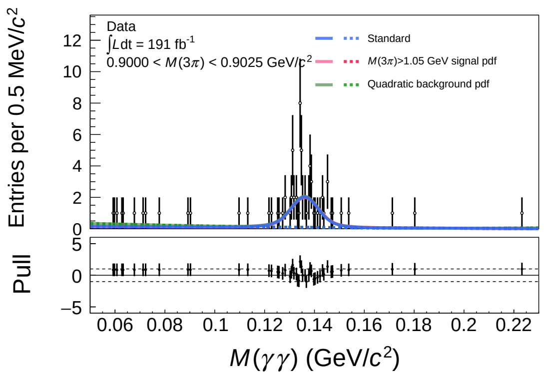

(c) 900 MeV

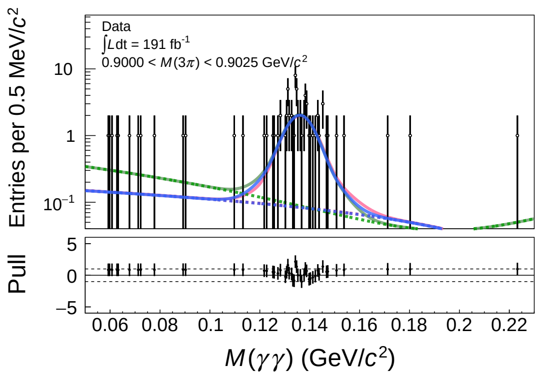

(d) 900 MeV (log-scale)

Figure 4.21: Two-photon invariant mass $M_{\gamma\gamma}$ distribution of the $M_{3\pi}$ mass range (a)(b) 0.7825–0.7850 GeV/c^2 and 0.9000–0.9025 GeV/c^2. The points with error bars represent the data. The solid and dashed curves are the total and background functions of the fit result. The pull is shown in the bottom panel.

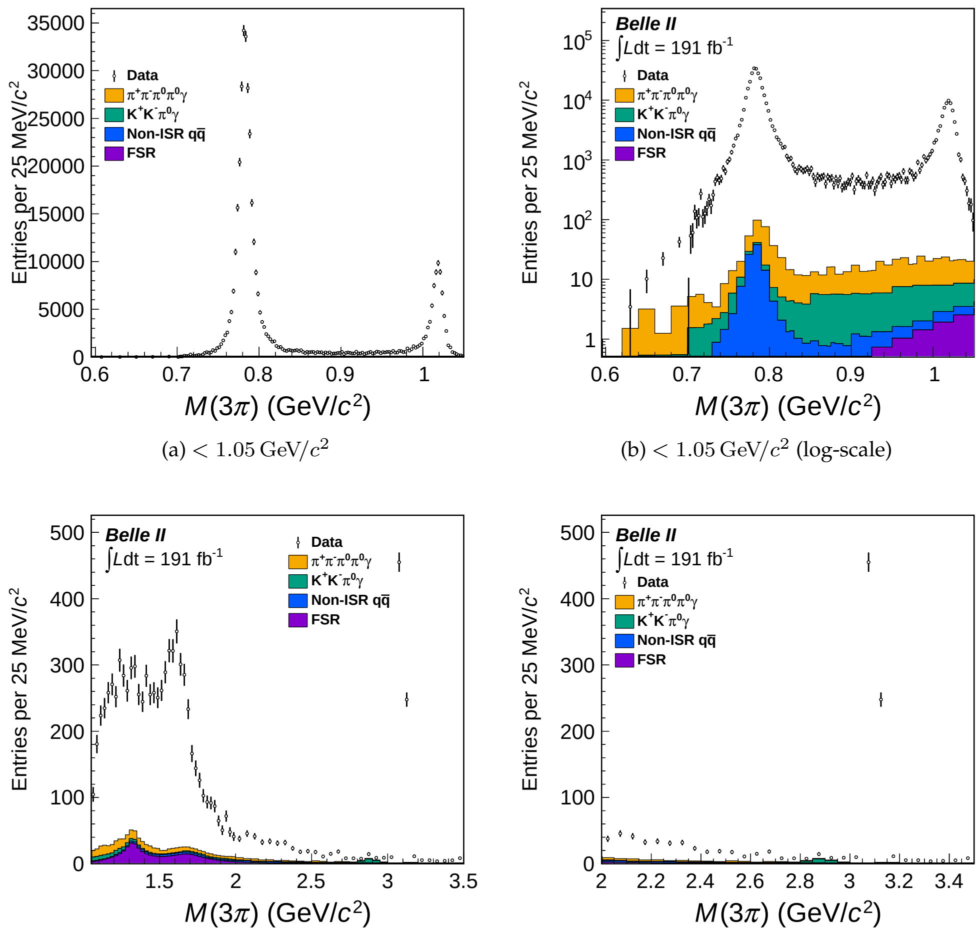

(a) < 1.05 GeV/c^2 (b) < 1.05 GeV/c^2 (log-scale)

(c) 1.1-3.5 GeV/c^2 (d) 2.0-3.5 GeV/c^2

Figure 4.22: $M_{3\pi}$ distribution for data (The closed circles with error bar). The number of signal events is obtained by a fit of $M_{\gamma\gamma}$ in each $M_{3\pi}$ bin and integrated the signal function over the 0.123-0.145 range in $M_{\gamma\gamma}$. The stacked histogram shows the estimated background distribution obtained in the same way as the signal. The number of events in each bin is normalized to the 25 MeV/c^2 bin width.

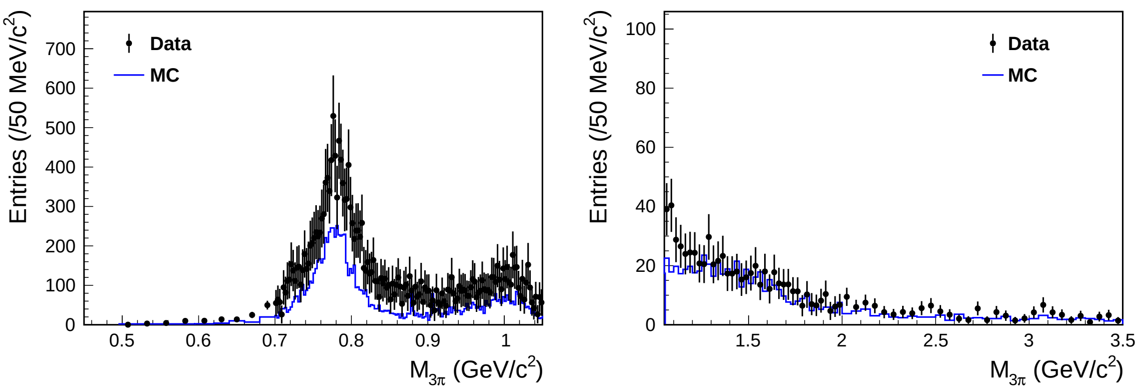

(a) < 1.05 GeV/c^2 (b) > 1.05 GeV/c^2

Figure 4.23: $M_{3\pi}$ distribution for the combinatorial background in each bin, the number of backgrounds is obtained by fitting the $M_{\gamma\gamma}$ distribution with signal and a smooth (uniform) function.

Chapter 5

Background estimation

Major backgrounds that remained after signal selection are the following:

- $e^+e^- \to K^+K^-\pi^0\gamma_{\mathrm{ISR}}$ process
- $e^+e^- \to \pi^+\pi^-\pi^0\pi^0\gamma_{\mathrm{ISR}}$ process
- Non-ISR $q\overline{q}$ background
- Final-state radiation (FSR) background

The distribution of background estimated by the MC program can be seen in Fig. 4.13 (b). FSR background is not plotted in Fig. 4.13. In $M_{3\pi} < 1.05\,\mathrm{GeV}/c^2$, where $\pi^+\pi^-\pi^0\gamma$ signal is characterized by the ω and ϕ resonances having a large cross section, the combinatorial π^0 background is dominated. This background event is attributed to the pairing of π^0 with spurious gamma due to the boosted π^0 becoming a merged ECL cluster. Also, $\pi^+\pi^-\pi^0\pi^0\gamma$ background with intermediate states of $\omega\pi^0$ cannot be ignored. In $M_{3\pi} > 1.05\,\mathrm{GeV}/c^2$, $\pi^+\pi^-\pi^0\pi^0\gamma$ and non-ISR $q\overline{q}$ background is significant. The expected background estimated by the available MC program is 1% to 20%, which differs depending on the $M_{3\pi}$ values as shown in Fig. 5.1.

In this chapter, we discuss how to test this expectation of the background done by MC samples. We prepare several control samples to validate the correctness of the background MC simulation. The selection criteria for each control sample are chosen so that each background is enhanced.A possible difference in data and simulation are corrected by determining the data-MC scale factor for each background component as a function of 3π mass, $N_{CS}^{\mathrm{data}}/N_{CS}^{\mathrm{MC}}$, using the control samples. Multiplying this factor to the background MC events distribution that passes the standard signal selection, the number of the estimated background in the signal sample is obtained as

$$N_{i,\mathrm{SS}} = N_{i,\mathrm{SS}}^{\mathrm{MC}} \cdot \frac{N_{CS}^{\mathrm{data}}}{N_{CS}^{\mathrm{MC}}}, \tag{5.1}$$

where i-th is the index of $M_{3\pi}$ bin, and $N_{i,\mathrm{SS/CS}}^{\mathrm{MC}}$ is the number of simulated events in the signal/control sample. In some places, The signal and control samples are denoted by SS and CS, respectively.

For FSR background, unlike the above, it is tough to verify using control-sample extraction with data because this process has the same final state, three pions and one photon. Estimation is therefore carried out using theoretical prediction and parameters measured in several other experiments.

5.1 $K^+K^-\pi^0\gamma$ background

A data-MC scale factor of $K^+K^-\pi^0\gamma$ background is evaluated using a control sample (Kaon-ID control sample) that enhances the $K^+K^-\pi^0\gamma$ components. The Kaon-ID control sample is selected by modifying the signal selection to require that both tracks are identified as kaons ($\mathcal{P}_{\pi/K} < 0.1$). To reduce contamination from the $\pi^+\pi^-\pi^0$ events by misidentification, the events around the ω and ϕ resonances are not used.

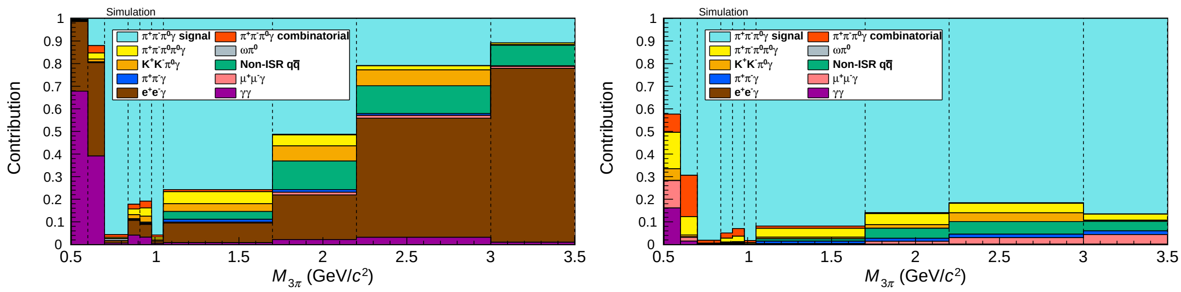

(a) w/ Bkg. suppression cut

(b) w/o Bkg. suppression cut

Figure 5.1: Fraction of background for different $M_{3\pi}$ region (a) before and (b) after applying the background suppression criteria.

The cross section spectrum distribution of $e^+e^- \to K^+K^-\pi^0$ below 3.5 GeV is characterized by resonances around 1.5–1.7 GeV and 2.0–2.5 GeV via $K^\pm K^{*\mp}$ intermediate states and sharp J/psi around 3.09 GeV (Fig. 5.2[104].

Figure 5.3(a) shows the $\pi^+\pi^-\pi^0$ invariant mass distribution of the Kaon-ID control sample. The closed circles with error bars are the data, the pumpkin is the $K^+K^-\pi^0\gamma$ MC simulation, and the blue is the $\pi^+\pi^-\pi^0\gamma$ MC simulation. The latter $\pi^+\pi^-\pi^0\gamma$ events are contaminated in the Kaon-ID control sample by misidentification, estimated by the MC simulation normalized to the luminosity and subtracted from the data. Since the invariant mass of the hadronic system is calculated with four-momentum assuming a charged pion mass, the position of the resonance in the $K^+K^-\pi^0\gamma$ sample, which has kaon tracks, appears lower on the $M_{3\pi}$ than the actual resonance mass. For example, the $J/\psi \to K^+K^-\pi^0$ process, which has a resonance at $M_{K^+K^-\pi^0} = 3.1\,\mathrm{GeV}/c^2$, can be seen to produce a peak at about $M_{3\pi} = 2.8\,\mathrm{GeV}/c^2$ in Fig. 5.3a. The obtained scale factor is shown in the bottom panel of Fig. 5.3 (a). The factor varies from 0.5 to 2.0. The distribution of the signal sample using Eq. (5.1) relation is shown as the closed circle in Fig. 5.3(b). The statistical error of the Kaon-ID control sample determines the error of the scaled background.

To determine the background level in the signal sample, it is necessary to verify the consistency of the kaon identification efficiency between the data and the simulation. This was confirmed using a sample of $D^{*\pm} \to D^0[K^\mp\pi^\pm]\pi^\pm$ processes. Specifically, the performance of kaon identification is found to be degraded for events with a small number of tracks in an event, such as the current signal event, and

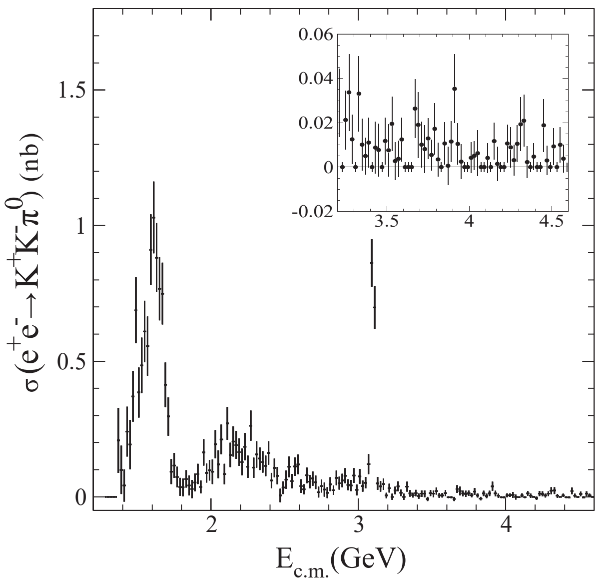

Figure 5.2: The $e^+e^- \to K^+K^-\pi^0$ cross section measured at *BABAR*. Adopted from Ref. [104].

this tendency is confirmed to be reproducible in the simulation. The correction factor for the data-MC differences is obtained by dividing the events into track momentum and pole angle bin.

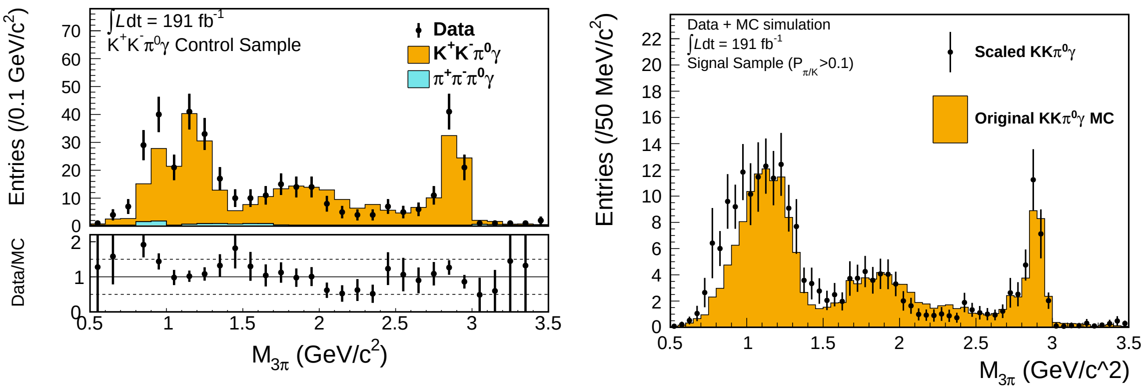

(a) Kaon-ID control sample

(b) Signal sample

Figure 5.3: $M_{3\pi}$ distribution of (a) the Kaon-ID control sample and (b) the signal sample. The stacked histogram is normalized to the integrated luminosity in (a) and is scaled with the data-MC scale factor in (b).

5.2 $4\pi\gamma$ background

We prepare a control sample which enhances the $\pi^+\pi^-\pi^0\pi^0\gamma$ contribution by changing the selection criteria slightly from the signal selection criteria (Table 4.2) to $\chi^2_{4\mathrm{C},2\pi5\gamma} < 30$ and $100 < \chi^2_{4\mathrm{C},2\pi3\gamma} < 1000$, and call it $4\pi\gamma$ control sample. To keep the high efficiency, we select two π^0 s with wider mass region $0.110 < M_{\gamma\gamma} < 0.158\,\mathrm{GeV}/c^2$ without angular cut and make a 4C-KFit assuming $e^+e^- \to \pi^+\pi^-\pi^0\pi^0\gamma$ process. For the $4\pi\gamma$ control sample, the $M_{3\pi}$ distribution is shown in Fig. 5.4 with 100 MeV-bin width, and in Fig. 5.5 (a)-(b) with 5 MeV-bin width by expanding the low $M_{3\pi}$ region. A clear ω peak is due to the $e^+e^- \to \omega\pi^0\gamma \to \pi^+\pi^-\pi^0\pi^0\gamma$ process.

In Fig. 5.4, the closed circles with error bars are the data of $4\pi\gamma$ control sample. The yellow histogram is the contribution from $\pi^+\pi^-\pi^0\pi^0\gamma$. The contamination from other processes, blue ($\pi^+\pi^-\pi^0\gamma$) and grey (others) are negligible and subtracted from the data. The ratio between data and simulation is shown in the bottom panel. In the $M_{3\pi}$ region above 1.1 GeV/c^2, we use this data-MC ratio divided by R_{π^0} for an additional π^0,

$$\frac{N^{\mathrm{data}}_{i,\mathrm{CS}}}{N^{\mathrm{MC}}_{i,\mathrm{CS}} \cdot R_{\pi^0}}, \tag{5.2}$$

for the correction factor of the $\pi^+\pi^-\pi^0\pi^0\gamma$ MC, for the $M_{3\pi}$ region. Where R_{π^0} is the data-MC correction of π^0 efficiency, discussed in section 6.5.

For the $M_{3\pi}$ mass region below 1.1 GeV/c^2, since there is a sharp peak of the ω signal, a detailed study with a lineshape fitting was performed to take into account the mass peak shift of the ω resonance between the signal sample and control samples using the $4\pi\gamma$ control sample. On $M_{3\pi}$ distribution below 1.1 GeV/c^2, we model the $M_{3\pi}$ mass distribution with the ω signal and smooth background,

$$F_{CS}(M_{3\pi}) = f \cdot \mathrm{Voigt}(M_{3\pi}) + \mathrm{Gauss}(M_{3\pi}), \tag{5.3}$$

where f is the fraction of ω resonance relative to non-ω component. The Voigt function is introduced to express the ω resonance shape that is a convolution of the Lorentzian representing the ω resonance shape and the Gaussian for the finite resolution of the detector. We use the second term, a Gaussian form, to parametrize the non-ω components up to 1.1 GeV/c^2.

The fit results on the $M_{3\pi}$ with Eq. (5.3) in the $4\pi\gamma$ control sample for the simulation and data to determine $R_{4\pi\gamma,\omega}$ are shown in Figs. 5.5 (a) and 5.5 (b). The fitting range on $M_{3\pi}$ is 0.6–1.1 GeV/c^2. The fraction of the ω resonance fraction to the non-ω, f, is 0.236 ± 0.007 for the simulation and 0.290 ± 0.021 for the data.

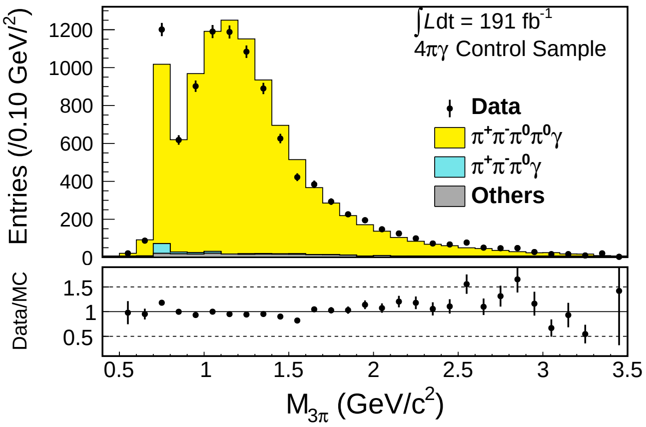

Figure 5.4: $M_{3\pi}$ distribution of the $4\pi\gamma$ control sample. The stacked histogram is normalized to the integrated luminosity. The bottom panel shows the Data-MC scale factor for $4\pi\gamma$ control sample background estimation.

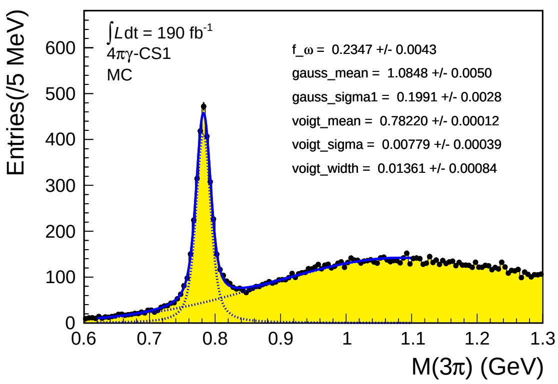

(a) MC

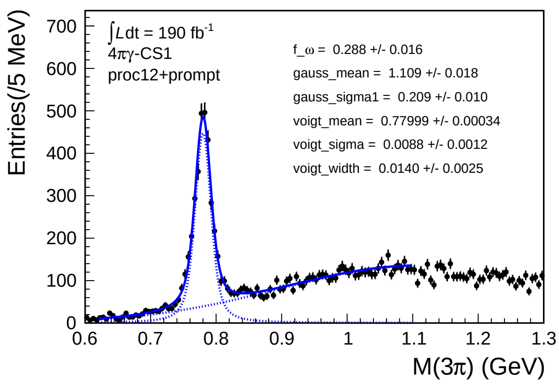

(b) Data

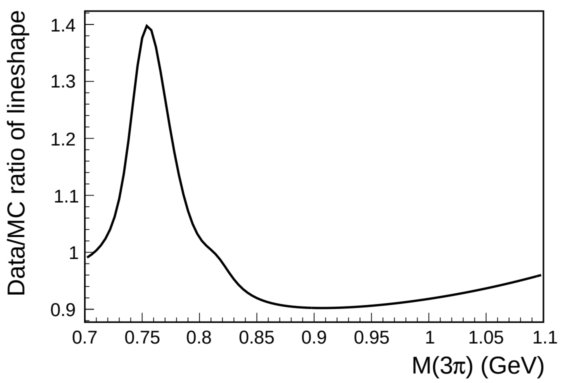

(c) Scale factor

Figure 5.5: Fit to the $M_{3\pi}$ distribution of the $4\pi\gamma$ control sample for (a) MC simulation and (b) data. The solid line is the fit result, and the dashed line is the result multiplied by the scale factor. (c) The obtained scale factor for $\pi^+\pi^-\pi^0\pi^0\gamma$ MC simulation.

The $4\pi\gamma$ data-MC scale factor as a function of 3π mass, $R_{4\pi\gamma,\mathrm{SS}}$, is applied as follows:

$$R_{4\pi\gamma,\mathrm{SS}}(M_{3\pi}) = \frac{1}{R_{\pi^0}} \cdot \frac{F_{CS}^{\mathrm{data}}(M_{3\pi})}{F^{\mathrm{MC}}(M_{3\pi})} \tag{5.4}$$

where, R_{π^0} is a data-MC correction of π^0 efficiency determined in section 6.5. When we adopt the R_{π^0} determined using 10% data, $R_{\pi^0} = 0.97$. We obtain the data-MC scale factor Eq. (5.4) as shown in Fig. 5.5(c).

Figure 5.6 shows the $M_{3\pi}$ distribution of $\pi^+\pi^-\pi^0\pi^0\gamma$ background in the signal sample after applying the data-MC scale factors; Eq. (5.4) is used for $M_{3\pi} < 1.1\ \mathrm{GeV}/c^2$ and Fig. 5.4 (b) is used above $1.1\ \mathrm{GeV}/c^2$.

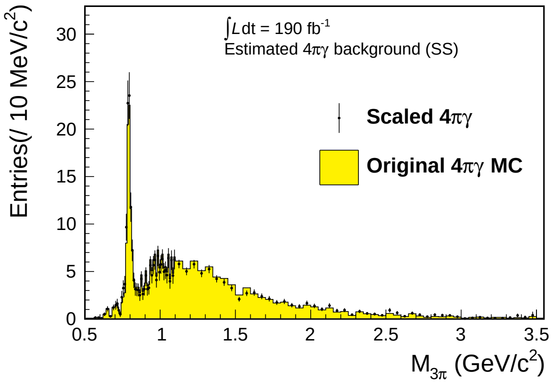

Figure 5.6: Estimated $M_{3\pi}$ distribution of $\pi^+\pi^-\pi^0\pi^0\gamma$ in the signal sample. The yellow is the original $4\pi\gamma$ MC simulation, and the closed circles with error bars are the after scaling.

5.3 Background from non-ISR $e^+e^- \to$ hadrons

Among non-ISR $e^+e^- \to hadrons$, the largest source of the background is from $e^+e^- \to \pi^+\pi^-\pi^0\pi^0$. In this process, a high-momentum π^0 or photon decayed from this π^0 can be misidentified as an ISR photon in the signal. Using the non-ISR $q\bar{q}$ ($q = u, d, s$ and c) MC sample, the event fraction for the total number of signal events after the standard signal selection is estimated to be around 0.3% (0.09%). Although overall background is small, these are the dominant background at high 3π mass region above $M_{3\pi} > 1.1\ \mathrm{GeV}/c^2$ (see Figs. 4.13 (b) and 5.1). To confirm the correctness of these background predictions by $q\bar{q}$ MC samples generated by the KKMC, we prepare two control samples that enhance the $q\bar{q}$ components in data. We call $q\bar{q}$ control sample 1 for events that satisfy $100 < \chi^2_{4C,2\pi3\gamma} < 1000$ and no $M_{\gamma_{\rm ISR}\gamma}$ and cluster second moment of ISR is larger than 1.5. In addition, the $e^+e^- \to \omega\pi^0 \to \pi^+\pi^-\pi^0\pi^0$ process, which is not reproduced in KKMC, is verified using the $q\bar{q}$ control sample 3, the events that satisfy cluster second moment of ISR is more significant than 1.5.

$M_{\gamma_{\rm ISR}\gamma}$: $q\bar{q}$ control sample 1

Figure 5.7(a) shows the data (points) and MC simulation (stacked histogram) distribution of $M_{\gamma_{\rm ISR}\gamma}$ for $q\bar{q}$ control sample 1, integrated over the whole $M_{3\pi}$ region using 191 fb^{-1}. The green (+ grey) histograms are the $q\bar{q}$ contribution, while the yellow histogram is the $\pi^+\pi^-\pi^0\pi^0\gamma$ contamination. There are clean π^0 s from data and relevant MC processes. To estimate small non-π^0 components, we fit the $M_{\gamma_{\rm ISR}\gamma}$ with a Gaussian for π^0 plus a constant for the non-π^0 background. The fit result of the $M_{\gamma_{\rm ISR}\gamma}$ distribution is shown in Fig. 5.7(b). This fit counts the number of π^0, corresponding to the number of $q\bar{q}$ (plus $4\pi\gamma$) yield. Figure 5.7(c) shows the $M_{3\pi}$ distribution of $q\bar{q}$ +$4\pi\gamma$ components, obtained by fitting $M_{\gamma_{\rm ISR}\gamma}$ in each $M_{3\pi}$ bin by a Gaussian, for data and non-ISR $q\bar{q}$ MC and $4\pi\gamma$ ISR MC samples. We subtract the $\pi^+\pi^-\pi^0\pi^0\gamma$ contamination in the $q\bar{q}$ control sample 1, by using the scale-factor of the $\pi^+\pi^-\pi^0\pi^0\gamma$ discussed in section 5.2, and subtracted from the $q\bar{q}$ control sample 1. Figure 5.7(e) is the data-MC correction factor for the $q\bar{q}$-MC sample determined from Fig. 5.7(c). Using this factor for the correction, the expected $M_{3\pi}$ distribution of the $q\bar{q}$ background in the signal sample is given by the closed circles in Fig. 5.7(d). While the blue-shaded histogram in Fig. 5.7(d) is the original expectation by non-ISR $q\bar{q}$ MC sample (KKMC).

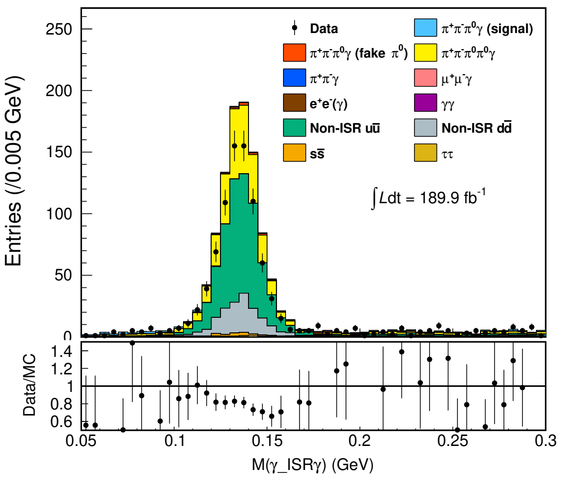

(a) Data-MC comparison

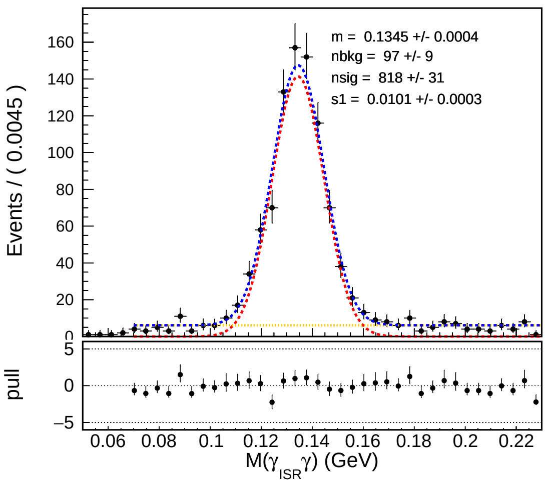

(b) Merged fitting

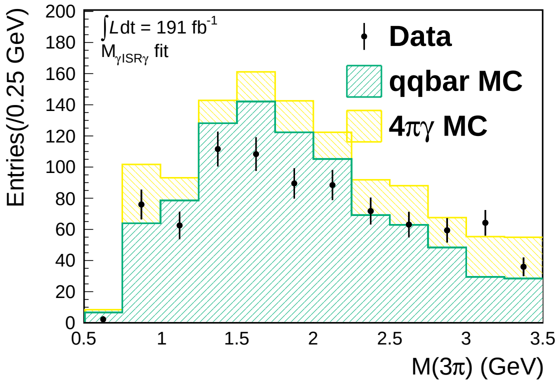

(c) Control sample

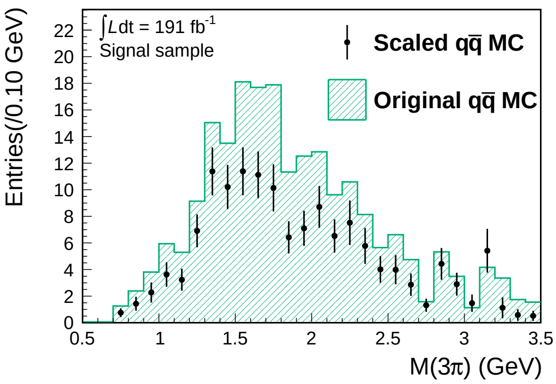

(d) Signal sample

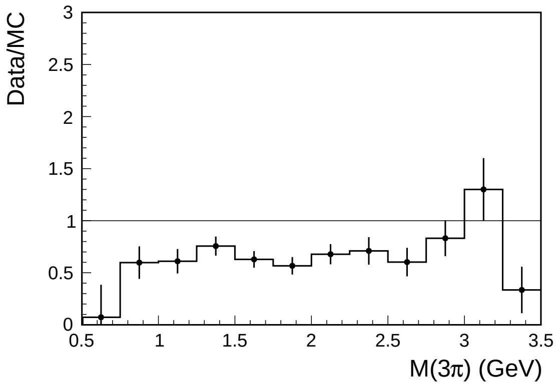

(e) Scale factor

Figure 5.7: Relevant histograms used for the estimation of non-ISR $q\bar{q}$ bacground using the $q\bar{q}$ control sample 1. (a) $M_{\gamma_{\mathrm{ISR}}\gamma}$ distribution in the $q\bar{q}$ control sample 1. (b) A fit result of $M_{\gamma_{\mathrm{ISR}}\gamma}$ distribution without dividing into $M_{3\pi}$ bin. The lines show the fit result, red for signal, yellow for background, blue for the sum. (c) $M_{3\pi}$ distribution obtained by fitting $M_{\gamma_{\mathrm{ISR}}\gamma}$ in each $M_{3\pi}$ bin. The shaded histogram is non-ISR $q\bar{q}$ ($u\bar{u}$, $d\bar{d}$, and $s\bar{s}$) and $\pi^+\pi^-\pi^0\pi^0\gamma$ MC samples normalized to the integrated luminosity. (d) $M_{3\pi}$ distribution of the estimated $q\bar{q}$ background in the signal sample. The points show the estimated background with 191 fb^{-1}, and the solid line is the MC samples scaled with the luminosity. (e) The scale factor of the non-ISR $q\bar{q}$ background.

Second moment of the ISR cluster : $q\bar{q}$ control sample 2

This sample, $q\bar{q}$ control sample 2, is independent of the $q\bar{q}$ control sample 1. Figure 5.8 shows the cluster second moment distribution of ISR in the $q\bar{q}$ control sample 2 before applying the cluster second moment selection.

The $M_{3\pi}$ distribution for the $q\bar{q}$ control sample 2 is compared between data and simulation in Fig. 5.9(a). The $q\bar{q}$ background dominates the control sample, but there is 10-20% contamination from $3\pi\gamma$. We subtract the contamination of $3\pi\gamma$ and $4\pi\gamma$, in $q\bar{q}$ control sample 2, shown in the shaded black histogram in Fig. 5.9(a) with the luminosity scale. After subtracting $3\pi\gamma$ and $4\pi\gamma$ contributions, we determine the data-MC correction factors as a function of 3π mass. The results are shown in Fig. 5.9(c). The closed circles in Fig. 5.9(b) show the estimated $q\bar{q}$ background for the signal sample obtained by applying the data-MC correction shown in Fig. 5.9(c) to the original $q\bar{q}$ MC (Kkmc) prediction shown by the histogram.

To test the dependence on the criterion of the cluster second moment, the threshold of cluster second moment is changed from 1.3 to 2.1 to check the data-MC difference of cluster second moment distribution (Fig. 5.9 (d)). The distribution difference of estimated $q\bar{q}$ background is consistent with statistical uncertainty.

The resultant scaled $q\bar{q}$ background distributions obtained from $q\bar{q}$ control sample 1 and $q\bar{q}$ control sample 2 control samples are compared in Fig. 5.10. Both scale factors obtained from the different methods show a good agreement. These distributions agree well with each other within statistical error.

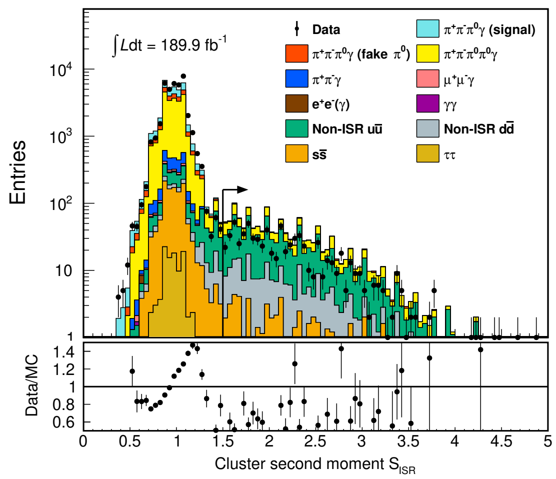

Figure 5.8: Distribution of cluster second moment of ISR $S_{\rm ISR}$ in $q\bar{q}$ control sample 2 before applying the cluster second moment selection. The points with error bars are the data, and stacked histograms are the simulation.

5.3.1 Background from the $e^+e^- \to \omega\pi^0 \to \pi^+\pi^-\pi^0\pi^0$: $q\bar{q}$ control sample 3 process

The process $e^+e^- \to \omega\pi^0 \to \pi^+\pi^-\pi^0\pi^0$ is categorized in non-ISR $q\bar{q}$. Still, it is not adequately modeled in Kkmc MC simulation, so this process needs to be estimated independently. Figure. 5.11 shows the generator-level $M_{3\pi}$ distribution of $e^+e^- \to \pi^+\pi^-\pi^0\pi^0$ process in Kkmc $u\bar{u}$ MC simulation. The ω peak does not appear, and it is doubtful that the $e^+e^- \to \pi^+\pi^-\pi^0\pi^0$ process via a $\omega\pi^0$ intermediate state is implemented on Kkmc. We estimate the cross section in the following data-driven ways. The cross section of $\pi^+\pi^-\pi^0\pi^0$ channel around $\sqrt{s} = 10.58\,\mathrm{GeV}$ is $\sigma(10.58\,\mathrm{GeV}) = (6.01^{+1.29}_{-1.97} \pm 0.50)$ fb [105].

To check this process, an MC sample with $\Upsilon(4S) \to \omega[\to \pi^+\pi^-\pi^0[\to \gamma\gamma]]\pi^0[\to \gamma\gamma]$ decay is prepared using a simple generator EvtGen, and is passed the detector simulation program. In this process, the π^0 that does not originate from ω usually has a high momentum since the π^0 and ω are produced back-to-back in the e^+e^- c.m. system, as shown in Fig 5.12. These events certainly show a ω resonance peak in $M_{3\pi}$ as shown in Fig 5.13 (a). For this MC sample, we require the same condition of the signal selection, i.e., $\chi^2_{4C,2\pi3\gamma} < 50$ and ($M_{\gamma_{\rm ISR}\gamma} < 0.10\,\mathrm{GeV}/c^2$ or $M_{\gamma_{\rm ISR}\gamma} > 0.17\,\mathrm{GeV}/c^2$). The second moment of the ISR cluster, it shown in Fig. 5.13 (b), has relatively higher values than the expected distribution created by a

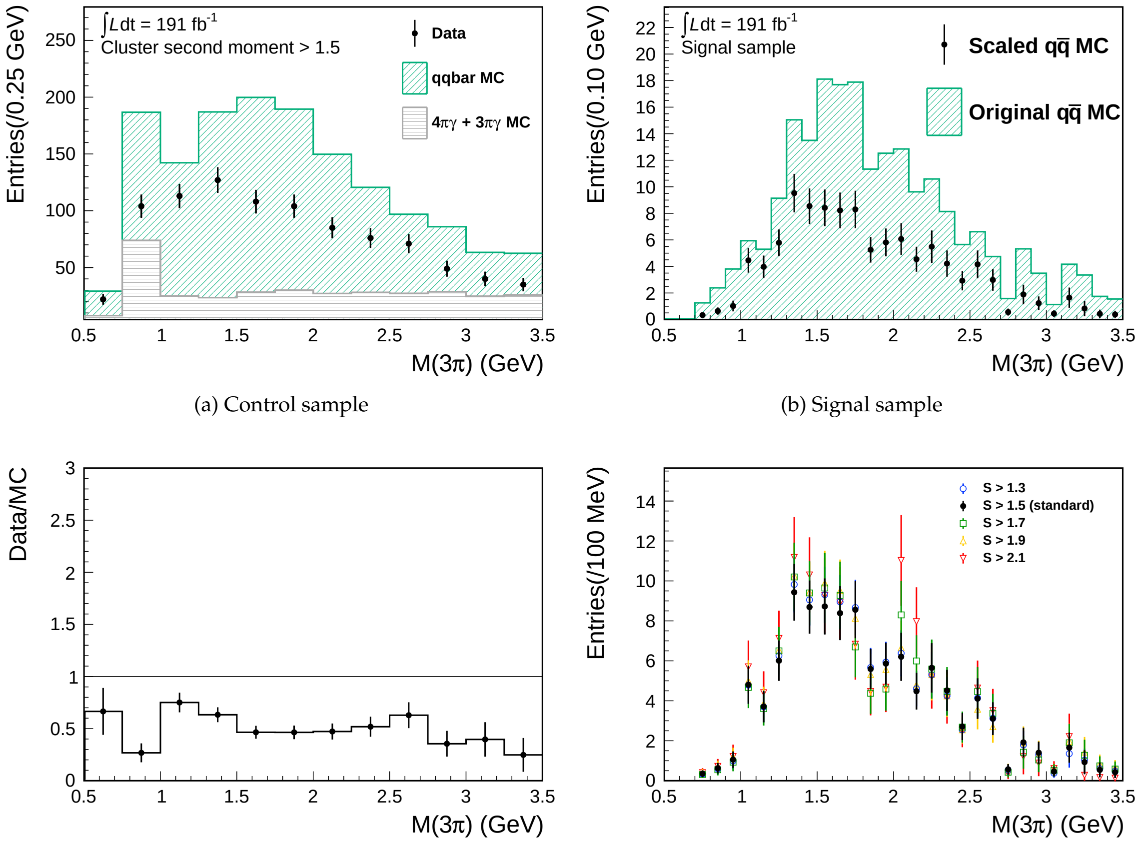

(a) Control sample

(b) Signal sample

(c) scale factor

(d) Threshold scan

Figure 5.9: (a) $M_{3\pi}$ distribution in $q\overline{q}$ control sample 2. The $q\overline{q}$ MC sample is the sum of $u\overline{u}$, $d\overline{d}$, $s\overline{s}$ and $c\overline{c}$. The MC sample is normalized to the data luminosity. (b) $M_{3\pi}$ distribution of the $q\overline{q}$ background in the signal sample. The histogram is the original MC expectation, and the closed circle is the scaled one. (c) Data-MC scale factor for $q\overline{q}$ background determined using the control sample, $q\overline{q}$ control sample 2. (d) $M_{3\pi}$ distribution in $q\overline{q}$ control sample 2 scanning the thresholds of cluster seconds moment of ISR The points show different thresholds for the cluster second moment of ISR.

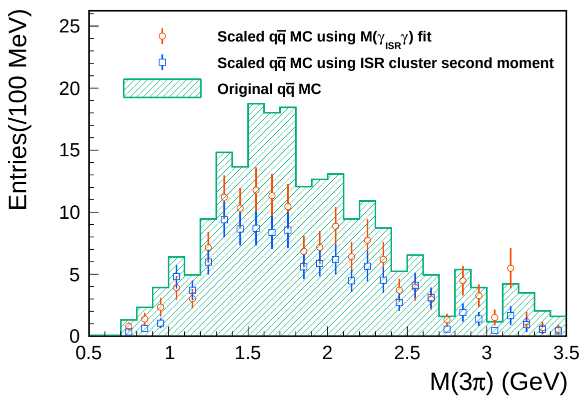

Figure 5.10: Estimated $M_{3\pi}$ distribution of $q\overline{q}$ background in the signal sample using $q\overline{q}$ control sample 2. The circles show the result by using $q\overline{q}$ control sample 1 (Fig. 5.7 (d)). The rectangles show the result by using $q\overline{q}$ control sample 2 (Fig. 5.9 (b)). The filled histogram shows the distribution of the original $u\overline{u}$, $d\overline{d}$ and $s\overline{s}$ MC (KKMC).

single photon (see Fig. 4.10 (b)). To enhance the $e^+e^- \to \omega\pi^0$ background, we require that the second moment of the ISR cluster is more significant than 1.5. The $M_{3\pi}$ distribution for this $q\bar{q}$ control sample 3 is shown in Fig. 5.14 for the data.

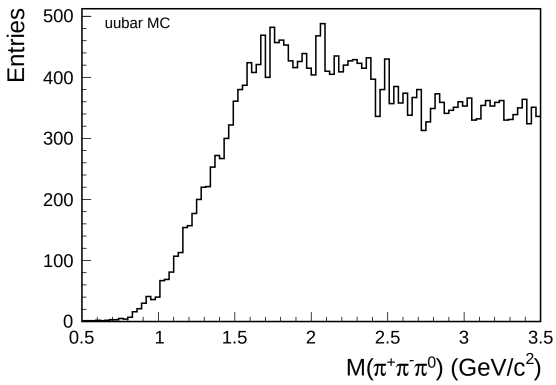

Figure 5.11: Generator level $M_{3\pi}$ distribution of $\pi^+\pi^-\pi^0\pi^0$ process in $u\bar{u}$ MC.

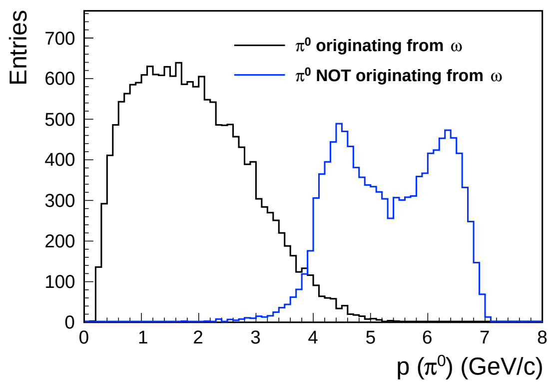

Figure 5.12: Momentum of π^0 in $\omega\pi^0$ MC, where π^0 is reconstructed from two-photon combination. The black histogram shows the π^0 originating from ω, and the blue histogram shows the π^0 not originating from ω. The statistics are arbitrary.

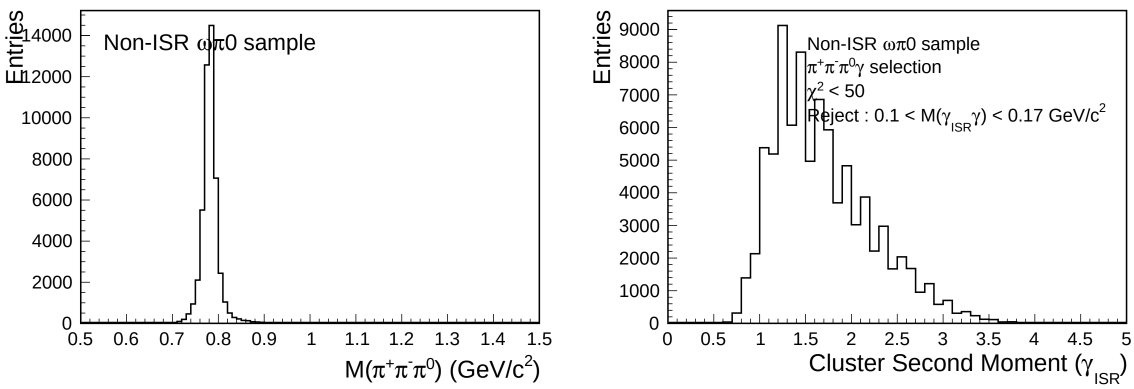

(a) $M(\pi^+\pi^-\pi^0)$

(b) Cluster second moment

Figure 5.13: (a) $M_{3\pi}$ distribution of $\omega\pi^0$ MC in the signal sample. (b) Cluster second moment S_{ISR} of $\omega\pi^0$ MC in the signal sample (signal sample requires $S_{\mathrm{ISR}} < 1.3$). The statistics are arbitrary.

By fitting the $M_{3\pi}$ distribution in Fig. 5.14 by an omega-signal-shape function (Breit-Wigner), we obtain 97.0 ± 9.9 events for the data. The solid histogram represents the $3\pi\gamma$, $4\pi\gamma$, and $q\bar{q}$ MC samples with a luminosity scale, and the number of events is 18.5 ± 1.3 events; the number of $\omega\pi^0$ process in the control sample $N^{\mathrm{data}}_{\omega\pi^0, S_{\mathrm{ISR}}>1.5}$ is 94.5 ± 10.0. On the other hand, using the $\omega\pi^0$ MC, the ratio of the number of events for $S_{\mathrm{ISR}} < 1.3$ (i.e., the signal sample) and $S_{\mathrm{ISR}} > 1.5$ is obtained to be $N^{\mathrm{MC}}_{S_{\mathrm{ISR}}<1.3}/N^{\mathrm{MC}}_{S_{\mathrm{ISR}}>1.5} = (0.497 \pm 0.004)$. Thus, we obtain the expected $\omega\pi^0$ background in the signal sample as

$$N^{\mathrm{data}}_{\omega\pi^0,SS} = \frac{N^{\mathrm{MC}}_{S_{\mathrm{ISR}}<1.3}}{N^{\mathrm{MC}}_{S_{\mathrm{ISR}}>1.5}} \cdot N^{\mathrm{MC}}_{\omega\pi^0,S_{\mathrm{ISR}}>1.5} = 39.1 \pm 5.0_{\mathrm{stat.}}. \tag{5.5}$$

The distribution of $e^+e^- \to \omega\pi^0$ in the signal sample is obtained by normalising the $M_{3\pi}$ shape of $\omega\pi^0$ MC so that the number of events is 39.1 events, and is shown in Fig. 5.15. The results estimated by the same method when the threshold for the cluster second moment of the control sample is varied from 1.4

to 2.5 are shown in Fig 5.16. The most significant difference, ± 8.5 events, 22%, is taken as the systematic error for the distribution.

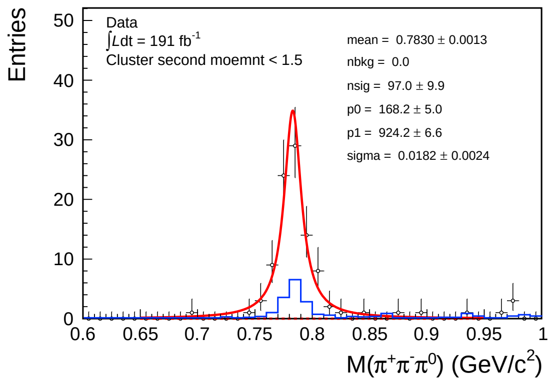

Figure 5.14: $M_{3\pi}$ distribution in the control sample with cluster second moment of ISR more than 1.5. The points show data, solid (blue) histogram shows $3\pi\gamma$ and $4\pi\gamma$ MC, and the line is fitting with the Breit-Wigner function.

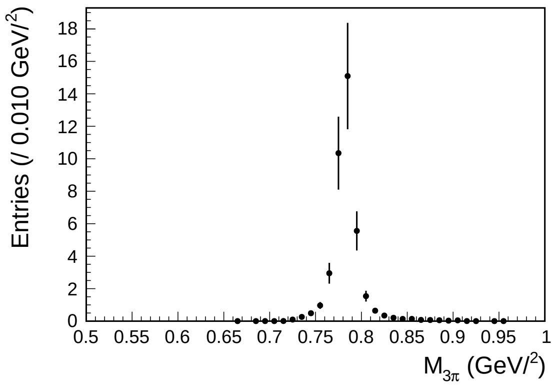

Figure 5.15: The estimated number of events of $e^+e^- \to \omega\pi^0$ process in the signal sample.

Here, the cross section of $e^+e^- \to \omega\pi^0$ at $\sqrt{s} = 10.58\,\text{GeV}$ can be measured from the number of events $N^{\text{data}}_{\omega\pi^0, S_{\text{ISR}}>1.5}$ and the efficiency in the control sample. According to the $\omega\pi^0$ MC, the efficiency is $(4.38 + / - 0.03)\%$ including the trigger efficiency, where the error is the statistical error. The cross section in the $191\,\text{fb}^{-1}$ data is therefore $\sigma(10.58\,\text{GeV}) = (6.60 \pm 0.70_{\text{stat.}})$ fb, which is consistent to the measurement at the Belle $\sigma(10.58\,\text{GeV}, \text{Belle}) = (6.01^{+1.29}_{-1.97} \pm 0.50)$ fb [105].

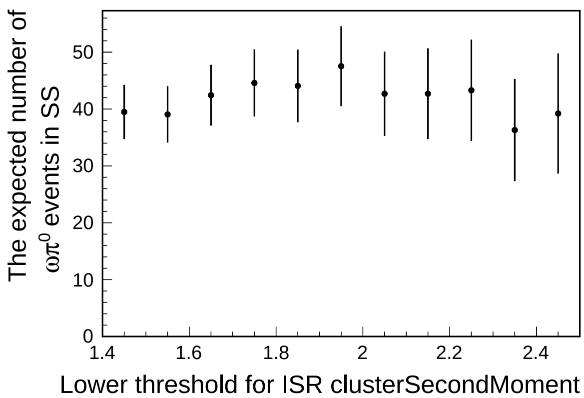

Figure 5.16: The estimated number of events of $e^+e^- \to \omega\pi^0$ process in the signal sample as a function of the threshold of cluster second moment of the control sample. The error bars show the statistical uncertainties.

5.4 Background with a final-state radiation photon

The effect of the photon from the final-state-radiation (FSR) needs to be considered, but it is less known compared to the ISR and non-ISR processes. This FSR background in $\pi^+\pi^-\pi^0$ cross section measurement at the B-factory is discussed in Sec. V of Ref [60]. The leading order final state radiation (LO FSR) process can be categorized into two groups: emission from final-state charged pions depicted in the Feynman diagrams of Figs. 5.17 (a) and (b), and emission from quarks that then hadronize into $\pi^+\pi^-\pi^0$ as shown in Fig. 5.17 (c). These processes are essentially a cross section of the process at $\sqrt{s'} = 10.58\,\text{GeV}$ and are outside the energy range of this measurement, so these are treated as background events.

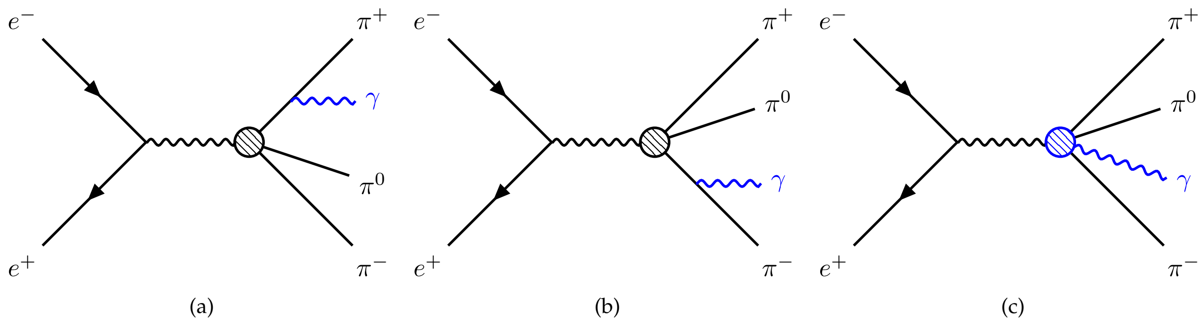

Figure 5.17: Feynman diagrams of $e^+e^- \to \pi^+\pi^-\pi^0$ process with LO FSR photon emission. (a) and (b) represent the photon emission from positive and negative pion, respectively. (C) represents the photon emission from the quarks.

FSR emission from final-state pions

Regarding the emission from final-state pions, firstly, we consider the non-radiative process $e^+e^- \to \pi^+\pi^-\pi^0$ around $\sqrt{s} = 10.58\,\text{GeV}$. Since measurement of the process at the energy does not exist, the measured cross section at $\sqrt{s} = 3.67\,\text{GeV}$ is extrapolated using perturbative QCD calculation. The cross section for $e^+e^- \to VP$ process, where V is a vector meson and P is a pseudo-scalar meson, is expected to follow a scaling rule of $1/s^n$, with $n = 4$ being favored in the perturbative QCD prediction. To check the scaling rule, fit based on cross sections measured at both $\sqrt{s} = 3.67\,\text{GeV}$ and $10.58\,\text{GeV}$ results in $n = 3.83$ for the $e^+e^- \to K^{*\pm}(782)K^{\mp}$ and $n = 3.75$ for the $e^+e^- \to \omega\pi^0$, which is in good agreement with this prediction [106]. Assuming $1/s^{3.75}$ scaling rule, the cross section of $e^+e^- \to \pi^+\pi^-\pi^0$ at $\sqrt{s} = 10.58\,\text{GeV}$ is expected to be 4.7 fb as the cross section measured at $\sqrt{s} = 3.67\,\text{GeV}$ is $(13.1^{+1.9}_{-1.7} \pm 2.1)$ fb [107].

Next, we consider the probability of FSR emission from a charged pion. The FSR photon should have $E^{\text{c.m.}}$ greater than 4.7 GeV so that the $M_{3\pi}$ is less than 3.5 GeV in leading-order FSR process (Figs. 5.17 (a) and (b)). The FSR probability is calculated based on the $e^+e^- \to \pi^+\pi^-\gamma$ cross section of the FSR process. The probability of FSR emission with an energy above 4.7 GeV in this analysis condition is approximately $0.23\alpha/\pi$ for the non-radiative 3π process [108]. In the process $e^+e^- \to \pi^+\pi^-\pi^0$, with a $\rho\pi$ intermediate state assumed to be dominant, the most energetic pion is limited to one of three pions. Therefore, divided by a factor of three, the cross section of $e^+e^- \to \pi^+\pi^-\pi^0\gamma_{\text{FSR}}$ is expected to the 0.001 fb level. According to the 191 fb^{-1} data, the observed signal would be less than 0.02 events, indicating a sufficiently negligible process.

FSR emission from quarks

For the FSR emission from the quarks, following the *BABAR* paper, we consider the following processes: $e^+e^- \to \eta\gamma, a_1(1260)\gamma, a_2(1320)\gamma, \pi(1300)\gamma, a_1(1640)\gamma, a_2(1700)\gamma$. In the $\eta\gamma$ final state, the mass of the η meson is well below the $M_{3\pi}$ mass, around $0.55\,\text{GeV}/c^2$. The number of events in the full data is negligible (around 16 events). For this estimation, we use the measured cross section of 4.5 fb [109], the detection efficiency of 25% determined by simulation and the integrated luminosity of 191 fb^{-1}.

For the processes $e^+e^- \to \gamma^*(q) \to M\gamma_{\text{FSR}}$, where M is a pseudo-scaler or axial-vector meson, the cross section and the photon-angular distribution can be given, at large CM energy, via the perturbative-QCD as

$$\frac{d\sigma(e^+e^- \to M\gamma)}{d\cos\theta_\gamma} = \frac{\pi^2\alpha^3}{4}|F_{M\gamma\gamma}|^2(1+\cos^2\theta_\gamma), \quad (5.6)$$ [1]

where θ_γ is the polar angle of the photon, $F_{M\gamma\gamma}$ is a meson-photon transition form factor for the helicity-zero state, which dominates at large momentum transfer (q),

$$q|F_{M\gamma\gamma}| = \frac{1}{3}\frac{|f_M|}{\sqrt{2}}I_M. \quad (5.7)$$

[1]According to Ref. [60], a primary source of this equation is private communication to V. L. Chemyak.

and where I_M is an integral depending on the shape of the meson distribution amplitude, f_M is the meson decay constant. The cross section as a function of 3π mass is given, in the case of the incoherent sum of the Breit-Wigner, by,

$$\sigma(\sqrt{s'}) = \sum_M |\mathrm{BW}_M(\sqrt{s'})|^2, \tag{5.8}$$

where

$$\mathrm{BW}_M(\sqrt{s'}) = \frac{\sqrt{C_M \mathcal{B}(M \to \pi^+\pi^-\pi^0)}}{m_M^2 - s' - i m_M \Gamma_M} \cdot \frac{\sqrt{W_{\rho\pi}(s')}}{\sqrt{W_{\rho\pi}(m_M^2)}}, \tag{5.9}$$

$\sqrt{s'}$ is energy of hadronic system, M is mesons, $a_1(1260)$, $a_1(1640)$, $a_2(1320)$, and $a_2(1700)$, C_M is normalization factor, $\mathcal{B}(M \to \pi^+\pi^-\pi^0)$ is a branching ratio of $M \to \pi^+\pi^-\pi^0$ process, m_M is the mass, Γ_M is the total width, $W_{\rho\pi}(s)$ is the 3π phase space factor assuming 3π decay via a $\rho\pi$ intermediate state. The normalization factor C_M is normalized to the total cross section calculated by Eq. (5.6). The detection efficiency for the signal selection is calculated using the MC simulation of $e^+e^- \to a_2(1320)\gamma \to \pi^+\pi^-\pi^0\gamma$ process, which is 25%. The values of parameters used in this simulation are summarized in Table. 5.1. The estimated $M(3\pi)$ distribution of $a_1(1260)\gamma$, $a_2(1320)\gamma$, $a_1(1640)\gamma$, and $a_2(1700)\gamma$ backgrounds in full data is shown in Fig 5.18 by the solid histogram. Interference between amplitudes of resonances may affect this spectrum. In that case, we obtain the cross section by a formula

$$\sigma(\sqrt{s'}) = |\mathrm{BW}_{a_1(1260)} + \mathrm{BW}_{a_1(1640)} \cdot e^{i\phi_{a_1(1640)}}|^2 + |\mathrm{BW}_{a_2(1320)} + \mathrm{BW}_{a_2(1700)} \cdot e^{i\phi_{a_2(1700)}}|^2, \tag{5.10}$$

where ϕ_M is the relative phase of the two resonances with the same quantum number. The interference between a_1 and a_2 is not taken into account. The spectrum with the relative phases of 0° (180°) is shown as the dashed (dotted) spectrum in Fig. 5.18. The difference from the incoherent spectrum is assigned as a systematic uncertainty.

Table 5.1: Summary of parameters used for FSR background estimation. An integral depending on the shape of the meson distribution amplitude I_M, the meson decay constants f_M, the total cross section σ_M, the mass M_M, the total width Γ_M and the branching ration $\mathcal{B}(e^+e^- \to \pi^+\pi^-\pi^0)$ are summarized.

Process $e^+e^- \to M\gamma$	I_M	f_M (MeV)	σ_M (fb)	M_M (GeV/c^2)	Γ_M (GeV/c^2)	$\mathcal{B}(M \to \pi^+\pi^-\pi^0)$
$a_1(1260)\gamma$	6	200 [110]	6.4 [60]	1.230 [111]	0.420 [112]	0.86 [113, 114]
$a_2(1320)\gamma$	10	110 [115]	5.4 [60]	1.655 [111]	0.254 [111]	0.70 [111]
$a_1(1640)\gamma$	6	180 [60]	5.1 [60]	1.318 [111]	0.107 [111]	0.30 [116]
$a_2(1700)\gamma$	10	130 [60]	7.2 [60]	1.698 [111]	0.265 [111]	0.50
$a_1(1930)\gamma$	6	160 [60]	6.0 [60]	1.930 [111]	0.155 [111]	0.30
$a_2(2030)\gamma$	10	90 [60]	5.1 [60]	2.030 [111]	0.205 [111]	0.30

For $a_1(1930)$ and $a_2(2030)$, the expected number of events is 45 and 37 events in total, assuming that the branching ratios are 30% and the detection efficiency is 25%. Figure 5.19 shows the expected distribution. These contributions is translated into a systematic uncertainty, which corresponds around 10% of the total systematic uncertainty on the 3π cross section.

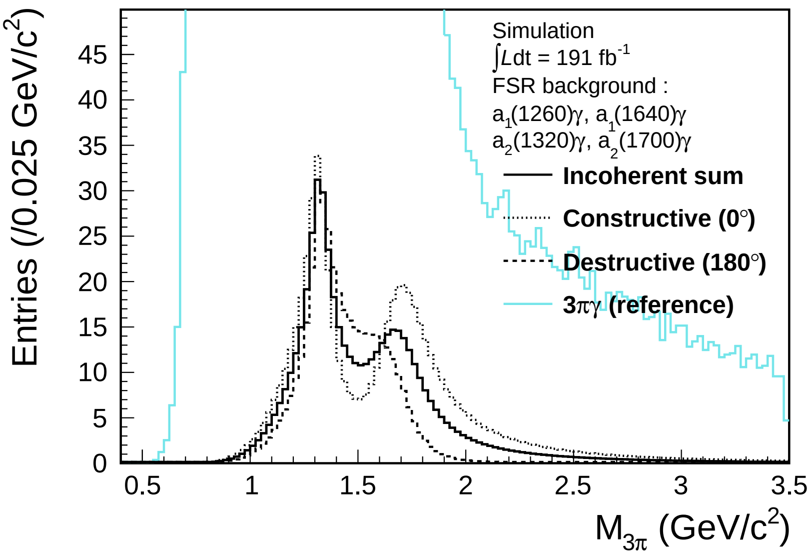

Figure 5.18: $M_{3\pi}$ spectrum expected from the FSR processes $e^+e^- \to M\gamma \to \pi^+\pi^-\pi^0$, where $M = a_1(1260), a_2(1320), a_1(1640), a_2(1700)$. The solid histogram represents the incoherent sum of the processes. The dashed (dotted) histogram demonstrates the constructive (destructive) interference effect between the $a_1(1260)$ and $a_1(1640)$ amplitudes and the $a_2(1320)$ and $a_2(1700)$ amplitudes. The light blue histogram is $\pi^+\pi^-\pi^0\gamma$ signal events as a reference.

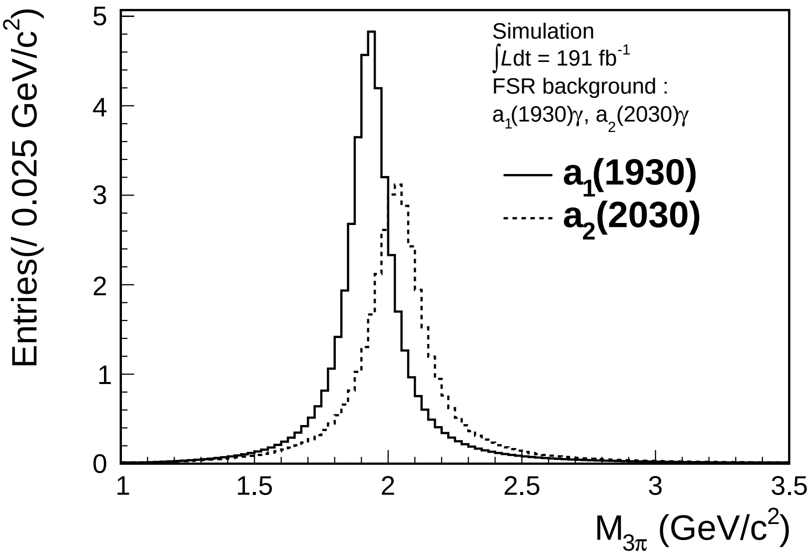

Figure 5.19: $M_{3\pi}$ spectrum expected from the FSR processes $e^+e^- \to M\gamma \to \pi^+\pi^-\pi^0$, where the solid histogram is $M = a_1(1930)$, while dotted is $a_2(2030)$

Chapter 6

Signal efficiency

Signal efficiency is the ratio of observed signal events to generated events as a function of the 3π invariant mass. The signal efficiency includes detector acceptance, trigger efficiency, particle detection efficiency, and selection efficiency. For the sake of calculation, generated events are preliminarily restricted by this condition that an ISR photon is emitted in $20^\circ < \theta^{\mathrm{c.m.}} < 160^\circ$ and the invariant mass of hadron and an ISR photon system is greater than $8\,\mathrm{GeV}/c^2$ to eliminate the majority of events where an ISR emitted along with small polar angle and is not detected.

In the first-order approximation, the signal efficiency is estimated from MC simulations using the Belle II detector simulation program. However, the simulation is not perfect; we check the correctness of the simulations by using several kinds of data samples and preparing data-MC corrections from these studies. The uncertainties in the corrections are also estimated. This chapter discusses the efficiency and its corrections via various checks performed using the data.

The correction factor (η_i) of the efficiency for i-th item is defined as

$$\eta_i = \frac{\varepsilon_{\mathrm{data},i}}{\varepsilon_{\mathrm{MC},i}} - 1 = R_i - 1,$$

where $\varepsilon_{\mathrm{data},i}$ is the i-th efficiency determined by the data, and $\varepsilon_{\mathrm{MC},i}$ is the one determined using the simulation, The data-MC ratio of the efficiency is $R_i \equiv \varepsilon_{\mathrm{data},i}/\varepsilon_{\mathrm{MC},i}$. Thus, corrected signal efficiency is expressed as

$$\varepsilon = \varepsilon_{\mathrm{MC}} \cdot \prod_i (1+\eta_i) \tag{6.1}$$

$$\approx \varepsilon_{\mathrm{MC}} \cdot \left(1 + \sum_i \eta_i\right), \tag{6.2}$$

where $\varepsilon_{\mathrm{MC}}$ is the total simulated efficiency discussed in section 6.1. The items i considered in this analysis are categorized into:

- Trigger efficiency (section 6.2)
- ISR photon efficiency (section 6.4)
- Tracking efficiency (section 6.3)
- π^0 detection efficiency (section 6.5)
- Efficiency of the 4C-KFit χ^2_{4C} selection (section 6.6)
- Background suppression efficiency (section 6.7)

Before discussing the evaluation details, we provide the summary of correction in Table 6.1. In conclusion, the data-simulation difference is about at most 2% for each item and 4.6% in total, and no strong $M_{3\pi}$ dependence in the correction factors is found, which confirms that the simulations reproduce the data well and shows the validity of this correction method.

Table 6.1: The summary of efficiency correction factors (η_i) and uncertainties ($\delta\eta_i\%$)

Source	**Correction factor** $< 1.05\,\mathrm{GeV}/c^2$	1.05–$2.00\,\mathrm{GeV}/c^2$	2.0–$3.5\,\mathrm{GeV}/c^2$	**Comments**
Trigger	-0.09 ± 0.08	-0.08 ± 0.08	-0.06 ± 0.10	Section 6.2
ISR photon detection	0.15 ± 0.67	0.15 ± 0.67	0.15 ± 0.67	Section 6.4
Tracking	-1.35 ± 0.80	-1.71 ± 0.83	-1.71 ± 0.83	Section 6.3
π^0	-1.43 ± 1.02	-1.43 ± 1.02	-1.43 ± 1.02	Section 6.5
χ^2	0.00 ± 0.60	0.30 ± 0.30	0.30 ± 0.30	Section 6.6
Selection	-1.90 ± 0.20	-1.78 ± 1.85	-1.78 ± 1.85	Section 6.7
Total correction	-4.61 ± 1.59	-4.55 ± 2.38	-4.53 ± 2.38	

6.1 Simulated efficiency

The signal efficiency depending on the 3π mass, $\varepsilon_{\mathrm{MC}}$ in Eq. (6.1), is defined as the ratio of the number of reconstructed events, after signal selection, to the number of generated events.

The generated event, the denominator, is required to be consistent with the condition used for the cross-section calculation; i.e., the polar angle of ISR photon is within $20^\circ < \theta < 160^\circ$, and the invariant mass of $\pi^+\pi^-\pi^0\gamma$ is more than $8\,\mathrm{GeV}/c^2$.

The numerator is the number of the reconstructed $\pi^+\pi^-\pi^0\gamma$ signal events pass the all event selection. The generator-level 3π invariant mass in a range of 0.5–4.0 GeV/c^2 is divided into 48 bins depending on the events statistics, where the bin width is $50\,\mathrm{MeV}/c^2$ in $0.7 < M_{3\pi} < 2.0\,\mathrm{MeV}/c^2$, and $100\,\mathrm{MeV}/c^2$ in the other region. Fits to the $M_{\gamma\gamma}$ distribution are performed to the sample in each $M_{3\pi}$ bin, and the component of the π^0 mass peak region (0.123–0.147 GeV/c^2) is counted as the numerator value. The fit parameters and configurations comply with the lineshape study (see section 4.5.1). Figure 6.1 shows the simulated efficiency using the $\pi^+\pi^-\pi^0\gamma$ MC sample of $2000\,\mathrm{fb}^{-1}$, a ten times larger sample than the data. In this simulation, we use the scale value 0.7641 for the effective value of trigger efficiency, assuming 100% efficiency for experiments 7–17 (corresponds to 53% of datasets), and 50% scaled down coefficient assuming 100% efficiency for experiment 18 (corresponds to 47% datasets). The solid line in Fig 6.1 is a fit with 3rd order polynomial function. We use this curve for the signal efficiency of the experimental data, $\varepsilon_{\mathrm{MC}}$. The typical effective signal efficiency is $(8.775 \pm 0.014)\%$ at the ω resonance, $(8.326 \pm 0.025)\%$ at the ϕ resonance, $(8.31 \pm 0.16)\%$ at 1.8 GeV/c^2 and $(6.63 \pm 0.23)\%$ at 3.1 GeV/c^2. The uncertainties are calculated from the covariance matrix of the fit function and derived from the MC statistics.

When broken down into the individual components, the event loss due to a change in acceptance by narrowing the ISR polar angle from 20°–160° in the e^+e^- c.m. system to the barrel region is significant: the efficiency of the ISR photon is about 40%. The subsequent largest loss, π^0 efficiency, is approximately 50%. The trigger efficiency is 77%, as mentioned above. The other efficiency levels are roughly 70% for two tracks satisfying the conditions, 80% for selection for $\chi^2_{4\mathrm{C},2\pi3\gamma} < 50$, and 90% for background reduction selection.

A slight deviation from the fitted curve around 2 GeV/c^2 is a statistical fluctuation. We have checked this with an additional MC sample.

6.2 Trigger efficiency

The level-1 trigger used in this analysis is summarized in Table 4.1. Two trigger conditions are used: *hie* for experiments 7–17 and *lml1* for experiment 18. The trigger simulation indicates that the efficiency of the signal is 100%, essentially. For experiment 18, since the ECL-based veto for QED processes is introduced for the *hie* trigger, we use the *lml1* trigger. The efficiency of *lml1* is 100% by the simulation, but this trigger line is scaled down by a factor of two in the data taking.

To check the correctness of the trigger simulation by data, we use the $e^+e^- \to \mu^+\mu^-\gamma_{\mathrm{ISR}}$ control sample, denoted by $\mu^+\mu^-\gamma$ control sample; in other words, we collect events triggered by tracker trigger lines with the muon-pair and evaluate the efficiency of ECL trigger lines using the ISR photon. The $e^+e^- \to \mu^+\mu^-\gamma_{\mathrm{ISR}}$ process provides a high statistics sample of 12 million events. It allows the use of information from KLM and the CDC, as muon is also detected in the KLM. We select the $\mu^+\mu^-\gamma$ control sample with the condition summarized in Table 6.2.

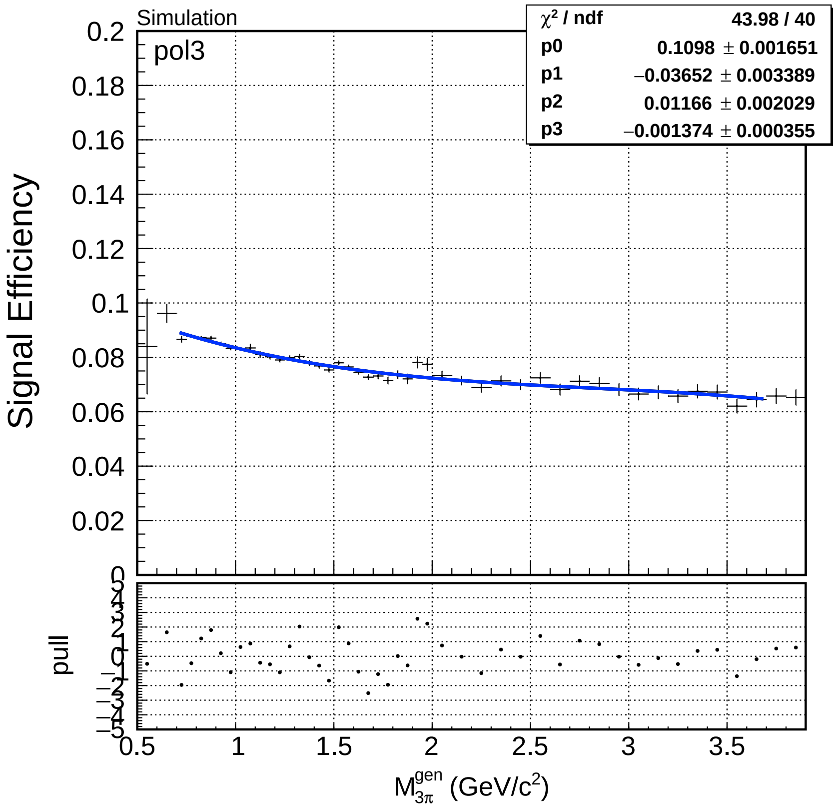

Figure 6.1: Signal efficiency as a function of the generated invariant mass of $\pi^+\pi^-\pi^0$. The solid line shows a fit result with the 3rd polynomial.

Table 6.2: Selection of $\mu^+\mu^-\gamma$ control sample for trigger efficiency study.

Quantity	Condition applied to select the control sample
	Muons
Transverse momentum	$p_T > 0.3\,\mathrm{GeV}/c$
Polar angle	$17.0° < \theta < 150°$
Closest distance to the IP	$dr < 0.5\,\mathrm{cm}$ and $\lvert dz\rvert < 2\,\mathrm{cm}$
CDC hits count	$N_{\mathrm{cdchit}} > 20$
Identified as muon	$\mathcal{P}_\mu > 0.5$
	ISR photon
ECL crystal count	$N_{\mathrm{crystal}} > 1.5$
Energy in e^+e^- c.m.=system	$E^{\mathrm{c.m.}} > 2\,\mathrm{GeV}$
Polar angle	$37.3° < \theta < 123.7°$
	Event basis
Tracks count	$N_{\mathrm{track}} == 2$
Event charge	$\Sigma Q_{\mathrm{track}} == 0$
Invariant mass of muon-pair	$M_{\mu^+\mu^-} < 3.5\,\mathrm{GeV}/c^2$
Invariant mass of $\mu^+\mu^-\gamma$	$M_{\mu^+\mu^-\gamma} > 8\,\mathrm{GeV}/c^2$
Recoil mass square of muon-pair	$M^2_{\mathrm{recoil}\mu^+\mu^-,} < 10\,\mathrm{GeV}^2/c^4$

The *hie* and *lml1* triggers are based on the ECL trigger. We determine the ECL trigger efficiency using the samples from orthogonal CDC and KLM track triggers. The ECL trigger efficiency can be measured

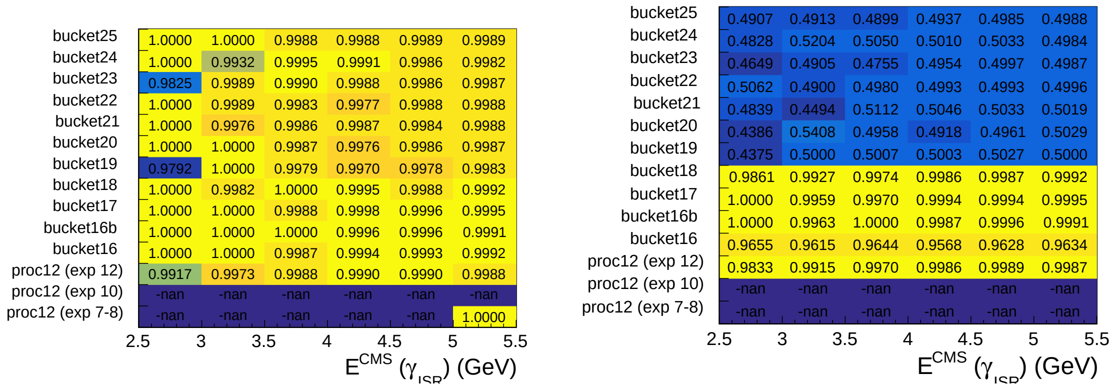

(a) *hie* (b) *lml1*

Figure 6.2: Trigger efficiency for ISR photon in terms of ISR c.m. energy and run dependency.

from the ratio

$$\varepsilon_{hie} = \frac{N(hie\ \wedge\ \text{CDC-KLM trigger lines})}{N(\text{CDC-KLM trigger lines})},$$

where N(CDC-KLM trigger lines) is the number of events that satisfy both CDC and KLM trigger lines. We use the events that satisfy trigger lines *cdcklm*, where one or two tracks on CDC are matched on KLM clusters. The numerator is the number of events that satisfy *hie* among the *cdcklm* events. For the *lml1* efficiency, *hie* is replaced with *lml1*.

The *hie* and *lml1* efficiencies depending on the energy in e^+e^- c.m. system and polar angle of the ISR photon are shown in Fig. 6.3. There is no strong dependence on the polar angle, while there is an efficiency drop in high and low energy, albeit at the level of statistical error. Figure 6.2 shows more detailed "run (production code)" [1] dependence. We apply the correction to the signal sample of data using the table that takes into account the ISR photon energy and the run dependence. As *cdcklm* are introduced from experiment 12, the efficiency in experiments 7–10 cannot evaluated using these lines. Therefore, we assume the efficiency performance in experiments 7–10 is the same as in experiment 12. The net correction of the l1-trigger efficiency ($\boldsymbol{\eta_{trig.}} \equiv R_{trig.} - 1$) averaged over the energy dependence and the run-dependence is $\mathbf{(-0.086 \pm 0.084)\%}$ for $M_{3\pi} < 1.05\,\mathrm{GeV}/c^2$, $\mathbf{(-0.082 \pm 0.080)\%}$ for 1–2 GeV/c^2, and $\mathbf{(-0.059 \pm 0.102)\%}$ for 2–3.5 GeV/c^2.

The efficiency of experiments 7–10 is confirmed using the alternative CDC-only trigger line, resulting in no significant change from experiment 12 and, at worst, 99.5%. However, an efficiency evaluation of *hie* using the CDC-only trigger line is not entirely independent of the ECL trigger because this bit is affected by the ECL-based veto for the QED process. Assuming that the conservative efficiency of experiments 7–10 is uniquely 0.95, the total correction factor is -0.107% in the region of $M_{3\pi} < 1.05\,\mathrm{GeV}/c^2$. This difference corresponds to an efficiency deterioration of -0.02%, and is negligible with respect to the statistical errors. This is also true in higher-mass regions.

The trigger efficiency for high-level trigger filtering, turned on from experiment 17, is confirmed using the signal sample of data until experiment 16. Since the efficiency is confirmed to be 100%, this is not taken into account to the systematic uncertainty.

[1]Production code is the same or finer unit of dataset as the experimental run when the object reconstruction software processes the acquired data. *bucket16(16b)* corresponds to experiment 14, *bucket17* corresponds experiment 16, *bucket18* corresponds to experiment 17, *bucket19-25* correspond to experiment 18.

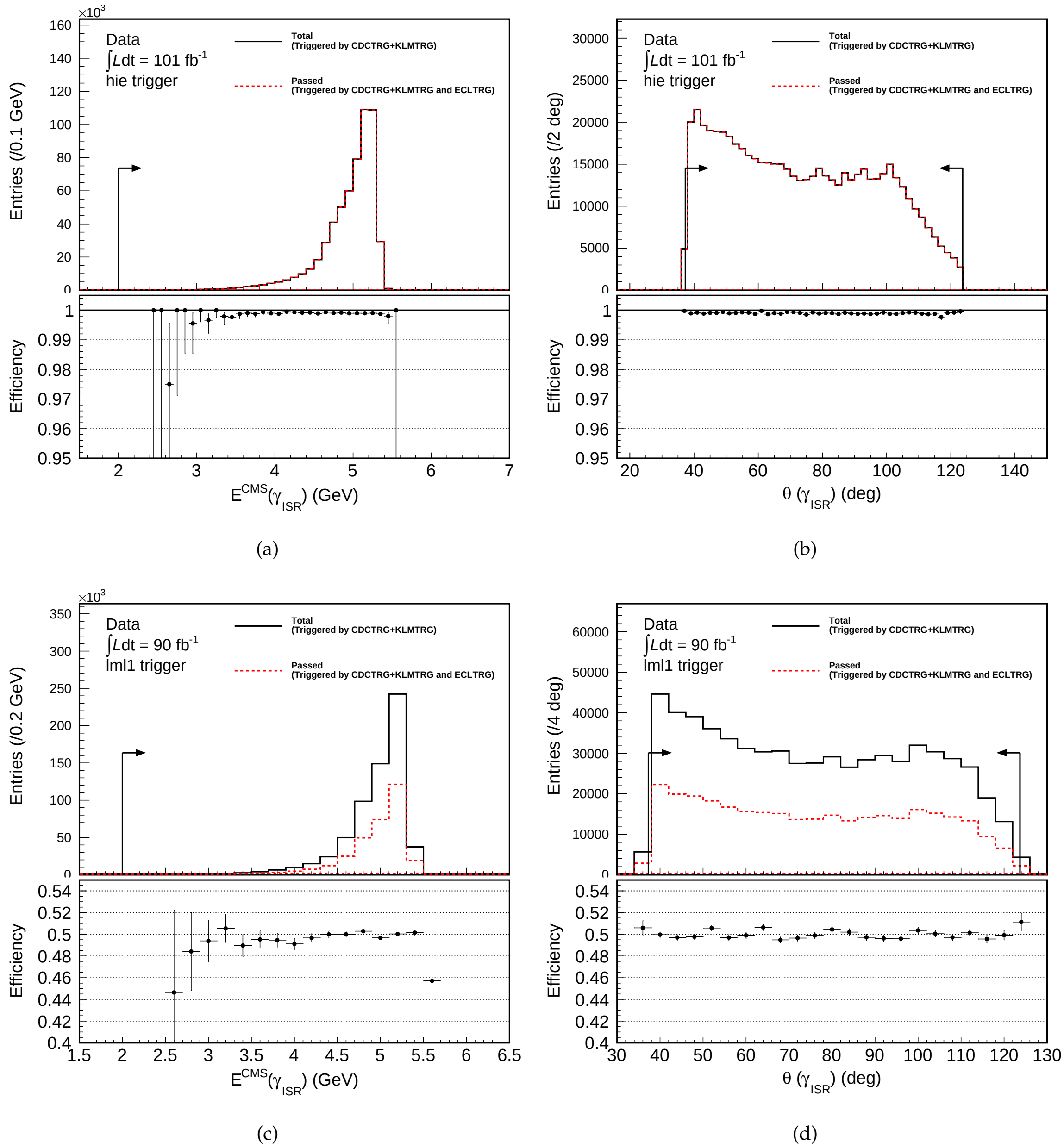

Figure 6.3: (a)(b) The c.m. energy (left) and polar angle (right) dependency of *hie* efficiency for ISR photon in the $e^+e^- \to \mu^+\mu^-\gamma$ control sample in experiment 7–17. (c)(d) that of *lml1* efficiency in experiment 18.

6.3 Tracking efficiency

Tracking efficiency is studied using data in several aspects:

- Basic tracking efficiency
- Track loss due to tracks in close proximity
- Selection efficiency of the number of CDC hits
- Duplicated tracks

As a result of the studies described in this section, the total correction factor for the tracking efficiency $\eta_{trig.}$ is $\mathbf{(-1.78 \pm 0.80)\%}$ for $M_{3\pi} < 1.05\,\mathrm{GeV}/c^2$,and $\mathbf{(-2.14 \pm 0.83)\%}$ for $M_{3\pi} > 1.05\,\mathrm{GeV}/c^2$.

Basic tracking efficiency

A tracking performance for a single track is studied by a tag-and-prove method using the $e^+e^- \to \tau^+\tau^-$ process [117]. This method uses events where the tau-pair decays to one charged lepton and three charged pions, respectively. Tag tracks are reconstructed from one lepton track and two pion tracks of good quality so that the net total charge is $\pm 1e$. The remaining track, estimated from the charge conservation, is a probe track. The detection efficiency of the probe track is evaluated in data and simulation as a function of momentum, polar angle, azimuthal angle and experimental run, respectively. The results show good agreement between the data and MC simulation. A systematic uncertainty of $\mathbf{(0.60)\%}$ for two tracks is applied as tracking efficiency.

Track loss due to tracks in close proximity

We also check for track losses, which could not be measured by the tag-and-probe method using tau-sample since the method assumes independent tracks. It is validated using the signal process $e^+e^- \to \pi^+\pi^-\pi^0\gamma$. The close two tracks likely cause its loss, especially in the case that the track intersects on the azimuthal plane, causing many shared wire hits on the CDC. To check this possibility quantitatively, we define the opening angle difference on the azimuthal plane as

$$\Delta\phi = \phi(\pi^+) - \phi(\pi^-).$$

The tracks cross on the azimuthal plane when $\Delta\phi$ is positive (see Fig. 6.4). Figure 6.5 shows the comparison between positive and negative $\Delta\phi$ in MC simulation, in the generator level (a) and the observed (reconstructed) level (b). Obviously, the distribution of $\Delta\phi$ in the generated events is symmetrical in positive and negative, and the yields are the same. A clear difference between the positive and negative

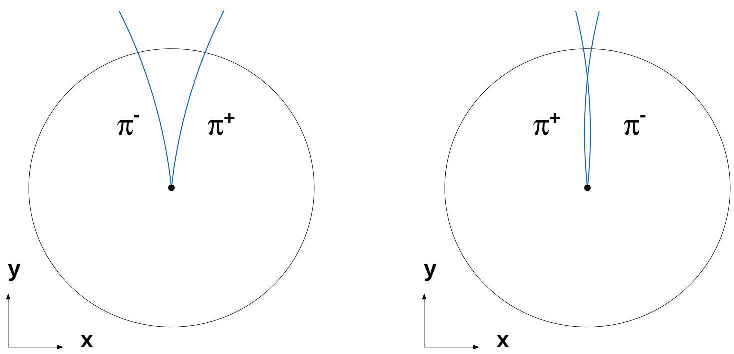

(a) $\Delta\phi < 0$ (b) $\Delta\phi > 0$

Figure 6.4: Visual representation of (a) crossing and (b) non-crossing track events. The center dot is the IP, and the circle is a CDC outer frame.

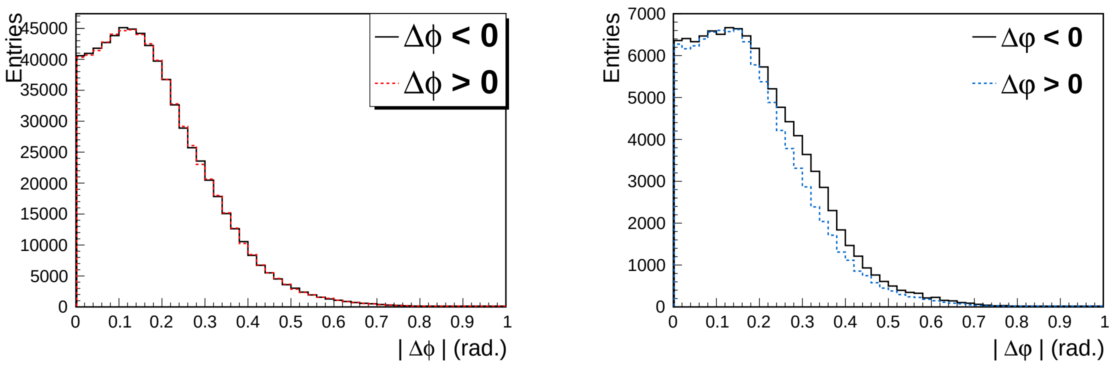

(a) Generated (b) Reconstructed

Figure 6.5: $\Delta\phi$ distribution of signal MC sample. The lines indicate $\Delta\phi < 0$ events (solid) and $\Delta\phi > 0$ (dashed) (a) shows the variable of generator-level information. (b) shows the measured variables.

tracks is observed in the reconstructed track, while there is no difference in the generator level. To show the fraction of the correlated track loss quantitatively, we define the variable f by

$$f = \frac{N(\Delta\phi < 0) - N(\Delta\phi > 0)}{2N(\Delta\phi < 0)},$$

where $N(\Delta\phi < 0)$ is the number of the events with $\Delta\phi < 0$. The difference in fractions between data and simulation is tested and corrected.

The $\Delta\phi$ distribution is compared in Fig 6.6 (a), and the calculated track loss as a function of the $|\Delta\phi|$ is shown in Fig 6.6 (b). A marked difference is observed in bins with the smallest $|\Delta\phi|$ The total track loss is $f_{\text{data}} = 0.050 \pm 0.005$ in data and $f_{\text{MC}} = 0.0398 \pm 0.0013$ in simulation at the ω and ϕ resonances. The data-MC ratio of the correlated track loss is

$$R_{trackloss} = \frac{1 - f_{\text{data}}}{1 - f_{\text{MC}}} = 0.9890 \pm 0.0053; \tag{6.3}$$

Thus a correction factor is $\mathbf{(-1.01 \pm 0.53)\%}$. The error is the statistical uncertainty for this control sample.

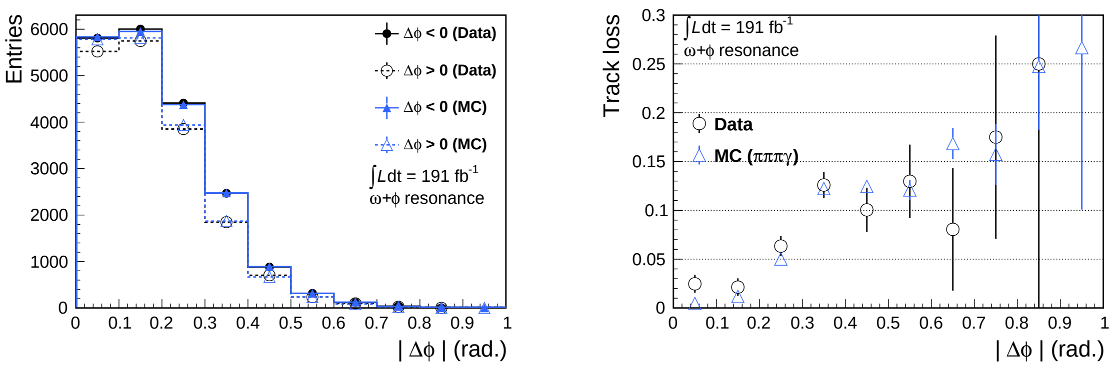

(a) (b)

Figure 6.6: $\Delta\phi$ distribution and its track loss for data and simulation. (a) The lines indicate $|\Delta\phi|$ distribution of $\Delta\phi < 0$ events (solid) and $\Delta\phi > 0$ (dashed) in data (black circle) and MC simulation (blue triangle). (b) The points with error bars show the event losses f depending on $\Delta\phi$ of data (circle) and MC (triangle).

Selection for the number of CDC wire hits

The number of CDC wire hits connected with the track must be more than twenty in the selection. The distribution of N_{cdchit} for data and simulation is shown separately in Fig. 6.7 for positive and negative charged particles. The figures show a relatively large discrepancy between the data and the simulation, especially for negative charged tracks, indicating the imperfect simulation. The efficiency of this selection $N(N_{\mathrm{cdchit}} > 20)/N(N_{\mathrm{cdchit}} > 0)$ is obtained using each mass region in the signal sample: i.e., the ratio of the events with and without this cut $N(N_{\mathrm{cdchit}} > 20)$. The ratio in data (simulation) is 99.0% (99.3%) at the ω and ϕ resonance, and is 97.2% (97.8%) for $1.05 < M_{3\pi} < 2.0\,\mathrm{GeV}/c^2$. The correction factor of the efficiency is obtained to be $\mathbf{(-0.25 \pm 0.06)\%}$ in the mass region below $1.05\,\mathrm{GeV}/c^2$ and $\mathbf{(-0.61 \pm 0.21)\%}$ in the mass region above $1.05\,\mathrm{GeV}/c^2$.

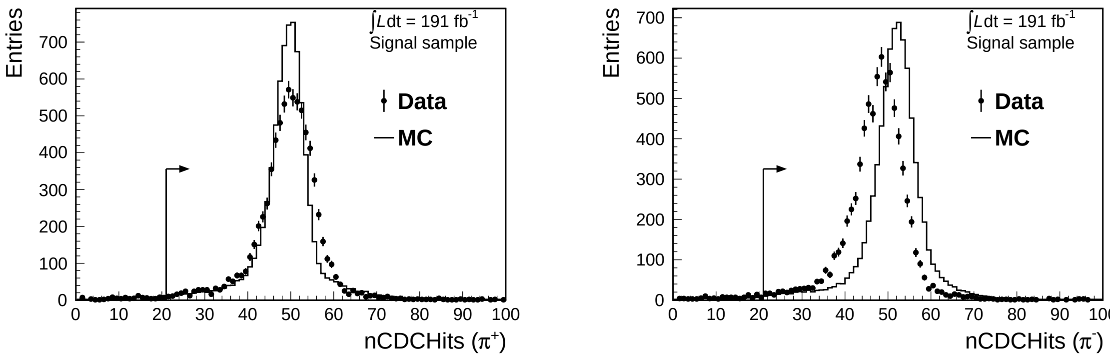

(a) $N_{\mathrm{cdchit}}(\pi^+)$ (b) $N_{\mathrm{cdchit}}(\pi^-)$

Figure 6.7: The number of measured points in CDC associated with each track N_{cdchit} in (a) positive and (b) negative tracks in the signal sample. The points with error bars represent data and the solid line shows $\pi^+\pi^-\pi^0\gamma$ MC samples.

Duplicated and sign-flip track

In the baseline selection, we require that there are exactly two tracks of opposite-sign. The event will be lost if there are three tracks, e.g., due to track duplication and a fake track. We test this possibility both for the data and the MC simulation. For the signal MC, the ratio of 3-track to 2-track events is $(0.0152 \pm 0.0017)\%$ in the ω and ϕ resonance, where the number of 3-track events is 6.5 in the data, and the statistical error is estimated to be around 0.01%. For data, the number of 3-track events is four out of 38538 2-track events, which is $(0.010 \pm 0.005)\%$. Thus, the events lost by the duplicated track are very small (0.015% [MC], 0.010% [data]), and the fraction agrees quite well for data and simulation.

Furthermore, events may be lost if a track is incorrectly identified with the wrong charge sign, especially for high-energy tracks. We selected the signal sample with the same-sign requirement and confirmed that the sign-flip track is zero in both data and simulation.

6.4 ISR photon effiecncy

A correction for ISR photon detection efficiency is obtained based on the study using an ISR process, $e^+e^- \to \mu^+\mu^-\gamma$ [118]. A muon pair is reconstructed, and the recoil-momentum vector is calculated from the four-vector of the initial state e^+e^- and the muon pair. The selection with the squared invariant mass of recoil system $M^2_{\mu^+\mu^-,\mathrm{recoil}} < 2\,\mathrm{GeV}^2/c^4$ can significantly reduce background events. The efficiency of a photon is evaluated by whether there are ECL clusters that match this recoil momentum in terms of energy and direction. The correction factor is evaluated as a function of the photon energy and polar angle.

In this analysis, the correction only for ISR photon is considered, and that of π^0-daughter photon is included in π^0 efficiency. Figure 6.8 depicts the correction factors as a function of $M_{3\pi}$ using the signal sample of $\pi^+\pi^-\pi^0\gamma$ MC. The correction factor $\boldsymbol{\eta_{ISR}}$ is $\mathbf{(+0.15 \pm 0.67)\%}$ overall mass range.

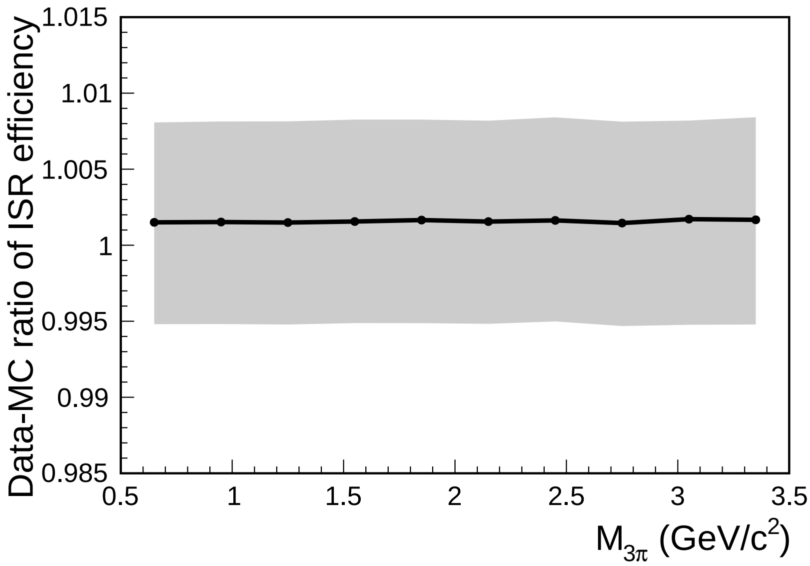

Figure 6.8: Data-MC ratio for the ISR photon detection efficiency as a function of $M_{3\pi}$. The error bars indicate total uncertainty.

The uncertainty is dominated by a systematic uncertainty coming from the data-MC differences for a background suppression selection and muon track quality.

6.5 π^0 detection efficiency

We evaluate the efficiency of the π^0 reconstruction using the process

$$e^+e^- \to \omega\gamma_{\rm ISR} \to \pi^+\pi^-\pi^0\gamma_{\rm ISR}. \tag{6.4}$$

Efficiency can be defined as

$$\varepsilon_i = \frac{N_{i,\rm full\_reco}(1 - r_{\rm bkg.})}{N_{i,\rm part\_reco}}, \tag{6.5}$$

where $N_{i,\rm part\_reco}$ is the number of *partial-reconstructed* $\omega\gamma$ events, $N_{i,\rm full\_reco}$ is the number of *full-reconstructed* $\omega\gamma$ events, $r_{\rm bkg.}$ is the fraction of background in the full-reconstructed $\omega\gamma$ events, and the ε_i is the efficiency of π^0 reconstruction for the data (i = data) and MC simulation (i = MC). The number of partial-reconstructed events, the denominator, means the number of $e^+e^- \to \omega\gamma$ events estimated without using information of π^0.The full-reconstructed events are the number of $e^+e^- \to \omega\gamma$ events where π^0 can be reconstructed among the partial-reconstructed events, corresponding to the number of found π^0. The prominent peak that the ω resonance makes on the 3π invariant mass distribution is used to separate it from the background event. To calculate the 3π invariant mass without using any information from the π^0-decay photons, the recoil (or missing) momentum is used instead of the π^0 momentum. The recoil four-momentum of $\pi^+\pi^-\gamma$ system is calculated as

$$p_{\pi^0_{\rm rec}} = p_{e^+e^-} - p_{\pi^+} - p_{\pi^-} - p_{\gamma_{\rm ISR}}, \tag{6.6}$$

where $p_{e^+e^-}$ is initial beam four-momentum, $p_{\pi^\pm}$ is four-momentum of charged pions, $p_{\gamma_{\rm ISR}}$ is four-momentum of ISR photon, and $p_{\pi^0_{\rm rec}}$ is thee recoil momentum of $\pi^+\pi^-\gamma$ system. The invariant mass of three pions is defined as

$$M_{\pi^+\pi^-\pi^0,\rm recoil} = \sqrt{(p_{\pi^+} + p_{\pi^-} + p_{\pi^0_{\rm rec}})^2}. \tag{6.7}$$

In addition, to increase the 3π mass resolution, a kinematic fit is applied with a constraint that the invariant mass of the recoil system is equal to the π^0 mass (1C-KFit). The $M_{\pi^+\pi^-\pi^0,\rm recoil}$ distribution shows a prominent peak of ω resonance by using the four momenta of 1C-KFit results (Fig. 6.9).

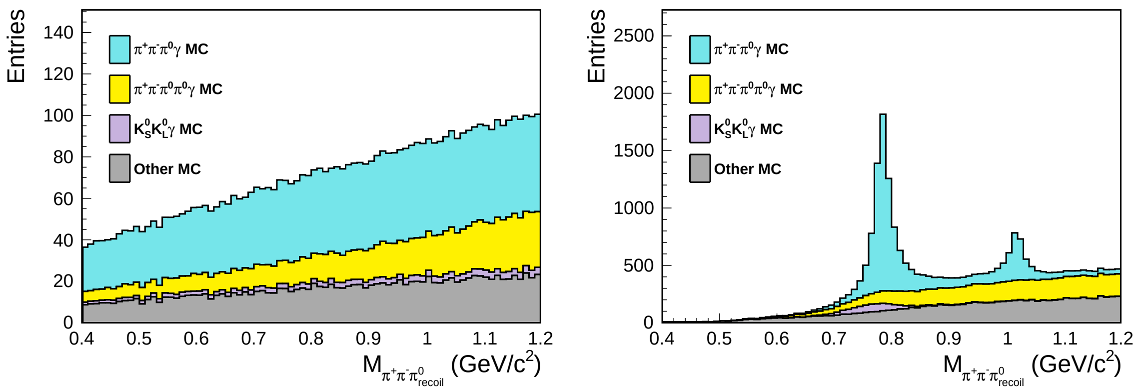

(a) Measured (b) 1C-KFit

Figure 6.9: $M_{\pi^+\pi^-\pi^0,\mathrm{recoil}}$ distribution of the MC simulation using (a) measured four-momenta and (b) four-momenta of 1C-KFit results.

The partial-reconstructed events are selected without requiring the detection of the photons from π^0 decay. We require that there are exactly two changed tracks, with net-charge zero, and identified as pion. The highest energy photon in the events is chosen as the ISR photon (γ_{ISR}). The same criteria given in the signal selection (Table 4.2) are applied to select pions and ISR photons. To further reduce the background, we apply all the background rejection cuts listed in Table 4.2 except the ones that need the π^0/photon information, $\chi^2_{4\mathrm{C},2\pi3\gamma}$ and $\chi^2_{4\mathrm{C},2\pi5\gamma}$.

The distribution of the χ^2 of the 1C-KFit, denoted by $\chi^2_{1\mathrm{C,rec.}}$, is shown in Fig. 6.10. The number of degrees of freedom (d.o.f) of this kinematic fit is three [119]. As the condition of the success of the 1C-KFit, we require χ^2 of the 1C-KFit to be less than ten, $\chi^2_{1\mathrm{C,rec.}} < 10$.

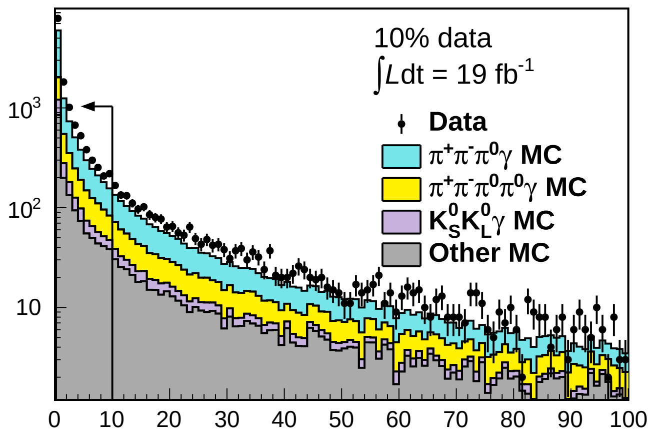

Figure 6.10: The $\chi^2_{1\mathrm{C,rec.}}$ distribution of partial-reconstructed events using the 10% of data.

Counting of the denominator : partial-reconstructed $\omega\gamma$ events

The number of the partial-reconstructed signal events $N_{i,\mathrm{part\_reco}}$ is obtained by fitting the $M_{\pi^+\pi^-\pi^0,\mathrm{recoil}}$ with the signal and the background. The $M_{\pi^+\pi^-\pi^0,\mathrm{recoil}}$ distribution of the partial-reconstructed events is plotted in Fig. 6.11. In the fit, the histogram templates obtained by MC simulation are used to model the shape of the signal and background. The ω signal shape is reproduced quite accurately for the signal reaction. The background is dominated by the $e^+e^- \to \pi^+\pi^-\pi^0\pi^0\gamma$, $e^+e^- \to K^0_S K^0_L\gamma$ and $e^+e^- \to q\bar{q}$ (including low-energy hadron production). The *others* pdf is dominated by $e^+e^- \to \pi^+\pi^-\gamma$, $e^+e^- \to \mu^+\mu^-\gamma$ and Bhabha. Although the process $\pi^+\pi^-\pi^0\pi^0\gamma$ involves the ω resonance in a

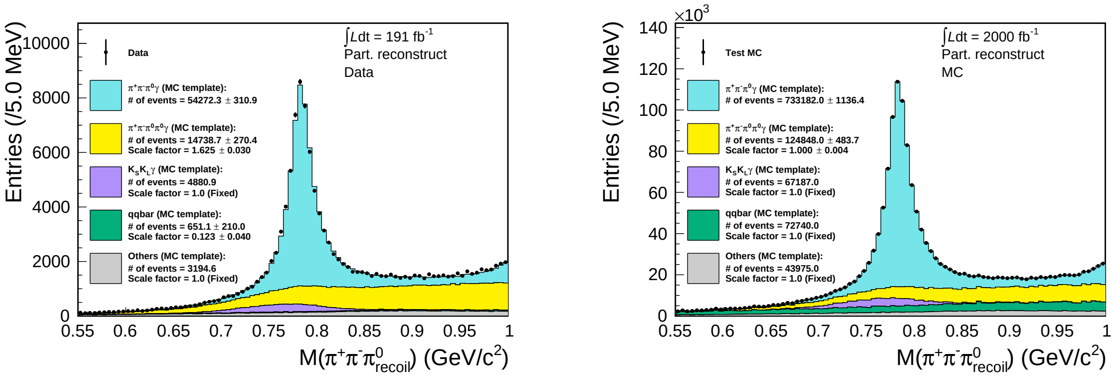

(a) Data

(b) Simulation

Figure 6.11: $M_{\pi^+\pi^-\pi^0,\mathrm{recoil}}$ distribution of the partial-reconstruction sample for π^0 efficiency evaluation in (a) data and (b) MC simulation. The stacked histogram in (a) shows the fit results, and that in (b) shows the distribution scaled with the integrated luminosity. The scale factor of the fitting result is indicated in the legend.

$\omega\pi^0\gamma$ intermediate state, this does not create a peak in $M_{\pi^+\pi^-\pi^0,\mathrm{recoil}}$ since the wrong momentum, the momentum of two π^0, is assigned to π^0_{rec}. While the background from $K^0_S K^0_L\gamma$ shows a peaking structure under the ω mass region in $M_{\pi^+\pi^-\pi^0,\mathrm{recoil}}$. This is caused by the fact that the process is dominated by the $e^+e^- \to \phi\gamma \to K^0_S K^0_L\gamma$ process, where two charged particles are from $K^0_S \to \pi^+\pi^-$ and the K^0_L is treated as the missing particle. Although the actual value of $M(K^0_S K^0_L)$ is the ϕ mass, the $M_{\pi^+\pi^-\pi^0,\mathrm{recoil}}$ shifted to the ω mass region, since π^0 mass assumed, instead of K^0_L, for the missing particle. Three parameters are floated in the fit: the number of signal events and the two scale factors corresponding to the $\pi^+\pi^-\pi^0\pi^0\gamma$ and $q\bar{q}$. The scale factors for the pdfs are defined as the ones that multiply the expected number of events from the known luminosity. We floated scale factors for $\pi^+\pi^-\pi^0\gamma$ (signal) $\pi^+\pi^-\pi^0\pi^0\gamma$ and $q\bar{q}$ pdfs and fixed scale factors of $K^0_S K^0_L\gamma$ and *others* pdfs. The fitting range is around omega resonance, $0.6 < M_{\pi^+\pi^-\pi^0,\mathrm{recoil}} < 0.95\,\mathrm{GeV}/c^2$.

The fitted results in data and MC are shown by the histograms in Fig 6.11. The number of partial-reconstructed events, $N_{i,\mathrm{part\_reco}}$, is then obtained by integrating over the signal shape (histogram) in the range $0.72 < M_{\pi^+\pi^-\pi^0,\mathrm{recoil}} < 0.84\,\mathrm{GeV}/c^2$. By integrating over the same range for the background, the background fraction for this sample is obtained to be 28%.

Counting of the numerator : full-reconstructed $\omega\gamma$ events

The number of full-reconstructed events $N_{i,\mathrm{full\_reco}}$ is estimated by $M_{\gamma\gamma}$ fit, i.e., the same procedure as the signal extraction. The full-reconstructed events are selected from the partial-reconstructed events by requiring the same $M_{\pi^+\pi^-\pi^0,\mathrm{recoil}}$ range, the identical criteria for the photon and π^0 selection and the χ^2 of the 4C fit $\chi^2_{4\mathrm{C},2\pi3\gamma} < 50$ as the signal selection shown in Table 4.2 [2] We do the 4C-KFit for all samples with $M_{\gamma\gamma} < 1.0\,\mathrm{GeV}/c^2$ and apply a cut $\chi^2_{4\mathrm{C},2\pi3\gamma} < 50$. . By additional 4C requirement, the number of signals is reduced by 85%. (see Table 4.2). The $M_{\gamma\gamma}$ distribution for the full-reconstructed events is shown in Fig. 6.12. Novosibirsk function is used for the signal shape, and the second polynomial is used for the background. The value, $N_{i,\mathrm{full\_reco}}$, is then obtained by integrating over the mass region $0.123 < M_{\gamma\gamma} < 0.147\,\mathrm{GeV}/c^2$. The peaking background that contains π^0 from $\pi^+\pi^-\pi^0\pi^0\gamma$ is subtracted based on the scale factor determined in section 5.2. The fraction of π^0 from the remaining $\pi^+\pi^-\pi^0\pi^0\gamma$ to the full-reconstructed events is $r_{\mathrm{bkg.}} = 0.51\%$, corresponding 140 ± 5 events. The background from $q\bar{q}$ is 0.03% (8 events), and that from $\tau^+\tau^-$ is negligible. A possible peaking background from $e^+e^- \to \omega\pi^0$ is estimated based on the data sample but is small enough to be insignificant (0.15% and 0.16% for partial- and full- reconstructed events).

[2] Note that a cut on $\chi^2_{4\mathrm{C},2\pi5\gamma}$ is not applied in this efficiency study since we are interested in the π^0 efficiency, and this cut is not used to select the reconstructed events.

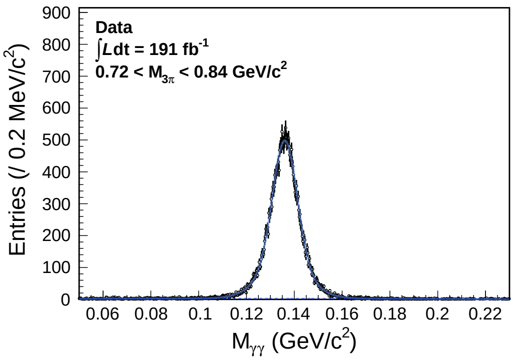

(a) Data

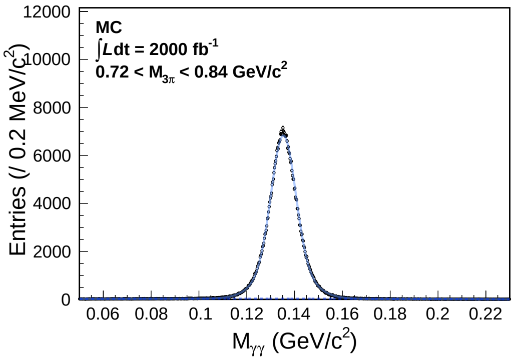

(b) MC

Figure 6.12: $M_{\gamma\gamma}$ distribution of the full-reconstructed events for (a)the data and (b) the MC simulation. The curves show the fit result with the pdf modeled with the Novosibirsk and Gaussian function for π^0 signal and quadratic function for combinatorial π^0 background. The solid line represents the total pdf, and the dashed line represents the background pdf.

Results

The π^0 efficiency using our signal selection for the π^0 and $\chi^2_{4C,2\pi3\gamma}$ requirement is $(50.2 \pm 0.3)\%$ for data and $(51.0 \pm 0.1)\%$ for MC simulation. The data-MC ratio is $R = 0.9856 \pm 0.0058$, where the uncertainty consists of 0.44% of statistical uncertainty and 0.38% of fitting uncertainty. The correction factor for the π^0 efficiency η_{π^0} is $\mathbf{(-1.43 \pm 1.01)\%}$. The detailed estimation of the systematic uncertainty in this method of the π^0 efficiency calibration is given in appendix A. The results are summarized in Table 6.3. As can be seen from the table, the uncertainties are dominated by the uncertainty in the background from the dominant background $\pi^+\pi^-\pi^0\gamma$, the peak background $K^0_S K^0_L\gamma$, event selection and the counting number of π^0 signal. The total systematic error is estimated to be 0.83%. That means the π^0 efficiency is known in the 1% accuracy.

Table 6.3: Summary of the systematic uncertainties (%) on the π^0 efficiency determined from $e^+e^- \to \pi^+\pi^-\pi^0\gamma_{ISR}$. Partially reconstructed events are selected from the recoil mass against the $\pi^+\pi^-\gamma_{ISR}$ system without using any π^0 related information. The total uncertainty is obtained by taking the quadratic sum of all items.

Source	Systematic uncertainty	Comments
Partial reconstructed events		
$\pi^+\pi^-\pi^0\pi^0\gamma$ background	± 0.13	Section A.1
$\phi \to K_S K_L \gamma_{ISR}$ background	± 0.33	Section A.1
$q\bar{q}$ background	± 0.06	Section A.1
Background model	± 0.07	Section A.1
ω signal model	± 0.09	Section A.1
Event selection	± 0.57	Section A.1
Full reconstructed events		
Counting method	± 0.12	Section A.2
π^0 signal model	± 0.46	Section A.2
$\pi^+\pi^-\pi^0\pi^0\gamma$ background	± 0.07	Section A.2
Total	± 0.83	

6.6 Efficiency for selection of kinematic fit chi-squared

We consider the signal efficiency for the selection of the chi-squared of the 4C kinematic fit $\chi^2_{\mathrm{4C},2\pi3\gamma} < 50$. The agreement of chi-squared distribution is affected by the reproducibility of energy, momentum, and position resolution in clustering and tracking. The chi-squared for the two photons of π^0 decay is included in the verification in the previous section and is taken into account in the correction factor for the π^0 efficiency. The chi-squared of the remaining ISR photon and two tracks is then verified using the $e^+e^- \to \mu^+\mu^-\gamma$ in this section.

The $\mu^+\mu^-\ \gamma$ control sample is reconstructed from ISR and two charged particles. The selection is identical to Table 6.2, which is used for the study of trigger efficiency, but to improve purity, only the selection for recoil mass square of the muons is changed to a tighter selection, $M^2_{\mu^+\mu^-,\mathrm{recoil}} < 4\,\mathrm{GeV}^2/c^4$. The $\mu^+\mu^-\gamma$ control sample is subject to the 4C-KFit under the hypothesis of $e^+e^- \to \mu^+\mu^-\gamma$ process. The chi-squared of the 4C-KFit result is denoted by $\chi^2_{\mathrm{4C},2\mu\gamma}$.

We define the efficiency of chi-squared selection at the threshold c as

$$\varepsilon_i(c) = \frac{N(\chi^2_{\mathrm{4C},2\mu\gamma} < c)}{N_0}, \tag{6.8}$$

where , $N(\chi^2_{\mathrm{4C},2\mu\gamma} < c)$ is the number of events with $\chi^2_{\mathrm{4C},2\mu\gamma} < c$, N_0 is the total events, and $\varepsilon_i(c)$ is the efficiency at c for the data (i = data) and MC simulation (i = MC). Data-MC ratio of the efficiency is expressed as

$$R_{\chi^2}(c) = \frac{\varepsilon_{\mathrm{data}}(c)}{\varepsilon_{\mathrm{MC}}(c)}. \tag{6.9}$$

Figure 6.13 displays both (top) the $\chi^2_{\mathrm{4C},2\mu\gamma}$ and (bottom) R_{χ^2} distributions. The R_{χ^2} is stable with in $\pm0.2\%$ for the c region from 20 to 50. The correction factor is determined based on the value of R_{χ^2} in this range. We take the average minimum and maximum values in this range as the correction factor and the differences between the minimum and maximum as the uncertainty. Hence, the correction factor for the χ^2 selection, η_{χ^2}, is $\eta_{\chi^2} = (0.0 \pm 0.3)\%$ for $M_{3\pi} < 1.05\,\mathrm{GeV}/c^2$, and $\eta_{\chi^2} = (0.3 \pm 0.3)\%$ for $M_{3\pi} > 1.05\,\mathrm{GeV}/c^2$. The chosen c range of 20–50 is reasonable, since we requires $\chi^2_{\mathrm{4C},2\pi3\gamma} < 50$ to the signal process and a relation of

$$\chi^2_{\mathrm{4C},2\pi3\gamma} \sim \chi^2_{\mathrm{4C},2\mu\gamma} + \chi^2_{\mathrm{4C},\pi^0\to\gamma\gamma}, \tag{6.10}$$

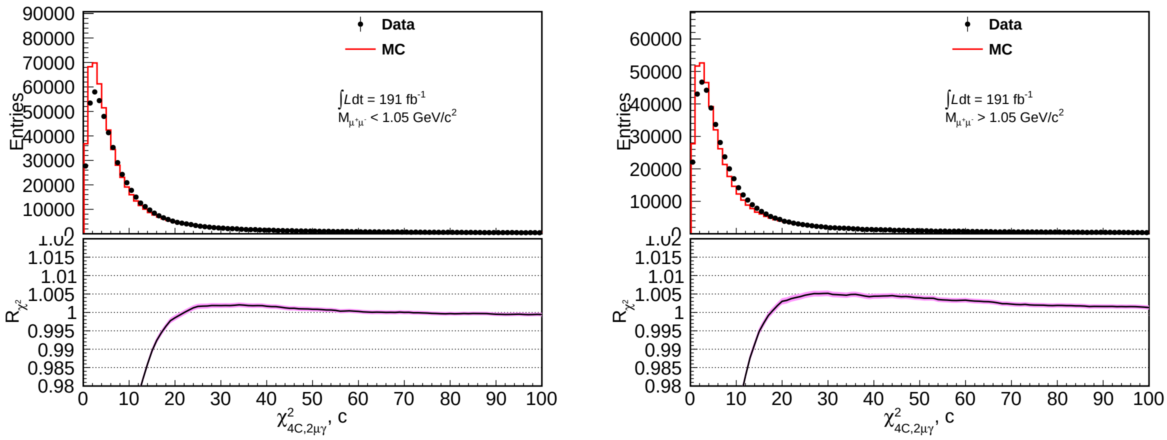

(a) $M_{\mu^+\mu^-} < 1.05\,\mathrm{GeV}/c^2$ (b) $M_{\mu^+\mu^-} > 1.05\,\mathrm{GeV}/c^2$

Figure 6.13: $\chi^2_{\mathrm{4C},2\mu\gamma}$ distribution (top) and R_{χ^2} curve (bottom) in the $e^+e^- \to \mu^+\mu^-\gamma$ control sample. (a) and (b) are the plots in the $M_{3\pi}$ mass region below and above $1.05\,\mathrm{GeV}/c^2$. In the top plots, the closed circles show the data, and the red histogram shows the MC simulation. The bottom plots show R_{χ^2} in a function of χ^2-thresholds c, where the pink bands are the statistical uncertainty.

where 99% of signal events has small $\chi^2_{4C,\pi^0\to\gamma\gamma}$ of less than 30.

For small c, large differences between data and simulation are observed. This is caused by ISR photon energy distribution differences, as shown in Fig. 6.14. The average value of energy has been calibrated in the MC sample. However, the shape differs between the data and the simulation because of an incomplete simulation.

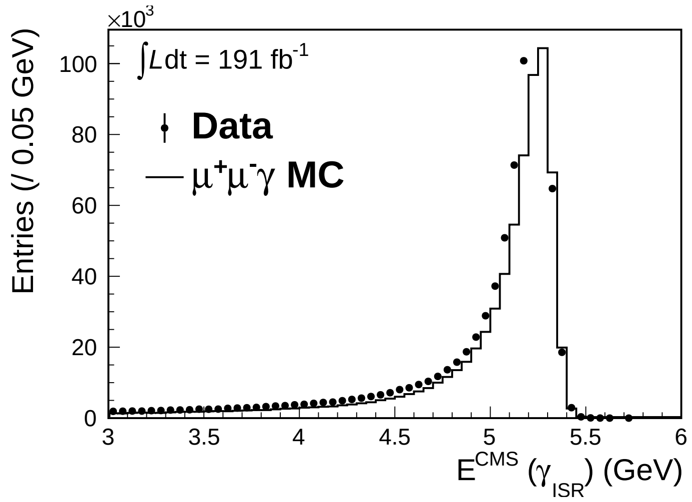

Figure 6.14: Energy of ISR photon in the e^+e^- c.m. system in the $\mu^+\mu^-\gamma$ control sample of data (points) and MC simulation (solid line). The number of processes other than $e^+e^- \to \mu^+\mu^-\gamma$ is relatively small.

In adapting to $3\pi\gamma$, the kinematics of the two tracks differ. To take this into account, the distribution of $R_{\chi^2}(c)$ was divided by the momentum of the muon and checked in Fig. 6.15. As can be seen, there is a momentum dependence of the $R_{\chi^2}(c)$ distribution. The half of the peak-to-peak difference in $20 < c < 50$ is taken, and the systematic error is set to 0.6% for $M_{3\pi} < 1.05\,\mathrm{GeV}/c^2$ and 0.3% for $M_{3\pi} > 1.05\,\mathrm{GeV}/c^2$.

From these results, the correction factor is we take the data-MC correction factor for the 4C χ^2 selection, δ_{χ^2}, to be $\delta_{\chi^2} = (0.0 \pm 0.6)\%$ for $M_{3\pi} < 1.05\,\mathrm{GeV}/c^2$, and $\delta_{\chi^2} = (0.3 \pm 0.3)\%$ for $M_{3\pi} > 1.05\,\mathrm{GeV}/c^2$.

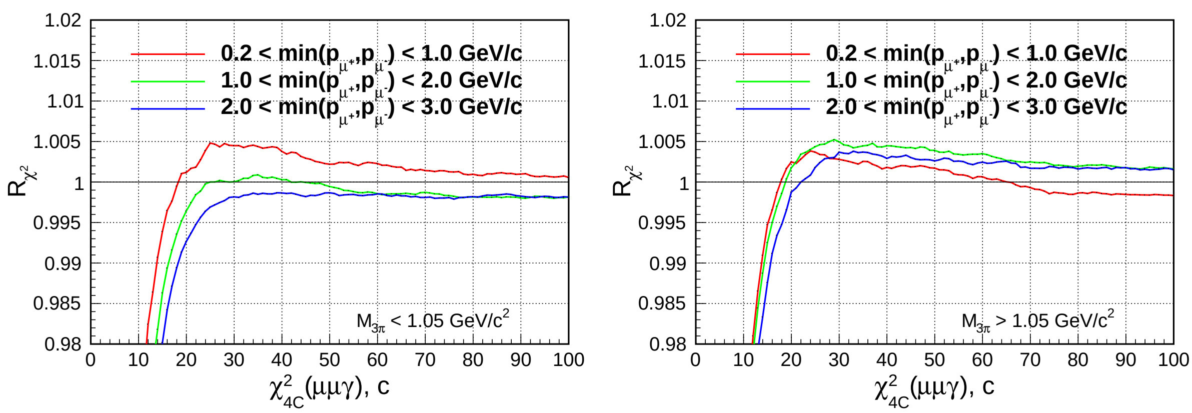

(a) $M(\mu^+\mu^-) < 1.05\,\mathrm{GeV}/c^2$

(b) $M(\mu^+\mu^-) > 1.05\,\mathrm{GeV}/c^2$

Figure 6.15: Ratio $\varepsilon_{\mathrm{data}}/\varepsilon_{\mathrm{MC}}$ as a function of the cut value c (see Eq. (6.9)) dividing the minimum momentum of muons.

6.7 Background suppression efficiency

In this section, the validation of the signal efficiency for the background suppression selections is discussed, which includes:

- Either one of the tracks is not an electron: $\mathcal{P}_{\pi/e} > 0.1$
- Either one of the tracks is not a kaon: $\mathcal{P}_{\pi/K} > 0.1$
- $\pi^+\pi^-\pi^0\pi^0\gamma$ rejection : $\chi^2_{4\mathrm{C},2\pi5\gamma} > 30$
- $q\bar{q}$ rejection : $M_{\pi^\pm\gamma_{\mathrm{ISR}}} > 2\,\mathrm{GeV}/c^2$
- $q\bar{q}$ rejection : $M_{\gamma_{\mathrm{ISR}}\gamma} < 0.11\,\mathrm{GeV}/c^2 \mathrm{or} M_{\gamma_{\mathrm{ISR}}\gamma} > 0.17\,\mathrm{GeV}/c^2$
- $q\bar{q}$ rejection : $\mathrm{Cluster\ second\ moment}\ S_{\mathrm{ISR}} > 1.3$
- $\pi^+\pi^-\gamma$ and $\mu^+\mu^-\gamma$ rejection : $M^2_{\pi^+\pi^-,\mathrm{recoil}} > 4\,\mathrm{GeV}^2/c^4$.

To obtain the efficiency of these selections for the signal event, the sharp resonances ω, ϕ and J/ψ are used to count the $e^+e^- \to \pi^+\pi^-\pi^0\gamma$ events before and after the selections are applied, and the ratio is compared between the data and the MC simulation. To minimize errors related to the multiple selections, the signal efficiency is not evaluated one by one but treats all background suppression selections together.

For verification in the region below $1.1\,\mathrm{GeV}/c^2$, the events around the ω ($0.72 < M_{3\pi} < 0.84\,\mathrm{GeV}/c^2$) and ϕ ($0.98 < M_{3\pi} < 1.05\,\mathrm{GeV}/c^2$) resonances are used. The purity of signal with (without) the background suppression selections is expected to be 99.6% (97.4%) based on the MC simulation. The signal efficiency in simulation is $\varepsilon_{\mathrm{MC},sel.} = 0.9125 \pm 0.00038$. Even if we assign conservative 100% uncertainty for backgrounds, the uncertainty increases by 0.01% at most. The efficiency in data is estimated as

$$\varepsilon_{\mathrm{data},sel.} = \frac{N_{\mathrm{pass}}(1 - r_{b,\mathrm{pass}})}{N_{\mathrm{all}}(1 - r_{b,\mathrm{all}})}, \tag{6.11}$$

where N_{pass} is the number of events passing the background suppression selections, N_{all} is the number of all events before applying the background suppression, and $r_{b,\mathrm{all/pass}}$ is the estimated fraction of background. To drop the combinatorial π^0 background in , N_{pass} and N_{all} are determined by fitting the $M_{\gamma\gamma}$.

For data, we obtained $N_{\mathrm{all}} = 41825 \pm 205$ and $N_{\mathrm{pass}} = 370102 \pm 193$. The background fraction to be subtracted, $r_{b,\mathrm{all/pass}}$, is listed in Table 6.4. The efficiency is calculated to be $\varepsilon_{\mathrm{data},sel.} = 0.8951 \pm 0.0020$. The data-MC ratio is $R_{sel.} = \varepsilon_{\mathrm{data},sel.}/\varepsilon_{\mathrm{MC},sel.} = 0.9810 \pm 0.0020$. The only statistical uncertainty is taken into account. Thus, a correction factor for the efficiency of background suppression selection $\boldsymbol{\eta_{sel.}}$ is $\mathbf{(-1.90 \pm 0.20)\%}$.

Table 6.4: Summary of estimated background fraction in the $\omega\gamma \to \pi^+\pi^-\pi^0\gamma$ and $\phi\gamma \to \pi^+\pi^-\pi^0\gamma$ samples before and after applying the background suppression.

Source	w/o selections ($r_{b,\mathrm{all}}$)	w/ selections ($r_{b,\mathrm{pass}}$)
$\pi^+\pi^-\pi^0\pi^0\gamma$	0.0063	0.0036
$K^+K^-\pi^0\gamma$	0.0022	0.0003
$q\bar{q}$	0.0003	0.0001
$\omega\pi^0$	0.0053	0.0012
Total	0.0142	0.0052

For the high mass region, we confirm it by fitting to the $J/\psi \to \pi^+\pi^-\pi^0$ resonance. The simulated efficiency is $\varepsilon_{\mathrm{MC},sel.} = 0.806 \pm 0.013$. The fitting result is shown in Fig. 6.16. The counting is 1783 ± 47 events without the selections and 1411 ± 39 events with selections. The efficiency in data is $\varepsilon_{\mathrm{data},sel.} = 0.791 \pm 0.015$. Thus, the correction factor $\boldsymbol{\eta_{sel.}}$ is $\mathbf{(-1.78 \pm 1.85)\%}$, which is applied to events in $M_{3\pi} > 1.1\,\mathrm{GeV}/c^2$.

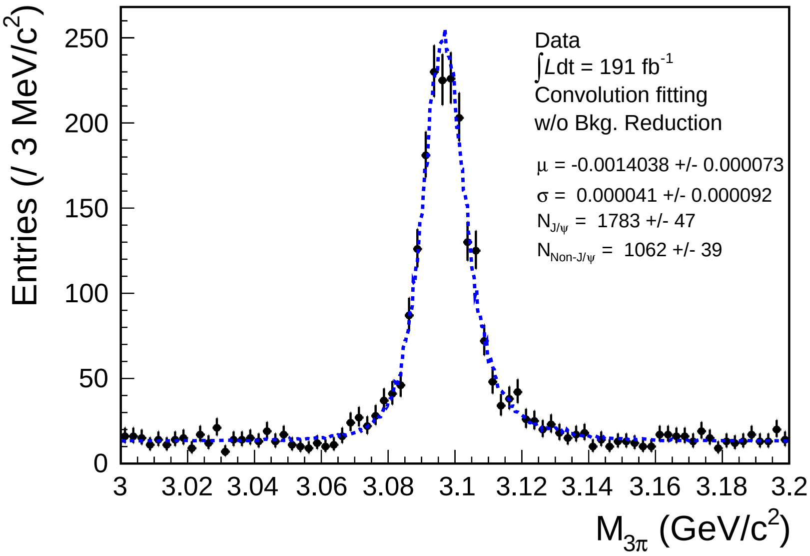

(a) w/o bkg. suppression selections

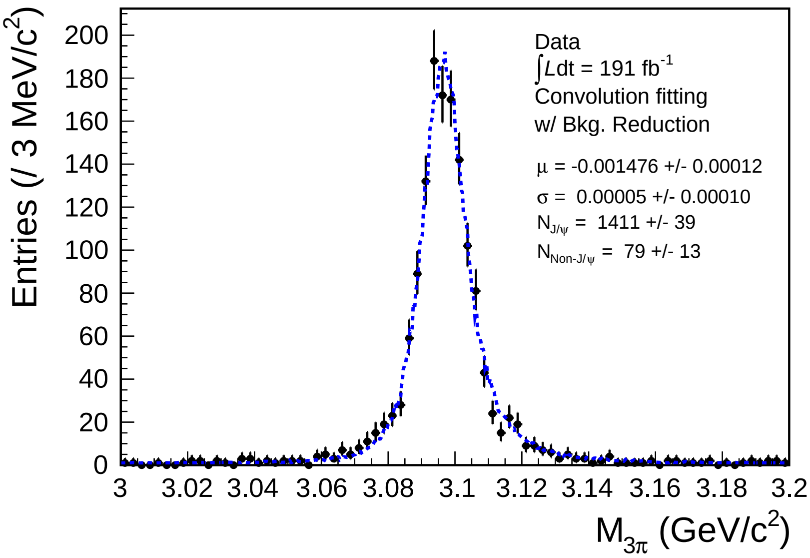

(b) w/ bkg. suppression selections

Figure 6.16: J/ψ spectrum and fit result with and without the background suppression.

Chapter 7

Unfolding

The distribution of 3π invariant mass in the signal process $e^+e^- \to \pi^+\pi^-\pi^0\gamma$ follows Eq. (2.46); we call this "generated" spectrum in this chapter. The finite resolution of the detector distorts the distribution of 3π invariant mass measured by the detector; we call this "measured" mass. The detector resolution in this measurement is derived from the tracking accuracy of the charged pions and the position and energy accuracy of the photon clusters. The finite resolution has to be mitigated to obtain the generated spectrum, especially in a case where the detector resolution is similar to or larger than the width of resonances in the spectrum. The correction procedure to mitigate the effect of detector resolution is called *unfolding*.

Considering the formulation of unfolding, a relation of measured mass in data x to generated mass y can be defined as a smooth function $f(x|y)$, called *resolution function*. In a case where the data is binned with the measured mass, as in this analysis, the spectrum can be expressed as a vector of yields in the mass bins $\vec{x}$ for the measured spectrum and $\vec{y}$ for generated spectrum. If the mass resolution is good enough for the bin width, then generated events in the i-th mass bin are measured directly in the i-th mass bin, i.e., $x_i \sim y_i$. However, if not, the number of generated events in the j-th bin could be transferred to other mass bins in the measured mass spectrum following the resolution function. The resolution function is discretized through the binning and is denoted by A_{ij}, which is called *transfer matrix*. Each element of A_{ij} indicates the amount of transition from the j-th bin of generated spectrum to the i-th bin of measured spectrum; the diagonal element denotes scenarios where the observed value is near the generated value. No transition between bins occurs, and the off-diagonal element indicates the transition of events. The integration across one generated spectrum bin yields a value of one by definition $\sum_j A_{ij} = 1$. The transfer occurs in all bins of the generated spectrum, and the number of measured events in the i-th bin x_i can be expressed as

$$x_i = \sum_j A_{ij} y_j + b_i, \tag{7.1}$$

where $\vec{b}$ is the measured spectrum of background events.

If a detector simulation is well-calibrated to reproduce detector response, A_{ij} can be calculated using the simulation. To estimate the generated spectrum from observed data, a straight way is finding the inverse matrix A^{-1} and solving $\vec{y} = A^{-1}(\vec{x} - \vec{b})$. However, this method usually leads to an "ill-posed matrix problem", where small statistical fluctuations in the signal and background events significantly affect the estimated $\vec{y}$. Several unfolding methods have been proposed to address this issue, starting with the Tikhonov regularization method, including the widely used singular value decomposition, which depends on the spectrum and response function to be solved. In this analysis, unfolding is performed using the iterative-dynamically-stabilized (IDS) method [120], specifically designed for such high-energy experiments.

The possible difference in the transfer matrix between data and simulation is corrected with the Gaussian convolution. The transfer matrix A_{ij} is obtained based on a simulated MC sample ten times larger than the data sample, shown in Fig. 7.1. The components far from diagonal come from mis-reconstructed events, including fake π^0 and muon track decayed from pion. The spectrum generated by Phokhara and the detector simulation can produce the measured spectrum. However, the possible difference of detector response is corrected by a convolution fitting to the ω, ϕ and J/ψ resonances,

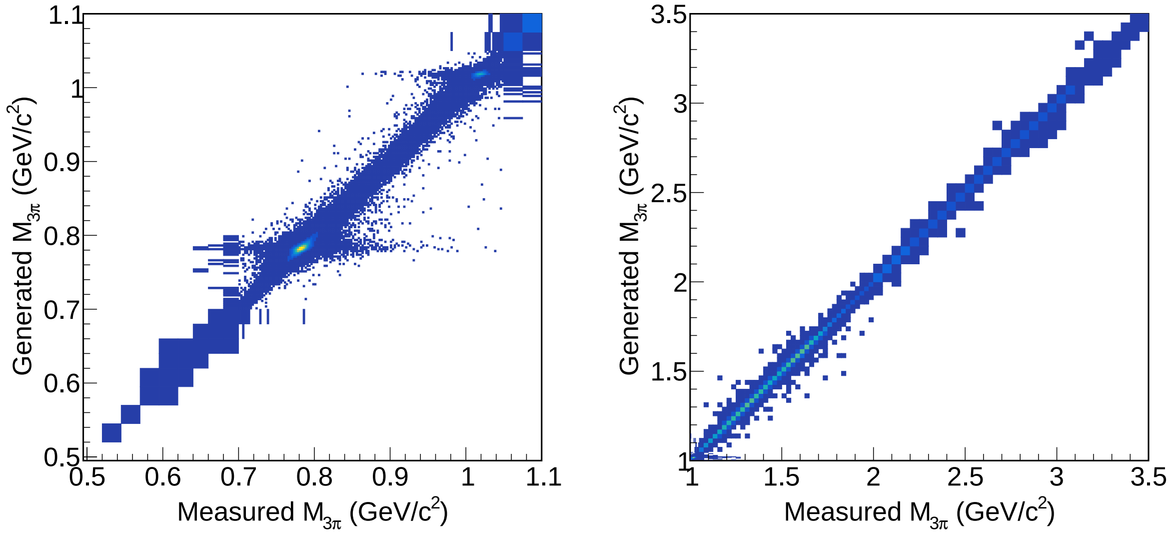

(a) 0.5–1.1 GeV/c^2 (b) 1.0–3.5 GeV/c^2

Figure 7.1: Transfer matrix of MC signal events. The horizontal axis indicates measured $M_{3\pi}$ applied the 5C-KFit, and the vertical axis indicates generated $M_{3\pi}$. The two plots show the different mass regions.

whose parameters are measured more precisely than the target of this analysis. The convoluted Gaussian function gives the correction factor by the μ and σ parameters. The obtained spectrum is modified as

$$x_i = \sum_j A_{ij} \left[\vec{y} * G\right]_j + b_i, \tag{7.2}$$

where, x_i is the measured number of event at the i-th bin, y is the vector of generated $M_{3\pi}$ spectrum, A_{ij} is the response function produced by MC simulation, G is the Gaussian and the operator $*$ represents the convolution.

In this chapter, the detector resolution is studied by a simulation (Section 7.1), the data-MC correction for transfer matrix (Section 7.2), and the unfolding results (Section 7.3) are described.

7.1 Mass resolution on detector simulation

The invariant mass of $M_{3\pi}$ in the measured spectrum is calculated from the four-momentum of final stats as a result of five-constraint kinematic fitting (5C-KFit) to relieve mass shift and smearing. In the 5C-KFit, the summed four-momentum of $\pi^+\pi^-\pi^0\gamma$ system is constrained to the e^+e^- beam four-momentum and the invariant mass of the photon pair is constrained to the nominal π^0 mass. Figure 7.2 shows the $M_{3\pi}$ distributions of $\pi^+\pi^-\pi^0\gamma$ MC sample. The red histogram shows the generated spectrum, the blue histogram shows the measured spectrum after 5C-KFit, and the dotted histogram shows the measured spectrum without 5C-KFit. We can see significant smearing effects on the ω and ϕ resonance. On the other hand, in the high mass region, the distribution discrepancy is small since the resonance width is larger than the detector resolution. The spectra in the figure also indicate an improvement in resolution due to the 5C-KFit. A $\pi^+\pi^-\pi^0$ mass resolution $\Delta M_{3\pi}$, $M_{3\pi}$ difference between generated and measured value, at the ω resonance is shown in Fig .7.3. The mass shift of the 5C-KFit spectrum is $-0.25\,\mathrm{MeV}/c^2$, which corresponds to a tenth of the narrowest bin width, and the standard deviation of $\Delta mpppz$ is $6.5\,\mathrm{MeV}/c^2$. Note that its full width at half maximum (FWHM) of mass resolution is $9.9\,\mathrm{MeV}/c^2$, which is competitive to the precursor measurement *BABAR*, $13\,\mathrm{MeV}/c^2$ [60]. The $M_{3\pi}$ dependence of the resolution is shown in Fig. 7.4. The width becomes worse depending on $M_{3\pi}$ increase. The kinematic fitting also suppresses the center value shift.

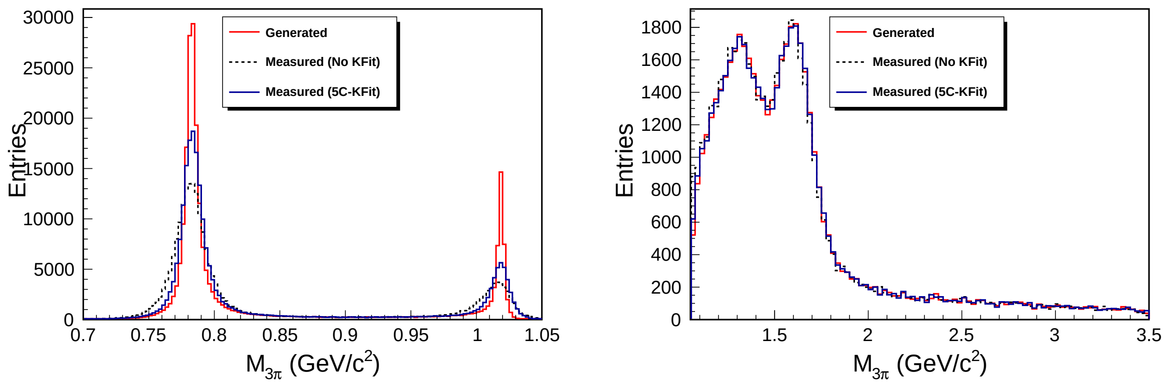

(a) $M_{3\pi} < 1.05\,\mathrm{GeV}/c^2$ (b) $1.05 < M_{3\pi} < 3.5\,\mathrm{GeV}/c^2$

Figure 7.2: $M_{3\pi}$ distribution of $\pi^+\pi^-\pi^0\gamma$ MC. The lines show the generated spectrum (solid red), measured spectrum using the 5C-KFit (solid blue), and measured spectrum without KFit (dashed black). The two plots show the different mass regions below and above $1.05\,\mathrm{GeV}/c^2$. The J/ψ resonance around $3.01\,\mathrm{GeV}/c^2$ is not simulated in the $\pi^+\pi^-\pi^0\gamma$ MC sample generated by PHOKHARA.

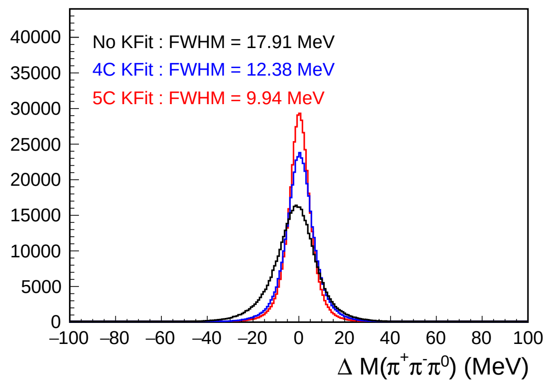

Figure 7.3: $M_{3\pi}$ difference between measured value and generated value. The lines show the resolution with no KFit (black), 4C-KFit (blue) and 5C-KFit (red), respectively.

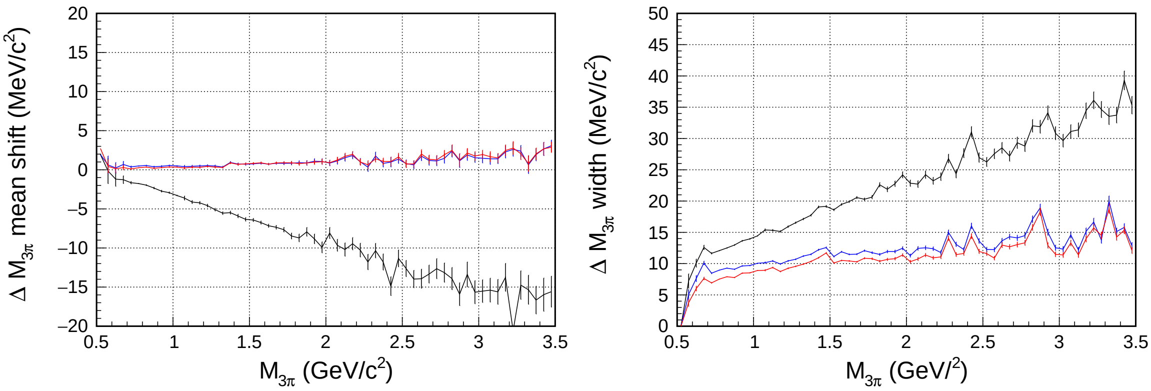

(a) Mean (b) Width

Figure 7.4: Mean and standard deviation of $\Delta M_{3\pi}$ in a function of $M_{3\pi}$. The error bars and lines show no-KFit (black), 4C-KFit (blue) and 5C-KFit (red) values.

7.2 Data-MC correction of mass resolution

The spectrum for the ω and ϕ resonances is obtained by $M_{\gamma\gamma}$ fits described in section 4.5. The generated spectrum in the MC sample and MC transfer matrix is obtained from the $\pi^+\pi^-\pi^0\gamma$ MC sample. The shape of the ω and ϕ resonance are, therefore, rely on the PHOKHARA generator. The parameters of the convoluted Gaussian, μ and σ, are floated. The μ and σ provide a possible shift of the center and the resolution (width) between data and simulation, respectively. Figure 7.5 shows the result of fitting to the data. The obtained parameters are $\mu = -0.463 \pm 0.062\,\mathrm{MeV}/c^2$ and $\sigma = 1.090 \pm 0.15\,\mathrm{MeV}/c^2$ for the ω, $\mu = -0.778 \pm 0.014\,\mathrm{MeV}/c^2$ and $\sigma = 0.020 \pm 0.0001\,\mathrm{MeV}/c^2$ for the ϕ. The results of varying both parameters by $+1\sigma$ are also shown.

Near the J/ψ resonance, $3.0 < M_{3\pi} < 3.2\,\mathrm{GeV}/c^2$, we can also confirm the mass bias and resolution As the width of J/ψ resonance is $\Gamma_{J/\psi} = (92.6 \pm 1.7)\ kevcc$ [37] and the detector resolution dominates the shape in the measured spectrum, it is a good clue to the comparison of mass resolution and mass scale between data and simulation. The J/ψ signal shape is modeled as the relativistic Breit-Wigner with the fixed J/ψ mass and decay width, and the non-resonant component is modeled as a linear function. The function is convoluted with the simulated transfer matrix and the Gaussian as Eq. (7.2). Figure 7.6 shows the result of fitting to the data. The parameters of convolution Gaussian are $\mu = -1.38 \pm 0.08\,\mathrm{MeV}/c^2$, and the resolution is $0.02 \pm 0.093\,\mathrm{MeV}/c^2$.

To conclude, in the lower mass regions around the ω resonance, there is likely to be Gaussian convolution of about $1\,\mathrm{MeV}/c^2$ in addition to the mass resolution of 6.5 MeV/c^2 obtained by simulation alone, then the corrected mass resolution is 6.6 MeV/c^2. In higher mass regions, the mass resolution in data agrees with the simulation. Also, for the mass bias, a mass-dependent difference from $-0.6\,\mathrm{MeV}/c^2$ to $-1.4\,\mathrm{MeV}/c^2$ is visible between data and simulation.

For intermediate regions between the resonances, e.g. 0.85–0.95 GeV/c^2 and 1.1–3.0 GeV/c^2, which are outside the fit range, the parameters obtained in the neighborhood resonance are to be used. For each mass region, The parameters of the ω fit are used for 0.50–0.90 GeV/c^2, the parameters of the ϕ fit are used for 0.9–2.0 GeV/c^2, and the parameters of the J/ψ fit are used for 2–3.5 GeV/c^2. In the intermediate regions, as the spectrum is smooth relative to the detector response, differences in resolution do not have a significant effect. They are confirmed to be sufficiently small compared to the statistical error.

7.3 Results of unfolding

The background spectrum estimated in section 4.5 is subtracted in measured $M_{3\pi}$ spectrum obtained in section 4.5 to obtain the background-subtracted spectrum. The background-subtracted spectrum is unfolded using the IDS method, implemented on an unfolding framework toolkit program ROOUN-

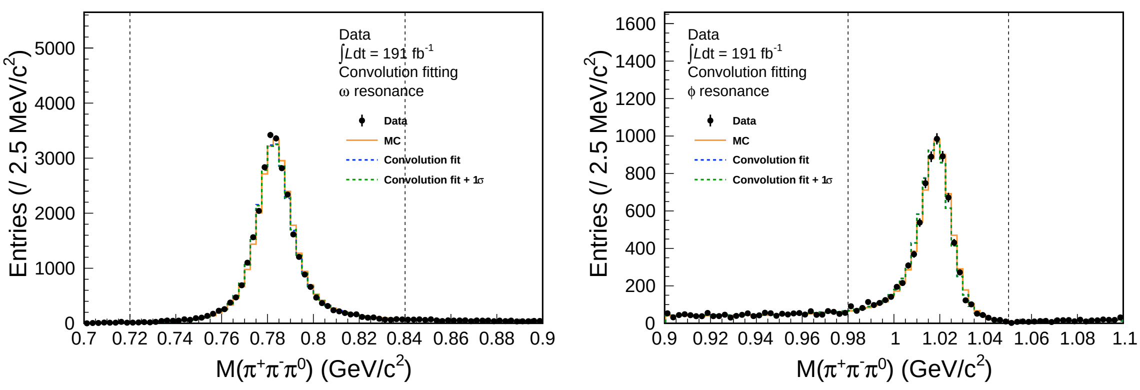

(a) (b)

Figure 7.5: Result of convolution fitting to (a) the ω resonance and (b) the ϕ resonance. The points with error bars show the data. The solid line shows the MC spectrum. The dashed line shows fit results convoluted with the Gaussian (blue), and results varied with a standard deviation $+1\sigma$ (green). The vertical lines indicate fit ranges.

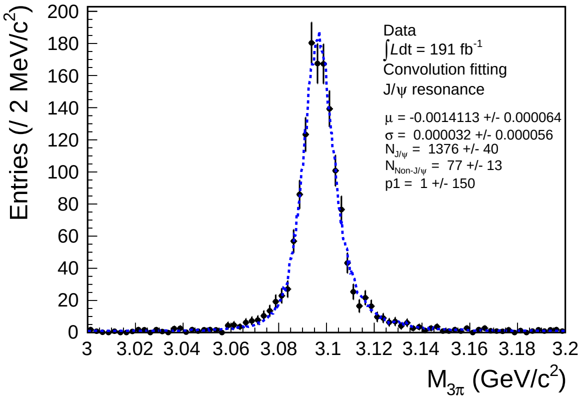

Figure 7.6: Fitting to the J/ψ resonance using the data. The points with error bars show the data. The dashed line shows fit results convoluted with the Gaussian.

FOLD2.0.0 [121]. We have checked that other unfolding algorithms, such as the singular value decomposition, provide results similar to those discussed here.

The result of unfolding is shown in Fig. 7.7. The solid histogram shows the background-subtracted spectrum before the unfolding, and the dotted histogram with error bars shows the unfolded spectrum. For the mass range of 3.0-3.2 GeV/c^2, the background-subtracted spectrum is replaced by the non-resonant component obtained by the fit with the J/ψ resonance before unfolding. This is because a narrow resonance such as J/ψ is accounted for exclusively in a_μ calculations [30] and follows convention. In the range of 0.62–3.5 GeV/c^2, the total number of events before and after unfolding is 47995.6 ± 220.2 and 47995.3 ± 243.3 , confirming that they are preserved.

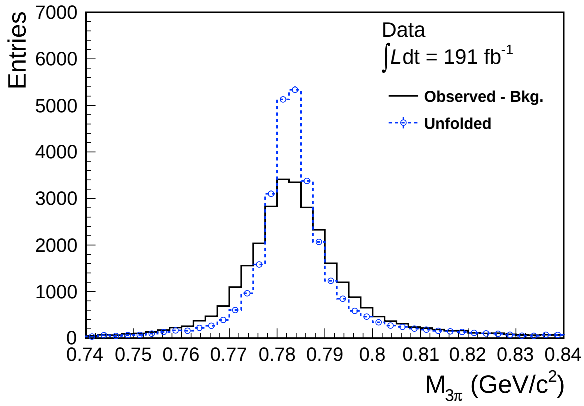

(a) 0.74–0.84 GeV/c^2

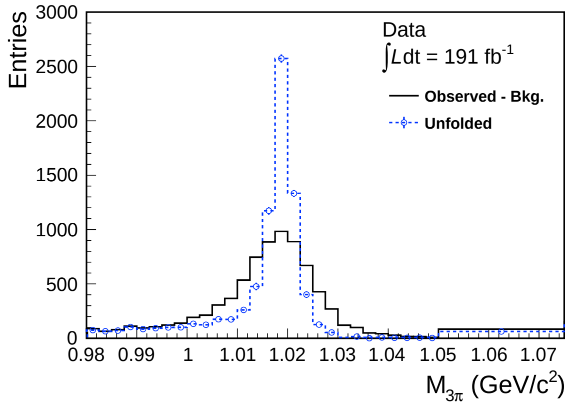

(b) 0.98–1.08 GeV/c^2

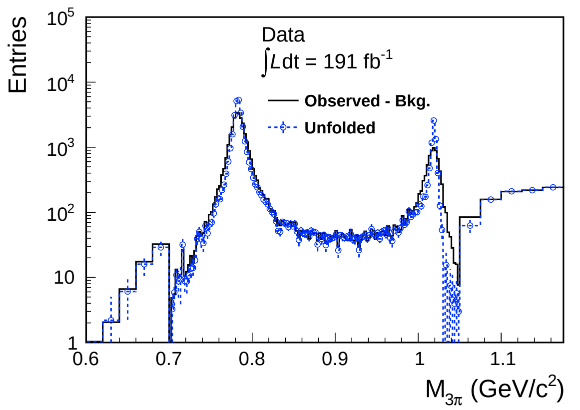

(c) 0.60–1.2 GeV/c^2

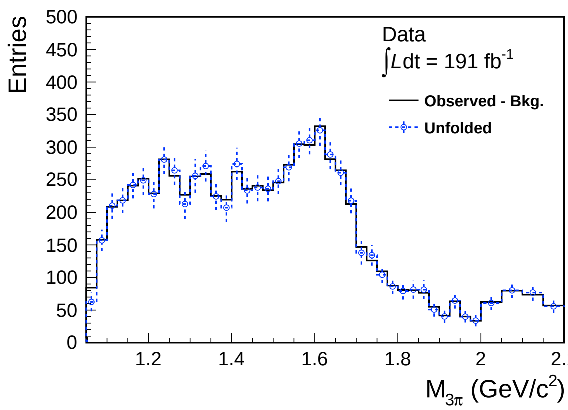

(d) 1.05–2.0 GeV/c^2

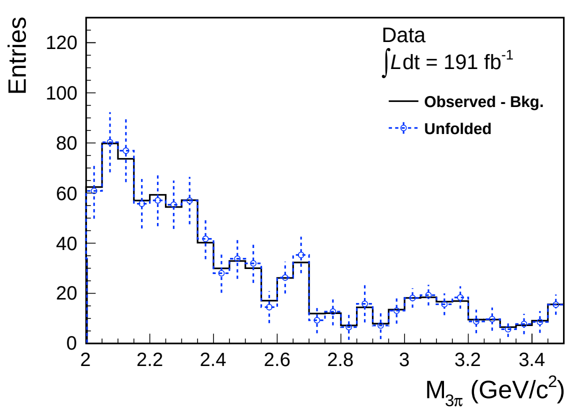

(e) 2.0-3.5 GeV/c^2

Figure 7.7: $M_{3\pi}$ spectra before and after applying the unfolding. The solid histogram shows the background-subtracted spectrum, and the dotted histogram with error bars shows the unfolded spectrum. The uncertainty on the unfolded spectrum is the diagonal square root of the diagonal element of the statistical covariance matrix.

Chapter 8

Result and discussion

This chapter describes the result of the $e^+e^- \to \pi^+\pi^-\pi^0$ cross section measurement and discussion using the spectrum. The result $e^+e^- \to \pi^+\pi^-\pi^0$ cross section measured using real data based on the values studied so far is reported in section 8.1. In section 8.2, the 3π contribution to $g-2$ calculated from the obtained cross section is discussed. Comparison of various parameters obtained from the measured cross section is useful as a cross check of the cross section. In section 8.3, the contribution to the running coupling constant is estimated similarly to a_μ. In section 8.4, light vector meson parameters are evaluated and discussed based on the spectrum.

It should be mentioned here that the obtained cross section, and a_μ contributions described in sections 8.1 and 8.2 are results of a review process within the experimental collaborators and will be published as an article. The sections 8.3 and 8.4, on the other hand, are PRELIMINARY discussions that have not undergone the same level of review.

8.1 Measurement of the $e^+e^- \to \pi^+\pi^-\pi^0$ cross section

The total *dressed* cross section can be obtained from Eq. (2.46) as

$$\sigma_{e^+e^-\to 3\pi}(m) = \frac{\left(\frac{dN_{\text{sig}}}{dm}\right)_{\text{unfolded}}}{\varepsilon \cdot \frac{dL_{\text{eff.}}}{dm} \cdot R_{\text{rad}}}.$$

The dressed cross section is defined as a cross section that removes the ISR (LO and NLO) effects from the measured one, including both FSR and VP contribution.

The unfolded signal spectrum $(dN_{\text{sig}}/dm)_{\text{unfolded}}$ is obtained by applying the unfolding to the event spectrum of the signal sample after the background subtraction, as discussed in chapter 7. ε is the corrected signal efficiency discussed in chapter 6. When the ISR polar angle in the center-of-mass frame is restricted within $\theta_{\min} < \theta_\gamma < \pi - \theta_{\min}$, the effective luminosity dL_{eff}/dm is given by Eqs. (2.41) and (2.47) as

$$\frac{dL_{\text{eff}}}{dm}(m) = \frac{2m}{s}\frac{\alpha}{\pi}\left(\frac{s^2+m^2}{s(s-m)}\ln\left(\frac{1+\cos\theta_\gamma}{1-\cos\theta_\gamma}\right) - \frac{s-m}{s}\cos\theta_\gamma\right)L_{\text{int}}. \tag{8.1}$$

where, L_{int} is the integrated luminosity, α is the fine-structure constant, s is squared center-of-mass energy $10.58^2\,\text{GeV}^2$, m_e is electron mass. We use this with $\theta_{\min} = 20°$ for calculation, which is sufficiently broad compared to the detector acceptance, and the MC efficiency is calculated based on the configuration.

The radiative correction $R_{\text{rad}}$is applied to take into account multiple ISR photons and obtain the cross section because Eq. (2.41) stands for effective luminosity with a single ISR. It is calculated by Monte Carlo simulation using the Phokhara generator. We generate events with NLO and LO ISR mode of $\mu^+\mu^-\gamma$ final state, turning on VP effects, and take the ratio of the cross section for each mass region of the hadronic system (in this case, the invariant mass of a muon-pair). This is because the radiative correction of ISR does not depend on the final state other than ISR. FSR simulation is turned off, and the invariant mass of muon-pair and tagged ISR must be more than $8\,\text{GeV}/c^2$. The ISR polar angle in the e^+e^- c.m. system is restricted in $20° < \theta_\gamma < 160°$. The ratio is 1.00795 ± 0.00068 for $0.62 < M_{\mu^+\mu^-} < 1.05\,\text{GeV}/c^2$, 1.00781 ± 0.00065 for $1.05 < M_{\mu^+\mu^-} < 2\,\text{GeV}/c^2$, and 1.01254 ± 0.00070

for $2.0 < M_{\mu^+\mu^-} < 3.5\,\text{GeV}/c^2$. The uncertainty from the PHOKHARA generator is estimated at 0.5% [89], which is assigned to systematic uncertainty.

The obtained dressed cross sections are listed in Tables 8.2 and 8.3. For a mass range of 3.0–3.2 GeV/c^2, the spectrum is replaced by the non-resonant component obtained by the J/ψ resonance fitted before the unfolding. A comparison with previous measurements is shown in Fig. 8.1,

8.1.1 Systematic uncertainty on the cross section measurement

The systematic uncertainty is summarized in Table 8.1. The systematic errors for the correction factor and radiative correction are evaluated in the three mass regions: 0.62–1.05 GeV/c^2, 1.05–2.0 GeV/c^2 and 2.0–3.5 GeV/c^2. The systematic errors for the background subtraction and unfolding are evaluated for each $M_{3\pi}$ bin. The systematic error in the vicinity of the large cross-section, the ω and ϕ resonances is around 1.9%.

MC efficiency

The MC statistics are described in section 6.1. The covariance matrix of the efficiency obtained by 3rd polynomial fitting to the MC simulation is used to evaluate the error at representative points in each mass region. This is the statistical error derived from the $e^+e^- \to \pi^+\pi^-\pi^0\gamma$ MC statistics of 2000 fb^{-1}, used in the evaluation.

Trigger

The systemic uncertainty in the efficiency correction for trigger efficiency is discussed in section 6.2. The main source is 0.08% (0.10% above 2.0 GeV/c^2) derived from the statistics of the $\mu^+\mu^-\gamma$ control sample used to evaluate the efficiency of *hie* and *lml1*. The systematic error for HLT filtering is less than 0.01%.

ISR photon detection

This is a systemic uncertainty in the efficiency correction for ISR photon discussed in section 6.4. The uncertainty has a systematic error of 0.67% with little dependence on 3π mass. This evaluation is described in detail in this Ref. [122], which studies photon detection efficiency using $e^+e^- \to \mu^+\mu^-\gamma$ events. The major source is due to the isolation selection of photons and the higher beam background in the later experiments period.

Tracking

The uncertainty of 0.80–0.83% is a systemic uncertainty in the efficiency correction for charged pion tracking discussed in section 6.3. This derives from the four studies of basic tracking efficiency, nCDCHits selection, track loss, and duplicated track. It is dominated by the efficiency evaluation study of single-pion tracks using the tag-and-probe method with tau-pair events and track loss on tracks with small opening angles. In the tag-and-probe method, visible charge asymmetry leads to a systematic uncertainty of 0.30% For track loss, the uncertainty of 0.53% is derived from a statistical error of the number of $e^+e^- \to \pi^+\pi^-\pi^0\gamma$ events in the ω and ϕ regions.

π^0 detection

The uncertainty of 1.02% is a systemic uncertainty in the efficiency correction for π^0 efficiency discussed in section 6.5. This systematic uncertainty is the largest uncertainty in the efficiency correction in the low mass region $< 1.1\,\text{GeV}/c^2$. It derives from the statistical error of $e^+e^- \to \omega\gamma\pi^+\pi^-\pi^0\gamma$ sample (0.44%), fitting error (0.38%), and systematic error as discussed in detail in appendix A (0.83%).

Selection efficiency of 4C-KFit χ^2_{4C}

The uncertainty of 0.6% ($M_{3\pi} < 1.05\,\text{GeV}/c^2$) and 0.3% ($M_{3\pi} > 1.05\,\text{GeV}/c^2$) is a systemic uncertainty in the efficiency correction for the selection by 4C-KFit discussed in section 6.6. This is a correction of the efficiency due to ISR and tracking in the selection $\chi^2_{4\text{C},2\pi3\gamma} < 50$ for the 4C-KFit. The maximum difference in efficiency ratios between data and MC in the $20 < \chi^2_{4\text{C},2\mu\gamma} < 50$ range estimated using $e^+e^- \to \mu^+\mu^-\gamma$

events is checked by dividing the momentum of muon into three ranges and is accounted for as systematic error.

Background suppression selection

The uncertainty of 0.20% (1.85% for $M_{3\pi}$ above $1.05\,\mathrm{GeV}/c^2$) is a systemic uncertainty in the efficiency correction for the background suppression selection discussed in section 6.7. To assess the efficiency of the background suppression selection, an estimate is made from the $e^+e^- \to \pi^+\pi^-\pi^0\gamma$ signal events in the ω, ϕ and J/ψ resonances with and without the selection. The statistical errors of $e^+e^- \to \pi^+\pi^-\pi^0\gamma$ are accounted for as systematic errors. Especially above $1.05\,\mathrm{GeV}/c^2$, the values evaluated using the J/ψ resonance are used, and the systematic uncertainty of 1.85% are the dominant systematic uncertainty in this mass range.

Generator

The simulation of higher-order ISR processes, two ISR and three ISR processes, may be incomplete in PHOKHARA. We estimate the magnitude of the change in signal efficiency due to possible miscalculation to be 0.7% and 0.95% uncertainties, respectively. A total of 1.2% is accounted for as the systematic error associated with the generator. Detailed study and calculation are described in App. B.

Integrated luminosity

The uncertainty for the integrated luminosity is 0.7%. The value is obtained from the offline measurement using Bhabha and $\gamma\gamma$ events [87]. In addition, a drift of beam energy during the data taking has been observed up to $6\,\mathrm{MeV}$ [123]. The effective luminosity change due to this drift is 0.11% at the ω resonance and 0.14% at the J/ψ resonance, which is accounted for a systematic uncertainty for the luminosity.

Radiative correction

The radiative correction associated with the NLO ISR effects is assessed using the PHOKHARA generator. The systematic uncertainty for the NLO ISR simulation in PHOKHARA is 0.5% [89].

Background subtraction

In chapter 5, we discussed how the MC prediction of the background contributions is checked using the unique control samples. The statistics and systematics of the control sample determine the uncertainty for the background subtraction. The systematic uncertainty is 0.3% at the ω and ϕ resonance, and is 0.5–1.0% for the range 1.1–1.8 GeV/c^2.

Unfolding

Several checks on the uncertainty for the unfolding have been carried out. We checked the dependence of four regularization parameters in the IDS unfolding method by varying them from the optimum values and observed no significant variation. In addition, a toy MC study with more than ten times more statistics checked the possible bias in the unfolding procedure. A generated toy spectrum is made by fluctuating each bin of the MC spectrum with statistical uncertainty, and the transfer matrix is used to produce a measured toy. The differences between the unfolded and generated toy spectrum are assigned as a systematic error: about 0.3% near the ω and ϕ resonances, and 0.9–4% above $1.05\,\mathrm{GeV}/c^2$. In the mass range below $0.7\,\mathrm{GeV}/c^2$, the systematic error is more than 10% and is tmain source of systematic error.

Table 8.1: The summary table of systematic uncertainty on the cross section.

Source of uncertainty	Uncertainty (%) < 1.05 GeV	1.05–2.00 GeV	2.0–3.5 GeV	Comments
MC efficiency	**0.14**	**0.27**	**0.57**	
MC statistics	0.14	0.27	0.57	Section 6.1
Trigger	**0.08**	**0.08**	**0.10**	
hie and lml1	0.08	0.08	0.10	Section 6.2
HLT filtering	0.00	←	←	
ISR photon detection	**0.67**	**0.67**	**0.67**	
Photon detection	0.67	0.67	0.67	$e^+e^- \to \mu^+\mu^-\gamma$ Section 6.4
Tracking	**0.80**	**0.83**	**0.83**	
Tracking efficiency	0.60	←	←	τ tag-and-probe Ref. [124]
Track loss (stat)	0.53	←	←	Section 6.3
CDC NHits (stat)	0.06	0.21	←	Section 6.3
Duplicated track (stat.)	0.01	←	←	Section 6.3
$\boldsymbol{\pi^0}$	**1.02**	**1.02**	**1.02**	
Statistics and fitting	0.58	←	←	Section 6.5
Full reco : $\pi^+\pi^-\pi^0\pi^0\gamma$ background	0.13	←	←	Appendix A
Full reco : $\phi \to K^0_S K^0_L \gamma$ background	0.33	←	←	Appendix A
Full reco : $q\bar{q}$ background	0.06	←	←	Appendix A
Full reco : Background model	0.07	←	←	Appendix A
Full reco : ω signal model	0.09	←	←	Appendix A
Full reco : Event selection	0.57	←	←	Appendix A
Part reco : Counting method	0.12	←	←	Appendix A
Part reco : π^0 signal method	0.46	←	←	Appendix A
Part reco : $\pi^+\pi^-\pi^0\pi^0\gamma$ background	0.07	←	←	Appendix A
$\boldsymbol{\chi^2}$	**0.60**	**0.30**	**0.30**	
$\mu^+\mu^-\gamma\ \chi^2$	0.60	0.30	←	Section 6.6
Selection	**0.20**	**1.85**	**1.85**	
Background suppression cut	0.20	1.85	←	Section 6.7
Generator	**1.18**	**1.18**	**1.18**	
PHOKHARA NLO excess	0.70	←	←	Section 8.1
PHOKHARA NNLO	0.95	←	←	Section 8.1
Luminosity	**0.64**	**0.64**	**0.64**	
Integrated luminosity	0.63	←	←	Bhabha Ref. [87]
Beam energy variation	0.11	←	←	Section 8.1
Radiative corrections	**0.50**	**0.50**	**0.50**	
PHOKHARA	0.50	←	←	Section 8.1
Background subtraction	**0.3–0.5**	**0.2–6.8**	**3.3–34**	
Unfolding	**0.7–15**	**0.2–5.1**	**0.3–11**	
Total systematics	**2.2–15**	**2.9–8.2**	**5.7–34**	

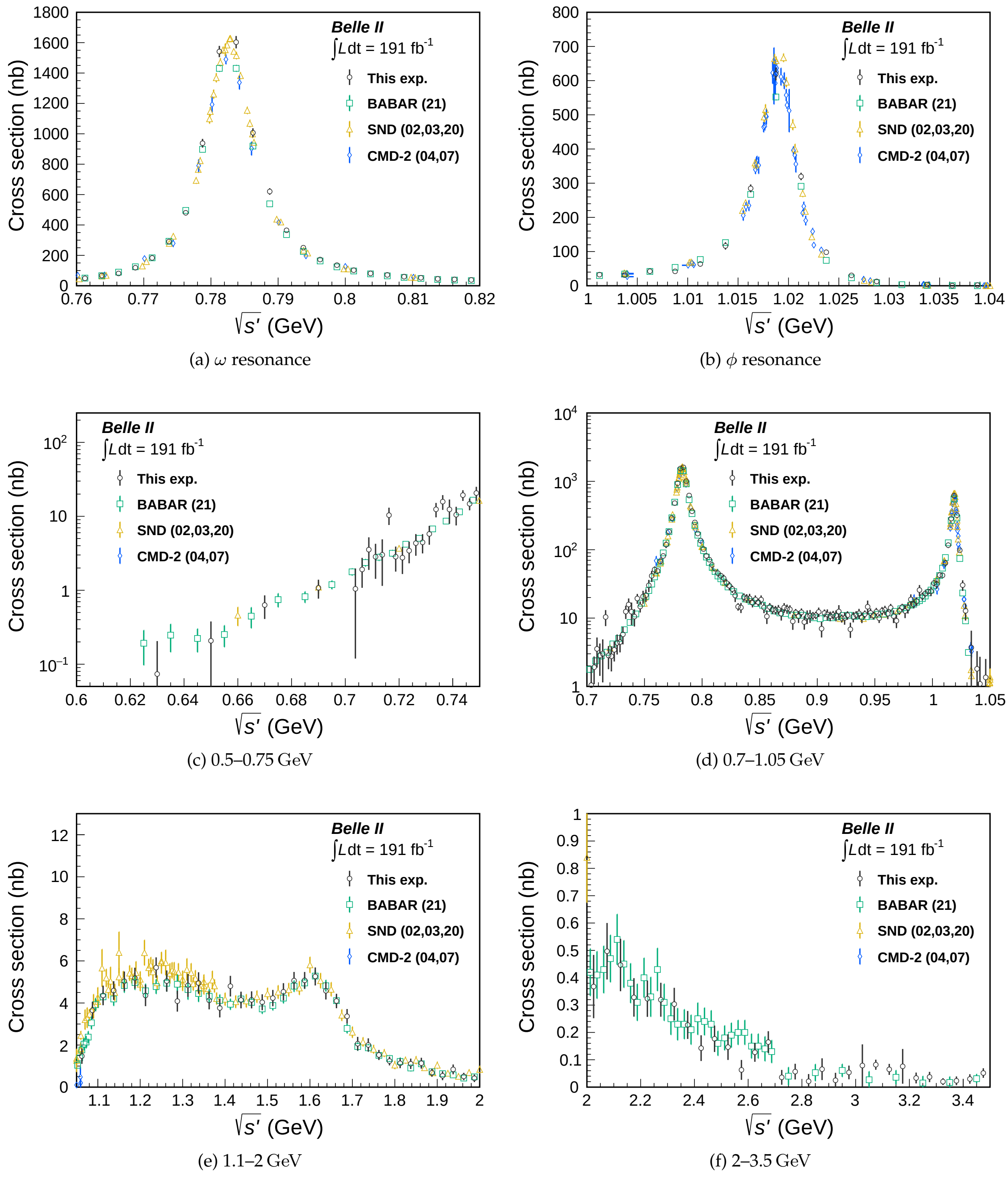

(a) ω resonance

(b) ϕ resonance

(c) 0.5–0.75 GeV

(d) 0.7–1.05 GeV

(e) 1.1–2 GeV

(f) 2–3.5 GeV

Figure 8.1: The dressed cross section of the $e^+e^- \to \pi^+\pi^-\pi^0$ process. The open circles with error bars show the result of this study. The box points (orange) show the result of *BABAR* (2021) [60], the triangle points (violet) show the result of BESIII (2019) [61], the circle points (pink) show the result of SND (2002,2003,2020) [52, 53, 125], and the diamond points (green) show the result of CMD-2 (2004,2007) [57, 58].

Table 8.2: Summary of hadronic energy ($\sqrt{s'}$), the number of events after unfolding (N_{unf}), the efficiency (ε), and the cross section ($\sigma_{3\pi}$) of $e^+e^- \to \pi^+\pi^-\pi^0$ in an energy range of 0.62–1.05 GeV. The uncertainties on the cross section are the statistical errors and systematic errors, respectively. The statistical uncertainties for the unfolding and the cross section are square roots of the diagonal components of the unfolding covariance matrix.

$\sqrt{s'}$ (GeV)	N_{unf}	ε (%)	σ (nb)	$\sqrt{s'}$ (GeV)	N_{unf}	ε (%)	σ (nb)
0.6200–0.6400	2 ± 3	9.16 ± 0.15	$0.07 \pm 0.13 \pm 0.02$	0.8700–0.8725	52 ± 8	8.18 ± 0.13	$14.26 \pm 2.12 \pm 0.89$
0.6400–0.6600	5 ± 4	9.16 ± 0.15	$0.21 \pm 0.17 \pm 0.02$	0.8725–0.8750	50 ± 7	8.18 ± 0.13	$13.65 \pm 1.81 \pm 1.07$
0.6600–0.6800	16 ± 5	9.16 ± 0.15	$0.63 \pm 0.22 \pm 0.03$	0.8750–0.8775	49 ± 6	8.17 ± 0.13	$13.40 \pm 1.64 \pm 1.11$
0.6800–0.7000	28 ± 8	9.16 ± 0.15	$1.08 \pm 0.31 \pm 0.05$	0.8775–0.8800	33 ± 7	8.17 ± 0.13	$8.95 \pm 1.92 \pm 1.12$
0.7000–0.7025	-2 ± 2	8.52 ± 0.14	$-2.06 \pm 1.82 \pm 1.82$	0.8800–0.8825	44 ± 5	8.16 ± 0.13	$12.06 \pm 1.38 \pm 0.62$
0.7025–0.7050	3 ± 2	8.51 ± 0.14	$1.04 \pm 0.77 \pm 0.52$	0.8825–0.8850	39 ± 7	8.16 ± 0.13	$10.57 \pm 1.97 \pm 0.70$
0.7050–0.7075	6 ± 2	8.51 ± 0.14	$1.91 \pm 0.75 \pm 0.36$	0.8850–0.8875	45 ± 6	8.15 ± 0.13	$12.14 \pm 1.56 \pm 0.66$
0.7075–0.7100	11 ± 4	8.50 ± 0.14	$3.54 \pm 1.40 \pm 0.89$	0.8875–0.8900	32 ± 7	8.15 ± 0.13	$8.74 \pm 1.88 \pm 0.63$
0.7100–0.7125	9 ± 4	8.50 ± 0.14	$2.84 \pm 1.30 \pm 0.55$	0.8900–0.8925	39 ± 8	8.14 ± 0.13	$10.55 \pm 2.08 \pm 1.19$
0.7125–0.7150	9 ± 6	8.49 ± 0.14	$3.01 \pm 1.80 \pm 0.51$	0.8925–0.8950	40 ± 6	8.14 ± 0.13	$10.82 \pm 1.64 \pm 1.62$
0.7150–0.7175	32 ± 8	8.49 ± 0.14	$10.36 \pm 2.43 \pm 1.24$	0.8950–0.8975	40 ± 5	8.14 ± 0.13	$10.84 \pm 1.31 \pm 0.60$
0.7175–0.7200	9 ± 3	8.48 ± 0.14	$2.84 \pm 0.92 \pm 0.52$	0.8975–0.9000	41 ± 4	8.13 ± 0.13	$11.01 \pm 1.18 \pm 0.69$
0.7200–0.7225	9 ± 3	8.48 ± 0.14	$2.76 \pm 0.98 \pm 0.50$	0.9000–0.9025	46 ± 7	8.13 ± 0.13	$12.30 \pm 1.86 \pm 0.55$
0.7225–0.7250	11 ± 2	8.47 ± 0.14	$3.43 \pm 0.79 \pm 0.78$	0.9025–0.9050	26 ± 7	8.12 ± 0.13	$7.00 \pm 1.74 \pm 0.44$
0.7250–0.7275	14 ± 4	8.46 ± 0.14	$4.34 \pm 1.23 \pm 0.69$	0.9050–0.9075	44 ± 6	8.12 ± 0.13	$11.82 \pm 1.48 \pm 0.34$
0.7275–0.7300	14 ± 3	8.46 ± 0.14	$4.45 \pm 1.09 \pm 0.69$	0.9075–0.9100	42 ± 7	8.11 ± 0.13	$11.28 \pm 1.87 \pm 0.99$
0.7300–0.7325	18 ± 5	8.45 ± 0.14	$5.78 \pm 1.58 \pm 0.49$	0.9100–0.9125	40 ± 5	8.11 ± 0.13	$10.70 \pm 1.35 \pm 1.06$
0.7325–0.7350	39 ± 8	8.45 ± 0.14	$12.43 \pm 2.56 \pm 1.00$	0.9125–0.9150	42 ± 6	8.10 ± 0.13	$11.13 \pm 1.51 \pm 0.46$
0.7350–0.7375	50 ± 9	8.44 ± 0.14	$15.79 \pm 3.00 \pm 1.94$	0.9150–0.9175	41 ± 5	8.10 ± 0.13	$10.94 \pm 1.42 \pm 1.39$
0.7375–0.7400	39 ± 10	8.44 ± 0.14	$12.39 \pm 3.17 \pm 3.17$	0.9175–0.9200	47 ± 10	8.10 ± 0.13	$12.48 \pm 2.70 \pm 1.22$
0.7400–0.7425	33 ± 9	8.43 ± 0.14	$10.50 \pm 2.88 \pm 0.72$	0.9200–0.9225	38 ± 5	8.09 ± 0.13	$9.93 \pm 1.31 \pm 0.28$
0.7425–0.7450	62 ± 9	8.43 ± 0.13	$19.35 \pm 2.93 \pm 1.30$	0.9225–0.9250	38 ± 7	8.09 ± 0.13	$10.06 \pm 1.78 \pm 1.06$
0.7450–0.7475	47 ± 9	8.42 ± 0.13	$14.77 \pm 2.66 \pm 0.47$	0.9250–0.9275	42 ± 5	8.08 ± 0.13	$11.01 \pm 1.35 \pm 0.79$
0.7475–0.7500	66 ± 12	8.42 ± 0.13	$20.64 \pm 3.76 \pm 2.35$	0.9275–0.9300	26 ± 6	8.08 ± 0.13	$6.85 \pm 1.65 \pm 0.49$
0.7500–0.7525	70 ± 10	8.41 ± 0.13	$21.63 \pm 3.17 \pm 3.16$	0.9300–0.9325	40 ± 7	8.07 ± 0.13	$10.45 \pm 1.70 \pm 0.63$
0.7525–0.7550	97 ± 14	8.41 ± 0.13	$30.10 \pm 4.26 \pm 4.31$	0.9325–0.9350	43 ± 5	8.07 ± 0.13	$11.14 \pm 1.32 \pm 0.64$
0.7550–0.7575	134 ± 18	8.40 ± 0.13	$41.39 \pm 5.54 \pm 5.27$	0.9350–0.9375	45 ± 7	8.06 ± 0.13	$11.71 \pm 1.86 \pm 0.54$
0.7575–0.7600	166 ± 17	8.40 ± 0.13	$51.12 \pm 5.14 \pm 2.39$	0.9375–0.9400	39 ± 6	8.06 ± 0.13	$10.16 \pm 1.47 \pm 0.88$
0.7600–0.7625	159 ± 13	8.39 ± 0.13	$48.88 \pm 4.01 \pm 2.13$	0.9400–0.9425	44 ± 5	8.06 ± 0.13	$11.42 \pm 1.39 \pm 0.58$
0.7625–0.7650	220 ± 19	8.39 ± 0.13	$67.36 \pm 5.80 \pm 1.93$	0.9425–0.9450	57 ± 11	8.05 ± 0.13	$14.63 \pm 2.90 \pm 1.75$
0.7650–0.7675	265 ± 17	8.38 ± 0.13	$80.95 \pm 5.17 \pm 2.34$	0.9450–0.9475	46 ± 7	8.05 ± 0.13	$11.89 \pm 1.80 \pm 0.72$
0.7675–0.7700	389 ± 21	8.38 ± 0.13	$118.63 \pm 6.35 \pm 11.43$	0.9475–0.9500	43 ± 5	8.04 ± 0.13	$10.92 \pm 1.40 \pm 0.26$
0.7700–0.7725	603 ± 29	8.37 ± 0.13	$183.30 \pm 8.86 \pm 4.57$	0.9500–0.9525	48 ± 7	8.04 ± 0.13	$12.37 \pm 1.68 \pm 0.34$
0.7725–0.7750	959 ± 36	8.37 ± 0.13	$290.79 \pm 10.98 \pm 7.94$	0.9525–0.9550	39 ± 5	8.03 ± 0.13	$9.97 \pm 1.39 \pm 0.57$
0.7750–0.7775	1588 ± 41	8.36 ± 0.13	$480.21 \pm 12.35 \pm 11.41$	0.9550–0.9575	50 ± 7	8.03 ± 0.13	$12.75 \pm 1.73 \pm 0.31$
0.7775–0.7800	3110 ± 64	8.36 ± 0.13	$938.09 \pm 19.25 \pm 21.37$	0.9575–0.9600	52 ± 8	8.03 ± 0.13	$13.15 \pm 1.93 \pm 0.31$
0.7800–0.7825	5124 ± 43	8.35 ± 0.13	$1541.62 \pm 12.86 \pm 34.87$	0.9600–0.9625	46 ± 6	8.02 ± 0.13	$11.57 \pm 1.63 \pm 1.04$
0.7825–0.7850	5342 ± 63	8.35 ± 0.13	$1603.13 \pm 19.00 \pm 36.07$	0.9625–0.9650	56 ± 8	8.02 ± 0.13	$14.14 \pm 1.95 \pm 0.38$
0.7850–0.7875	3365 ± 63	8.34 ± 0.13	$1007.06 \pm 18.93 \pm 22.62$	0.9650–0.9675	42 ± 8	8.01 ± 0.13	$10.70 \pm 1.99 \pm 1.06$
0.7875–0.7900	2079 ± 50	8.34 ± 0.13	$620.45 \pm 15.02 \pm 15.34$	0.9675–0.9700	36 ± 8	8.01 ± 0.13	$9.13 \pm 1.96 \pm 0.41$
0.7900–0.7925	1226 ± 32	8.33 ± 0.13	$364.90 \pm 9.58 \pm 12.33$	0.9700–0.9725	51 ± 5	8.00 ± 0.13	$12.78 \pm 1.36 \pm 0.88$
0.7925–0.7950	844 ± 24	8.33 ± 0.13	$250.54 \pm 6.98 \pm 6.88$	0.9725–0.9750	58 ± 6	8.00 ± 0.13	$14.48 \pm 1.58 \pm 0.59$
0.7950–0.7975	583 ± 20	8.32 ± 0.13	$172.52 \pm 5.85 \pm 4.25$	0.9750–0.9775	51 ± 8	8.00 ± 0.13	$12.69 \pm 2.03 \pm 1.79$
0.7975–0.8000	459 ± 19	8.32 ± 0.13	$135.69 \pm 5.53 \pm 3.37$	0.9775–0.9800	57 ± 8	7.99 ± 0.13	$14.22 \pm 2.08 \pm 1.56$
0.8000–0.8025	348 ± 24	8.31 ± 0.13	$102.39 \pm 7.11 \pm 4.93$	0.9800–0.9825	75 ± 11	7.99 ± 0.13	$18.72 \pm 2.73 \pm 2.17$
0.8025–0.8050	276 ± 22	8.31 ± 0.13	$81.14 \pm 6.39 \pm 4.39$	0.9825–0.9850	64 ± 7	7.98 ± 0.13	$15.93 \pm 1.79 \pm 1.02$
0.8050–0.8075	244 ± 12	8.30 ± 0.13	$71.49 \pm 3.61 \pm 2.47$	0.9850–0.9875	71 ± 9	7.98 ± 0.13	$17.62 \pm 2.21 \pm 1.15$
0.8075–0.8100	205 ± 17	8.30 ± 0.13	$59.85 \pm 4.96 \pm 1.62$	0.9875–0.9900	104 ± 15	7.98 ± 0.13	$25.73 \pm 3.83 \pm 2.72$
0.8100–0.8125	180 ± 14	8.29 ± 0.13	$52.57 \pm 4.13 \pm 1.62$	0.9900–0.9925	84 ± 10	7.97 ± 0.13	$20.83 \pm 2.37 \pm 1.32$
0.8125–0.8150	156 ± 13	8.29 ± 0.13	$45.31 \pm 3.65 \pm 2.38$	0.9925–0.9950	93 ± 9	7.97 ± 0.13	$22.84 \pm 2.20 \pm 0.68$
0.8150–0.8175	144 ± 10	8.28 ± 0.13	$41.71 \pm 3.04 \pm 1.46$	0.9950–0.9975	99 ± 9	7.96 ± 0.13	$24.47 \pm 2.20 \pm 0.67$
0.8175–0.8200	132 ± 15	8.28 ± 0.13	$38.26 \pm 4.39 \pm 1.94$	0.9975–1.0000	100 ± 11	7.96 ± 0.13	$24.60 \pm 2.65 \pm 2.51$
0.8200–0.8225	113 ± 11	8.28 ± 0.13	$32.49 \pm 3.27 \pm 2.52$	1.0000–1.0025	133 ± 12	7.95 ± 0.13	$32.47 \pm 3.01 \pm 1.42$
0.8225–0.8250	103 ± 12	8.27 ± 0.13	$29.65 \pm 3.57 \pm 2.31$	1.0025–1.0050	128 ± 16	7.95 ± 0.13	$31.20 \pm 4.00 \pm 1.53$
0.8250–0.8275	93 ± 11	8.27 ± 0.13	$26.59 \pm 3.15 \pm 0.88$	1.0050–1.0075	174 ± 14	7.95 ± 0.13	$42.48 \pm 3.33 \pm 2.46$
0.8275–0.8300	75 ± 12	8.26 ± 0.13	$21.42 \pm 3.47 \pm 2.47$	1.0075–1.0100	173 ± 8	7.94 ± 0.13	$42.16 \pm 2.03 \pm 1.58$
0.8300–0.8325	51 ± 6	8.26 ± 0.13	$14.68 \pm 1.66 \pm 0.79$	1.0100–1.0125	262 ± 25	7.94 ± 0.13	$63.75 \pm 5.98 \pm 3.89$
0.8325–0.8350	50 ± 8	8.25 ± 0.13	$14.25 \pm 2.24 \pm 0.89$	1.0125–1.0150	481 ± 35	7.93 ± 0.13	$116.54 \pm 8.42 \pm 6.60$
0.8350–0.8375	71 ± 8	8.25 ± 0.13	$20.24 \pm 2.23 \pm 1.65$	1.0150–1.0175	1177 ± 37	7.93 ± 0.13	$284.82 \pm 8.94 \pm 7.24$
0.8375–0.8400	69 ± 9	8.24 ± 0.13	$19.50 \pm 2.65 \pm 1.09$	1.0175–1.0200	2565 ± 37	7.93 ± 0.13	$619.46 \pm 8.87 \pm 17.02$
0.8400–0.8425	69 ± 8	8.24 ± 0.13	$19.46 \pm 2.29 \pm 2.22$	1.0200–1.0225	1326 ± 34	7.92 ± 0.13	$319.66 \pm 8.30 \pm 7.09$
0.8425–0.8450	59 ± 8	8.23 ± 0.13	$16.73 \pm 2.25 \pm 0.86$	1.0225–1.0250	407 ± 30	7.92 ± 0.13	$97.99 \pm 7.26 \pm 2.16$
0.8450–0.8475	66 ± 9	8.23 ± 0.13	$18.68 \pm 2.57 \pm 1.03$	1.0250–1.0275	126 ± 17	7.91 ± 0.13	$30.34 \pm 4.10 \pm 3.42$
0.8475–0.8500	61 ± 6	8.22 ± 0.13	$17.13 \pm 1.73 \pm 1.30$	1.0275–1.0300	53 ± 15	7.91 ± 0.13	$12.75 \pm 3.48 \pm 0.67$
0.8500–0.8525	66 ± 10	8.22 ± 0.13	$18.58 \pm 2.79 \pm 0.65$	1.0300–1.0325	-3 ± 9	7.91 ± 0.13	$-3.37 \pm 9.40 \pm 9.40$
0.8525–0.8550	51 ± 8	8.21 ± 0.13	$14.27 \pm 2.28 \pm 0.99$	1.0325–1.0350	15 ± 9	7.90 ± 0.13	$3.70 \pm 2.12 \pm 1.89$
0.8550–0.8575	38 ± 8	8.21 ± 0.13	$10.59 \pm 2.21 \pm 0.94$	1.0350–1.0375	1 ± 6	7.90 ± 0.13	$0.15 \pm 1.49 \pm 0.18$
0.8575–0.8600	52 ± 7	8.20 ± 0.13	$14.53 \pm 1.99 \pm 0.44$	1.0375–1.0400	8 ± 6	7.89 ± 0.13	$1.81 \pm 1.43 \pm 0.32$
0.8600–0.8625	48 ± 7	8.20 ± 0.13	$13.41 \pm 1.90 \pm 0.49$	1.0400–1.0425	5 ± 7	7.89 ± 0.13	$1.09 \pm 1.58 \pm 0.35$
0.8625–0.8650	47 ± 7	8.20 ± 0.13	$13.14 \pm 1.85 \pm 0.47$	1.0425–1.0450	4 ± 5	7.89 ± 0.13	$0.95 \pm 1.13 \pm 0.52$
0.8650–0.8675	48 ± 7	8.19 ± 0.13	$13.36 \pm 1.88 \pm 1.08$	1.0450–1.0475	6 ± 4	7.88 ± 0.13	$1.36 \pm 1.05 \pm 0.51$
0.8675–0.8700	42 ± 7	8.19 ± 0.13	$11.58 \pm 1.81 \pm 1.55$	1.0475–1.0500	3 ± 3	7.88 ± 0.13	$0.68 \pm 0.82 \pm 0.22$

Table 8.3: Summary of hadronic energy ($\sqrt{s'}$), the number of events after unfolding ($N_{\rm unf}$), the efficiency (ε), and the cross section ($\sigma_{3\pi}$) of $e^+e^- \to \pi^+\pi^-\pi^0$ in an energy range of 1.05–3.50 GeV. The uncertainties on the cross section are the statistical errors and systematic errors, respectively. The statistical uncertainties for the unfolding and the cross section are square roots of the diagonal components of the unfolding covariance matrix.

$\sqrt{s'}$ (GeV)	$N_{\rm unf}$	ε (%)	σ (nb)	$\sqrt{s'}$ (GeV)	$N_{\rm unf}$	ε (%)	σ (nb)
1.050–1.075	63 ± 15	7.86 ± 0.13	$1.48 \pm 0.35 \pm 0.10$	1.900–1.925	38 ± 11	6.95 ± 0.17	$0.54 \pm 0.16 \pm 0.14$
1.075–1.100	159 ± 17	7.82 ± 0.13	$3.65 \pm 0.39 \pm 0.13$	1.925–1.950	61 ± 13	6.94 ± 0.17	$0.84 \pm 0.18 \pm 0.15$
1.100–1.125	194 ± 20	7.78 ± 0.19	$4.36 \pm 0.44 \pm 0.15$	1.950–1.975	37 ± 9	6.92 ± 0.17	$0.51 \pm 0.13 \pm 0.11$
1.125–1.150	208 ± 19	7.75 ± 0.19	$4.59 \pm 0.41 \pm 0.17$	1.975–2.000	31 ± 10	6.91 ± 0.17	$0.42 \pm 0.13 \pm 0.12$
1.150–1.175	232 ± 20	7.71 ± 0.18	$5.03 \pm 0.44 \pm 0.15$	2.000–2.050	55 ± 12	6.88 ± 0.17	$0.37 \pm 0.08 \pm 0.08$
1.175–1.200	244 ± 22	7.68 ± 0.18	$5.18 \pm 0.47 \pm 0.16$	2.050–2.100	76 ± 12	6.85 ± 0.17	$0.50 \pm 0.08 \pm 0.07$
1.200–1.225	208 ± 23	7.64 ± 0.18	$4.36 \pm 0.48 \pm 0.16$	2.100–2.150	70 ± 13	6.83 ± 0.17	$0.45 \pm 0.08 \pm 0.05$
1.225–1.250	276 ± 22	7.61 ± 0.18	$5.68 \pm 0.45 \pm 0.18$	2.150–2.200	53 ± 10	6.80 ± 0.17	$0.33 \pm 0.06 \pm 0.03$
1.250–1.275	249 ± 23	7.58 ± 0.18	$5.04 \pm 0.47 \pm 0.19$	2.200–2.250	54 ± 10	6.78 ± 0.17	$0.32 \pm 0.06 \pm 0.02$
1.275–1.300	206 ± 24	7.54 ± 0.18	$4.09 \pm 0.47 \pm 0.16$	2.250–2.300	54 ± 10	6.75 ± 0.17	$0.32 \pm 0.06 \pm 0.02$
1.300–1.325	247 ± 26	7.51 ± 0.18	$4.84 \pm 0.52 \pm 0.17$	2.300–2.350	53 ± 10	6.73 ± 0.17	$0.30 \pm 0.06 \pm 0.02$
1.325–1.350	257 ± 25	7.48 ± 0.18	$4.95 \pm 0.48 \pm 0.17$	2.350–2.400	40 ± 9	6.71 ± 0.17	$0.23 \pm 0.05 \pm 0.02$
1.350–1.375	218 ± 22	7.45 ± 0.18	$4.13 \pm 0.41 \pm 0.13$	2.400–2.450	26 ± 8	6.69 ± 0.17	$0.14 \pm 0.05 \pm 0.01$
1.375–1.400	201 ± 22	7.42 ± 0.18	$3.76 \pm 0.41 \pm 0.17$	2.450–2.500	33 ± 8	6.67 ± 0.17	$0.18 \pm 0.05 \pm 0.02$
1.400–1.425	261 ± 25	7.39 ± 0.18	$4.80 \pm 0.45 \pm 0.19$	2.500–2.550	28 ± 8	6.65 ± 0.17	$0.15 \pm 0.04 \pm 0.01$
1.425–1.450	229 ± 20	7.37 ± 0.18	$4.14 \pm 0.36 \pm 0.16$	2.550–2.600	12 ± 7	6.63 ± 0.17	$0.06 \pm 0.03 \pm 0.01$
1.450–1.475	232 ± 21	7.34 ± 0.18	$4.15 \pm 0.37 \pm 0.16$	2.600–2.650	25 ± 7	6.61 ± 0.17	$0.13 \pm 0.03 \pm 0.01$
1.475–1.500	229 ± 20	7.31 ± 0.18	$4.03 \pm 0.35 \pm 0.15$	2.650–2.700	33 ± 8	6.60 ± 0.17	$0.16 \pm 0.04 \pm 0.01$
1.500–1.525	244 ± 21	7.29 ± 0.17	$4.23 \pm 0.36 \pm 0.15$	2.700–2.750	7 ± 5	6.58 ± 0.17	$0.04 \pm 0.03 \pm 0.01$
1.525–1.550	265 ± 22	7.26 ± 0.17	$4.53 \pm 0.38 \pm 0.16$	2.750–2.800	12 ± 6	6.56 ± 0.17	$0.06 \pm 0.03 \pm 0.01$
1.550–1.575	300 ± 22	7.24 ± 0.17	$5.06 \pm 0.38 \pm 0.16$	2.800–2.850	5 ± 5	6.55 ± 0.17	$0.02 \pm 0.02 \pm 0.01$
1.575–1.600	305 ± 22	7.21 ± 0.17	$5.08 \pm 0.37 \pm 0.15$	2.850–2.900	14 ± 8	6.53 ± 0.17	$0.07 \pm 0.04 \pm 0.02$
1.600–1.625	321 ± 24	7.19 ± 0.17	$5.26 \pm 0.39 \pm 0.17$	2.900–2.950	6 ± 6	6.51 ± 0.17	$0.02 \pm 0.03 \pm 0.01$
1.625–1.650	283 ± 24	7.17 ± 0.17	$4.58 \pm 0.38 \pm 0.16$	2.950–3.000	12 ± 6	6.49 ± 0.17	$0.05 \pm 0.02 \pm 0.01$
1.650–1.675	256 ± 19	7.14 ± 0.17	$4.09 \pm 0.31 \pm 0.15$	3.000–3.050	18 ± 4	6.48 ± 0.17	$0.08 \pm 0.02 \pm 0.08$
1.675–1.700	214 ± 20	7.12 ± 0.17	$3.37 \pm 0.32 \pm 0.14$	3.050–3.100	19 ± 4	6.46 ± 0.17	$0.082 \pm 0.018 \pm 0.004$
1.700–1.725	133 ± 19	7.10 ± 0.17	$2.06 \pm 0.29 \pm 0.15$	3.100–3.150	16 ± 5	6.44 ± 0.17	$0.065 \pm 0.020 \pm 0.004$
1.725–1.750	130 ± 17	7.08 ± 0.17	$2.00 \pm 0.26 \pm 0.18$	3.150–3.200	19 ± 5	6.42 ± 0.17	$0.08 \pm 0.02 \pm 0.06$
1.750–1.775	101 ± 14	7.06 ± 0.17	$1.53 \pm 0.21 \pm 0.11$	3.200–3.250	8 ± 5	6.40 ± 0.17	$0.03 \pm 0.02 \pm 0.01$
1.775–1.800	83 ± 12	7.04 ± 0.17	$1.24 \pm 0.18 \pm 0.10$	3.250–3.300	9 ± 5	6.38 ± 0.17	$0.037 \pm 0.019 \pm 0.003$
1.800–1.825	77 ± 14	7.02 ± 0.17	$1.13 \pm 0.20 \pm 0.12$	3.300–3.350	5 ± 3	6.36 ± 0.17	$0.020 \pm 0.012 \pm 0.004$
1.825–1.850	76 ± 14	7.01 ± 0.17	$1.11 \pm 0.21 \pm 0.13$	3.350–3.400	6 ± 4	6.34 ± 0.17	$0.023 \pm 0.015 \pm 0.005$
1.850–1.875	79 ± 15	6.99 ± 0.17	$1.14 \pm 0.21 \pm 0.15$	3.400–3.450	8 ± 4	6.31 ± 0.18	$0.030 \pm 0.017 \pm 0.005$
1.875–1.900	48 ± 11	6.97 ± 0.17	$0.69 \pm 0.16 \pm 0.11$	3.450–3.500	14 ± 4	6.29 ± 0.18	$0.05 \pm 0.02 \pm 0.01$

8.2 Calculation of $a_\mu(3\pi)$

The LO HVP contribution to muon anomalous magnetic moment is given by the first term of Eq. (2.23)

$$a_\mu(3\pi) = \frac{\alpha}{3\pi^2}\int_{m_\pi^2}^{\infty}\frac{K(s)}{s}R_{\text{had}}(s)ds, \tag{8.2}$$

where $R_{\text{had}}(s) = \sigma_0(e^-e^- \to \text{hadrons})/\sigma(e^-e^- \to \mu^+\mu^-)$ is the hadronic R-ratio, σ_0 is bare cross section, $\sigma(e^-e^- \to \mu^+\mu^-) = 4\pi\alpha^2/3s$, and $K(s)$ is the QED kernel function Eq. (2.22).

The bare cross section σ_0 should include FSR but exclude ISR and VP effects. Therefore, we can obtain the bare cross section from the measured cross section by [126]

$$\sigma_0 = \sigma^{\text{dressed}}\frac{1}{|1+\Pi(s)|^2} = \sigma^{\text{dressed}}|1-P(s)|^2, \tag{8.3}$$

where σ^{dressed} is the dressed cross section, including the VP effect, and $\Pi(s)$ is a self-energy function of photon and $P(s)$ is a polarization operator. The vacuum polarization correction $|1-P(s)|^2$, which the first principles cannot calculate. The value and uncertainty for the table of $P(s)$ is summarized in and referred to Ref. [127]. The used function is plotted in Fig. 8.2. The systematic uncertainty on $a_\mu(3\pi)$ is 0.018% for 0.62–1.05 GeV and 0.005% for $M_{3\pi}$ above 1.05 GeV.

Although the table of the dressed cross section is a function of energy, it is converted to m^2 when we perform the integral. In the calculation of a given bin, the minimum and maximum values of the bin are converted to squared values and the center of a converted bin is used for calculation.

As a result, the calculated contribution to a_μ in a range of 0.62–1.8 GeV and 0.62–2.0 GeV is

$$a_\mu|_{0.62-1.8\,\text{GeV}} = (48.91 \pm 0.23_{\text{stat}} \pm 1.07_{\text{syst}}) \times 10^{-10},$$
$$a_\mu|_{0.62-2.0\,\text{GeV}} = (49.03 \pm 0.23_{\text{stat}} \pm 1.07_{\text{syst}}) \times 10^{-10}.$$

Systematic uncertainty on the anomalous magnetic moment contribution

The statistical uncertainty on $a_\mu(3\pi)$ using 191 fb^{-1} data is 0.5%, which includes the statistical uncertainty due to background subtraction. The systematic uncertainty on $a_\mu(3\pi)$ is 1.85% in total, summarized in Table 8.4.

The uncertainty on the cross section is calculated from Eq. (8.2) with the systematic errors of the cross section, summarized in Table 8.1. Contributions in low energy region especially at the ω and ϕ resonances are significant to $a_\mu(3\pi)$: For the integral in 0.65–2.0 GeV, the contribution to $a_\mu(3\pi)$ of each energy region is 92.2% from 0.65–1.05 GeV, 7.5% for 1.05–1.8 GeV, and 0.3% for 1.80–2.00 GeV. Therefore, the systematic uncertainty on $a_\mu(3\pi)$ is dominated by the uncertainty on the cross section below 1.05 GeV. The total systematics of efficiency correction of 1.6%, the largest error is the π^0 efficiency, followed by the tracking efficiency. The uncertainty for the integrated luminosity and radiative correction are energy-dependent

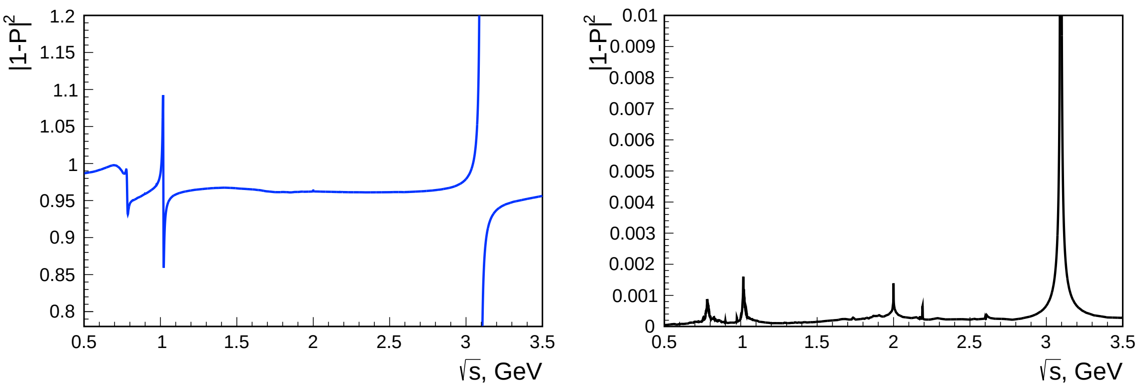

(a) Value (b) Uncertainty

Figure 8.2: The value and uncertainty for $|1-P(s)|$. The value is referred to Ref. [127].

Table 8.4: The contributions to the relative systematic uncertainty on $a_\mu(3\pi)$ (%).

Source of uncertainty	**Uncertainty (%)**
MC statistics	0.15
Efficiency correction	1.63
Generator	1.18
Luminosity	0.64
Radiative correction	0.50
Background subtraction	0.02
Unfolding	0.12
Vacuum polarization corrections	0.04
Total	**2.19**
statistical uncertainty	**0.47**
Total uncertainty	**2.23**

and are 0.71% and 0.5%, respectively. The change in $a_\mu(3\pi)$ due to the data-MC scale factor in the background estimation is around 0.2%, which is accounted for as a systematic error in the background subtraction.

A distribution difference between the unfolded spectrum and true raises less than 0.01% The reason why this difference in distribution does not have a significant impact is that the calculation of a_μ itself is the integral of the reaction cross section with respect to the invariant mass of the hadron system, so the unfolding operation, which makes corrections among neighboring bins, does not contribute significantly to its integral value. The relative change in the value of $a_\mu(3\pi)$ when using different parameters is -0.011% when using the omega-fit parameters and -0.121% when using the phi-fit parameters. This 0.12% is accounted for as a systematic error.

8.3 The running of the fine structure constant

We also introduce the running of the fine structure constant as a parameter for which the $e^+e^- \to hadrons$ cross section is used in a similar way to a_μ. The QED coupling constant, α, varies in value depending on the energy due to higher order corrections such that the vacuum polarization appears in its photon propagator. This running coupling constant, a coupling constant that increases with increasing energy, can be expressed as

$$\alpha(s) = \frac{\alpha_0}{1 - \Delta\alpha_{\text{lep}}(s) - \Delta\alpha^{(5)}_{\text{had}}(s) - \Delta\alpha_{\text{top}}(s)}, \tag{8.4}$$

where α_0 is the constant at low energy $s = 0$ and is called the *bare* fine structure constant, $\alpha_0 = e^2/4\pi\varepsilon_0 \sim 1/137$. $\Delta\alpha_{\text{lep}}(s)$ is the term such that lepton pairs cause vacuum polarization. The HVP contribution is divided into $\Delta\alpha^{(5)}_{\text{had}}(s)$, which takes into account the light five quarks (u, d, s, c, b) and $\Delta\alpha_{\text{top}}(s)$ is the top quark contribution. The light quark contribution, $\Delta\alpha^{(5)}_{\text{had}}(s)$, is calculated using the dispersive integral as in a_μ^{HVP}, [30]

$$\Delta\alpha^{(5)}_{\text{had}}(q^2) = -\frac{\alpha q^2}{3\pi}\text{P}\int_{s_{th}}^{\infty} ds \frac{R(s)}{s(s-q^2)}, \tag{8.5}$$

where P represents the principal value of the integral, $R(s)$ is the hadronic R-ratio. The value of the running coupling constant at the Z-boson mass, $q^2 = M_Z^2$, is a parameter used in the electroweak fit, which is useful for the SM test. The current global average of $\Delta\alpha^{(5)}_{\text{had}}(M_Z^2)$ is, [30, 30]

$$\Delta\alpha^{(5)}_{\text{had}}(M_Z^2) = (276.1 \pm 1.1) \times 10^{-4}. \tag{8.6}$$

The main systematic error in this value originates from this light hadron contribution error. Figure 8.3 shows the contribution and uncertainty fraction from each energy region. Unlike $a_\mu^{\text{HVP,LO}}$ in Eq. (2.23), the R-ratio is not subject to the $1/s^2$ suppression. Therefore, the R-ratio contribution at high energies is more significant than in a_μ^{HVP}. About half of the contribution is the contribution in the region above 11 GeV as estimated in perturbative QCD calculation, while the other half is calculated using the measured R-ratio. Considering contribution in the range below 2 GeV, the main channels are [30]

$$\Delta\alpha_{\pi^+\pi^-}(M_Z^2) = (34.29 \pm 0.12) \times 10^{-4} \tag{8.7}$$
$$\Delta\alpha_{\pi^+\pi^-\pi^0}(M_Z^2) = (4.69 \pm 0.09) \times 10^{-4} \tag{8.8}$$
$$\Delta\alpha_{\pi^+\pi^-\pi^+\pi^-}(M_Z^2) = (4.02 \pm 0.05) \times 10^{-4} \tag{8.9}$$
$$\Delta\alpha_{\pi^+\pi^-\pi^0\pi^0}(M_Z^2) = (5.00 \pm 0.20) \times 10^{-4}. \tag{8.10}$$

The 3π channel accounts for a contribution of around 8% and an error of around 5%.

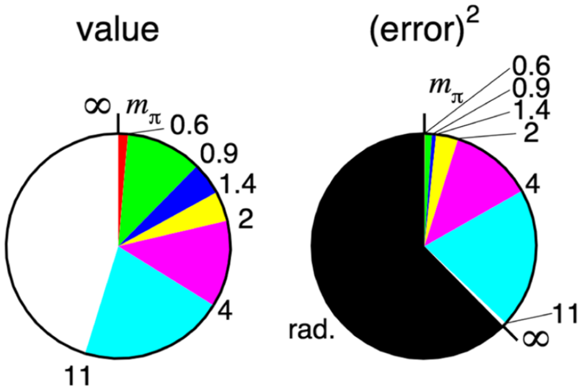

Figure 8.3: Fraction of (left) the contribution and (right) error^2 to the total from each energy region. The energy boundaries are m_π, 0.6,0.9,1.43,2.0,4.0,11.2, and ∞ GeV. The black is the contribution from the radiative correction uncertainty. Adopted from Ref. [26].

As a result, the contribution to $\Delta\alpha^{(5)}_{\text{had}}(M_Z^2)$ calculated using the obtained cross section in a range of 0.62–2.0 GeV is

$$\Delta\alpha_{\pi^+\pi^-\pi^0}(M_Z^2) = (4.91 \pm 0.03_{\text{stat.}} \pm 0.11_{\text{syst.}}) \times 10^{-4}. \tag{8.11}$$

Comparing this result with the average of previous experiments, [30]

$$\Delta\alpha_{\pi^+\pi^-\pi^0}(M_Z^2) = (4.69 \pm 0.09) \times 10^{-4},$$

precision has reached a similar level in one experiment. The systematic error is 2.2%, which is slightly larger than that of $a_\mu^{\text{HVP,LO}}$ due to the larger contribution above 1.1 GeV. Although the values are 5% higher than the world average, they agree at 1.5 standard deviations. The better agreement of the mean values compared to $a_\mu^{\text{HVP,LO}}$ is probably due to the better agreement of the cross section above 1.1 GeV with the other experiments.

8.4 Branching fraction of the $J/\psi \to \pi^+\pi^-\pi^0$ process

The branching fraction for the $J/\psi \to \pi^+\pi^-\pi^0$ process is tested by a fit to the J/ψ resonance.

The $e^+e^- \to J/\psi \to \pi^+\pi^-\pi^0$ MC for this study is generated by ISR simulation with the Phokhara and simulated the $\pi^+\pi^-\pi^0$ decay via $\rho\pi$ intermediate state. For simplicity, the mass distribution of J/ψ is defined as the flat distribution in a narrow range of 3096.7–3097.1 GeV/c^2. It is reasonable because the resonance is sufficiently narrower than a detector resolution. The detection efficiency estimated by the MC is $\varepsilon = 9.03 +/-0.21)\%$. This efficiency is used for the calculation of branching fraction. The radiative correction around 3.1 GeV/c^2 is 1.0149 ± 0.0002.

The J/ψ resonance is fitted with the Lorentz function convoluted by the resolution function. The mass and width are fixed to the PDG values. The resolution function is obtained from the response function of the simulation convoluted with the Gaussian function, which represents the data-MC difference. The non-resonant component is assumed to have a linear function. Figure 8.4 shows the fit result for the data. The parameters of the Gaussian smearing determined by this fit are used in the unfolding (See chapter 7). The number of J/ψ signal is 1376 ± 40 events. The cross section of $e^+e^- \to J/\psi\,\gamma_{\rm ISR}$ can be expressed as

$$\sigma_{e^+e^-\to J/\psi\,\gamma_{\rm ISR}}(s)|_{20^\circ<\theta_\gamma<160^\circ} = \frac{12\pi\Gamma_{ee}\cdot\Gamma_{\rm tot}}{(s-m_{J/\psi})^2+m^2_{J/\psi}\cdot\Gamma_{\rm tot^2}}\cdot W(s), \tag{8.12}$$

where $m_{J/\psi}$ and $\Gamma_{\rm tot} = (92.6 \pm 1.7)$ keV are the mass and the full width of J/ψ, $\Gamma_{ee} = 5.53 \pm 0.10$ is the partial width of J/ψ. The calculated branching fraction is

$$\mathcal{B}(J/\psi \to 3\pi) = (2.149 \pm 0.062_{\rm stat} \pm 0.074_{\rm syst} \pm 0.039_{\Gamma_{ee}})\%. \tag{8.13}$$

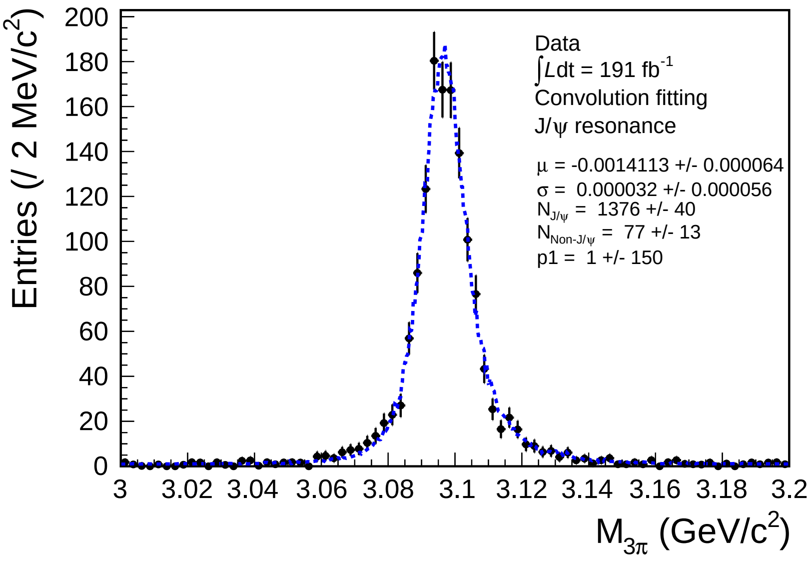

Figure 8.4: $M_{3\pi}$ distribution around the J/ψ resonance for the data. The $M_{3\pi}$ is offset by the nominal J/ψ mass. The points with error bars show the data. The dashed line shows fit results convoluted with the Gaussian.

8.5 Discussion

We saw the results of the cross section measurement in section 8.1, the $a_\mu^{\rm HVP,LO}$ contribution in section 8.2, the $\Delta\alpha_{\pi^+\pi^-\pi^0}$ contribution in section 8.3 and the branching fraction of $J/\psi \to \pi^+\pi^-\pi^0$ in section 8.4. In this section, we discuss the comparison with previous measurements in terms of values and errors.

Cross section and a_μ comparison

A comparison on cross section is shown in Fig. 8.5, where the relative difference between the previous and this measurements $(\sigma_{\rm previous} - \sigma_{\rm Belle\,II})/\sigma_{\rm Belle\,II}$ are plotted. In comparing *BABAR*, they are binning almost the same energy range of 0.62–3.5 GeV with almost similar bin widths. The ω resonance is overall higher than the *BABAR*, SND, and CMD. For the ϕ region, a clear shift in the resonance mass is visible compared to *BABAR*, with the Belle II mass being higher. For the range 1.1–2.0 GeV, although systematic deviations are observed, the shapes of the resonances are in good agreement with each other.

The cross section above can be checked with the J/ψ resonance. The measured branching fraction of the $J/\psi \to \pi^+\pi^-\pi^0$ process $\mathcal{B} = (2.149 \pm 0.062_{\rm stat} \pm 0.074_{\rm syst} \pm 0.039_{\Gamma_{ee}})\%$, which is the measurement with a precision of 5%, is consistent with the previous measurements : the PDG value $(2.10\pm0.08)\%$ [37], *BABAR* $(2.265 \pm 0.070)\%$ [60], and BESIII $(2.188 \pm 0.052)\%$ [61].

The comparisons of a_μ contribution to the previous results are summarized in Table 8.5. A comparison with the *BABAR* experiment, a B-factory experiment with a similar experimental setup, shows that the values are indeed larger by $a_\mu(3\pi, \text{BABAR}) - a_\mu(3\pi, \text{Belle II}) = (+3.3 \pm 1.3) \times 10^{-10}$, a difference of 6.9%, and deviate by a significance of 2.5σ. Although the BESIII results are consistent with us, these are preliminary and not published. The global fit results DHMZ [29], KNT [30] are the global fit results used in the white paper but do not include the BABAR and BESIII results; HHKS [65]HHKS includes the BABAR 2021 results. Compared with the values the global fit given by the HHKS, the difference is $+6.7\%$, $(+3.1 \pm 1.2) \times 10^{-10}$. Given that the difference between the a_μ experimental value and the SM prediction is currently $\Delta a_m u = (24.9 \pm 4.8) \times 10^{-10}$ (Table 2.1), substituting this result for the 3π contribution with this result reduces the difference to the experimental value by around 10%. This kind of cherry-picking that uses only the value of this experiment is inappropriate as a scientific argument, and future discussions based on combination fitting with other experiments are necessary.

Table 8.5: The summary of a_μ of this experiment and the values in the previous experiments. The difference is the result of subtracting our value in the corresponding energy range, and the numbers in square brackets indicate the relative difference.

	Energy range	$a_\mu(3\pi)$ $(\times 10^{-10})$	Difference from this study $(\times 10^{-10})$
This study	0.62–1.8 GeV	$48.91 \pm 0.23 \pm 1.07$	-
This study	0.62–2.0 GeV	$49.03 \pm 0.23 \pm 1.07$	-
This study	0.70–3.5 GeV	$49.08 \pm 0.23 \pm 1.08$	-
BABAR 2021 [60]	0.62–2.0 GeV	$45.86 \pm 0.14 \pm 0.58$	(-3.2 ± 1.3) [-6.9%]
BESIII 2019 [61]	0.70–3.5 GeV	$49.77 \pm 0.53 \pm 0.17$	$(+0.7 \pm 1.2)$ [+1.4%]
DHMZ20 [29]	0.62–1.8 GeV	$46.21 \pm 0.40 \pm 1.40$	(-2.7 ± 1.8) [-5.8%]
KNT20 [30]	0.62–1.97 GeV	46.74 ± 0.94	(-2.3 ± 1.5) [-4.9%]
HHKS23 [65]	0.62–1.80 GeV	$45.91 \pm 0.37 \pm 0.94$	(-3.0 ± 1.2) [-4.9%]

Comparison with *BABAR*

This analysis method is similar to the *BABAR* analysis in many respects. Differences are considered in considering the causes of the significant differences in the cross section from the other experiments, particularly *BABAR*. The main differences are picked up and listed in Table 8.6

The basic method is the same since it is an asymmetric e^+e^- collision experiment at the c.m. energy of 10.58 GeV and uses the radiative return method. The size of the dataset is about 40%. This difference is not significant in a_μ^{HVP} result because of the systematic error dominance.

For selection, almost the same type of selection criteria are used, although the acceptances and thresholds are set differently. As for the ISR polar angle range, the trigger condition requirements make the range more stringent than that of *BABAR*. The one of the differences between the selection conditions is the kienamtic fit: *BABAR* constrains four momentum (but without using the measured energy of ISR) and a π^0 mass. In contrast, for the purpose of $M_{\gamma\gamma}$ fitting, we only constrain four momentum (with measured ISR energy).

The background items we checked are generally the same as *BABAR*, but the treatment of combinatorial $\gamma\gamma$ backgrounds is different. On our side, it is a dominant background event in the mass region below 1.1 GeV and is removed by bin-by-bin $M_{\gamma\gamma}$ fit. It is not mentioned in *BABAR* and I guess it was negligibly small. Similarly, the best candidate selection for multiple candidates in an event due to spurious photon is done in our analysis, but it is not mentioned on the *BABAR*.

For the efficiency correction, the correction items, the control samples and methods are exactly the same. The items with the largest correction terms, i.e., the items with the worst simulation reproducibility, are different, with Belle II showing a maximum data-MC difference of 1.9% in background suppression efficiency.

Our systematic error of 2.2% is larger than that of *BABAR*, 1.3%. The signal MC generator is different, *BABAR* uses AfkQed [128, 129, 130], and our measurement uses Phokhara. It induces The systematic error of 1.2% due to the generator, and is the largest systematic error in our measurement now. As for signal efficiency, the systematic uncertainty for ISR detection efficiency (0.2% vs. 0.7%) and $\pi 0$ efficiency (0.5% vs. 1.0%) are particularly larger for Belle II. The uncertainty for the luminosity is also larger in Belle II, but this is because we conservatively estimate the uncertainty by the amount of tracking uncertainty. The background filter (high-level trigger) efficiency is the largest source of systematic error in BABAR, but less than 0.1% in Belle II.

Prospects

Improvement of the reproducibility of the detector simulation and the method itself are needed to improve the uncertainty for the signal efficiency. Regarding the improvement of the detector simulation,

Table 8.6: Comparison of major differences between the *BABAR* measurement [60] and us (Belle II).

	BABAR [60]	This study
e^+e^- c.m. energy	10.58 GeV (91%) + 10.54 GeV (9%)	10.58 GeV
Int. Luminosity	469 fb^{-1}	191 fb^{-1}
Signal MC generator	AfkQed	Phokhara (ver. 9.1)
Selection		
π^0 selection	$0.10 < M_{\gamma\gamma} < 0.17\,\mathrm{GeV}/c^2$	$M_{\gamma\gamma}$ fit
Kinematic fit for selection	4C plus π^0 mass const. (ISR energy is not used)	4C fit under $2\pi3\gamma$ hypothesis
Background		
Combinatorial $\gamma\gamma$ bkg.	Negligible (No discussion)	$M_{\gamma\gamma}$ fit
Background fraction at ω	0.5%	0.25%
Efficiency correction		
Leading correction	π^0 efficiency $(-3.4 \pm 0.5)\%$	Background suppression $(-1.90 \pm 0.2)\%$
Sub-leading correction	Background filter $(-1.4 \pm 0.7)\%$	π^0 efficiency $(-1.43 \pm 1.0)\%$
Dominant systematic error for $a_\mu(3\pi)$		
Signal efficiency	1.1%	1.6%
Generator	-	1.2%
Luminosity	0.4%	0.6%
Total	1.3%	2.2%

the MC simulated samples in this study are “run-independent”. However, since the MC simulation taking into account run-dependent information, i.e., random sampling of background hits and adaptation of detector conditions at each data acquisition time, is already becoming available as part of the Belle II framework, we can expect an improvement in reproducibility. This will lead to lower data-MC difference in background suppression efficiency, etc. In addition, larger datasets may allow for better control of systematic errors , e.g., by applying tighter selections to control samples.

The uncertainty in the trigger efficiency is worthy of special mention. To briefly describe a background of trigger development in the Belle II experiment, the $e^+e^- \to hadrons$ measurement in the Belle experiment is the predecessor experiment operated in 1999–2010, which was not designed for ISR-related measurement. Measurements of the cross section for $\pi^+\pi^-$ and $\pi^+\pi^-\pi^0$ channels were attempted but were suffered from inefficiency due to the trigger veto of QED processes. From the experience, the QED process veto is improved, and new trigger lines independent from the veto are introduced in the Belle II detector. This study also confirmed that the high trigger efficiency and the low uncertainty associated with are achieved due to these efforts. This indicates that good trigger performance is ensured for not only the 3π measurement but also the measurement of the other $e^+e^- \to hadrons$ channels in the future.

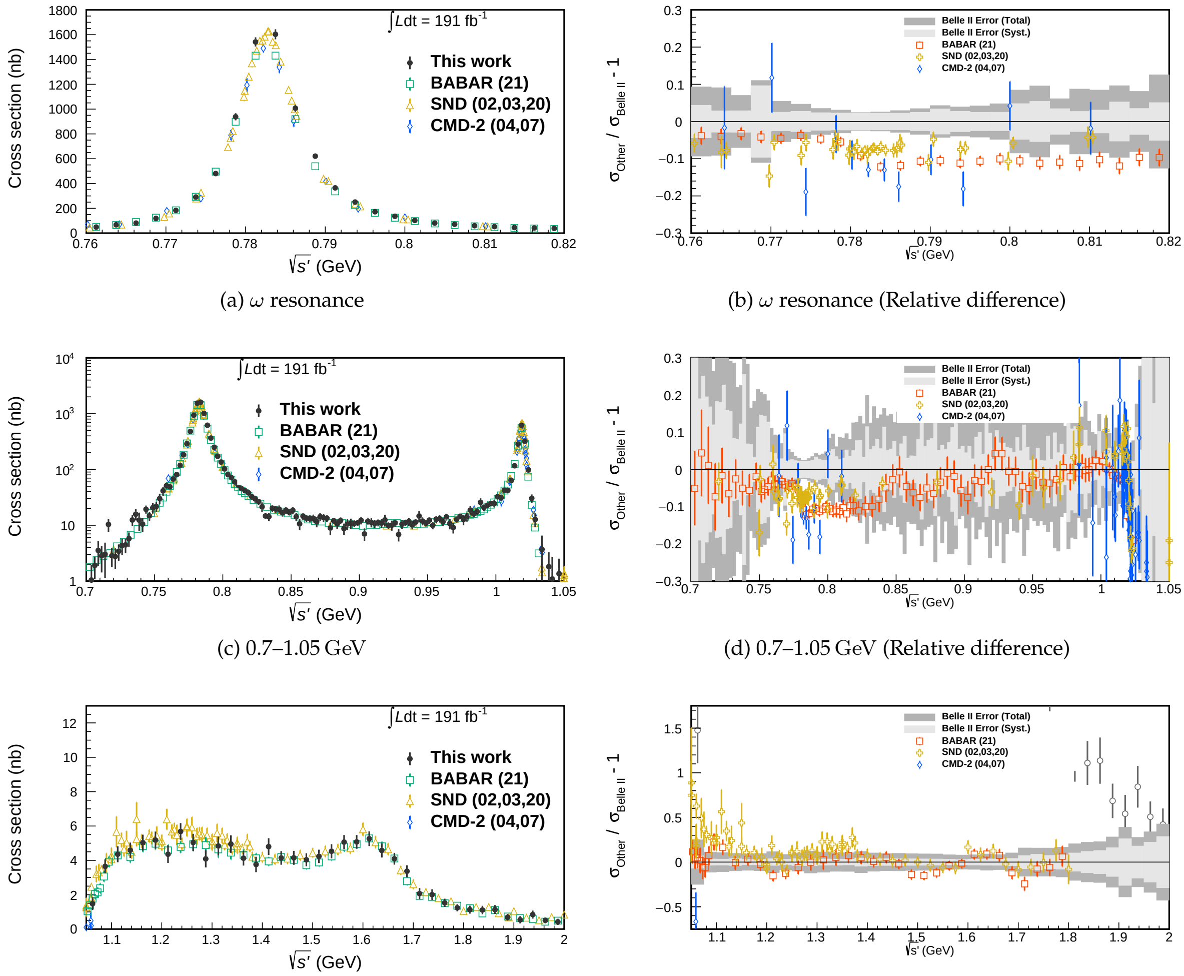

(a) ω resonance

(b) ω resonance (Relative difference)

(c) 0.7–1.05 GeV

(d) 0.7–1.05 GeV (Relative difference)

(e) 1.1–2 GeV

(f) 1.1–2 GeV (Relative difference)

Figure 8.5: Values (left column) and relative differences (right column) of the $e^+e^- \to \pi^+\pi^-\pi^0$ cross section from this study. The light and dark shaded boxes show the systematic and total uncertainty in this study. The square points (orange) show the result of *BABAR* (2021) [60], the crosses (brown) shows the result of SND (2002,2003,2015,2020) [52, 53, 125]. and the diamonds (blue) hows the result of CMD-2 (2004,2007) [57, 58].

Chapter 9

Conclusion

Precision measurements of hadron production cross sections in electron-positron annihilations play an important role in testing perturbative QCD at low energies, in hadronic spectroscopy and as input for the HVP contribution in the prediction of fundamental parameters. Among these contributions, the anomalous magnetic moment of the muon is a crucial physical quantity and one for which the existence of physics beyond the Standard Model of elementary particles has been suggested. Both experimental and theoretical values reach the order of 100 ppb accuracy, with deviations in the of 5 standard deviations. However, there are differences not only between experimental and theoretical values but also between two approaches to predict the HVP contributions, dispersive relation and lattice QCD. The main sources of uncertainty for the HVP calculation in the dispersive method are due to measurement accuracy and differences in the $e^+e^- \to hadrons$ cross section measurements. Further measurements of the $e^+e^- \to hadrons$ cross section by independent experiments would be vital to verify these differences and obtain clues to the new physics.

In this study, the cross section measurement for the $e^+e^- \to \pi^+\pi^-\pi^0$ process was performed, the final state with the second most significant contribution to the HVP term in muon $g-2$, and the measured cross section spectrum was used to discuss the HVP contribution of the muon $g-2$, the contribution to the running coupling constant, and the parameters of the J/ψ to three pion decay. The cross section in the hadron energy below 3.5 GeV was measured using the radiative return method, which employs a process involving the initial-state radiation photons in the final state. This analysis uses the data of 191 fb^{-1} obtained from the SuperKEKB/Belle II experiment, in which e^+e^- collisions were carried out at a e^+e^- center-of-mass energy of 10.58 GeV. This measurement is an independent experiment from previous measurements. For the cross section measurement, studies were conducted to extract the signal by event selection, estimate residual background yields, estimate accurate signal detection efficiency, and mitigate the detector resolution from the signal spectrum. Various control samples were used for residual background and signal detection efficiency estimations, and data-simulation corrections based on data-driven evaluations were actively used. In the detection efficiency correction, which is a major source of systematic error, the efficiency was evaluated for several items: trigger, tracking, ISR photon, π^0 and selection, with a maximum difference between data and simulation of about 2% for each item and a total of about 5% for the detector. It was confirmed that the simulation reproduced the data well.

As a result, the $e^+e^- \to \pi^+\pi^-\pi^0$ cross sections were measured in the range 0.62–3.5 GeV. The cross sections of the ω and ϕ resonances, which contribute significantly to a_μ, were measured in the precision of 2.2% and are 5% and 10% larger than the results of precursor measurements. Based on this measured cross section, the 3π contribution of a_μ in the range 0.62–.8 GeV is calculated to be $a_\mu(3\pi) = (48.91 \pm 0.23 \pm 1.07) \times 10^{-10}$. The statistical error is 0.5%, and the systematic error is 2.2%, which is the second precise measurement after the *BABAR* result's systematic error of 1.3% for a wide range of measurements in one experiment. Compared to the most precise global fit of the 3π contribution, it is about 3.1×10^{-10} larger. The results of this measurement show that the difference between the current theoretical and experimental muon $g-2$ is relieved by 10% of the difference.

The measurements identified several achievements and challenges in detector performance for future $e^+e^- \to hadrons$ cross section measurements in the Belle II experiment. This study shows that light hadron cross sections can be performed at the Belle II experiment using the same type of radiative return method, and establishes the basic methodology for such measurements. Trigger efficiency, which was the biggest challenge from the previous Belle experiment, has been confirmed to be dramatically improved, and the systematic error can be reduced to the 0.1% level. It was shown that further improvements in detector simulation, MC event generator, future increases in statistics could be expected to reduce the systematic uncertainty in the measurements.

Acknowledgements

I would like to express my deepest appreciation to Prof. Toru Iijima. Since joining this laboratory, I have gained a broad perspective, a variety of skills and experience thanks to the very wide range of opportunities he has given me. It has allowed me to fully immerse myself in the fascination of particle physics and high-energy particle experiments, and to enjoy a fruitful life as a student.

The members of the Nagoya Belle analysis group provided me with their invaluable comments and supports throughout this analysis: Dr. Yosuke Maeda provided me with a foundation and some ideas to help get me started; Dr. Yuji Kato and Prof. Qidong Zhou shared their expert analysis procedures and techniques; and Prof. Kenji Inami, who gave me some sharp questions and suggestions.

I would like to give a huge thank to the collaborators in the Belle II experiments, and SuperKEKB and the accelerator group for their extraordinary work in maintaining such a stable data taking and beam operation. I would like to thank those who provided very useful technical comments, invaluable solutions, and much help. As a co-author, Prof. Boris Shwartz helped me stay on track when I started this analysis, reviewed the overall analysis items, and provided solutions and comments on very technical questions. Prof. Hisaki Hayashii has been involved as a member of the review committee of the collaboration, and has provided me with many professional questions and comments over the past year and a half since he was assigned to the committee. The number of mail exchanges probably accounts for more than half of all the exchanges on the mailing list. Obviously, I cannot fail to mention his contribution to improve the quality of the analysis. Prof. Christopher Hearty and James Libby have been of tremendous help in moving the analysis forward as review committee, working group convenor, or physics coordinator. I would like to thank the many people who helped me to improve the quality in writing a journal paper, and especially like to thank Prof. Thomas Browder and Prof. Diego Tonelli for accompanying me on many very careful reviews.

Although not directly involved in this analytical study, I would also like to thank the people who greatly helped me with my research on equipment development during my master's and doctoral studies. Prof. Tsutomu Mibe, Prof. Yutaro Sato Prof. Masashi Otani, Prof. Yasuhiro Kondo, Prof. Yoshihito Iwasaki have provided me with much guidance and support in my researches at the the J-PARC muon g-2/EDM experiment, mainly in my master's course, and it had a tremendous influence on my decision to continue research in a PhD course. Prof. Taichiro Koga and Prof. Yoshihito Iwasaki helped in the development of the trigger module at the Belle II experiment. I had to do a lot of remote communication due to the overlap of COVID-19, but they were very patient with me and helped me a lot of meetings and discussions. I was able to learn the joy of device development and trigger development using FPGA.

I have been in the N-lab for a very long time in completing this doctoral research. I would like to thank the staffs and students of the laboratory for making my student life very pleasant and enjoyable. The many students, including alumni, who spent time with me from the time I joined in 2016 until I graduated in 2024 were extremely helpful in making my student life at the N-lab enjoyable. They consulted with me about various research topics and reported back to me, which greatly helped me to increase my knowledge.

This work was supported by Japan Society for the Promotion of Science (JSPS) Research Fellowship for Young Scientists-DC and JSPS KAKENHI Grant Numbers JP19J21763, JP23H05433, and JP18H05226.

Finally, I am very grateful to my parents for all the financial support they have been willing to give me, and most importantly, I thank them from the bottom of my heart for letting me do what I wanted to do without saying a word about my decisions and choices, even when I decided to take extra years to get my PhD!

Appendix A

Systematic uncertainty of the π^0 efficiency

In section 6.5, we discuss how to validate the π^0 efficiency using the process $e^+e^- \to \omega\gamma_{\rm ISR} \to \pi^+\pi^-\pi^0\gamma_{\rm ISR}$. We discuss the π^0 efficiency as well as the data-MC ratio of the π^0 efficiency by taking the ratio of the fully reconstructed events divided by the partially reconstructed events of the process $e^+e^- \to \omega\gamma$. We need to consider the systematic errors on the number of the partially reconstructed and the fully reconstructed events. The summary of various source of the systematic errors is given in Table 6.3 (see section 6.5).

A.1 Systematic uncertainty on the partial reconstructed events

To determine the partial reconstructed events, we fit the $M_{\pi^+\pi^-\pi^0,\rm recoil}$ with a signal and various background terms. In a standard fit, shown in Fig. 6.11 (or Fig A.1(a)), the scale factors of the signal and $\pi^+\pi^-\pi^0\pi^0\gamma$, $q\overline{q}$ pdfs are floated, and that of $K^0_SK^0_L\gamma$ and others are fixed. For the systematic errors, we discuss the uncertainty of the shape the signal and the background templates, and variation between various kind of alternative fits. The summary of the various fits is given in Table A.1 and the results of the fit is shown in Figs. A.1 and A.2. Notations used in this table are as follows.

- Two different shapes are used for $q\overline{q}$ MC, $q\overline{q}$ without ISR $q\overline{q}$ (QA), with ISR-$q\overline{q}$ (QB),
- Fit/Float non-ISR qq-bar components (QAX),
- Add second order polynominal (2),
- Replace $q\overline{q}$ component with the 2nd order polynomial,
- Introduce the Gaussian to the likelihood to take into account the uncertainty of the scale-factors for the contributions, $\pi^+\pi^-\pi^0\pi^0\gamma$ (C),
- Introduce the Gaussian to the likelihood to take into account the uncertainty of the scale-factors for the contributions, $K^0_SK^0_L\gamma$ (K).

Uncertainty on the $\pi^+\pi^-\pi^0\pi^0\gamma_{\rm ISR}$ background

We determine the line shape of the $\pi^+\pi^-\pi^0\pi^0\gamma_{\rm ISR}$ background, using a control sample ($4\pi\gamma$-control sample 2). The $M_{\pi^+\pi^-\pi^0,{\rm recoil}}$ distribution for $4\pi\gamma$ control sample 2 is shown in Fig. A.3. A small ω signal seen in this figure is due to the feed-down from the signal ($3\pi\gamma$). Except this contribution, the shape of the $M_{\pi^+\pi^-\pi^0,{\rm recoil}}$ in $4\pi\gamma$ control sample 2 is explained well by the $\pi^+\pi^-\pi^0\pi^0\gamma$ MC. From this study we determine the data-MC scale factor of the $\pi^+\pi^-\pi^0\pi^0\gamma$ to be $R_{4\pi\gamma} = 1.15 \pm 0.2$.

In the partial reconstructed events, although the fraction is small, there are additional background such as $\pi^+\pi^-3\pi^0\gamma_{\rm ISR}$, $\pi^+\pi^-\eta\gamma_{SR}$. These components are not simulated., To include these background to $\pi^+\pi^-\pi^0\pi^0\gamma$, we do two kind of fits, one is the standard fit where the scale-factor of $\pi^+\pi^-\pi^0\pi^0\gamma_{\rm ISR}$ is floated without any constraint. The other one is the one that treats as the $\pi^+\pi^-\pi^0\pi^0\gamma_{\rm ISR}$ scale-factor ($R_{4\pi\gamma}$) as the nuisance parameter; we added the pdf of Gaussian in the likelihood to take into account the uncertainty of $R_{4\pi\gamma}$. we take 1.15 for the mean and 0.2 for the sigma of Gaussian. A symbol "C" is used for this fit in Table A.1 and Figs. A.1 and A.2. The fit result of $R_{4\pi\gamma}$ for CQA is 1.57 ± 0.12 (Fig. A.2(g)).

From the difference of the standard fit and the fit that treats the $4\pi\gamma$ as the nuisance parameter in Table A.1 (CQA), we estimate the uncertainty due to $\pi^+\pi^-\pi^0\pi^0\gamma_{\rm ISR}$ background to be $\pm 0.13\%$ (The difference between CQA - standard=-0.001, by taking plus-minus of this difference conservatively.).

Uncertainty on the $\phi\gamma_{\rm ISR} \to K_S K_L \gamma_{\rm ISR}$ background

The process $e^+e^- \to \phi\gamma_{\rm ISR} \to K_S^0(\to \pi^+\pi^-)K_L^0\gamma_{\rm ISR}$ making an broad peak under the contributes as an peaking background for ω (Fig. A.1(a)).

The contribution of this background in the partial reconstructed events can be seen as a sharp peak if we see the invariant mass of $\pi^+\pi^-$ in Fig. A.4, where a condition of the ω mass region, $0.72 < M_{\pi^+\pi^-\pi^0,{\rm recoil}} < 0.84\,{\rm GeV}/c^2$ is required in the partial reconstructed events. The purple histogram is the prediction of $e^+e^- \to \phi\gamma_{\rm ISR} \to K_S^0K_L^0\gamma_{\rm ISR}$ by the PHOKHARA, normalized to the data luminosity. The program PHOKHARA reproduces this background both on the shape as well as the absolute scale.

For the further check on the prediction, we show, in Fig. A.5 for the sample in the K_S^0 mass region $0.48 < M_{\pi^+\pi^-} < 0.52\,{\rm GeV}/c^2$, the invariant mass $M_{\pi^+\pi^-\pi^0,{\rm recoil}}$, the momentum recoil against the $\pi^+\pi^-\gamma_{\rm ISR}$ system, and the invariant mass of $\pi^+\pi^-K^0_{L,rec}$ system where the 1-C fit (assuming K_L^0 missing) result of the recoil momentum is use in the momentum vector of K_L^0. The yield is normalized to the luminosity.

From this distribution, we determined the scale-factor for this $\phi \to K_S^0K_L^0$ background,be

$$f_{K_S^0K_L^0\gamma} = 1.07 \pm 0.08,$$

where the error comes from the statistical error of the data. In the fit of the partial reconstructed events for the efficiency measurement, the scale of the $K_S^0K_L^0\gamma$ background is fixed to this center value. And the error of the scale factor is taken into account by a Gaussian in the likelihood function. This give the uncertainty from $K_S^0K_L^0\gamma$ to be $\Delta R/R_{\rm std.} = \pm 0.33\%$.

Uncertainty on the $q\bar{q}$ background

The $q\bar{q}$ backgrounds include the standard continuum $q\bar{q}$ hadron production as well as the resonance production in the $e^+e^- \to \gamma_{\rm ISR} + hadrons$ processes except the ones of $\pi^+\pi^-\pi^0\gamma_{\rm ISR}$, $\pi^+\pi^-\pi^0\pi^0\gamma_{\rm ISR}$, $\pi^+\pi^-\gamma_{\rm ISR}$ and $K_S^0K_L^0\gamma_{\rm ISR}$. These $q\bar{q}$ backgrounds are modeled by the KKMC program.

We take the KKMC prediction to model *shape* of the $q\bar{q}$ background and floated the normalization in the standard fit. As the alternative fit (QA), we use the model that do not include the ISR components in the $q\bar{q}$ background. From the difference of these two models, we obtain the systematic to be $\Delta R/R_{\rm std.} = \pm 0.03\%$. One the other hand, the difference between floated (QA) and fixed (QAX) to the $q\bar{q}$ scale-factor is $\Delta R/R_{\rm std.} = -0.06\%$

Uncertainty of the background shape

So far, we use the MC prediction for the background shape. To further estimate the uncertainty coming from the possible background shape difference, we add the 2nd order polynomial function to the one obtained by the MC.in the fit Those fits are symbolized by "2" in Table A.1. The difference between with 2nd order-pol. and the without it are found to be +0.05% (QA-QA2), +0.07% (QAX-QAX2) in Table A.1. From this, the systematic uncertainty of background shape is estimated to be $\Delta R/R_{\rm std.} = \pm 0.07\%$.

Table A.1: The summary of various fit for the $M_{\pi^+\pi^-\pi^0,\mathrm{recoil}}$ for the partial reconstructed events. "Configuration" is the name of the configuration of the fit (See text for the detail). $N_{\mathrm{part}}^{\mathrm{data}}$ is the number of partial-reconstructed ω signals obtained in the data by a fit of the given configuration. $\Delta N_{\mathrm{part}}^{\mathrm{data}}$ is error of it. $\varepsilon^{\mathrm{data}}$ is the efficiency of π^0 determined in the data. R is the ratio of the π^0 efficiency between the data and the MC, $\varepsilon^{\mathrm{data}}/\varepsilon^{\mathrm{MC}}$. ΔR is the statistical error of R. "Description" provides an short explanation of each fit.

Configuration	$N_{\mathrm{part}}^{\mathrm{data}}$	$\Delta N_{\mathrm{part}}^{\mathrm{data}}$ $(\Delta N/N_{\mathrm{std.}})$	$\varepsilon^{\mathrm{data}}$	R	ΔR $(\Delta R/R_{\mathrm{std.}})$	Description
standard	54272.3 ± 310.9	$+0.0$ $(+0.00\%)$	0.5016 ± 0.0029	0.9857 ± 0.0058	$+0.0000$ $(+0.000\%)$	Standard
G	54323.0 ± 309.9	$+50.7$ $(+0.09\%)$	0.5012 ± 0.0029	0.9847 ± 0.0058	-0.0009 (-0.093%)	$\gamma\gamma$ MC x2 (fixed)
QA	54289.9 ± 313.7	$+17.6$ $(+0.03\%)$	0.5015 ± 0.0029	0.9853 ± 0.0059	-0.0003 (-0.032%)	MC14 $q\overline{q}$ w/o ISR events (floated)
QB	54272.3 ± 310.9	$+0.0$ $(+0.00\%)$	0.5016 ± 0.0029	0.9857 ± 0.0058	$+0.0000$ $(+0.000\%)$	MC14 $q\overline{q}$ w/ ISR events (floated)
QA2	55057.9 ± 341.3	$+785.6$ $(+1.45\%)$	0.4945 ± 0.0031	0.9716 ± 0.0062	-0.0141 (-1.427%)	MC14 $q\overline{q}$ w/o ISR events (floated) + pol2
QB2	54412.2 ± 234.3	$+139.9$ $(+0.26\%)$	0.5004 ± 0.0022	0.9831 ± 0.0045	-0.0025 (-0.257%)	MC14 $q\overline{q}$ w/ ISR events (floated) + pol2
QAX	54306.0 ± 309.8	$+33.7$ $(+0.06\%)$	0.5013 ± 0.0029	0.9850 ± 0.0058	-0.0006 (-0.062%)	MC14 $q\overline{q}$ w/o ISR events (fixed)
QBX	54729.6 ± 310.2	$+457.3$ $(+0.84\%)$	0.4975 ± 0.0029	0.9774 ± 0.0057	-0.0082 (-0.836%)	MC14 $q\overline{q}$ w/ ISR events (fixed)
QAX2	55050.3 ± 339.7	$+778.0$ $(+1.43\%)$	0.4946 ± 0.0031	0.9717 ± 0.0062	-0.0139 (-1.413%)	MC14 $q\overline{q}$ w/o ISR events (fixed) + pol2
QBX2	54785.6 ± 314.5	$+513.3$ $(+0.95\%)$	0.4969 ± 0.0029	0.9764 ± 0.0058	-0.0092 (-0.937%)	MC14 $q\overline{q}$ w/ ISR events (fixed) + pol2
QD2	55056.9 ± 340.9	$+784.6$ $(+1.45\%)$	0.4945 ± 0.0031	0.9716 ± 0.0062	-0.0140 (-1.425%)	
CQA	54339.3 ± 352.7	$+67.0$ $(+0.12\%)$	0.5010 ± 0.0033	0.9844 ± 0.0065	-0.0012 (-0.123%)	$q\overline{q}$ MC w/o ISR (float) + Constrain $4\pi\gamma$ and $K_S^0 K_L^0 \gamma$
CQA2	54329.3 ± 234.1	$+57.0$ $(+0.11\%)$	0.5011 ± 0.0022	0.9846 ± 0.0045	-0.0010 (-0.105%)	$q\overline{q}$ MC w/o ISR (float) + pol2 + Constrain $4\pi\gamma$ and $K_S^0 K_L^0 \gamma$
CQB	54306.4 ± 347.3	$+34.1$ $(+0.06\%)$	0.5013 ± 0.0032	0.9850 ± 0.0065	-0.0006 (-0.063%)	$q\overline{q}$ MC w/ ISR (float) + Constrain $4\pi\gamma$ and $K_S^0 K_L^0 \gamma$
CQB2	54557.8 ± 348.5	$+285.5$ $(+0.53\%)$	0.4990 ± 0.0032	0.9805 ± 0.0064	-0.0052 (-0.523%)	$q\overline{q}$ MC w/ ISR (float) + pol2 + Constrain $4\pi\gamma$ and $K_S^0 K_L^0 \gamma$
CQD	54119.0 ± 342.7	-153.3 (-0.28%)	0.5031 ± 0.0032	0.9884 ± 0.0064	$+0.0028$ $(+0.283\%)$	
CQD2	54908.9 ± 367.4	$+636.6$ $(+1.17\%)$	0.4958 ± 0.0034	0.9742 ± 0.0067	-0.0114 (-1.159%)	
K	54496.1 ± 310.0	$+223.8$ $(+0.41\%)$	0.4996 ± 0.0029	0.9816 ± 0.0058	-0.0040 (-0.411%)	No $q\overline{q}$ MC (fixed) + $K_S^0 K_L^0 \gamma$ (floated)
KQA	54449.8 ± 381.7	$+177.5$ $(+0.33\%)$	0.5000 ± 0.0035	0.9824 ± 0.0070	-0.0032 (-0.326%)	No $q\overline{q}$ MC (floated) + $K_S^0 K_L^0 \gamma$ (floated)
FXK	58832.7 ± 360.5	$+4560.4$ $(+8.40\%)$	0.4628 ± 0.0030	0.9093 ± 0.0059	-0.0764 (-7.751%)	$4\pi\gamma$ (fixed) + $K_S^0 K_L^0 \gamma$ (floated)
KQB	54442.8 ± 372.2	$+170.5$ $(+0.31\%)$	0.5001 ± 0.0034	0.9826 ± 0.0069	-0.0031 (-0.313%)	MC14 $q\overline{q}$ MCw/ ISR events (floated) + $K_S^0 K_L^0 \gamma$ (floated)

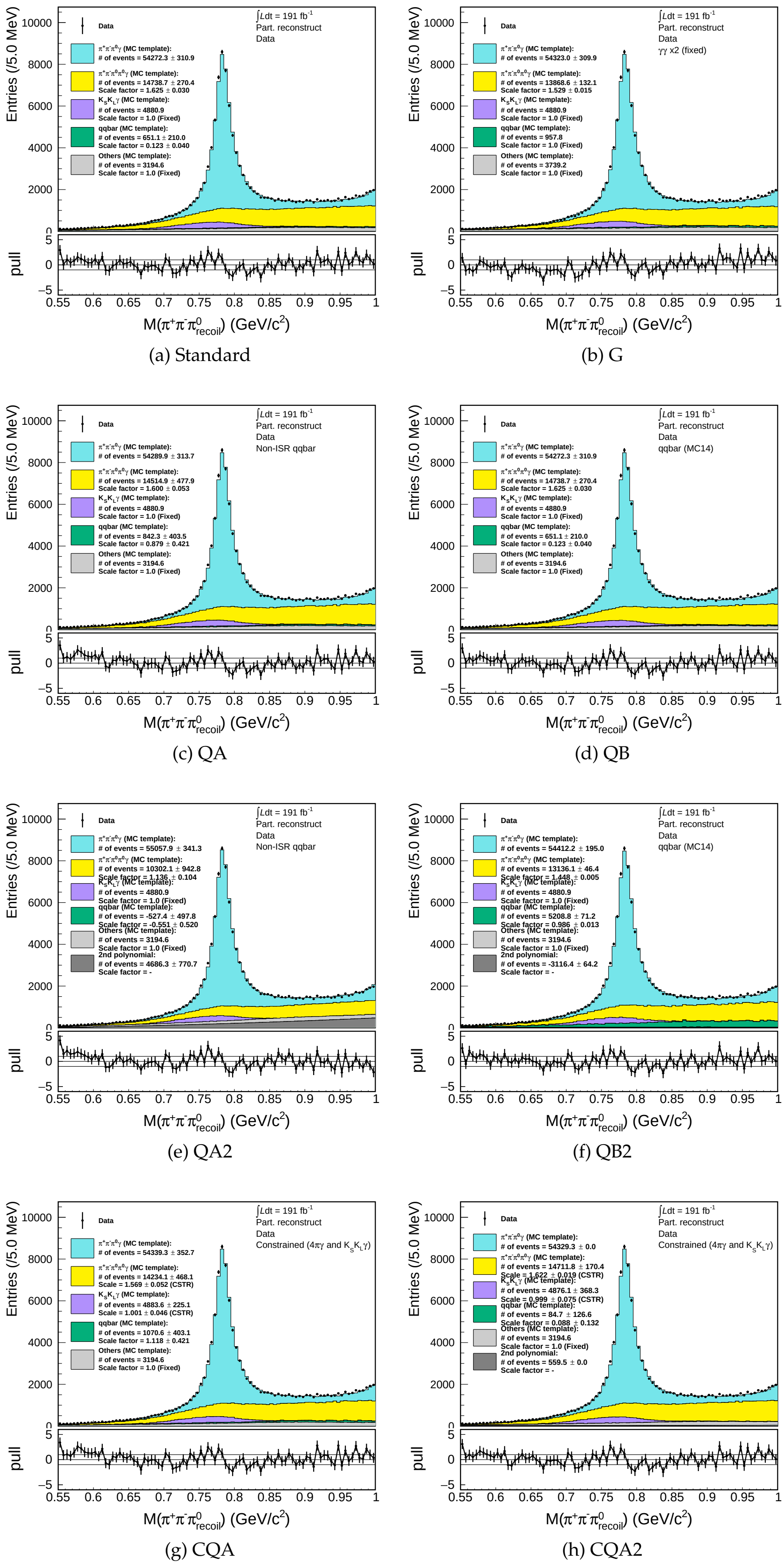

(a) Standard (b) G

(c) QA (d) QB

(e) QA2 (f) QB2

(g) CQA (h) CQA2

Figure A.1: The $M_{\pi^+\pi^-\pi^0,\mathrm{recoil}}$ fit results with different conditions for background pdf hypothesis. The data uses the 10% of data. The number of events in legend indicates that in the $0.72 < M_{\pi^+\pi^-\pi^0,\mathrm{recoil}} < 0.84\,\mathrm{GeV}/c^2$. The configuration is summarized in Table A.1.

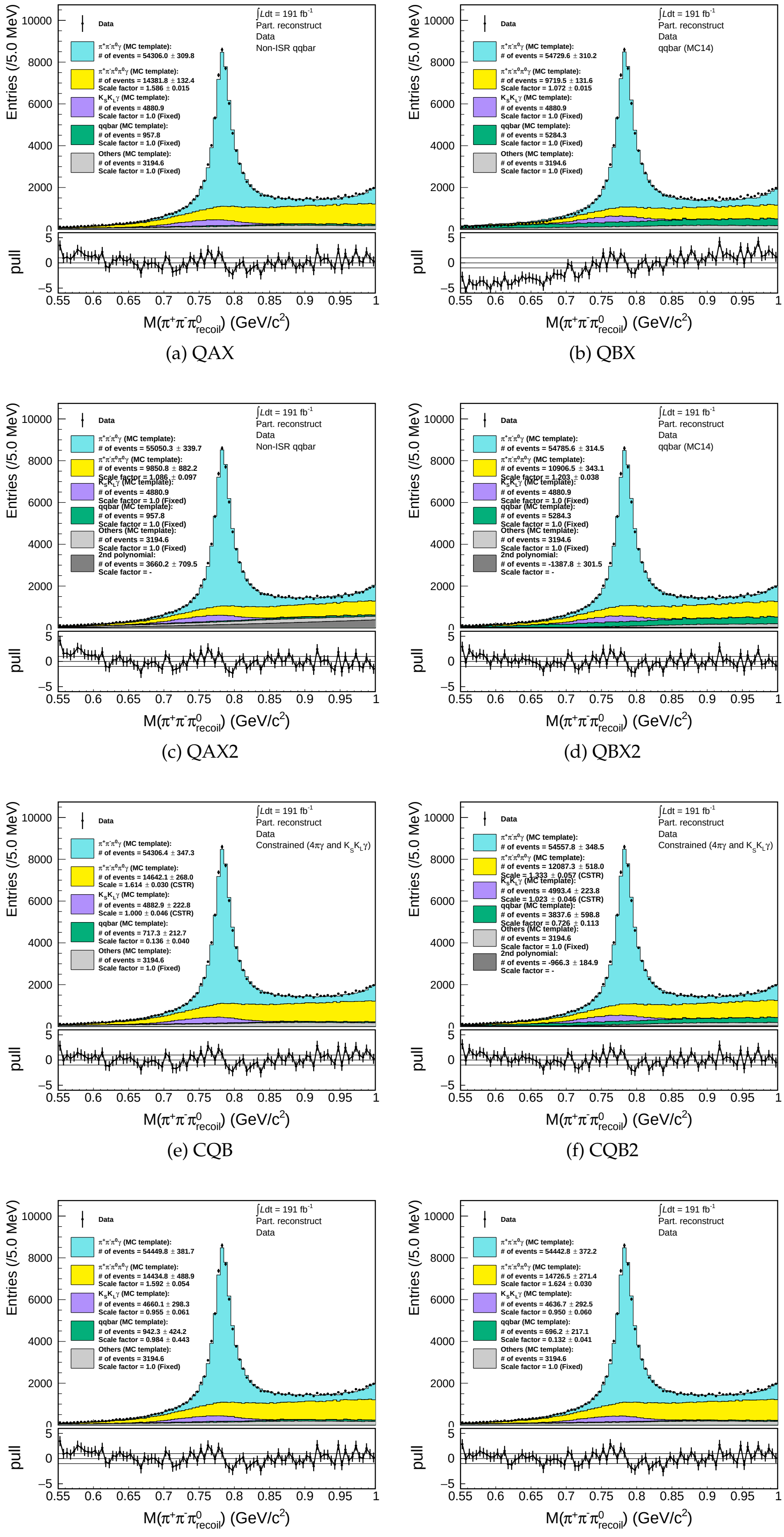

(a) QAX (b) QBX

(c) QAX2 (d) QBX2

(e) CQB (f) CQB2

(g) KQA (h) KQB

Figure A.2: The $M_{\pi^+\pi^-\pi^0,\mathrm{recoil}}$ fit results with different conditions for background pdf hypothesis. The data uses the 10% of data. The number of events in legend indicates that in the $0.72 < M_{\pi^+\pi^-\pi^0,\mathrm{recoil}} < 0.84\,\mathrm{GeV}/c^2$. The configuration is summarized in Table A.1.

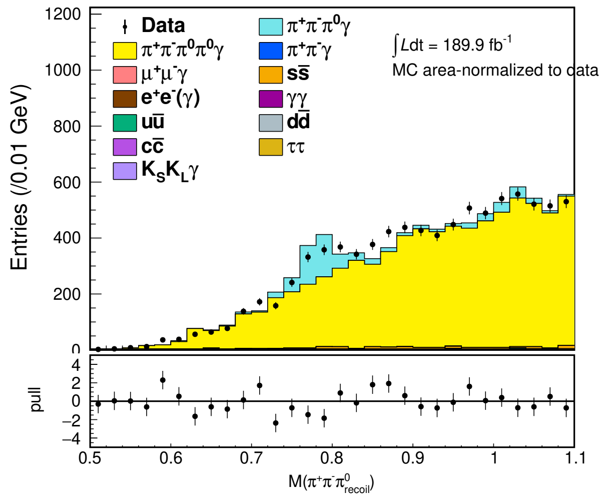

Figure A.3: The $M_{\pi^+\pi^-\pi^0,\text{recoil}}$ distribution of the $\pi^+\pi^-\pi^0\pi^0\gamma$ control sample using data.

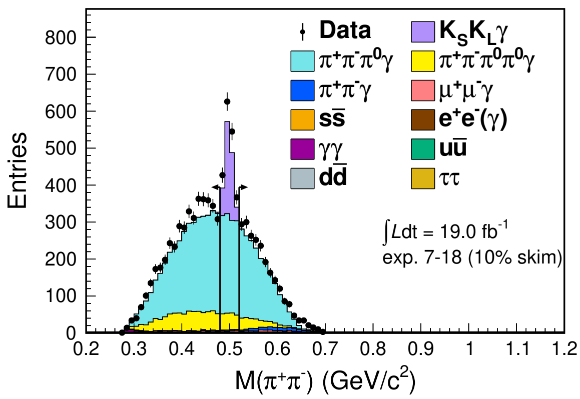

Figure A.4: The pion-pair invariant mass distribution of partial-reconstructed events using the 10% of data. The MC predictions are normalized to the data luminosity using the cross section given by PHOKHARA. The criteria $\chi^2_{1C,\text{rec.}} < 40$ and $0.72 < M_{\pi^+\pi^-\pi^0,\text{recoil}} < 0.84\,\text{GeV}/c^2$ are applied.

Uncertainty on the ω signal shape

We estimate the uncertainty due to the signal template by changing the nuisance parameters that are used to determine the ω signal shape (such as resolution) by one standard deviation. The $M_{\pi^+\pi^-\pi^0,\text{recoil}}$ fit is applied to the full-reconstructed events with the signal pdf convolved with the Gaussian to model the difference of signal shape, where the mean and sigma are free parameters. The largest difference comes from a change of mean, which represents the mass shift, the change of numerator is $\Delta R/R_{\text{std.}} = \pm 0.09\%$.

Uncertainty on the$\pi^+\pi^-\gamma$ and $\mu^+\mu^-\gamma$ background

The shape for these background is shown in Fig. A.6. These are selected from the enriched sample for these processes. These contribution in partial reconstructed events is small and can be neglected.

Uncertainty on the $e^+e^- \to \omega\pi^0$ contribution

This process can become the peaking potential background when the high energy π^0 mis-identified as a ISR photon. These background is, however, found to be negligible using the control sample selected a cluster second moment.

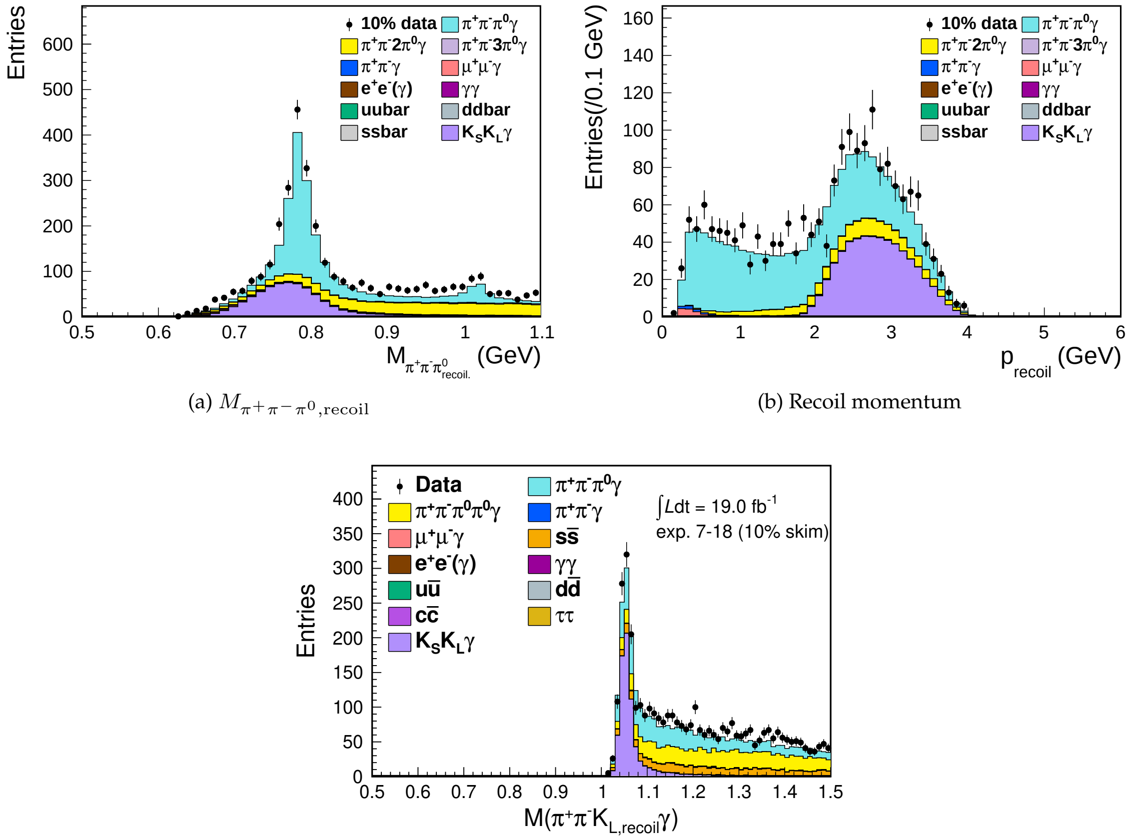

(a) $M_{\pi^+\pi^-\pi^0,\mathrm{recoil}}$

(b) Recoil momentum

(c) $M_{\pi^+\pi^-K_L,\mathrm{recoil}}$

Figure A.5: The data and MC comparison of $M_{\pi^+\pi^-\pi^0,\mathrm{recoil}}$, $M_{\pi^+\pi^-K_L,\mathrm{recoil}}$, and recoil momentum. The data points shows the 10% of data. The stacked histogram shows the MC samples scaled to the luminosity of data.

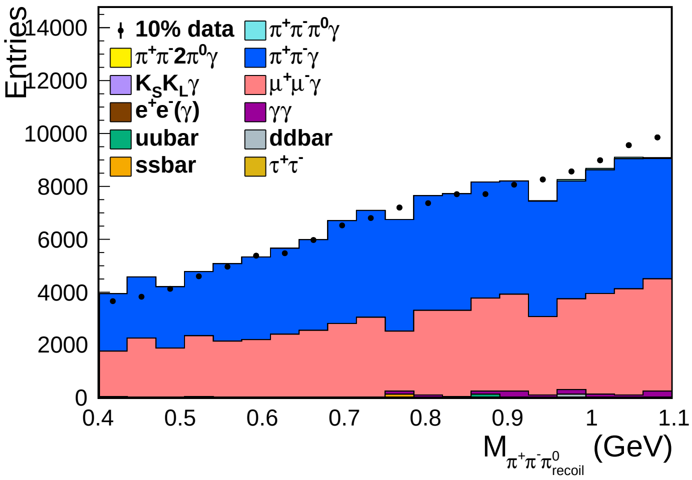

Figure A.6: The $M_{\pi^+\pi^-\pi^0,\mathrm{recoil}}$ distribution of the $\pi^+\pi^-\gamma$ and $\mu^+\mu^-\gamma$ enhanced sample using 100% of data. The sample is extracted by applying $M^2_{\mathrm{recoil}} < 4\,\mathrm{GeV}^2/c^4$ instead of the cut $M^2_{\mathrm{recoil}} > 4\,\mathrm{GeV}^2/c^4$.

Uncertainty on the event selection of partial reconstructed events

For the signal selection, we require $\chi^2_{1\mathrm{C,rec}} < 10$ to select of partial reconstructed $e^+e^- \to \pi^+\pi^-\pi^0\gamma_{ISR}$ events. To estimate the systematic uncertainty on this selection, we change the selection criteria from 1 to 100. By this change, the fraction of the background contamination in the partial reconstructed events is changed from 20% to 28%. From this study, we set the uncertainty due to the change of the event selection to be $\pm 0.56\%$.

A.2 Systematic uncertainty on the full reconstructed events

Uncertainty on the counting method of full reconstructed events

We count the number of full reconstructed events from the fit on $M_{\pi^+\pi^-\pi^0,\mathrm{recoil}}$, or fit on $M_{\gamma\gamma}$ distribution. The resultant results are quite consistent each other. From the difference of these results, we assigned the systematic uncertainty of the counting method to be $\Delta R/R_{\mathrm{std.}} = 0.23\%$.

Uncertainty on the π^0 signal shape

We estimate this uncertainty by changing the nuisance parameters that are used to model the π^0 signal shape (such as sigma ... in Novosibirsk function) in the likelihood by one sigma. The largest difference arise from the ratio of Novosibirsk function and Gaussian, $\Delta R/R_{\mathrm{std.}} = 0.46\%$.

Fraction of the $\pi^+\pi^-\pi^0\pi^0\gamma$ background (r_g)

The number of $\pi^+\pi^-\pi^0\pi^0\gamma$ events in the full-reconstructed events is given by counting the number of π^0-MC-truth events in $0.72 < M_{\pi^+\pi^-\pi^0,\mathrm{recoil}} < 0.84\,\mathrm{GeV}/c^2$, multiplied by the $\pi^+\pi^-\pi^0\pi^0\gamma$ data-MC scale factor of 1.15 ± 0.13, to be $r_{b,4\pi\gamma} = 0.0051 \pm 0.0005$, where the uncertainty is dominated by the error of the data-MC scale factor. These backgrounds from $e^+e^- \to \omega\pi^0$ is negligible. .

Appendix B

Additional ISR photon generation with PHOKHARA program

BABAR has reported discrepancies in the data for the ISR calculation of the PHOKHARA generator, which is used to generate our signal MC [18, 131]. They performed a study of $e^+e^- \to \mu^+\mu^-\gamma/\pi^+\pi^-\gamma$ events with the 1 to 3 hard ISR photon emissions and confirmed the following points:

- Events with additional hard photons emitted at a small angle (SA) to the beam axis (i.e., LO ISR+additional SA photon) are produced 20% more in PHOKHARA than in the data.
- Events with an additional photon emitted at a large angle (LA) to the beam axis agree well with PHOKHARA and the data.
- Next-to-next leading order (NNLO) events with two additional photons, i.e., three hard ISR photons, which is not simulated in the PHOKHARA, are measured to be (3.5 ± 0.4)%.

In our analysis, this may affect the radiative correction, which is the ratio of the probability, including higher-order ISR emission, to the probability of LO ISR emission and the signal efficiency due to event selection. In this appendix, we will examine the effects of these two items and confirm the generator-derived systematic error.

B.1 Radiative correction

We will confirm the total ISR emission rate of PHOKHARA by comparing it with KKMC, which uses different technique for multiple photon calculation. The *BABAR* measurement confirms that the LO, NLO, and NNLO photon calculations in KKMC agree with the data [18].

To test this, we created an $e^+e^- \to \mu^+\mu^-\gamma(\gamma)$ process with the following configuration:

- PHOKHARA
  - NLO ISR mode: up to two ISR photons are simulated. (`LO=0, NLO=1`)
  - VP and FSR corrections are turned off a (`QED=0, Alpha=0`) to see only ISR contribution
- KKMC
  - FSR and FSR interference are turned off (`KeyFSR=0, KeyINT=0, KeyQSR=0`)
  - EW and HVP corrections are turned off (`KeyELW=0, KeyZet=0, MinMassCEEX=0`)

Then, $e^+e^- \to \mu^+\mu^-\gamma$ are reconstructed at the generator level from a muon-pair and the highest energy photon in the c.m. system, requiring the invariant mass greater than $8\,\mathrm{GeV}/c^2$. The polar angle of the LO ISR in the c.m. system is limited to 20°–160°. This criterion, $M(\mu^+\mu^-\gamma) > 8\,\mathrm{GeV}/c^2$, eliminates NLO events such that there are additional photons with $E^* > 2.3\,\mathrm{GeV}$. The dataset is normalized by the integrated luminosity of sample, calculated from the number of generated events and the cross section obtained as a generator log output.

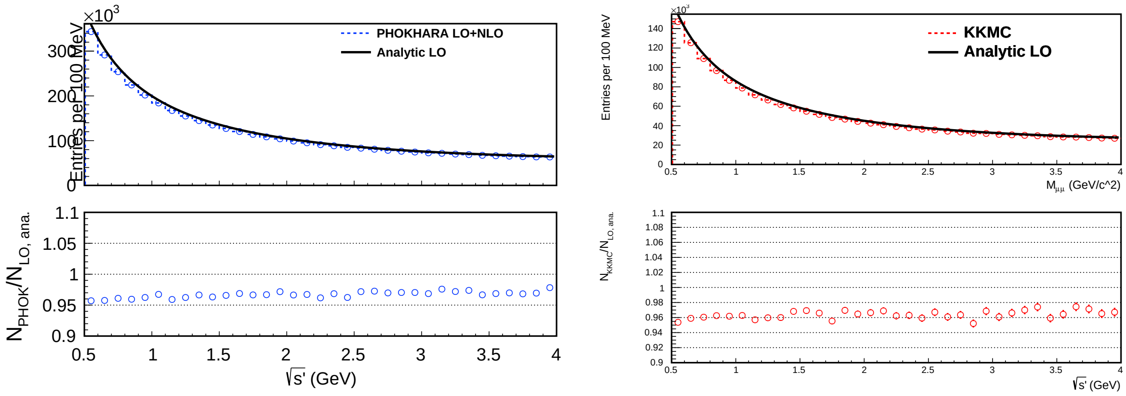

(a) PHOKHARA (b) KKMC

Figure B.1: Cross section of $e^+e^- \to \mu^+\mu^-\gamma$ process in a function of muon-pair invariant mass at the generator level. The points in the top panels show the cross section calculated by (a) PHOKHARA and (b) KKMC. The black line shows the analytical function of the LO ISR emission. The lower panels are the ratio of the LO+NLO ISR MC simulation to the LO ISR analytical function.

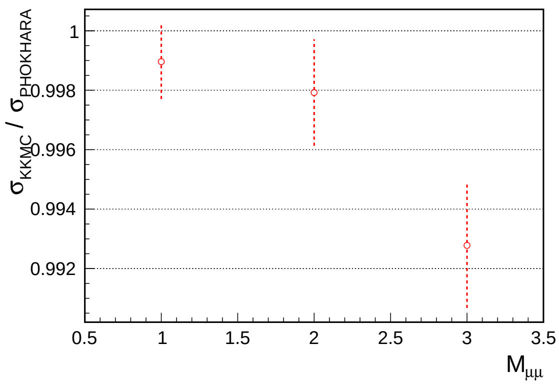

Figure B.2: Ratio of cross section calculated by KKMC to that by PHOKHARA in a function of muon-pair invariant mass. The error bars are statistical uncertainty.

Figure B.1 shows a comparison of the number of events for the LO + NLO simulation in the generator with the analytic function (Eq. (2.41)), which represents the probability of emission of the LO ISR. The bottom panels show the ratio, which is practically a radiative correction; it takes a value of about 1.01 depending on $M(\mu^+\mu^-)$ as we use in Sec. 8.1. The ratio of PHOKHARA to KKMC is shown in Fig. B.2, which indicates that the PHOKHARA and KKMC distributions are consistent within a systematic error of 0.5%, which is considered to be the uncertainty of unaccounted higher-order effect in PHOKHARA [89].

From these results, we concluded that the total emission rate of LO + NLO (+NNLO) is well simulated in PHOKHARA and the radiative correction used in Sec. 8.1 is reliable within the uncertainty of PHOKHARA, 0.5%.

B.2 Underestimation of signal efficiency due to NLO excess

This section discusses the impact of data-MC difference of NLO and NNLO events on the signal efficiency. First, we will analyze our data to confirm if there is an excess in SA NLO events generated by PHOKHARA. Next, we will estimate the amount of underestimation of signal efficiency and systematic error due to the excess

The criterion of $\chi^2_{4C,2\pi3\gamma} < 50$ is the selection sensitive to NLO events in our analysis. The conservation of four-momentum requires the absence of additional hard ISR photons. We prepared a sample using

$e^+e^- \to \pi^+\pi^-\pi^0\gamma$ MC with a selection other than $\chi^2_{4C,2\pi3\gamma} < 50$ cuts. Figure B.3 shows the distribution of NLO ISR energies reconstructed at the generator level for this sample. The red histogram in Fig. B.3 (b) displays the result of applying $\chi^2_{4C,2\pi3\gamma} < 50$ cuts to this sample. It suggests that most events with additional ISR photons of energy greater than 100 MeV are removed by the $\chi^2_{4C,2\pi3\gamma} < 50$ criteria.

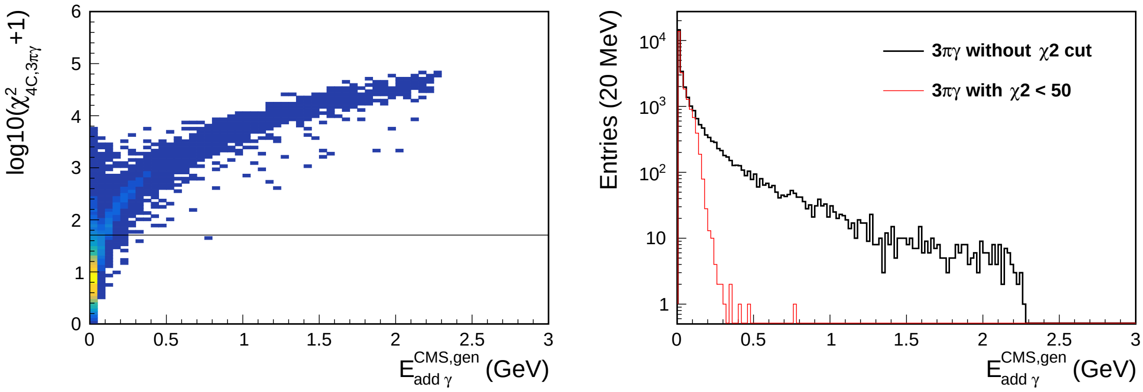

(a) (b)

Figure B.3: (a) Distribution of $\chi^2_{4C,2\pi3\gamma}$ of reconstructed $e^+e^- \to \pi^+\pi^-\pi^0\gamma$ events and energy of additional ISR photon in the c.m. system at the generator level. (b) Distribution of energy of additional ISR photon in the c.m. system at the generator level (black) before and (red) after $\chi^2_{4C,2\pi3\gamma} < 50$ selection.

The event selection is slightly modified to be able to include SA NLO events ($e^+e^- \to \pi^+\pi^-\pi^0\gamma_{\rm ISR}\gamma_{\rm SA}$). The three-constraint (3-C) kinematic fit is used instead of the 4C-KFit. This fit is performed by constraining the p_x and p_y balance at the c.m. system, assuming that the missing momentum vector is of a massless particle. In other words, the kinematic fit is performed in the presence of additional (undetected) photons $\gamma_{\rm SA}$ with degrees of freedom in the p_z direction. The missing momentum resulting from this 3-C KFit is treated as the momentum of the SA ISR.

To enhance the signal-to-noise ratio, we use the ω-resonance events and analyze the χ^2 distribution of 3C-KFit, as depicted in Fig. B.4(a). Note that χ^2_{3C} is less than $\chi^2_{4C,2\pi3\gamma}$ due to the constraint being less than 4C-KFit. The result confirms the effectiveness of selecting $\chi^2_{3C} < 50$ in significantly reducing background events.

Figure B.4 (b) displays the energy distribution of the SA ISR for this sample. The simulated sample is normalized to the number of events in the data. Events with LO ISR or low-energy NLO ISR, known as LO topology events, result in an energy peak around 0. Events with $|E| < 0.1$ GeV are classified as LO events, while those with $E > 0.1$ GeV are classified as SA NLO events. Figure B.4 (c) shows a comparison in coarse bins. The data-MC ratios for the LO and SA NLO events are 1.036 ± 0.06 and 0.85 ± 0.01 for the SA NLO events, consistent with those reported by *BABAR*. To conclude, in our analysis, it is found that Phokhara over-generates NLO events by approximately 20%, and the extra events are rejected in selections with $\chi^2_{4C,2\pi3\gamma} < 50$.

We estimate the impact of this SA NLO excess on efficiency: the fraction of $E > 100\,\mathrm{MeV}$ events rejected by $\chi^2_{4C,2\pi3\gamma} < 50$ is 14.5% according to signal MC simulation. According to *BABAR* measurements, the SA NLO fraction in data is 0.82 ± 0.03 [131]. Considering that the SA NLO is increasing by $(20 \pm 0.05)\%$ in simulation, the change in signal efficiency is as follows

$$0.145 \times 0.82 \times 0.20 = 0.024. \tag{B.1}$$

Therefore, the signal efficiency is underestimated by $(2.4{\pm}0.7)\%$, that is, the cross section is overestimated.

In addition, consider the effect of the NNLO of $(3.4 \pm 0.4)\%$ [131]. Since Phokhara can only simulate up to NLO events, we estimate the effect of overestimating the efficiency by including NNLO as NLO. From the *BABAR* measurement, the ratio of NNLO to NLO is $0.034/0.22 = 0.155$. From the calculation of NLO net correction, the efficiency reduction is 2.4% when NLO simulation is 20% larger. Therefore, the overestimation of efficiency associated with the phenomenon of NLO event 15.5% is $0.155 \times 0.024/0.20 = (-0.019 \pm 0.005)$ at most. This is the opposite direction of the NLO net correction obtained in the previous section.

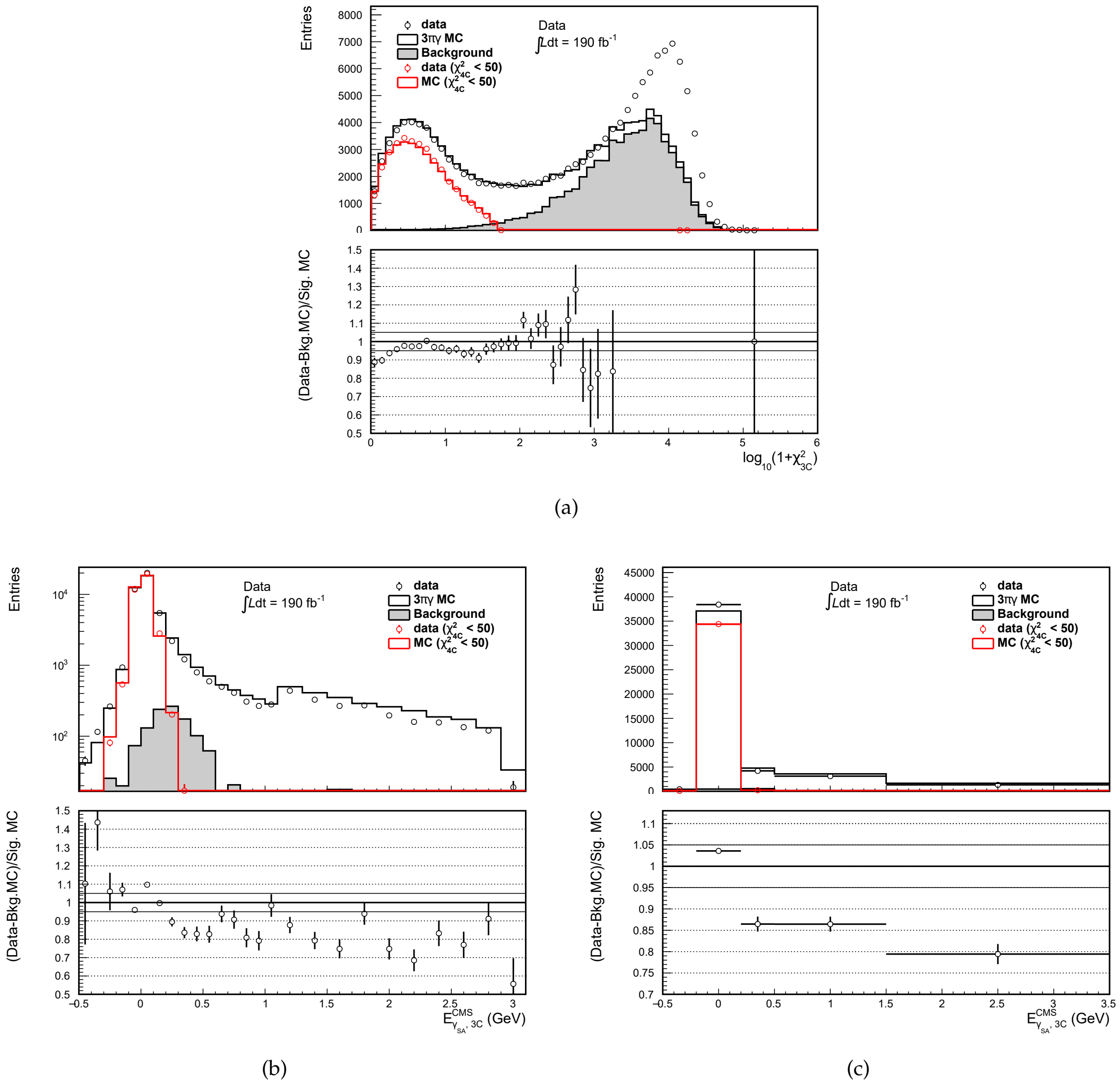

Figure B.4: (a) Distribution of χ^2_{3C} of $e^+e^- \to \pi^+\pi^-\pi^0\gamma$ MC sample. (b)(c) Distribution of energy of γ_{SA} in the c.m. system after $\chi^2_{3C} < 50$ selection in (b) fine and (c) coarse binning. The bottom panels are ratios of the data subtracted from background MC samples to the signal MC sample.

NLO and NNLO net correction sum is $2.4 - 1.9 = (0.5 \pm 0.9)\%$. However, we determined not to apply the 0.5% correction, keeping the cross section unchanged, and assign a systematic uncertainty of 1.2%. For NNLO in particular, since we do not have such a generator available, precise correction using the NNLO generator is a future work. The systematic uncertainty is estimated by a quadratic sum of the error of NLO correction (0.7%) and half of the NNLO corrections (0.95%).

Bibliography

[1] G. Aad et al., ATLAS, "Observation of a new particle in the search for the Standard Model Higgs boson with the ATLAS detector at the LHC", Phys. Lett. B **716** (2012) 1–29, arXiv:1207.7214 [hep-ex].

[2] S. Chatrchyan et al., CMS, "Observation of a New Boson at a Mass of 125 GeV with the CMS Experiment at the LHC", Phys. Lett. B **716** (2012) 30–61, arXiv:1207.7235 [hep-ex].

[3] G. W. Bennett et al., Muon g-2, "Final Report of the Muon E821 Anomalous Magnetic Moment Measurement at BNL", Phys. Rev. D **73** (2006) 072003, arXiv:hep-ex/0602035.

[4] B. Abi et al., Muon g-2, "Measurement of the Positive Muon Anomalous Magnetic Moment to 0.46 ppm", Phys. Rev. Lett. **126** (2021) no. 14, 141801, arXiv:2104.03281 [hep-ex].

[5] D. P. Aguillard et al., Muon g-2, "Measurement of the Positive Muon Anomalous Magnetic Moment to 0.20 ppm", Phys. Rev. Lett. **131** (2023) no. 16, 161802, arXiv:2308.06230 [hep-ex].

[6] T. Aoyama et al., "The anomalous magnetic moment of the muon in the Standard Model", Phys. Rept. **887** (2020) 1–166, arXiv:2006.04822 [hep-ph].

[7] S. Borsanyi et al., "Leading hadronic contribution to the muon magnetic moment from lattice QCD", Nature **593** (2021) no. 7857, 51–55, arXiv:2002.12347 [hep-lat].

[8] A. Anastasi et al., KLOE-2, "Combination of KLOE $\sigma\big(e^+e^- \to \pi^+\pi^-\gamma(\gamma)\big)$ measurements and determination of $a_\mu^{\pi^+\pi^-}$ in the energy range $0.10 < s < 0.95$ GeV^2", JHEP **03** (2018) 173, arXiv:1711.03085 [hep-ex].

[9] F. Ambrosino et al., KLOE, "Measurement of $\sigma(e^+e^- \to \pi^+\pi^-\gamma(\gamma)$ and the dipion contribution to the muon anomaly with the KLOE detector", Phys. Lett. B **670** (2009) 285–291, arXiv:0809.3950 [hep-ex].

[10] F. Ambrosino et al., KLOE, "Measurement of $\sigma(e^+e^- \to \pi^+\pi^-)$ from threshold to 0.85 GeV^2 using Initial State Radiation with the KLOE detector", Phys. Lett. B **700** (2011) 102–110, arXiv:1006.5313 [hep-ex].

[11] D. Babusci et al., KLOE, "Precision measurement of $\sigma(e^+e^- \to \pi^+\pi^-\gamma)/\sigma(e^+e^- \to \mu^+\mu^-\gamma)$ and determination of the $\pi^+\pi^-$ contribution to the muon anomaly with the KLOE detector", Phys. Lett. B **720** (2013) 336–343, arXiv:1212.4524 [hep-ex].

[12] J. P. Lees et al., BaBar, "Precise Measurement of the $e^+e^- \to \pi^+\pi^-(\gamma)$ Cross Section with the Initial-State Radiation Method at BABAR", Phys. Rev. D **86** (2012) 032013, arXiv:1205.2228 [hep-ex].

[13] F. V. Ignatov et al., CMD-3, "Measurement of the $e^+e^- \to \pi^+\pi^-$ cross section from threshold to 1.2 GeV with the CMD-3 detector", arXiv:2302.08834 [hep-ex].

[14] F. V. Ignatov et al., CMD-3, "Measurement of the pion formfactor with CMD-3 detector and its implication to the hadronic contribution to muon (g-2)", arXiv:2309.12910 [hep-ex].

[15] M. Fujikawa et al., Belle, "High-Statistics Study of the tau- —> pi- pi0 nu(tau) Decay", Phys. Rev. D **78** (2008) 072006, arXiv:0805.3773 [hep-ex].

[16] S. Anderson et al., CLEO, “Hadronic structure in the decay tau- —> pi- pi0 neutrino(tau)”, Phys. Rev. D **61** (2000) 112002, `arXiv:hep-ex/9910046`.

[17] S. Schael et al., ALEPH, “Branching ratios and spectral functions of tau decays: Final ALEPH measurements and physics implications”, Phys. Rept. **421** (2005) 191–284, `arXiv:hep-ex/0506072`.

[18] M. Davier, A. Hoecker, A. M. Lutz, B. Malaescu, and Z. Zhang, “Tensions in $e^+e^- \to \pi^+\pi^-(\gamma)$ measurements: the new landscape of data-driven hadronic vacuum polarization predictions for the muon $g-2$”, `arXiv:2312.02053 [hep-ph]`.

[19] C. M. Carloni Calame, M. Passera, L. Trentadue, and G. Venanzoni, “A new approach to evaluate the leading hadronic corrections to the muon g-2”, Phys. Lett. B **746** (2015) 325–329, `arXiv:1504.02228 [hep-ph]`.

[20] G. Colangelo, M. Hoferichter, and P. Stoffer, “Puzzles in the hadronic contributions to the muon anomalous magnetic moment”, in 21st Conference on Flavor Physics and CP Violation. 8, 2023. `arXiv:2308.04217 [hep-ph]`.

[21] T. Aoyama, M. Hayakawa, T. Kinoshita, and M. Nio, “Quantum electrodynamics calculation of lepton anomalous magnetic moments: Numerical approach to the perturbation theory of QED”, PTEP **2012** (2012) 01A107.

[22] T. Aoyama, T. Kinoshita, and M. Nio, “Theory of the Anomalous Magnetic Moment of the Electron”, Atoms **7** (2019) no. 1, 28.

[23] A. Czarnecki, W. J. Marciano, and A. Vainshtein, “Refinements in electroweak contributions to the muon anomalous magnetic moment”, Phys. Rev. D **67** (2003) 073006, `arXiv:hep-ph/0212229`. [Erratum: Phys.Rev.D 73, 119901 (2006)].

[24] C. Gnendiger, D. Stöckinger, and H. Stöckinger-Kim, “The electroweak contributions to $(g-2)_\mu$ after the Higgs boson mass measurement”, Phys. Rev. D **88** (2013) 053005, `arXiv:1306.5546 [hep-ph]`.

[25] M. Davier, A. Hoecker, B. Malaescu, and Z. Zhang, “Reevaluation of the hadronic vacuum polarisation contributions to the Standard Model predictions of the muon $g-2$ and $\alpha(m_Z^2)$ using newest hadronic cross-section data”, Eur. Phys. J. C **77** (2017) no. 12, 827, `arXiv:1706.09436 [hep-ph]`.

[26] A. Keshavarzi, D. Nomura, and T. Teubner, “Muon $g-2$ and $\alpha(M_Z^2)$: a new data-based analysis”, Phys. Rev. D **97** (2018) no. 11, 114025, `arXiv:1802.02995 [hep-ph]`.

[27] G. Colangelo, M. Hoferichter, and P. Stoffer, “Two-pion contribution to hadronic vacuum polarization”, JHEP **02** (2019) 006, `arXiv:1810.00007 [hep-ph]`.

[28] M. Hoferichter, B.-L. Hoid, and B. Kubis, “Three-pion contribution to hadronic vacuum polarization”, JHEP **08** (2019) 137, `arXiv:1907.01556 [hep-ph]`.

[29] M. Davier, A. Hoecker, B. Malaescu, and Z. Zhang, “A new evaluation of the hadronic vacuum polarisation contributions to the muon anomalous magnetic moment and to $\boldsymbol{\alpha}(\mathbf{m_Z^2})$”, Eur. Phys. J. C **80** (2020) no. 3, 241, `arXiv:1908.00921 [hep-ph]`. [Erratum: Eur.Phys.J.C 80, 410 (2020)].

[30] A. Keshavarzi, D. Nomura, and T. Teubner, “$g-2$ of charged leptons, $\alpha(M_Z^2)$, and the hyperfine splitting of muonium”, Phys. Rev. D **101** (2020) no. 1, 014029, `arXiv:1911.00367 [hep-ph]`.

[31] A. Kurz, T. Liu, P. Marquard, and M. Steinhauser, “Hadronic contribution to the muon anomalous magnetic moment to next-to-next-to-leading order”, Phys. Lett. B **734** (2014) 144–147, `arXiv:1403.6400 [hep-ph]`.

[32] T. Aoyama, M. Hayakawa, T. Kinoshita, and M. Nio, “Complete Tenth-Order QED Contribution to the Muon g-2”, Phys. Rev. Lett. **109** (2012) 111808, `arXiv:1205.5370 [hep-ph]`.

[33] R. Bouchendira, P. Clade, S. Guellati-Khelifa, F. Nez, and F. Biraben, “New determination of the fine structure constant and test of the quantum electrodynamics”, Phys. Rev. Lett. **106** (2011) 080801, `arXiv:1012.3627 [physics.atom-ph]`.

[34] L. Morel, Z. Yao, P. Cladé, and S. Guellati-Khélifa, “Determination of the fine-structure constant with an accuracy of 81 parts per trillion”, Nature **588** (2020) no. 7836, 61–65.

[35] X. Fan, T. G. Myers, B. A. D. Sukra, and G. Gabrielse, “Measurement of the Electron Magnetic Moment”, Phys. Rev. Lett. **130** (2023) no. 7, 071801, `arXiv:2209.13084 [physics.atom-ph]`.

[36] D. Hanneke, S. Fogwell, and G. Gabrielse, “New Measurement of the Electron Magnetic Moment and the Fine Structure Constant”, Phys. Rev. Lett. **100** (2008) 120801, `arXiv:0801.1134 [physics.atom-ph]`.

[37] R. L. Workman et al., Particle Data Group, “Review of Particle Physics”, PTEP **2022** (2022) 083C01.

[38] F. Jegerlehner, The Anomalous Magnetic Moment of the Muon, vol. 274. Springer, Cham, 2017.

[39] R. Barbieri and E. Remiddi, “Electron and Muon 1/2(g-2) from Vacuum Polarization Insertions”, Nucl. Phys. B **90** (1975) 233–266.

[40] F. Jegerlehner and A. Nyffeler, “The Muon g-2”, Phys. Rept. **477** (2009) 1–110, `arXiv:0902.3360 [hep-ph]`.

[41] S. J. Brodsky and E. De Rafael, “SUGGESTED BOSON - LEPTON PAIR COUPLINGS AND THE ANOMALOUS MAGNETIC MOMENT OF THE MUON”, Phys. Rev. **168** (1968) 1620–1622.

[42] A. Nyffeler, “Hadronic light-by-light scattering in the muon g $-$ 2”, EPJ Web Conf. **218** (2019) 01001, `arXiv:1710.09742 [hep-ph]`.

[43] T. Moroi, “The Muon anomalous magnetic dipole moment in the minimal supersymmetric standard model”, Phys. Rev. D **53** (1996) 6565–6575, `arXiv:hep-ph/9512396`. [Erratum: Phys.Rev.D 56, 4424 (1997)].

[44] M. Endo, K. Hamaguchi, S. Iwamoto, and T. Kitahara, “Supersymmetric interpretation of the muon g – 2 anomaly”, JHEP **07** (2021) 075, `arXiv:2104.03217 [hep-ph]`.

[45] G. Krnjaic, G. Marques-Tavares, D. Redigolo, and K. Tobioka, “Probing Muonphilic Force Carriers and Dark Matter at Kaon Factories”, Phys. Rev. Lett. **124** (2020) no. 4, 041802, `arXiv:1902.07715 [hep-ph]`.

[46] M. A. Buen-Abad, J. Fan, M. Reece, and C. Sun, “Challenges for an axion explanation of the muon $g-2$ measurement”, JHEP **09** (2021) 101, `arXiv:2104.03267 [hep-ph]`.

[47] P. Athron, C. Balázs, D. H. J. Jacob, W. Kotlarski, D. Stöckinger, and H. Stöckinger-Kim, “New physics explanations of a_μ in light of the FNAL muon g $-$ 2 measurement”, JHEP **09** (2021) 080, `arXiv:2104.03691 [hep-ph]`.

[48] S. Iguro, T. Kitahara, M. S. Lang, and M. Takeuchi, “Current status of the muon g-2 interpretations within two-Higgs-doublet models”, Phys. Rev. D **108** (2023) no. 11, 115012, `arXiv:2304.09887 [hep-ph]`.

[49] G. Bonneau and F. Martin, “Hard photon emission in e+ e- reactions”, Nucl. Phys. B **27** (1971) 381–397.

[50] M. Benayoun, S. I. Eidelman, V. N. Ivanchenko, and Z. K. Silagadze, “Spectroscopy at B factories using hard photon emission”, Mod. Phys. Lett. A **14** (1999) 2605–2614, `arXiv:hep-ph/9910523`.

[51] M. N. Achasov et al., “Measurements of the parameters of the $\phi(1020)$ resonance through studies of the processes $e^+e^- \to K^+K^-$, K_SK_L, and $\pi^+\pi^-\pi^0$”, Phys. Rev. D **63** (2001) 072002, `arXiv:hep-ex/0009036`.

[52] M. N. Achasov et al., “Study of the process $e^+e^- \to \pi^+\pi^-\pi^0$ in the energy region s**(1/2) from 0.98-GeV to 1.38-GeV”, Phys. Rev. D **66** (2002) 032001, `arXiv:hep-ex/0201040`.

[53] M. N. Achasov et al., "Study of the process $e^+e^- \to \pi^+\pi^-\pi^0$ in the energy region s**(1/2) below 0.98-GeV", Phys. Rev. D **68** (2003) 052006, arXiv:hep-ex/0305049.

[54] V. M. Aul'chenko et al., "Study of the e$^+$ e$\check{}$ $\to \pi^+\pi\check{}\,\pi^0$ process in the energy range 1.05–2.00 GeV", J. Exp. Theor. Phys. **121** (2015) no. 1, 27–34.

[55] R. R. Akhmetshin et al., "Measurement of phi meson parameters with CMD-2 detector at VEPP-2M collider", Phys. Lett. B **364** (1995) 199–206.

[56] R. R. Akhmetshin et al., "Study of dynamics of $\phi \to \pi^+\pi^-\pi^0$ decay with CMD-2 detector", Phys. Lett. B **434** (1998) 426–436.

[57] R. R. Akhmetshin et al., CMD-2, "Reanalysis of hadronic cross-section measurements at CMD-2", Phys. Lett. B **578** (2004) 285–289, arXiv:hep-ex/0308008.

[58] R. R. Akhmetshin et al., "Study of $\phi \to \pi^+\pi^-\pi^0$ with CMD-2 detector", Phys. Lett. B **642** (2006) 203–209.

[59] B. Aubert et al., BABAR, "Study of $e^+e^- \to \pi^+\pi^-\pi^0$ process using initial state radiation with BaBar", Phys. Rev. D **70** (2004) 072004, arXiv:hep-ex/0408078.

[60] J. P. Lees et al., BABAR, BaBar, "Study of the process $e^+e^- \to \pi^+\pi^-\pi^0$ using initial state radiation with BABAR", Phys. Rev. D **104** (2021) no. 11, 112003, arXiv:2110.00520 [hep-ex].

[61] M. Ablikim et al., BESIII, "Measurement of the $e^+e^- \to \pi^+\pi^-\pi^0$ Cross Section from 0.7 GeV to 3.0 GeV via Initial-State Radiation", arXiv:1912.11208 [hep-ex].

[62] A. Cordier et al., "Cross-section of the Reaction $e^+e^- \to \pi^+\pi^-\pi^0$ for Center-of-mass Energies From 750-MeV to 1100-MeV", Nucl. Phys. B **172** (1980) 13–24.

[63] S. I. Dolinsky et al., "Summary of experiments with the neutral detector at the e^+e^- storage ring VEPP-2M", Phys. Rept. **202** (1991) 99–170.

[64] A. Antonelli et al., DM2, "Measurement of the $e^+e^- \to \pi^+\pi^-\pi^0$ and $e^+e^- \to \omega\pi^+\pi^-$ reactions in the energy interval 1350-MeV - 2400-MeV", Z. Phys. C **56** (1992) 15–20.

[65] M. Hoferichter, B.-L. Hoid, B. Kubis, and D. Schuh, "Isospin-breaking effects in the three-pion contribution to hadronic vacuum polarization", JHEP **08** (2023) 208, arXiv:2307.02546 [hep-ph].

[66] K. Akai, K. Furukawa, and H. Koiso, SuperKEKB, "SuperKEKB Collider", Nucl. Instrum. Meth. A **907** (2018) 188–199, arXiv:1809.01958 [physics.acc-ph].

[67] Y. Ohnishi et al., "Accelerator design at SuperKEKB", PTEP **2013** (2013) 03A011.

[68] T. Abe et al., "Preliminary version of Technical Design Report of SuperKEKB", , 2014.

[69] "KEKB B factory design report", .

[70] W. Altmannshofer et al., Belle II, "The Belle II Physics Book", PTEP **2019** (2019) no. 12, 123C01, arXiv:1808.10567 [hep-ex]. [Erratum: PTEP 2020, 029201 (2020)].

[71] KEK, "Luminosity history", https://www-superkekb.kek.jp/index.html, 2022.

[72] T. Abe, Belle II, "Belle II Technical Design Report", arXiv:1011.0352 [physics.ins-det].

[73] I. Adachi, T. E. Browder, P. Križan, S. Tanaka, and Y. Ushiroda, Belle II, "Detectors for extreme luminosity: Belle II", Nucl. Instrum. Meth. A **907** (2018) 46–59.

[74] K. Adamczyk et al., Belle II SVD, "The design, construction, operation and performance of the Belle II silicon vertex detector", JINST **17** (2022) no. 11, P11042, arXiv:2201.09824 [physics.ins-det].

[75] N. Braun, A. Glazov, E. Paoloni, and C. Praz, "Study of the d0 track resolution", . Figure from BELLE2-NOTE-PH-2018-040.

[76] B. Wang et al., Belle II DEPFET, PXD, "Operational experience of the Belle II pixel detector", Nucl. Instrum. Meth. A **1032** (2022) 166631.

[77] T. V. Dong, S. Uno, M. Uchida, H. Ozaki, N. Taniguchi, E. Nakano, and K. Trabelsi, "Calibration and alignment of the Belle II central drift chamber", Nucl. Instrum. Meth. A **930** (2019) 132–141.

[78] S. Iwata et al., "Particle identification performance of the prototype aerogel RICH counter for the Belle II experiment", PTEP **2016** (2016) no. 3, 033H01, `arXiv:1603.02503 [physics.ins-det]`.

[79] M. Yonenaga et al., "Performance evaluation of the aerogel RICH counter for the Belle II spectrometer using early beam collision data", PTEP **2020** (2020) no. 9, 093H01, `arXiv:2008.06251 [physics.ins-det]`.

[80] S. P. Maharana;, V. V. S;, and S. Sandilya, "Charged Particle Identification Performances in Belle II", .

[81] U. Tamponi, "The TOP counter of Belle II: status and first results", `arXiv:1811.04532 [hep-ex]`.

[82] B. I. C. P. Group, "Muon and electron identification efficiencies and hadron-lepton mis-identification rates at Belle II for Moriond 2022", .

[83] A. Abashian et al., Belle, "The Belle Detector", Nucl. Instrum. Meth. A **479** (2002) 117–232.

[84] D. Levit et al., "Trigger Timing Interface for the Read-Out Upgrade of the Belle II DAQ", IEEE Trans. Nucl. Sci. **70** (2023) no. 6, 941–948.

[85] T. Hara, Belle II Computing Group, "Computing at the Belle II experiment", J. Phys. Conf. Ser. **664** (2015) no. 1, 012002.

[86] M. Nakao et al., "Performance of the Unified Readout System of Belle II", IEEE Trans. Nucl. Sci. **68** (2021) no. 8, 1826–1832, `arXiv:2010.15485 [physics.ins-det]`.

[87] J. Zhou, X. Zhou, and C. Shen, "Offline measurements of integrated luminosities of Moriond 2023 datasets (internal)", .

[88] S. Agostinelli et al., GEANT4, "GEANT4: A Simulation toolkit", Nucl.Instrum.Meth. **A506** (2003) 250–303.

[89] G. Rodrigo, A. Gehrmann-De Ridder, M. Guilleaume, and J. H. Kuhn, "NLO QED corrections to ISR in e^+e^- annihilation and the measurement of $\sigma(e^+e^- \to hadrons)$ using tagged photons", Eur. Phys. J. C **22** (2001) 81–88, `arXiv:hep-ph/0106132`.

[90] H. Czyz, A. Grzelinska, J. H. Kuhn, and G. Rodrigo, "Electron-positron annihilation into three pions and the radiative return", Eur. Phys. J. C **47** (2006) 617–624, `arXiv:hep-ph/0512180`.

[91] A. Natochii, S. E. Vahsen, H. Nakayama, T. Ishibashi, and S. Terui, "Improved simulation of beam backgrounds and collimation at SuperKEKB", Phys. Rev. Accel. Beams **24** (2021) no. 8, 081001, `arXiv:2104.02645 [physics.acc-ph]`.

[92] T. Kuhr, C. Pulvermacher, M. Ritter, T. Hauth, and N. Braun, Belle II Framework Software Group, "The Belle II Core Software", Comput. Softw. Big Sci. **3** (2019) no. 1, 1, `arXiv:1809.04299 [physics.comp-ph]`.

[93] Belle II collaboration, "Belle II Analysis Software Framework (basf2)", `https://doi.org/10.5281/zenodo.5574115`.

[94] V. Bertacchi et al., Belle II Tracking Group, "Track finding at Belle II", Comput. Phys. Commun. **259** (2021) 107610, `arXiv:2003.12466 [physics.ins-det]`.

[95] S. Spataro, Belle II Tracking Group, "Track Fitting for the Belle II Experiment", EPJ Web Conf. **214** (2019) 02039.

[96] J. Rauch and T. Schlüter, "GENFIT — a Generic Track-Fitting Toolkit", J. Phys. Conf. Ser. **608** (2015) no. 1, 012042, `arXiv:1410.3698 [physics.ins-det]`.

[97] T. Bilka et al., "Implementation of GENFIT2 as an experiment independent track-fitting framework", arXiv:1902.04405 [physics.data-an].

[98] R. Brun, F. Bruyant, M. Maire, A. C. McPherson, and P. Zanarini, "GEANT3", .

[99] N. Dawe. https://github.com/ndawe/tikz-track, 2016.

[100] "Belle 2 Software Documentation", Online. https://software.belle2.org/sphinx/light-2210-devonrex/analysis/doc/Variables.html?highlight=cluster%20second%20moment#variable-clusterSecondMoment.

[101] J. Tanaka, Precise Measurements of Charm Meson Lifetimes and Search for $D^0 - -D^0$ Mixing. PhD thesis, University of Tokyo, 3, 2002. https://belle.kek.jp/belle/theses/doctor/2002/tanaka.pdf.

[102] P. Avery, "Applied Fitting Theory", .

[103] H. Ikeda et al., Belle, "A detailed test of the CsI(Tl) calorimeter for BELLE with photon beams of energy between 20-MeV and 5.4-GeV", Nucl. Instrum. Meth. A **441** (2000) 401–426.

[104] B. Aubert et al., BABAR, "Measurements of $e^+e^- \to K^+K^-\eta$, $K^+K^-\pi^0$ and $K_s^0K^\pm\pi^\mp$ cross-sections using initial state radiation events", Phys. Rev. D **77** (2008) 092002, arXiv:0710.4451 [hep-ex].

[105] C. P. Shen et al., Belle, "Measurement of $e^+e^- \to \omega\pi^0$, $K^*(892)\bar{K}$ and $K_2^*(1430)\bar{K}$ at $\sqrt{s}$ near 10.6 GeV", Phys. Rev. D **88** (2013) no. 5, 052019, arXiv:1309.0575 [hep-ex].

[106] C.-D. Lü, W. Wang, Y. Xing, and Q.-A. Zhang, "Perturbative QCD analysis of exclusive processes $e^+e^- \to VP$ and $e^+e^- \to TP$", Phys. Rev. D **97** (2018) no. 11, 114016, arXiv:1802.09718 [hep-ph].

[107] G. S. Adams et al., CLEO, "Decay of the psi(3770) to light hadrons", Phys. Rev. D **73** (2006) 012002, arXiv:hep-ex/0509011.

[108] N. N. Achasov, V. V. Gubin, and E. P. Solodov, "The Interference in the reaction e^+e^- to gamma $\pi^+\pi^-$ and the search for the decay $\phi \to \gamma f(0) \to \gamma\pi^+\pi^-$", Phys. Rev. D **55** (1997) 2672–2682, arXiv:hep-ph/9610282.

[109] B. Aubert et al., BABAR, "Measurement of the eta and eta-prime transition form-factors at q**2 = 112-GeV**2", Phys. Rev. D **74** (2006) 012002, arXiv:hep-ex/0605018.

[110] R. C. Verma, "Decay constants and form factors of s-wave and p-wave mesons in the covariant light-front quark model", J. Phys. G **39** (2012) 025005, arXiv:1103.2973 [hep-ph].

[111] P. A. Zyla et al., Particle Data Group, "Review of Particle Physics", PTEP **2020** (2020) no. 8, 083C01.

[112] M. Aghasyan et al., COMPASS, "Light isovector resonances in $\pi^-p \to \pi^-\pi^-\pi^+p$ at 190 GeV/c", Phys. Rev. D **98** (2018) no. 9, 092003, arXiv:1802.05913 [hep-ex].

[113] K. Chen, C.-Q. Pang, X. Liu, and T. Matsuki, "Light axial vector mesons", Phys. Rev. D **91** (2015) no. 7, 074025, arXiv:1501.07766 [hep-ph].

[114] D. Barberis et al., WA102, "A Study of the centrally produced pi0 pi0 pi0 channel in p p interactions at 450-GeV/c", Phys. Lett. B **507** (2001) 14–18, arXiv:hep-ex/0104017.

[115] H.-Y. Cheng, Y. Koike, and K.-C. Yang, "Two-parton Light-cone Distribution Amplitudes of Tensor Mesons", Phys. Rev. D **82** (2010) 054019, arXiv:1007.3541 [hep-ph].

[116] T. Barnes, F. E. Close, P. R. Page, and E. S. Swanson, "Higher quarkonia", Phys. Rev. D **55** (1997) 4157–4188, arXiv:hep-ph/9609339.

[117] B. II, "Measurement of the tracking efficiency and fake rate with $e^+e^- \to \tau^+\tau^-$ events", .

[118] H. Svidras, M. Röhrken, S. Wehle, and K. Tackmann, "Measurement of the data to MC ratio of photon reconstruction efficiency of the Belle II calorimeter using radiative muon pair events", .

[119] T. Ferber, "OrcaKinFit: Kinematic Fitting for Belle II", . https://docs.belle2.org/record/483.

[120] B. Malaescu, "An Iterative, Dynamically Stabilized(IDS) Method of Data Unfolding", in PHYSTAT 2011, pp. 271–275. 2011. arXiv:1106.3107 [physics.data-an].

[121] T. Adye, "Unfolding algorithms and tests using RooUnfold", in PHYSTAT 2011, pp. 313–318. CERN, Geneva, 2011. arXiv:1105.1160 [physics.data-an].

[122] Belle II collaboration. in preparation.

[123] E. D. L. Cruz-Burelo, M. Hernandez-Villanueva, A. Rostomyan, and N. Rad, "Measurement of the τ lepton mass at Belle II", . https://docs.belle2.org/record/3369.

[124] T. B. I. T. Group, "Tracking Performance in Early Belle II Data", . (Internal note).

[125] M. N. Achasov et al., SND, "Study of dynamics of the process $e^+e^- \to \pi^+\pi^-\pi^0$ in the energy range 1.15–2.00 GeV", Eur. Phys. J. C **80** (2020) no. 10, 993, arXiv:2007.14595 [hep-ex].

[126] F. V. Ignatov. PhD thesis, Novosibirsk State U., 2008.

[127] F. Ignatov. https://cmd.inp.nsk.su/~ignatov/vpl/.

[128] H. Czyz and J. H. Kuhn, "Four pion final states with tagged photons at electron positron colliders", Eur. Phys. J. C **18** (2001) 497–509, arXiv:hep-ph/0008262.

[129] M. Caffo, H. Czyz, and E. Remiddi, "BHAGEN95: A Monte Carlo program for Bhabha scattering at LEP-1 / SLC and LEP-2 energies", Nuovo Cim. A **110** (1997) 515–536, arXiv:hep-ph/9704443.

[130] M. Caffo, H. Czyz, and E. Remiddi, "Order alpha**2 leading logarithmic corrections in Bhabha scattering at LEP / SLC energies", Phys. Lett. B **327** (1994) 369–376.

[131] J. P. Lees et al., BABAR, "Measurement of additional radiation in the initial-state-radiation processes $e^+e^- \to \mu^+\mu^-\gamma$ and $e^+e^- \to \pi^+\pi^-\gamma$ at BABAR", Phys. Rev. D **108** (2023) no. 11, L111103, arXiv:2308.05233 [hep-ex].